THE PROPAGATION OF THE INTERNAL TIDE AROUND A BEND IN KNIGHT INLET, B.C.

by

ANTHONY JAMES WEBB

B.A., University of Cambridge, England, 1980

M.Sc., University College of North Wales, 1981

A THESIS SUBMITTED IN PARTIAL FULFILMENT OF

THE REQUIREMENTS FOR THE DEGREE OF

DOCTOR OF PHILOSOPHY

in

THE FACULTY OF GRADUATE STUDIES

Oceanography

We accept this thesis as conforming

to the required standard

THE UNIVERSITY OF BRITISH COLUMBIA

SEPT 1985

In presenting this thesis in partial fulfilment of the requirements for an advanced degree at the University of British Columbia, I agree that the Library shall make it freely available for reference and study. I further agree that permission for extensive copying of this thesis for scholarly purposes may be granted by the head of my department or by his or her representatives. It is understood that copying or publication of this thesis for financial gain shall not be allowed without my written permission.

Department of OCEANOGRAPHY

The University of British Columbia
1956 Main Mall
Vancouver, Canada
V6T 1Y3

Date 3rd October 1985

Abstract

This thesis seeks to answer the question "how much of the internal tide propagating up Knight Inlet, B.C. is reflected by a right-angled bend ?" The internal tide in Knight Inlet is generated by the interaction of the barotropic tide with a shallow sill seaward of the bend. It then propagates in both directions as a travelling Kelvin wave. The up-inlet propagating wave then encounters the bend, where some of it may be reflected. This question is looked at with both theory (Chapter 2) and observations (Chapter 3).

The theoretical study investigates the propagation of a Kelvin wave around a bend in a channel. The solution of the linearised long wave equations is expressed as a truncated series of cross-channel modes in each of three regions. The solution is matched across the two common boundaries by a least squares point matching process. The "rectangular bend" gives unsatisfactory results because of a singularity in the velocity field at the sharp inside corner. However, the "annular bend" gives good results. The bend acts as a diffraction grating, with total transmission for certain bend angles and "lobes" of high reflection for intermediate angles. Bends to the left give rise to the same reflection as bends to the right of the same angle, even if the incident Kelvin wave has a small cross-channel decay scale. For the parameters corresponding to the M_2 internal tide in Knight Inlet, the energy flux reflection coefficient is very small, much less than 1%. The method of solution breaks down inexplicably for diurnal tides.

The observational study is based upon $2\frac{1}{3}$ months of cyclesonde current meter data from four stations in Knight Inlet taken during the summers of 1981 and 1983. The vertical profiles of amplitude and phase of the M_2 constituent of longitudinal velocity and density fluctuations are found to be the same from month to month at a particular station, but different from station to station. These complex amplitude profiles are decomposed into a truncated series of normal modes for waves propagating both up-inlet and down-inlet. The phase speeds and zero-crossing depths of the normal modes do not agree with those calculated by Farmer and Smith (1980a) using 1977 data. Two simple models of the stratification are used to explain the differences in the normal modes in terms of differences

in the Brunt-Väisälä frequency profile used to calculate them. At the two stations up-inlet of the sill, acceptable fits can be obtained using only two up-inlet propagating waves, indicating that the data are compatible with the low reflection found in the theoretical study. When down-inlet waves are included in the fit, their amplitudes are found to be small, although care must be taken to avoid trying to fit too many modes since some of them are highly correlated in the depth range for which data are available. At the two stations seaward of the sill, the up-inlet energy flux is of the same order of magnitude as the down-inlet flux, indicating a second source of internal tide seaward of those two stations. The results indicate that only 30–50% of the power removed from the barotropic tide is being fed into the internal tide in the summer. This conclusion is at variance with that of Stacey (1985), whose model shows that most of the power lost from the barotropic tide is being fed into the internal tide. A consistent interpretation of these results is that most of the power lost from the barotropic tide initially goes into the internal tide, but that 50–70% of it is rapidly dissipated through turbulence within a couple of kilometers of the sill.

The low frequency component of the velocity signals from the cyclesonde data is also presented (Chapter 4), with a brief analysis . The monthly averaged residual velocity profiles are also found to be fairly repeatable from month to month at a particular station, but different from station to station. These profiles could be useful in validating general circulation models.

Table of Contents

List of Figures

List of Tables

Acknowledgements

I would like to thank my research supervisor, Professor S. Pond, for his steadfast moral support and guidance over the last four years, Professors P.H. LeBlond and L.A. Mysak for their help and teaching, Doctors D.M. Farmer and H.J. Freeland for originally suggesting the problem and for their continued interest in it, B. de Young for the use of his spectral analysis program and for hours of discussion, Doctor M. Foreman for the use of his harmonic analysis program, the officers and crew of the C.S.S. Vector for their assistance in the data collection, D. Toffoli for typing and proof-reading this thesis and my parents for their encouragement.

This research was supported by the Natural Sciences and Engineering Research Council of Canada (Grant A-8301). I appreciate personal support from the Canadian Commonwealth Scholarship and Fellowship Plan.

1. Introduction

1.1 Historical Background

The first oceanographic measurements in Knight Inlet were made by G.L. Pickard in a series of surveys of B.C. inlets by the Institute of Oceanography at U.B.C. starting in 1949. The results are described in Pickard (1956, 1961). The first of these two papers is mainly a description of the geometries of B.C. inlets, whereas the second is a thorough account of their water characteristics (salinity, temperature, oxygen and turbidity) and changes thereof. He also carried out the first current measurements in Knight Inlet using current drag and Ekman current meters (Pickard and Rodgers 1959). Since then U.B.C. personnel returned every year except 1960-62 up to 1974 as part of their survey of the water characteristics of B.C. fjords. Pickard (1975) gives an account of the long term variations of the deep water properties in Knight Inlet as well as elsewhere, using these data.

Current measurements were not, however, routinely done. Before the arrival of internally recording current meters in the 1960s, any kind of direct current measurement required an enormous amount of effort, since the ship had to anchor. Since such measurements could be done for at most a few days, the effects of variations in wind stress and the lunar cycle could not be isolated from the "mean" circulation, so there was little point in any greater effort. For example, it was easier to measure the river discharge by inferring it from the heat budget of the inlet (based upon temperature and salinity measurements), than by direct measurement (Pickard and Trites 1957).

Knight Inlet is distinguished by being a long, regular inlet with a large fresh water input at the head, and a shallow sill. The interaction of the sill with the high summer stratification produces large internal waves, both of short period (a few minutes) and of tidal period (the "internal tide"). The short period internal waves were the subject of more recent extensive investigation by Farmer and Smith (1978, 1980a, 1980b). They used a large selection of modern instruments, including a string of Aanderaa current meters fitted with conductivity cells and fast response thermistors, three orthogonally mounted

precision mechanical current meters, an electromagnetic current meter and an acoustic current meter. In addition they took CTD surveys of the inlet, and used acoustic sounding techniques to generate images of the hydraulic jumps that occur in the vicinity of the sill. This was the first measurement of currents in Knight Inlet since Pickard and Rodgers' comparatively primitive attempt in July 1956.

In the last seven years a considerable amount of work has been done on Knight Inlet. A recent review of fjords by Farmer and Freeland (1983) is an excellent reference, as are the proceedings of the NATO conference on Fjord Oceanography, edited by Freeland, Farmer and Levings (1980). Both of these publications contain many references to Knight Inlet, both as an object of study in its own right, and as an example illustrating the mechanisms under discussion. Knight Inlet has very energetic processes occurring at the sill which generate large internal waves and tides, and for that reason is a popular site to investigate such phenomena. It has also become a testing ground for several different theories of fjord circulation; such comparisons are more easily made using data from a single fjord. The energy-transfer processes occurring between the tide, the resulting internal tides and the tidal-mean circulation play an important role in generating the mixing that is an essential element in determining the net fluxes of matter in fjords. It is the adequate parameterisation of mixing that remains the major deficiency in any modelling attempt to make quantitative predictions of the fluxes and resulting distribution of substances that are introduced into an estuary. This study therefore seeks to investigate the governing processes in a particular type of estuary, namely a deep, strongly stratified fjord.

1.2 Physical Oceanography of Knight Inlet

1.2.1 Physical Description of the Inlet and Freshwater Input

Knight Inlet is generally regarded as the most spectacular fjord in the SW sector of the province, towered over by snow-capped peaks as high as 3300 m. It is roughly 100 km long, measured from the head to the first subsidiary inlet, with an average width of 2.5 km. Knight Inlet is the third longest of the B.C. mainland inlets. *Figure 1* shows a plan view and longitudinal depth profile. The sill is clearly visible 75 km from the head, where the depth falls to 60 m. The sill is in the middle of a long straight reach, while the rest of the inlet from the head to the bend between Tomakstum Island and Adeane Point is sinuous. The sides of the inlet are quite steep, with typical slopes of 30° towards the mouth and 60° towards the head. The average mid-channel depth is 400 m, and the greatest depth is 550 m. In comparison Jervis Inlet, the deepest on the B.C. coast, has an average depth of 500 m and a greatest depth of 725 m.

Most of the freshwater enters at the head, with a mean annual discharge of 400 m^3/s. There are usually two peaks in the year, one in June of about 800 m^3/s due to snowmelt, and a lesser one in November due to rain. Pickard (1961) calls the summer peak "stored runoff," and the winter peak "direct runoff." The typical winter runoff is 50 m^3/s. Knight has the seventh largest freshwater discharge of all B.C, inlets, with Portland Inlet having the largest with an annual mean of 990 m^3/s. For this reason, a two-layer density structure is a good description of the inlet for most of the year. In fact, two two-layer estuary models have selected Knight as an archetype (Long 1975, Pearson and Winter 1975).

The mean (non-tidal) circulation is a consequence of the fresh-water discharge at the head. It forms a low salinity surface layer which flows seaward, gaining volume by the entrainment of saline water from below and gaining in speed. There is also a deepening of the brackish layer towards the mouth. An up-inlet flow at depth must compensate for the entrainment. The wind also has a large effect on the non-tidal circulation, but its speed and direction are unpredictable (varying on a time scale of a few days). When comparing circulation models with real data, the wind is often assumed to have a zero mean effect if

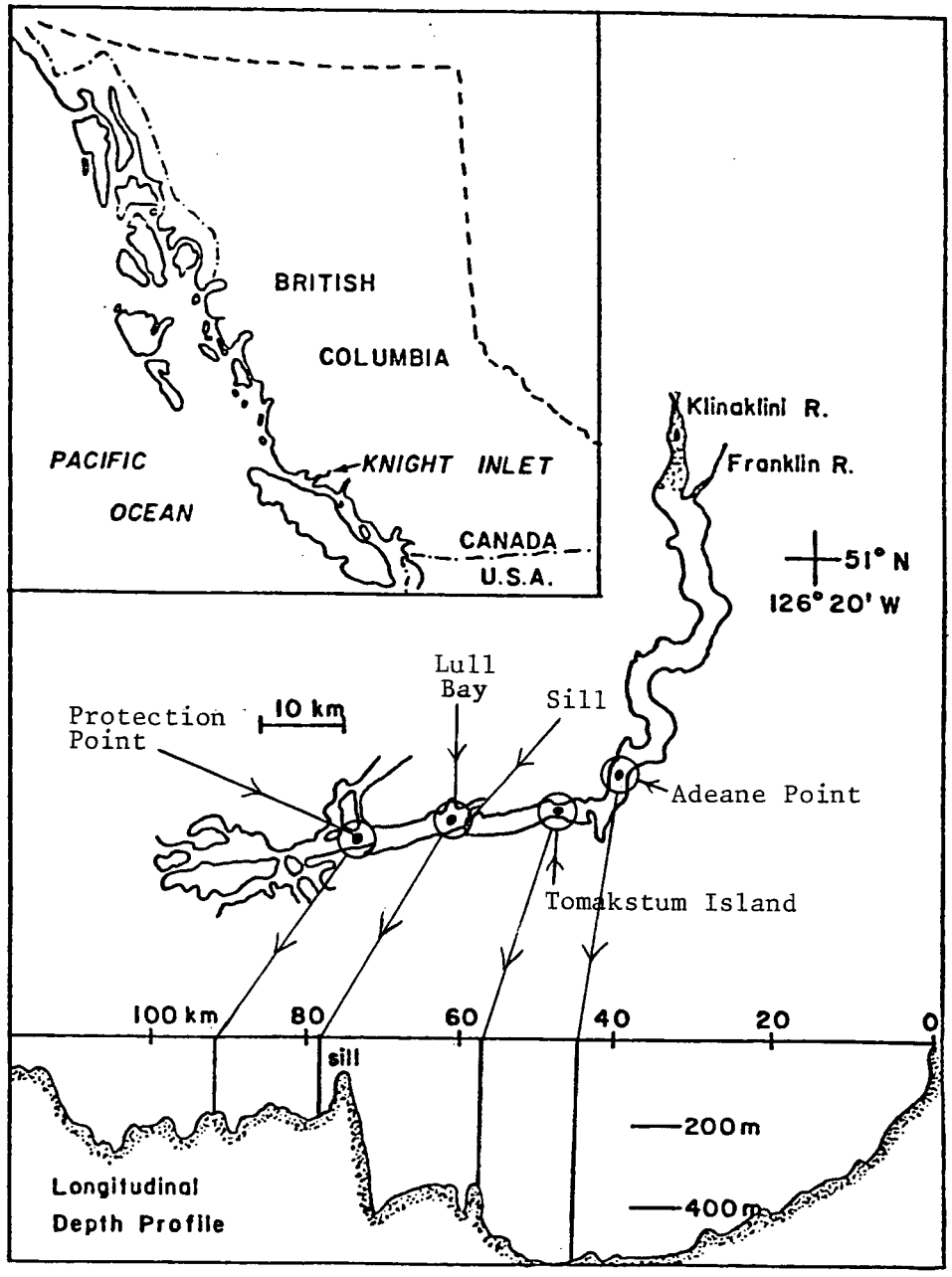

Figure 1 Plan view and longitudinal depth profile of Knight Inlet. (After Blackford 1984.)

averaged over a sufficiently long period.

1.2.2 Salinity

According to Pickard's (1961) classification of B.C. fjords, Knight is a type A1 inlet, with a low (less than 2 ‰) surface salinity at the head, and a high (around 20 ‰) surface salinity at the mouth. A type A1 inlet means one with a large runoff, in most cases from glaciers or snowfields. In the winter, however, the surface salinity and temperature are nearly constant along the inlet, because of the low runoff at that time. In terms of the vertical salinity profile, Knight has a type 1(a) profile at the head, and a type 1(b) profile elsewhere. This classification means that Knight Inlet has a homogeneous surface layer with a distinct halocline, which is sharper at the head of the inlet than elsewhere. The depth of the halocline increases from around 5 m at the head to around 15 m at the mouth.

In the range of values of temperature and salinity found in Knight Inlet, salinity has a much greater effect on density than temperature. In fact, density profiles take on more or less the same shape as salinity profiles.

Below the halocline, the salinity increases monotonically to the bottom. The salinity at 20 m is typically 29.8 ‰, at 50 m it is about 30.7 ‰, and at 100 m it is 31.0 ‰. This deep water value lies between typical values of 28 to 30 ‰ for southern mainland inlets, and of 32 to 34 ‰ for northern inlets. Pickard (1961) suggests that this northwards increase in deepwater salinity is associated with the directness or otherwise of the connection with the Pacific (as the source of the most saline water).

1.2.3 Temperature

In the summer, temperature profiles in the "shallow zone" (the upper 20 m or so) are a mirror image about a vertical axis of the salinity profile because the water in the shallow zone is a result of mixing of the warmer fresh surface water with the cold saline deep water. *Figure 2* shows an excellent example of a straight T–S curve arising from the mixing of two water types. Typical summer figures are 14° C at the surface and 8° C in the underlying water.

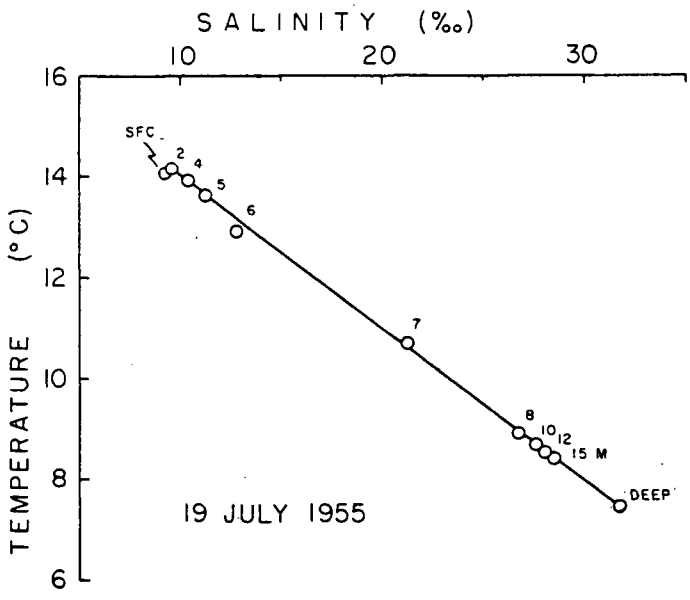

Figure 2 T–S curve near the sill. (From Pickard 1961.)

Below the thermocline associated with the halocline, the temperature profiles often show maxima or minima at intermediate depths. A temperature minimum at about 50 to 100 m in depth is present in Knight Inlet, and is a general feature of B.C. inlets (most noticable in Bute Inlet). The temperature decreases from a summer value of roughly 9° C at 20 m to a minimum of 8° C at 50 m, and then gradually rises again to a bottom value of 8.5° C. This temperature minimum has been attributed to winter cooling and wind mixing of the upper part of the water column, followed in spring and summer by a warming of the surface. The higher density stratification in spring and summer tends to inhibit wind mixing and thus serves to preserve the effects of the distributed heat loss that occurred in winter.

1.2.4 Time Variations in Temperature and Salinity

The most noticeable signal in temperature and salinity time series is the internal tide. It is caused by the barotropic tide forcing stratified water to flow over the sill leading to a vertical oscillation at tidal period of the isopycnals and isohalines by as much as $50\,m$ peak-to-peak in the straight section of the inlet. Equivalently there are temperature deviations of $0.05°\,C$ and salinity deviations of $0.4\,‰$ at depths of 50–150 m. The signal is modulated on the spring/neaps cycle.

An annual signal is also present at most depths. The variability decreases with increasing depth. The only available data to show this annual signal well are a set of 23 cruises over the period 1972–74 (Pickard 1975). Both temperature and salinity below $100\,m$ show a maximum around December, with peak-to-peak values of $0.5°\,C$ and $0.6\,‰$ respectively. Pickard describes the signal in Knight to be "sinusoidal", as opposed to "peaked" or "saw tooth" as found elsewhere. The amount of dissolved oxygen also shows an annual sinusoidal variation of $1\,ml/l$ peak-to peak, with a maximum around March. The dissolved oxygen in Knight Inlet ranges from 3 to $5\,ml/l$ below $100\,m$, with higher values above $100\,m$. It is nowhere anoxic. Pickard suggests that these annual variations are caused by longitudinal advection, rather than vertical advection, diffusion etc, and that this longitudinal advection occurs during a late winter replacement of the deep water. The annual variation of river runoff and air temperature have a direct effect on the salinity and temperature of the surface waters. In the winter the halocline and associated pycnocline are almost non-existent (see *Figure 3*). In the spring, they are evident at the head of the inlet, but not at the mouth.

As for longer term variations (i.e. over several years), certain trends are evident. The temperature at $100\,m$ rose by about $1°\,C$ from 1951 to 1964 and then fell by about $1.2°\,C$ to 1974, whereas the changes at 300 and $500\,m$ were of the order of $0.8°\,C$. Pickard suggests that this trend is associated with a rise in the average winter air temperature of about $2°\,C$ from 1952 to 1963 and a fall by the same amount to 1973. Because vertical heat exchange with the surface is very small below $100\,m$, he attributes the change to

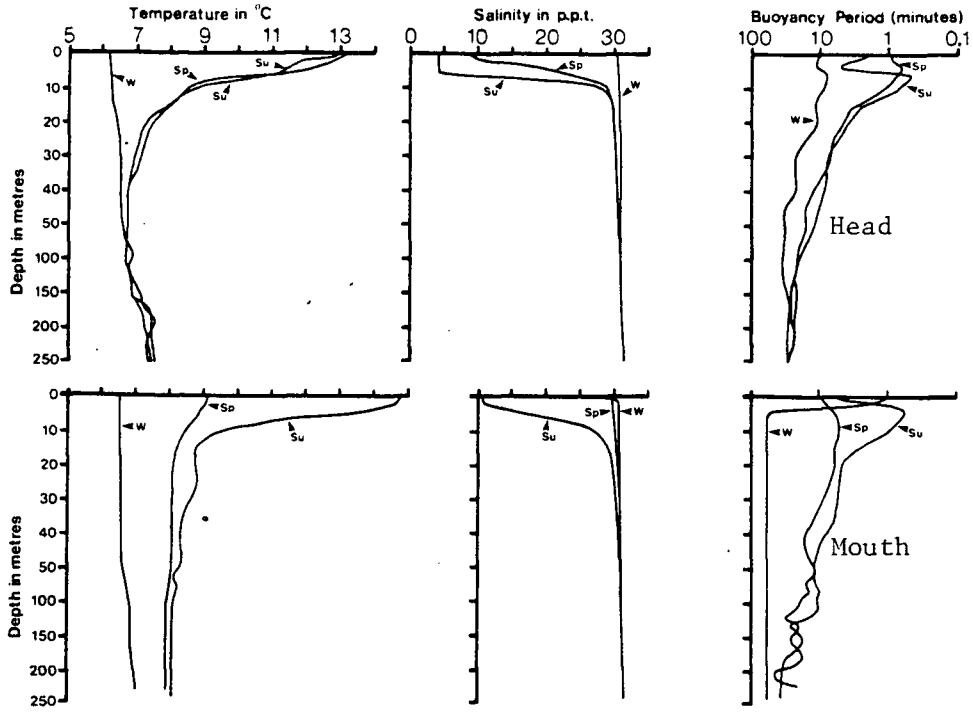

Figure 3 Representative temperature, salinity and buoyancy profiles.
Su = summer, W = winter, Sp = spring. Note the change of scale at 50 m.
(From Farmer and Freeland 1983.)

longitudinal advection due to the mean estuarine circulation. The fact that any water flowing up-inlet at depth has to surmount the sill at 60 m means that heat exchange with the surface is possible.

1.2.5 Early Current Measurements

As was stated earlier, the first current measurements in the 1950s (Pickard and Rodgers 1959) were rather crude, and not much more was done until 1976 in connection with the work by Farmer et al. on internal waves at the sill.

Generally, the currents can be described as an oscillating component at tidal period superimposed on a mean flow. It might seem that the oscillating component is due to tidal forcing from the ocean (and is independent of river runoff), and the mean flow is due to gravitational circulation (and is independent of tidal forcing). However, when interpreting these two components of the currents, one must bear in mind that when both forcing terms are present, the system may not respond with a sum of the responses to each individual forcing term, because the equations describing fluid flow are non-linear. Therefore the observed mean circulation would not necessarily be the same in the absence of tidal forcing.

Pickard and Rodgers describe the currents at two stations, taken every half hour for three days in July 1956. Over the sill, the currents were up to $150\,cm/sec$ at the surface, and $50\,cm/sec$ at $70\,m$. The oscillatory component was in the same phase from surface to bottom. With no wind, the mean current profile was the classic two-layer system, with outflow in the upper half and inflow below. With an up-inlet wind, the mean profile was 3-layer, with up-inlet flow in the upper $10\,m$ and the bottom $20\,m$. At a deeper station ($350\,m$) between the sill and the first bend, speeds up to $25\,cm/sec$ were still observed at depths as great as $300\,m$. The oscillatory component of the current was not constant in phase with respect to depth. The mean profile was a 3- or 4-layer flow, depending on the wind direction (amongst other things). Had more data been available to them, however, they would have seen a great deal of variability in such 25 hour means. They found that the mean circulation was sufficiently strong at the deep station to overcome the oscillatory component at the surface and wipe out any up-inlet flow there, but that this was not the case at the sill.

1.2.6 The Interaction of the Barotropic Tide With The Sill

The basic mechanism of flow interaction with the sill in Knight Inlet was first determined in August 1977 by Farmer and Smith (1978, 1980a, 1980b). *Figure 4* shows the detailed bathymetry around the sill. Strong currents during, say, an ebb tide, produce supercritical conditions over the sill, with a return to subcritical flow behind the sill because of the presence of an internal hydraulic jump or a large amplitude lee wave. As the tide slackens, the disturbance moves slowly back over the sill and travels upstream, evolving as an internal surge or bore. The precise response depends upon two things: the stratification and the strength of the tidal current.

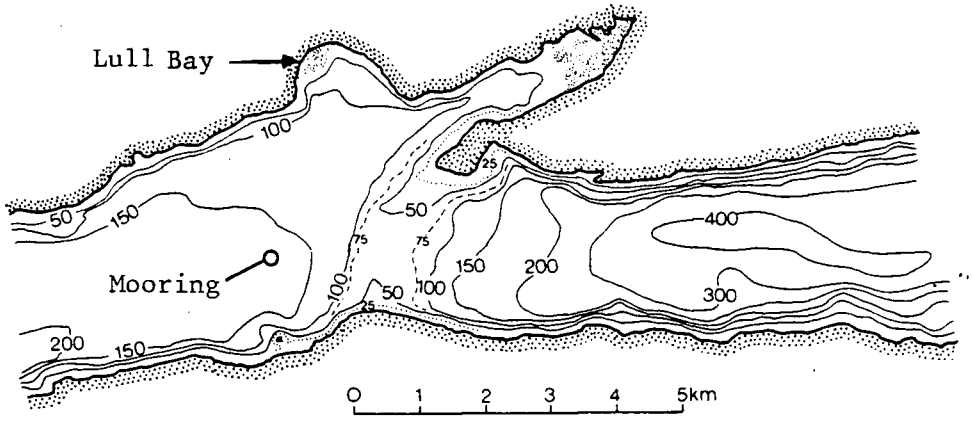

Figure 4 Detailed bathymetry around the sill. Depth contours are shown in metres. (From Farmer and Freeland 1983.)

For a given energy level, conservation of mass and momentum implies that a two-layer flow has two possible modes, one as a supercritical flow and the other as a subcritical flow. In supercritical flow, the Froude number (which is defined as the ratio of the flow speed in the upper layer to the internal phase speed) exceeds unity, whereas in subcritical flow it is less than unity. The fluid velocity is greater and the upper layer thickness is less in the supercritical mode. The situation is complicated somewhat in the continuously stratified case by the existence of an infinite set of internal wave phase speeds corresponding to the internal modes, and these give rise to an infinite set of Froude numbers for a given flow. The Froude numbers increase with increasing mode number, so that it is possible, for

example, for a flow to be subcritical with respect to the first mode, but supercritical with respect to the second mode. A change in flow conditions from supercritical to subcritical is called a hydraulic jump. These jumps can be initiated by the presence of topography (e.g. at the sill) or a sudden widening of the channel.

Farmer and Smith's observations were made with profiling current meters and CTDs, with moored current meters and thermistor chains, with recording pressure (tide) gauges, and with high frequency (100–200 kHz) echo soundings. Ship location was determined using microwave positioning equipment. The echo sounder was used to obtain acoustic images of the structure of the flow over the sill and the resulting surges and intrusions, by making traverses of the sill with the ship. The acoustic signal would be reflected not only by the bottom, but also by biological organisms and density changes (microstructure), so that details of the flow could be traced. In addition, a variety of fast response current meters were used, which sampled at a high rate and gave useful information about the vertical component of the velocity.

In their first paper Farmer and Smith (1978) describe the results of the pilot study to determine the scales necessary to plan a more detailed experiment. This experiment included CTD measurements along the channel with some time series observations (using CTD and profiling current meters etc) at a station 6 km up-inlet of the sill. This distance is equivalent to a few tidal excursions, so the chaotic motions at the sill have had time to organise themselves into propagating internal waves in the upper layer. They observed amplitudes in excess of 10 m (based on the excursions of the isohalines) and periods of the order of 10 minutes. As the strongly stratified part of the water column was only 15–20 m deep, it became evident that non-linear effects were important. They interpreted the data using a model of non-linear (because of finite-amplitude effects) internal waves in a strongly sheared flow, and examined conditions leading to shear flow instability. They found that the calculated phase speeds of the waves were consistent with the observed phase speeds, and that the wave properties were strongly influenced by the shear.

In the other two papers Farmer and Smith (1980a,b) discuss acoustic images of the flow over the sill, and classify the wide variety of responses according to the Froude numbers for each of the internal modes. In mid-winter even the smallest tides will produce flows supercritical with respect to all internal modes, while in mid-summer most flows will be subcritical with respect to the first mode but may be supercritical with respect to the second.

Figure 5 shows schematically some of the phenomena that they found, including lee waves, hydraulic jumps, blocking, boundary layer separation and the spread and collapse of turbulent mixing layers shed from the sill crest. Blocking occurs when there is insufficient kinetic energy in the flow to raise the denser deeper fluid over the crest. Flow separation occurs when the boundary layer, in which the tangential velocity drops from its value in the interior of the fluid to zero on the fjord bed, becomes detatched from the bottom. The high shear across the boundary layer leads to instabilities and turbulence. The development of a large lee wave behind the sill tends to inhibit boundary layer seperation.

1.2.7 Tides

The tides in Knight Inlet are principally semi-diurnal, with the M_2 constituent of the surface elevation oscillation increasing in amplitude from $1.527\,m$ at the mouth to $1.582\,m$ at the head. The total range is 3–$5\,m$. For a pure barotropic standing wave the phase would be constant along the inlet, and the currents in quadrature. In fact, there is a difference of 1 or 2° because of friction and other energy sinks. The external Rossby radius is of the order of $2000\,km$, which is much wider than the inlet, so rotation can be ignored for the barotropic tide. The standing wave can be thought of as a superposition of two Kelvin waves (practically plane waves) of equal amplitude propagating in opposite directions, one being the incident wave and the other being its reflection from the head. Jamart and Winter (1980) made a finite element computation of the barotropic tide in Knight Inlet. They ignored the Coriolis term and had a simple linear dissipation term, but their results fairly well approximated the observed tidal flow, with complex flows in the area of the sill. They tuned their dissipation parameter so that the model produced the

(A). Schematic diagram of a mode 1 lee wave response to tidally forced flow over a sill. Upstream of the sill there is blocking (b) of the deep flow and separation (s) of the boundary layer beneath the trough of the lee wave downstream of the sill. As the tidal current slackens the lee waves are released successively to form a nonlinear wavetrain that travels over the sill crest and back along the fjord.

(B). Schematic representation of flow that is subcritical with respect to mode 1, but critical with respect to mode 2. In the early stages of the tidal flow the boundary layer separates from the sill crest, but subsequently separation is suppressed as mode 2 lee waves evolve. The upstream flow is modified by a small mode 1 internal wave that travels up-inlet away from the sill. The growing lee wave or jump eventually collapses to spread out as an undular bore as the flow slackens. A small wave (c) travels downstream. All of these features have been observed in Knight Inlet, B.C.

(C). Sketch of tidal mixing over a longer sill leading to collapse of water of intermediate density. The mixed water spreads outwards as an undular bore between the two layers from which it was formed. A small disturbance (c) travels in the downstream direction.

Figure 5 Schematic representation of the phenomena occurring at the sill. (From Farmer and Freeland 1983.)

same phase difference between the mouth and the head as was calculated by Freeland and Farmer (1980) from tide gauge data. The tidal excursion inside the inlet is of the order of 1 or 2 km.

As was previously mentioned, the internal tide is most easily seen as an oscillation in the depth of isopycnal surfaces at tidal period. A typical phase speed of 0.8 m/s for the first M_2 internal mode for summer stratification (this concept arises from a linear, flat-bottomed model with a separable solution) gives rise to a wavelength of 36 km and an internal Rossby radius of 7 km.

The internal tide is generated by the passage of barotropic tidal flow over topography, such as a sill. The effect of sills in generating internal tides was first shown by Zeilon (1912, 1934), as referenced in LeBlond and Mysak (1978). Halpern (1971a,b) identified groups of higher frequency waves as well as a semi-diurnal internal tide generated by tidal flow over a bank. Baines (1982) discusses the generation of internal tides by the continental rise in the ocean, and Blackford (1978) presents a non-linear model of the generation of the internal tide by tidal flow over a sill in a channel. When there is flow over topography a vertical component of velocity is required for the fluid to surmount the obstacle. This vertical component of velocity oscillates at that frequency, and acts as a forcing function to generate internal waves at tidal frequency. With the highly energetic and turbulent processes that occur at the sill in Knight Inlet, such vertical components of velocity are bound to be chaotic, at least on the downstream side of the sill, causing both a wide spectrum of modes and an irregular waveform to be generated. However, as the internal tide propagates away from the energetic region of generation into the "far field", the higher modes will dissipate due to their large vertical shear, and the waveform will become more regular. Another way of looking at the generation mechanism is that as the deep flow is blocked, the more dense fluid will tend to rise up the sill with the flow, but then fall again as the tidal current eases. This behaviour is depicted in *Figure 5a* to the left of the sill. This oscillation of isopycnals at tidal period at depths below the sill crest will generate an internal tide.

1.3 Aim of this Thesis

The main question that will be addressed in this thesis is how much of the internal tide, which is supposedly generated at the sill and propagates away from it in both directions, is reflected when it hits the first bend up-inlet of the sill, and how much is transmitted. In an analysis of four current meter records, Farmer and Freeland (1983) concluded that the amplitude of the outgoing internal tide at Tomakstum Island (see *Figure 1*)was 0.93 times that of the incoming wave. Because they only had measurements at two depths they were forced to assume that only one internal mode was present (see later discussion in Section 3.4). Farmer and Freeland assumed that this mode was the first. Later, Freeland (1984) modified the calculation to assume that this mode was the second, and obtained an amplitude ratio of 0.70.

However, their conclusion that the internal tide undergoes substantial reflection at the bend is in direct conflict with a result obtained by Blackford (1984). He modified his non-linear generation model to include a variable amount of reflection at a specified distance from the sill, and compared the resulting waveform of the internal tide with an observed waveform based upon the depth of the 30.5 ‰ isohaline which was obtained from a 24 hour series of CTD observations at two stations. He found much poorer agreement by using a high reflection coefficient than by using no reflection, which suggests that very little reflection occurs at the bend.

Another piece of evidence in favour of a low reflection coefficient at the bend comes from a numerical simulation of internal tide generation in sill fjords by Mørk and Gjevik (1982). Their model was two-layered and depth integrated, and simulated a barotropic Kelvin wave in the open ocean propagating along the coast past the mouth of the fjord. It induced a barotropic standing wave in the fjord, which in turn generated baroclinic waves at the sill. They found that with the parameters used, a 90° bend in the fjord had negligible effect on the propagation of the internal tide, in the sense that the baroclinic interface displacements as a function of time at two points on either side of the bend were the same as if the fjord was straight.

This thesis seeks to resolve the conflict between Freeland and Farmer on the one hand and Blackford and Mørk and Gjevik on the other. In order to do so, a theoretical study of the propagation of a Kelvin wave around two types of bend in a channel of rectangular cross-section was carried out. The method of solution was essentially numerical. It is described in Chapter 2. In addition, cyclesonde current meter and CTD data from Knight Inlet were analysed. It was attempted to express the vertical profiles of the phase and amplitude of the M_2 constituent of longitudinal velocity and density oscillations as a superposition of the first few internal modes, both up- and down-inlet propagating. In this way an estimate of the reflection coefficient at the bend for each mode was made. This analysis is described in Chapter 3.

The energetics of Knight Inlet are also discussed in Chapter 3. Freeland and Farmer (1980) estimated the power lost from the barotropic tide in the straight section from Montagu Point (near Protection Point) to the first bend (which includes the sill), and in the sinuous section from the first bend to the head. These estimates were based upon the phase of the surface elevation. They found that the power loss in the section containing the sill was approximately 20 times that in the sinuous section. They concluded that this high loss was due to the generation of internal waves and tide and hydraulic jumps at the sill. The power loss from the barotropic tide in the sill section was of the order of 7–9 MW.

Stacey (1985) developed a simple model to predict the amplitude of the internal modes generated by the sill (see Section 3.11). He found that the total power, summed over the first ten internal modes, radiated by the sill plotted monthly for 18 months followed the total power loss from the barotropic tide as calculated from the phase of the surface elevation very closely. This result implies that most of the energy being removed from the barotropic tide is being fed into the internal tide, and that therefore the internal tide, rather than high frequency internal waves or turbulence at the sill, is the most energetic response resulting from the interaction of the tides with the sill.

Any energy in the internal tide that does not radiate out into the open ocean must be

dissipated by bottom and side friction or through turbulence to cause mixing. Freeland and Farmer (1983), using CTD data, calculated that the divergence of the total energy flux of the mean circulation (i.e. the rate of work being fed into the mean circulation) was much greater in the straight section than in the sinuous section. The total energy flux of the mean circulation consists of both potential and kinetic energy flux, although the former is an order of magnitude greater than the latter. The mean circulation is driven by the buoyancy input from river runoff, but turbulent mixing causes the potential energy of the mean state to increase. The energy flux divergence in the straight reach was about 2 % of the barotropic tidal energy loss. This result is consistent with the idea of a multistep energy transfer (tidal energy loss converted to internal motions which lose energy to turbulence which mixes the water column) where efficiency could not be expected to be high.

1.3.1 Summary

This thesis will describe an attempt to resolve the conflict between the results of Freeland (1984) and those of Blackford (1984). The former indicate a significant reflection of the internal tide at the first bend in Knight Inlet, whereas the latter indicate a negligible reflection. The question will be approached both theoretically in Chapter 2 and experimentally, using cyclesonde current meter and CTD data from Knight Inlet, in Chapter 3. The energetics of Knight Inlet will also be discussed in Chapter 3. In Chapter 4 the low-frequency component of the velocity signals from the cyclesondes will be presented, with a brief analysis.

2. The propagation of a Kelvin wave around a bend in a channel

2.1 Introduction

The problem of the reflection of a Kelvin wave from the end of a channel was first solved by Taylor (1920). He found that it was not possible for a pair of Kelvin waves propagating in opposite directions to satisfy the condition of zero flow normal to the end wall, and that a whole spectrum of Poincaré waves had to be involved in the reflection process. The problem was re-examined by Hendershott and Speranza (1971) and Brown (1973). In this thesis Taylor's method was used to investigate the behaviour of a Kelvin wave incident upon a bend in a channel.

Previous models of Kelvin waves propagating around bends have not included an opposite wall; they have been bends in straight coastlines. Buchwald (1968) considered a right-angled bend, and Packham and Williams (1968) solved the problem for a bend of general angle. Because there was no opposite wall, a reflected Kelvin wave was not possible, and any energy not transmitted as a Kelvin wave had to be radiated as cylindrical Poincaré waves from the corner. They found that there was complete transmission in the case of sub-inertial frequency Kelvin waves, since the Poincaré waves are evanescent. In the case of super-inertial frequency Kelvin waves, Packham and Williams found that there was complete transmission only for wedge angles $\frac{\pi}{2n+1}$, where $n = 1, 2, 3, ...$ (see *Figure 34*).

Buchwald (1971) also considered the problem of a Kelvin wave propagating along a straight coastline past the mouth of a narrow channel. A Kelvin wave propagating into the channel was generated, as well as cylindrical Poincaré waves in the semi-infinite ocean provided that the frequency was super-inertial. He found that the amplitude of the Kelvin wave generated in the channel was proportional to the ratio of the channel width to the wavelength in the channel.

In this chapter, then, solutions of the linearised long wave equations in a flat-bottomed channel of rectangular cross-section are presented for the case of a Kelvin wave incident upon a bend.

2.2 Governing Equations

The linearised long wave equations, for a harmonic time dependence $e^{i\omega t}$, separated into vertical and horizontal dependences, are

$$i\omega\tilde{U} - f\tilde{V} = -\tilde{P}_x, \tag{2.1}$$

$$i\omega\tilde{V} + f\tilde{U} = -\tilde{P}_y, \tag{2.2}$$

$$gh_n(\tilde{U}_x + \tilde{V}_y) = -i\omega\tilde{P}. \tag{2.3}$$

(LeBlond and Mysak, 1978, equations 10.34-10.38)

$(\tilde{U},\ \tilde{V})$ and $\tilde{P}$ are the horizontal dependences of velocity and specific pressure (pressure/density) respectively, and h_n is the equivalent depth as derived from a vertical modes calculation. In the case of the barotropic tide, h_n is the depth of the channel.

Equations 2.1 and 2.2 can be solved for $\tilde{U}$ and $\tilde{V}$ in terms of $\tilde{P}$:

$$\tilde{U} = \frac{i\omega}{\omega^2 - f^2}\left(\frac{\partial}{\partial x} - i\tau\frac{\partial}{\partial y}\right)\tilde{P}, \tag{2.4}$$

$$\tilde{V} = \frac{i\omega}{\omega^2 - f^2}\left(\frac{\partial}{\partial y} + i\tau\frac{\partial}{\partial x}\right)\tilde{P}, \tag{2.5}$$

where

$$\tau \equiv \frac{f}{\omega}. \tag{2.6}$$

The equation of continuity (equation 2.3) then yields the wave equation in $\tilde{P}$:

$$(\nabla^2 + \tilde{k}^2)\tilde{P} = 0, \tag{2.7}$$

where

$$\tilde{k}^2 \equiv \frac{(\omega^2 - f^2)}{gh_n}. \tag{2.8}$$

At a boundary, the requirement that there be no normal velocity is expressed by the condition

$$\left(\frac{\partial}{\partial n} - i\tau\frac{\partial}{\partial s}\right)\tilde{P} = 0, \tag{2.9}$$

where n denotes the outward normal to the boundary, and s the direction along the boundary.

2.3 Special Solutions in a Straight Channel

The channel width is taken to be $2L$, and the length scale L is used to make the space co-ordinates non-dimensional. The co-ordinate system shown in *Figure 6* is adopted, where Region 1 is the channel under consideration, with a width of 2 units. The problem then becomes

$$(\nabla^2 + k^2)P = 0, \tag{2.10}$$

with

$$\left(\frac{\partial}{\partial x} - ir\frac{\partial}{\partial y}\right)P = 0 \qquad \text{at } x = 0, 2, \tag{2.11}$$

where

$$k^2 \equiv \frac{\omega^2 - f^2}{gh_n}L^2. \tag{2.12}$$

Note that k^2 is a non-dimensional parameter.

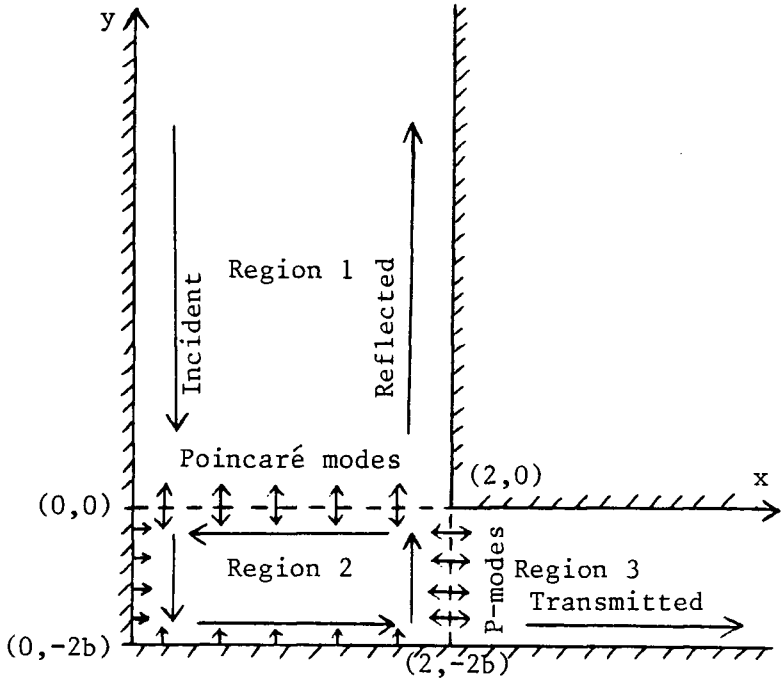

Figure 6 Schematic diagram of the "rectangular bend".
The co-ordinate system used in describing solutions in a straight channel is shown.

The solution for a Kelvin wave propagating in the direction of increasing y is

$$P = \exp\left\{(r[x-1] - iy)\frac{k}{\sqrt{1-r^2}}\right\}, \tag{2.13}$$

$$\mathcal{U} \equiv \left(\frac{\partial}{\partial x} - i\tau\frac{\partial}{\partial y}\right) P = 0, \tag{2.14}$$

$$\mathcal{V} \equiv \left(\frac{\partial}{\partial y} + i\tau\frac{\partial}{\partial x}\right) P = ik\sqrt{1-\tau^2}P, \tag{2.15}$$

where $\mathcal{U}$, $\mathcal{V}$ and P are proportional to $\tilde{U}$, $\tilde{V}$ and $\tilde{P}$. The corresponding expressions for the m^{th} Poincaré mode are

$$P = e^{-k_m y}\left(\cos t_m x - \frac{i\tau k_m}{t_m}\sin t_m x\right), \tag{2.16}$$

$$\mathcal{U} = e^{-k_m y}\left(\frac{\tau^2 k_m^2 - t_m^2}{t_m}\right)\sin t_m x, \tag{2.17}$$

$$\mathcal{V} = e^{-k_m y}\left((\tau^2-1)k_m \cos t_m x - \frac{i\tau k^2}{t_m}\sin t_m x\right), \tag{2.18}$$

for $m = 1, 2, 3, ...$, where

$$t_m \equiv \frac{m\pi}{2} \tag{2.19}$$

and

$$k_m \equiv +\sqrt{t_m^2 - k^2}. \tag{2.20}$$

In this thesis it is assumed that all the Poincaré modes are evanescent, i.e. $k^2 < \left(\frac{\pi}{2}\right)^2 = 2.4674$, and that the frequencies are super-inertial, i.e. $\tau \equiv \frac{f}{\omega} < 1$. Equations 2.12 and 2.20 show that all sub-inertial frequency Poincaré waves (e.g. diurnal tides) are evanescent, whereas super-inertial frequency Poincaré waves (e.g. semi-diurnal tides) will only propagate if the channel is wide enough or the phase speed $\sqrt{gh_n}$ is small enough. Kelvin waves propagate at all frequencies.

The corresponding expressions for Kelvin waves propagating in the opposite direction can be obtained be replacing k by $-k$ in 2.13–2.15, or for Poincaré waves decaying in the opposite direction by replacing k_m by $-k_m$ in 2.16–2.18. For reference, expressions for the non-dimensional wavelength of the incident Kelvin wave λ, and the non-dimensional Rossby radius R_n, are

$$\lambda = 2\pi\frac{\sqrt{1-\tau^2}}{k}, \tag{2.21}$$

$$R_n = \frac{\sqrt{1-\tau^2}}{\tau k}. \tag{2.22}$$

The appropriate length scale to convert these to dimensional quantities is L, the half-width of the channel.

2.4 Method of Solution in a "Rectangular Bend"

The domain of interest is a right-angled bend in a channel, where the width of the channel is two units before the bend, and a different width after the bend (see *Figure 6*). The domain is split up into three regions: two straight channels (Regions 1 and 3) and a rectangle (Region 2). The solution in Regions 1 and 3 are expressed as a sum of a Kelvin wave propagating away from the boundary with Region 2, and a truncated infinite series of evanescent Poincaré modes, which decay away from the same boundary. These waves all have unknown complex coefficients that must be determined. In addition, the solution in Region 1 has a further component, namely an incident Kelvin wave of unit amplitude and zero phase.

The solution in Region 2 is expressed as a sum of Kelvin waves propagating in the positive and negative y-direction, the corresponding Poincaré modes, and Kelvin waves propagating in the positive and negative x-direction, along with the corresponding Poincaré modes. Hence, if the Poincaré modes are truncated after M terms, then $6(M+1)$ complex coefficients are required to describe the solution everywhere.

All the basis functions satisfy the wave equation, and they satisfy the boundary condition of zero normal velocity everywhere along the boundaries except on the left-hand and lower boundaries of Region 2. The vanishing of normal velocity along these two boundaries remains to be imposed, as do the matching of pressure and velocity along the other two boundaries of Region 2. In fact, it is only necessary for the pressure and normal velocity to be matched across the other two boundaries, since if these two properties match then all other properties, including tangential velocity, must also match. Suppose that the pressure matches on either side of a boundary. Then the tangential component of the pressure gradient $\frac{\partial P}{\partial s}$ must match. Yet if the normal velocity $(\frac{\partial P}{\partial n} - i\tau\frac{\partial P}{\partial s})$ matches, then $\frac{\partial P}{\partial n}$ also matches. Hence ∇P matches, and so therefore does the tangential velocity $(\frac{\partial P}{\partial s} + i\tau\frac{\partial P}{\partial n})$.

Also $(\nabla^2 + k^2)P = 0$ on both sides of the boundary, which implies after differentiation that $(\nabla^2 + k^2)\nabla P = 0$, $(\nabla^2 + k^2)\nabla^2 P = 0, \ldots$, etc on both sides. Given that P and ∇P match, it follows by induction that $\nabla^2 P$, $\nabla^3 P$, $\nabla^4 P, \ldots$, etc, also match.

The matching process was split up into two stages, which reduced the problem from the inversion of a (complex) matrix of order $6(M + 1)$ to the inversion of three matrices of order $2(M + 1)$. If the second channel is the same width as the first, then two of these three matrices are the same, and there are then only two different matrices to invert.

2.4.1 First Stage

The first stage is the matching of normal velocity. The problem of a rectangular basin enclosed on three sides (zero normal velocity) with a prescribed normal velocity along the remaining open boundary is considered. The solution inside the rectangle can be expressed as a sum of a Kelvin wave propagating away from the open boundary as if in a channel, and its associated M Poincaré waves decaying away from the open boundary, along with a Kelvin wave propagating towards the open boundary and its associated Poincaré modes. The solution requires $2(M + 1)$ complex coefficients to be determined. The boundary conditions of zero normal velocity along the two side walls are automatically satisfied by the choice of basis functions, but the zero normal velocity along the fourth boundary, and the prescribed normal velocity along the open boundary must be forced by a suitable choice of coefficients.

The (complex) coefficients were calculated using a least squares method, minimising the sum of squares of the moduli of the difference between the normal velocities corresponding to the "fitted" superposition of basis functions and the required normal velocity. The sum of squares was calculated by dividing each boundary into $N - 1$ intervals, and then evaluating the basis functions and required normal velocities at N points distributed evenly along each of the two boundaries. The value of N was chosen to be sufficiently large ($\geq 2M$) that aliasing of the Poincaré modes did not occur. Hence the $2(M + 1)$ unknowns were calculated by a least sum of squares at $2N$ locations.

It is interesting here to compare this problem with that considered by Pnueli and Pekeris (1967), where they calculated the normal modes in a fully enclosed rectangular basin. The least squares analysis in both problems gives rise to a matrix equation of the form $Ax = b$, where A is a $2(M+1) \times 2(M+1)$ complex matrix, b is a $2(M+1)$ complex vector, and x is the $2(M+1)$ vector of complex coefficients that is to be determined. b is a linear transformation of the prescribed normal velocity along the open boundary of the rectangle, and would be zero for a fully enclosed rectangle. Hence, the relation that Pnueli and Peckeris calculated between k^2 and τ arises from the vanishing of the determinant of A. For a given k^2, τ is an eigenvalue of A. However, in this thesis, k^2 and τ are regarded as given, and the prescribed normal velocity is non-zero. If τ happens to be the eigenvalue of A for the particular value of k^2, then this method breaks down. The solution inside the rectangle would not be uniquely defined for a prescribed normal velocity; the addition of any superposition of normal modes of the corresponding closed basin would also be a solution.

It should be noted that the problem of a rectangular basin with prescribed normal velocity along any number of its sides is only a small extension to this problem. Because of the linearity of the equations, the solution for prescribed normal velocity along many sides is equal to the sum of the solutions for prescribed normal velocity along each side in turn.

The first stage, then, consists in applying this procedure $2M+3$ times with the following prescribed normal velocities to Region 2:

(i) The normal velocity corresponding to an incident Kelvin wave of unit amplitude and zero phase in Region 1.

(ii) The normal velocity corresponding to a reflected Kelvin wave of unit amplitude and zero phase in Region 1.

(iii) The normal velocity corresponding to each of M evanescent Poincaré modes, each of unit amplitude and zero phase, in Region 1.

(iv) The normal velocity corresponding to a transmitted Kelvin wave of unit amplitude and zero phase in Region 3.

(v) The normal velocity corresponding to each of M Poincaré modes, each of unit amplitude and zero phase, in Region 3.

Note that if Region 2 is square, then (iv) and (v) are identical to (ii) and (iii). This is the reduction of work that was referred to earlier.

2.4.2 Second Stage

The second stage is the matching of pressure. For each of the $2M + 3$ types of wave in the straight channels, the first stage of the calculation returns the pressure field inside Region 2 such that the normal velocity matches. For each of the $2M + 3$ types of wave of unit amplitude and phase, the difference between the pressure in Region 2 and that in Regions 1 and 3 is calculated along their two common boundaries. If the wave exists in Region 1, then the pressure in Region 3 is taken to be zero, and vice-versa.

The aim of the second stage is to find a combination of the $2M + 3$ types of wave in the straight channels that makes the sum of these "pressure anomalies" equal to zero. The amplitude and phase of the incident Kelvin wave are arbitrarily set to unit and zero, leaving $2(M + 1)$ complex coefficients to be calculated. This calculation is also done by a least sum of squares method, minimising the sum of squares of the modulus of the "pressure anomalies" at $2N$ locations. This procedure gives rise to a matrix equation of the same order as in the first stage, of the form $Ay = b$. Here y is the vector of complex coefficients and b is a linear transformation of the incident Kelvin wave. If there were no incident wave then b would be zero, implying that $y = 0$ (the trivial solution). If the incident wave contained some decaying Poincaré modes, then b would be changed.

Loosely speaking, the first stage of the calculation describes how a rectangle responds to various forcing terms, and the second stage describes how the rectangle and the two straight channels are connected. This method is an adaptation of the collocation method. However, in the collocation method boundary conditions are applied at the same number

of points as there are unknown coefficients. In this method at least twice as many points are used, and the conditions are applied in a least squares sense.

2.5 Results for the Rectangular Bend

The following results were obtained using 15 Poincaré modes ($M = 15$), and doing a least squares fit at 100 points along each boundary ($N = 100$). The success of each run was judged by the extent to which the pressure and velocity fields were continuous across the boundaries, and the extent to which the sum of the reflected and transmitted energy fluxes equaled the incident flux. The continuity of velocity can be evaluated by looking at the plot of current ellipses in *Figures 10, 12* and *16*: for points on the common boundary between two regions two ellipses are plotted according to the solution in each region. The two ellipses should be indistinguishable.

When the two channels were of equal width, the relative energy fluxes were calculated by simply squaring the absolute value of the coefficient of the relevant wave in the solution, be it the incident, reflected or transmitted wave. The reflected $\mathcal{R}$ and transmitted $\mathcal{T}$ fluxes were expressed as a percentage of the incident flux. There should be no energy loss, since there is no dissipation in the model. The Poincaré modes transmit no energy, since they are evanescent.

There are three free parameters in the problem, namely τ, the period of the oscillation, k, which is proportional to the ratio of the channel width to the Rossby radius, and b, the ratio of the second channel width to the first. Hence, the width of the second channel is $2b$ units in the model. In the approach used, two of these parameters were kept constant, and the third was varied. The standard values used to start each parameter search were

$$\tau = 0.803,$$

$$k^2 = 7.02 \times 10^{-3},$$

$$b = 1.$$

These were chosen to represent the first internal mode of the M_2 constituent of the internal

tide in Knight Inlet. The following parameters were used to arrive at these values:

$$\omega = 1.40518 \times 10^{-4}\ rad/sec,$$

$$f = 1.12887 \times 10^{-4}\ rad/sec \qquad \text{(at latitude 50.7° N)},$$

$$L = 1\ km,$$

$$c_n \equiv \sqrt{gh_n} = 100\ cm/sec.$$

2.5.1 Parameter Search 1: $\tau = 0.803$, $b = 1$, *variable* k^2

Figure 7 shows a plot of the reflection coefficient $\mathcal{R}$ against k^2 for constant τ and b. $\mathcal{R}$ is remarkably small ($< 10\%$) until just before the cutoff wavenumber at which Poincaré waves start to propagate, where there is a pronounced peak. For small k^2 (< 0.2), $\mathcal{R}$ is roughly linear in k^2, and the curve approaches the line $\mathcal{R} = 54.4\,k^2$ % as $k^2 \to 0$ (see the blowup in *Figure 8*). As a check on the computation, $\mathcal{R}$ and $100\% - \mathcal{T}$ are generally in excellent agreement, except near the peak.

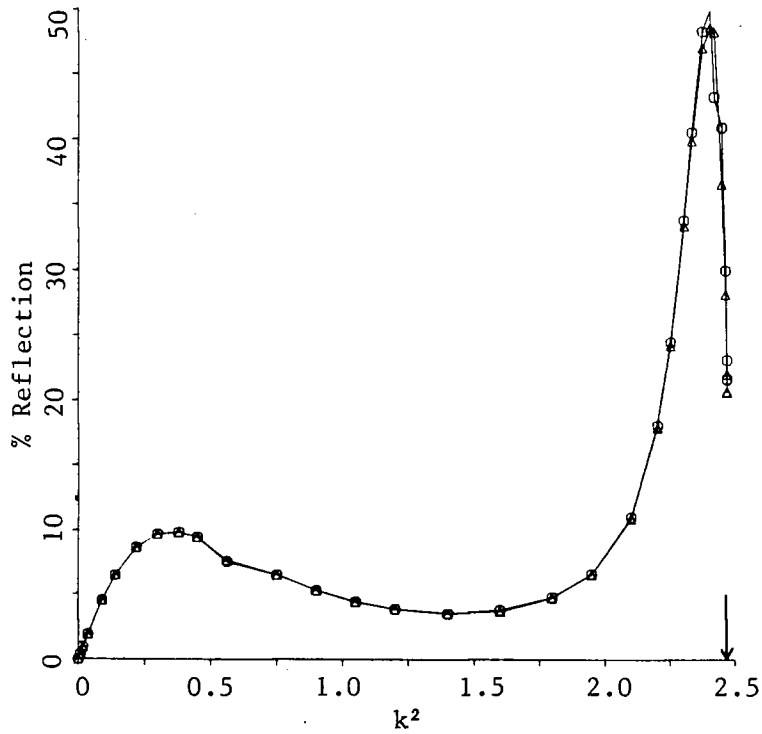

Figure 7 $\mathcal{R}$ vs k^2 for constant $\tau = 0.803$. $b = 1$.
The value of k^2 for which the first Poincaré mode starts to propagate is marked with an arrow. Circles = $\mathcal{R}$, triangles = $100\% - \mathcal{T}$.

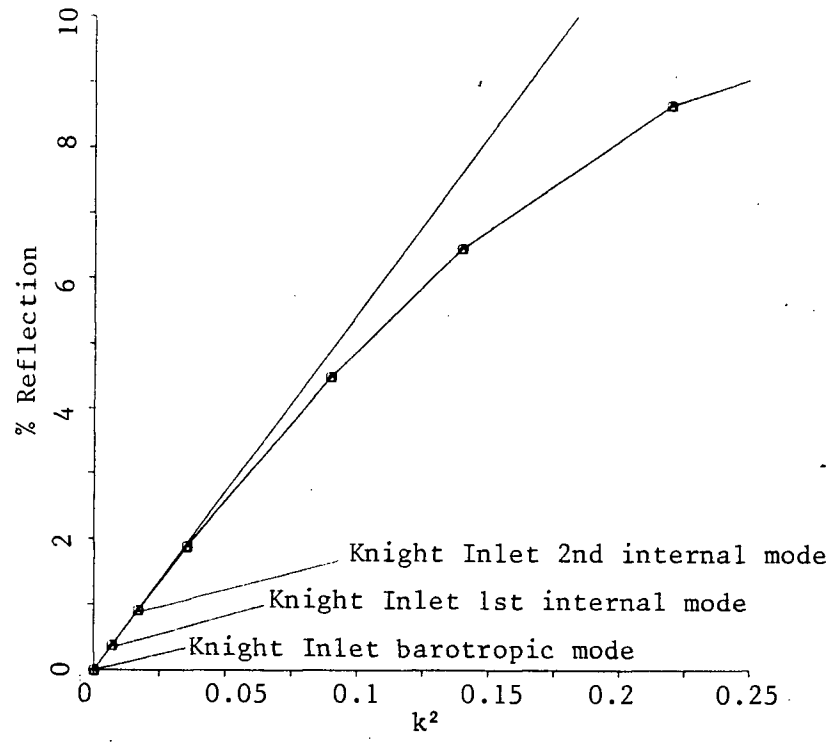

Figure 8 Blowup of *Figure 7* for small k^2.
The straight line is $\mathcal{R} = 54.4\,k^2$ %, which is the least squares fit for $k^2 < 0.05$.

The default values for Knight Inlet lie well within the linear part of the relationship. *Figures 9* and *10* show the pressure and velocity fields for these values of the parameters. Note that because of the assumed e^{iwt} time dependency, waves propagate in the direction of decreasing phase ($Arg\,P$). Velocity matching is not perfect, and there is a singularity in the velocity at the inside corner (see discussion in Section 2.6). The current ellipses in this and all figures showing velocity fields are scaled so that they are as large as possible without having to be plotted on top of each other.

Figures 11 and *12* show the pressure and velocity fields for $k^2 = 2.25$. This value lies in the peak of the curve of $\mathcal{R}$ vs k^2. Note the presence of amphidromes where the magnitude of the pressure oscillation is zero, and hence its phase is ambiguous. Non-zero normal velocity is visible in two of the ellipses, whereas the singularity at the inside corner has decreased. This latter phenomenon could be due to the decreased Rossby radius which causes an increased cross-channel decay of Kelvin waves, although the reflected wave is

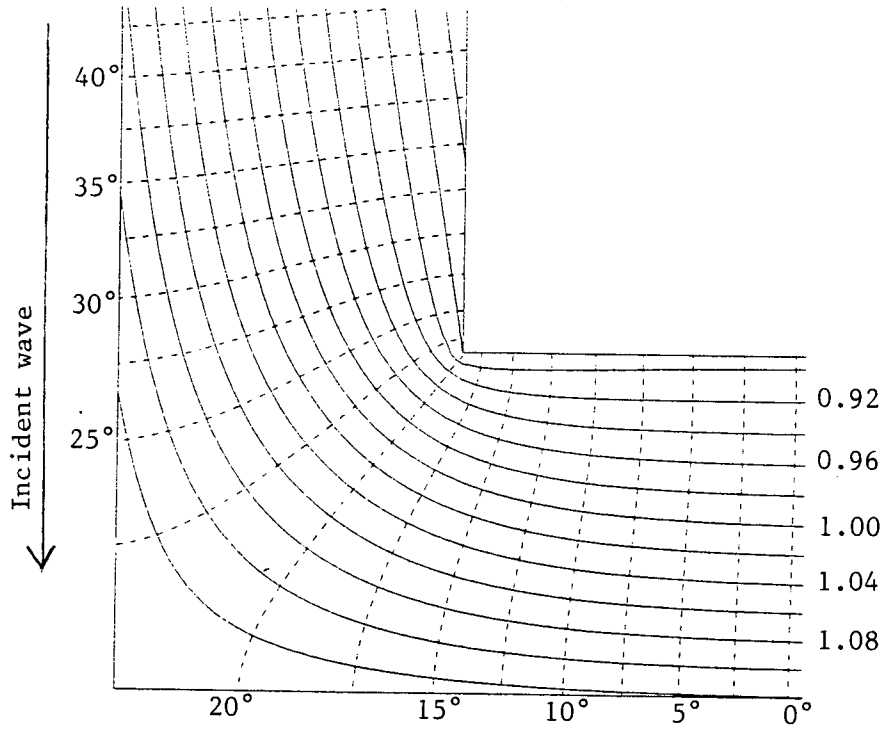

Figure 9 Pressure field for $k^2 = 7.02 \times 10^{-3}$, $\tau = 0.803$, $b = 1$.
Solid lines = $|\mathcal{P}|$ contours, dashed lines = $Arg\,\mathcal{P}$ contours.
$\lambda = 44.7$, $R_n = 8.8$, $\mathcal{R} = 0.38\,\%$, $100\% - \mathcal{T} = 0.38\,\%$.

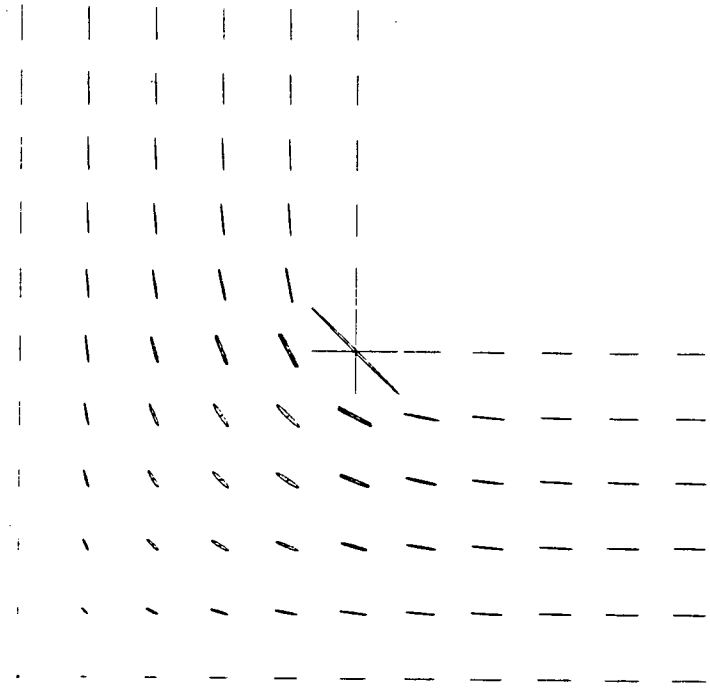

Figure 10 Velocity field corresponding to *Figure 9*.

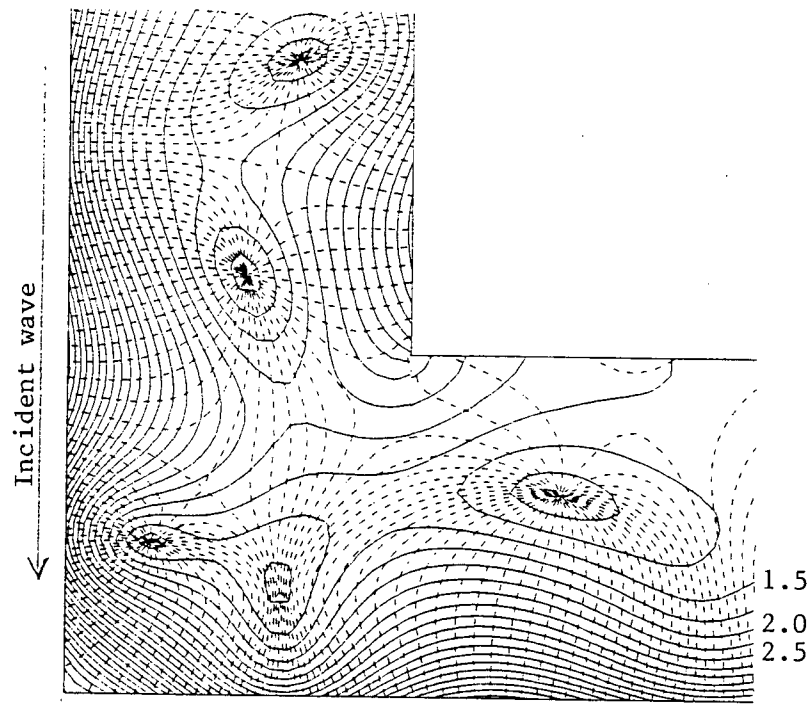

Figure 11 Pressure field for $k^2 = 2.25$, $\tau = 0.803$, $b = 1$. Solid lines = $|P|$ contours, dashed lines = $Arg\, P$ contours. $\lambda = 2.5$, $R_n = 0.49$, $\mathcal{R} = 24.48\,\%$, $100\% - \mathcal{T} = 24.22\,\%$.

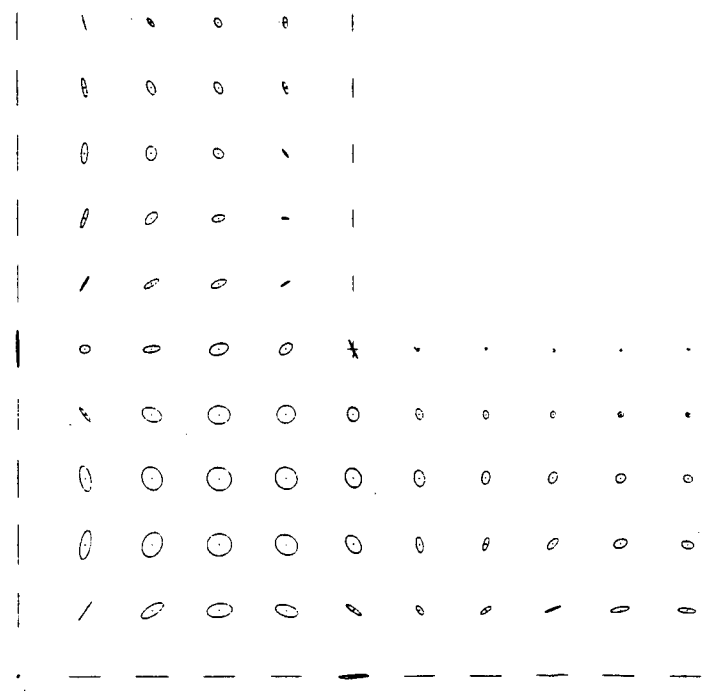

Figure 12 Velocity field corresponding to *Figure 11*.

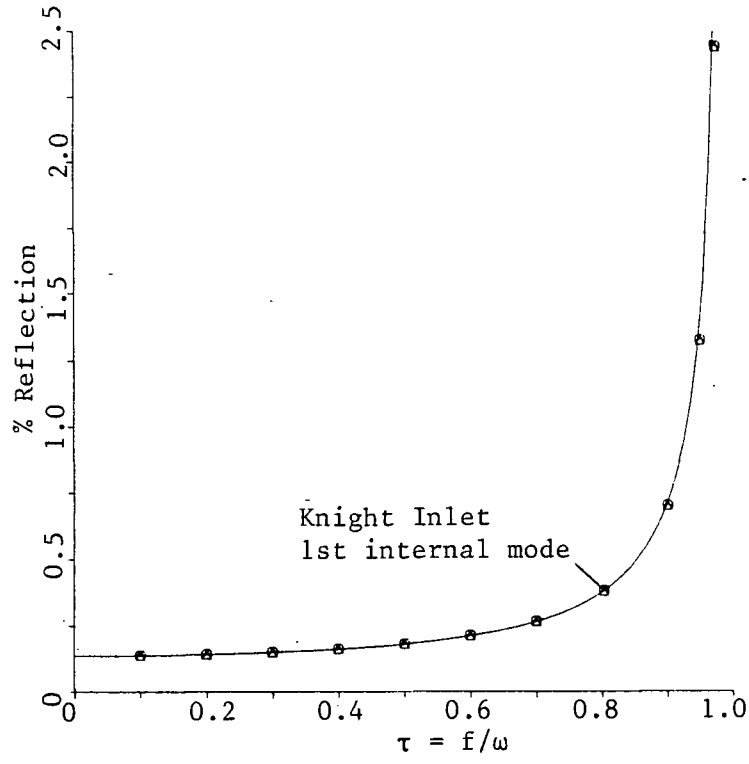

Figure 13 $\mathcal{R}$ vs τ for constant $k^2 = 7.02 \times 10^{-3}$. $b = 1$.
Circles = $\mathcal{R}$, triangles = $100\% - \mathcal{T}$.
The curve is $\mathcal{R} = \frac{0.135}{1-\tau^2}\,\%$, which is the least squares fit to a function of that form.

also of considerable magnitude.

2.5.2 Parameter Search 2: $k^2 = 7.02 \times 10^{-3}$, $b = 1$, *variable* τ

Figure 13 shows a plot of $\mathcal{R}$ vs τ for constant k^2 and b. A $\frac{1}{1-\tau^2}$ dependency was observed, with the constant of proportionality being 0.135. This result, combined with the constant of proportionality from the linear portion of the relationship between $\mathcal{R}$ and k^2 leads to the empirical relationship

$$\mathcal{R} = \frac{19.3\,k^2}{1-\tau^2}\,\% \quad \text{for small } k^2\ (< 0.2). \tag{2.23}$$

This is equivalent to

$$\mathcal{R} = 19.3\,\frac{L^2\omega^2}{c^2}\,\%, \tag{2.24}$$

or

$$\mathcal{R} = 1.96\,r^2\,\%, \tag{2.25}$$

where r is the ratio of the channel width to the wavelength of the incident wave.

2.5.3 Parameter Search 3: $k^2 = 7.02 \times 10^{-3}$, $\tau = 0.803$, *variable* b

Figure 14 shows the relationship between $\mathcal{R}$ and b. As expected, the amount of energy transmitted through the second channel decreases to zero as the width of the second channel decreases to zero. There is, however, a large discrepancy between $\mathcal{R}$ and $100\% - \mathcal{T}$, indicating that the solution is not reliable for $b < 1$. This breakdown is confirmed by *Figures 15* and *16*, where it can be seen that the velocity fields do not match.

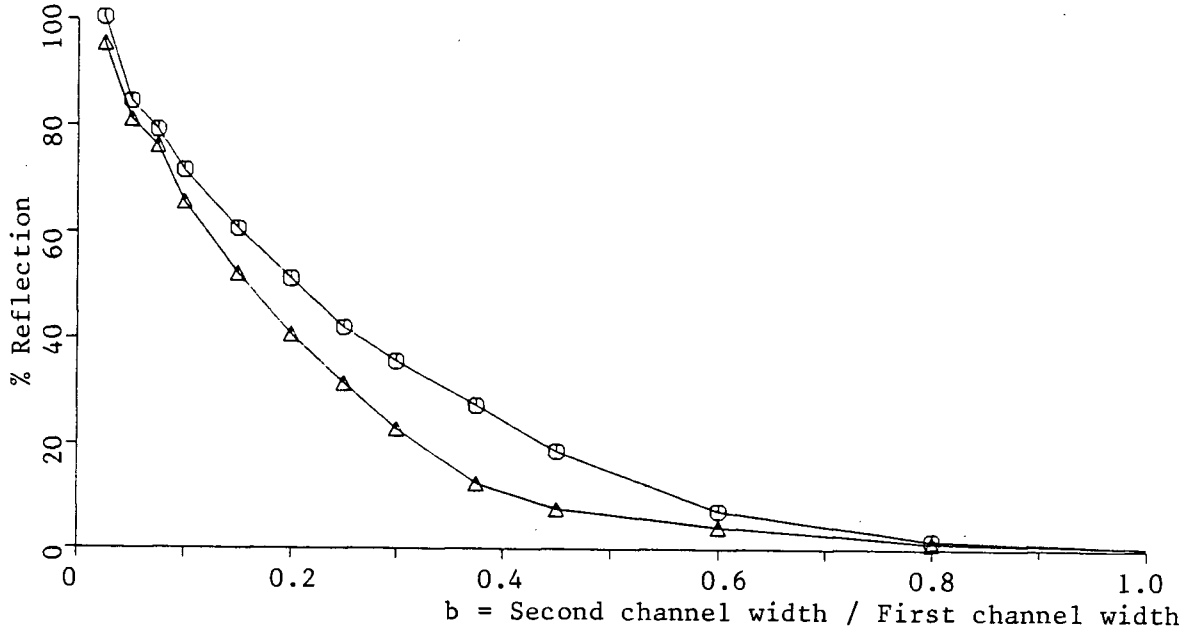

Figure 14 $\mathcal{R}$ vs b for constant $\tau = 0.803$ and $k^2 = 7.02 \times 10^{-3}$.
Circles = $\mathcal{R}$, triangles = $100\% - \mathcal{T}$.

The energy fluxes can not be simply calculated from the square of the magnitude of the relevant coefficient in the solution expansion, because the channels are no longer of the same width. The pressure and velocity fields both have a cross-channel structure proportional to e^{x/R_n}, and so the energy flux will depend on the channel width as

$$\int_{-b}^{b} (e^{x/R_n})^2 \, dx = R_n \sinh \frac{2b}{R_n}. \tag{2.26}$$

Hence, the square of the magnitude of the coefficient of the transmitted wave was multiplied by a factor of $\frac{\sinh(2b/R_n)}{\sinh(2/R_n)}$ before plotting to make it compatible with the fluxes obtained

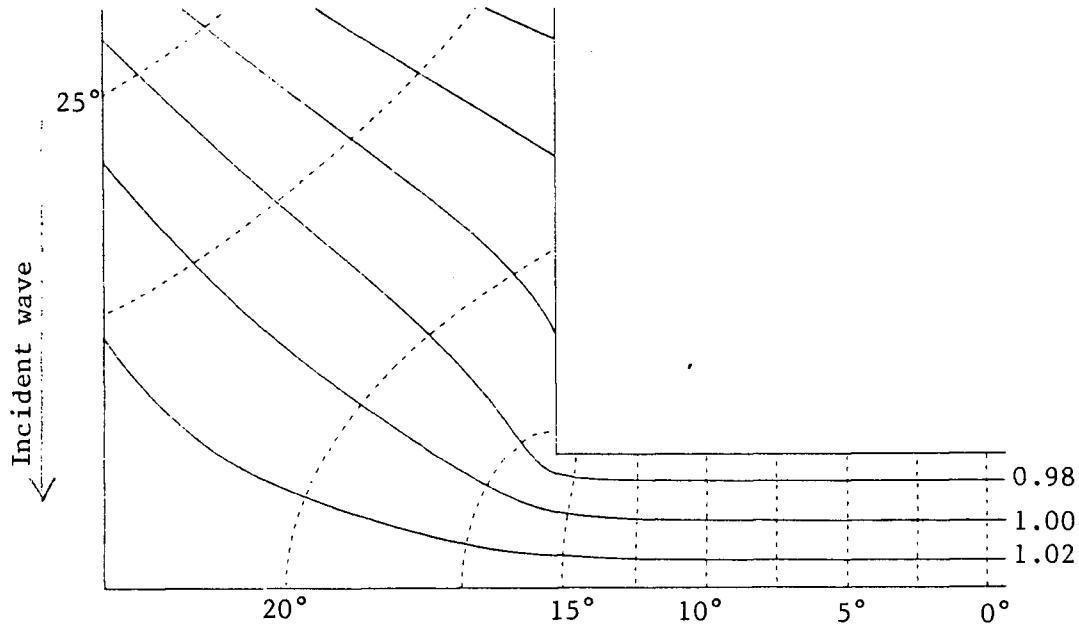

Figure 15 Pressure field for $k^2 = 7.02 \times 10^{-3}$, $\tau = 0.803$, $b = 0.3$.
Solid lines = $|P|$ contours, dashed lines = $Arg\, P$ contours.
$\lambda = 44.7$, $R_n = 8.8$, $\mathcal{R} = 35.72\,\%$, $100\% - \mathcal{T} = 22.89\,\%$.

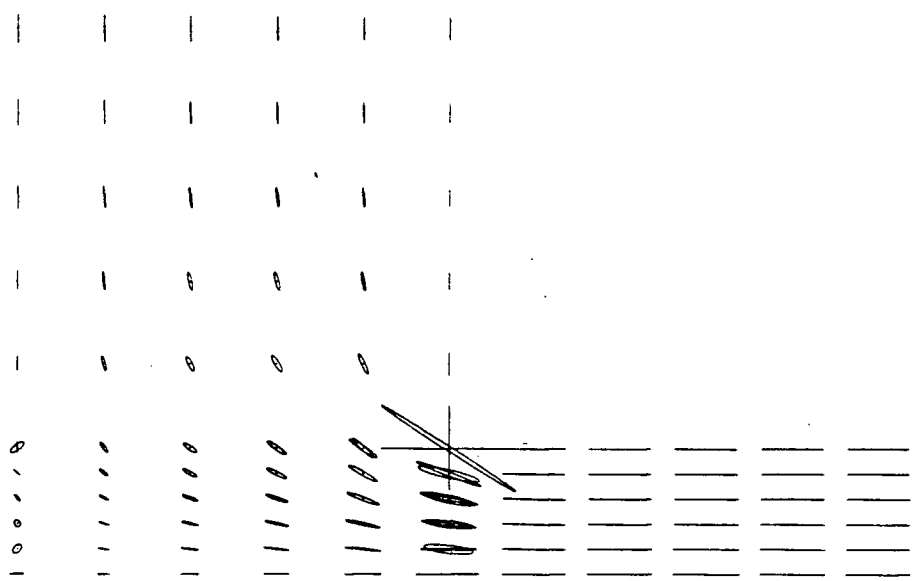

Figure 16 Velocity field corresponding to *Figure 15.*

by squaring the magnitudes of the coefficients of the incident and reflected waves. For large values of R_n ($O(1)$ or larger), this factor is approximately equal to b.

2.6 Discussion of the Solution Near the Inside Corner

Pnueli and Pekeris (1968) showed that near a corner of angular opening $\frac{\pi}{\mu}$ ($\mu < 1$), the solution is singular, and the pressure is approximated by the expression

$$P \rightarrow r^{\mu}(r\cos\mu\theta - i\sin\mu\theta) \; + \; \text{constant} \qquad \text{as } r \rightarrow 0, \tag{2.27}$$

where (r, θ) are polar coordinates whose origin is at the apex of the corner. Thus velocities are $O(r^{\mu-1})$, and are clearly singular in the present case where $\mu = \frac{2}{3}$.

The basis functions chosen for our solution are incapable of producing such a singularity, since a Fourier series representation of $r^{-\frac{1}{3}}$ does not converge. This difficulty manifests itself in the fact that it is impossible to match velocities in the region of the inside corner. The corner itself is the only point in the whole domain that is in each of the three regions, and hence there are three expressions for the velocity there. In Region 1 a condition of zero flow in the x-direction has been imposed, and in Region 3 a condition of zero y-direction flow has been imposed. The velocity in Region 2 has been constrained to match these velocities, at least in a least squares sense. The only way in which all these conditions can be consistent is if there is zero velocity at the inside corner. However, this constraint does not admit solutions of the form given by equation 2.27.

Figure 10 demonstrates the problem well. At the inside corner three current ellipses are plotted. The two calculated from the expressions for the solution in Regions 1 and 3 are simply straight lines parallel to the local boundary, whereas the third in Region 2 has its axis aligned at a 45° angle between them, as a consequence of the least squares matching. This observation might indicate that the solution shown in *Figure 10* is actually approaching the correct solution in a bend with a slightly smoothed inside corner. Unfortunately, there is the added deficiency of the failure of the current ellipses to match perfectly close to the inside corner. As one looks further away from the inside corner the matching improves, and becomes satisfactory after about $\frac{1}{4}$ of the channel width.

All that can really be said is that the solution is inadequate in the region of the inside corner. Hopefully, however, the details of the flow near the inside corner do not affect the general character of the solution, so that the solutions presented here for the rectangular bend give reasonable approximations to the amount of energy reflected and transmitted.

Because of this problem at the inside corner, a bend without a sharp discontinuity in the direction of the boundary was considered: the so-called "annular bend." As will be seen later, the results from the annular bend study are in general agreement with those from the rectangular bend, giving support to the idea that the results for the rectangular bend are in some sense close to the "true" solutions.

2.7 Method of Solution in an "Annular Bend"

Figure 17 shows the geometry of the annular bend. Again, the domain was split up into three regions, namely two straight channels and a sector of an annulus. This type of bend has two advantages over the rectangular bend . First, it is of variable angle ϕ, and, second, it has no obtuse angles in the boundary. It has the slight disadvantage of requiring that the two channels be of equal width. The previous free parameter of the second channel width has been replaced by two new free parameters: the angle of the bend ϕ, and the sharpness of the inside corner as measured by the inner radius of the annulus, r_0.

The solution in Regions 1 and 3 was represented in the same way as in the rectangular bend, but in Region 2 it was expressed as a superposition of "radial" Kelvin and Poincaré modes. If the solution $P(r,\theta)$ is separated into

$$P(r,\theta) = R(r)\,\Theta(\theta), \tag{2.28}$$

then the wave equation becomes

$$\Theta'' = -\nu^2\Theta \tag{2.29}$$

and

$$R'' + \frac{1}{r}R' + (-\frac{\nu^2}{r^2} + k^2)R = 0. \tag{2.30}$$

ν^2 is the separation constant. The solution to the θ problem is

$$\Theta = e^{\pm i\nu\theta}. \tag{2.31}$$

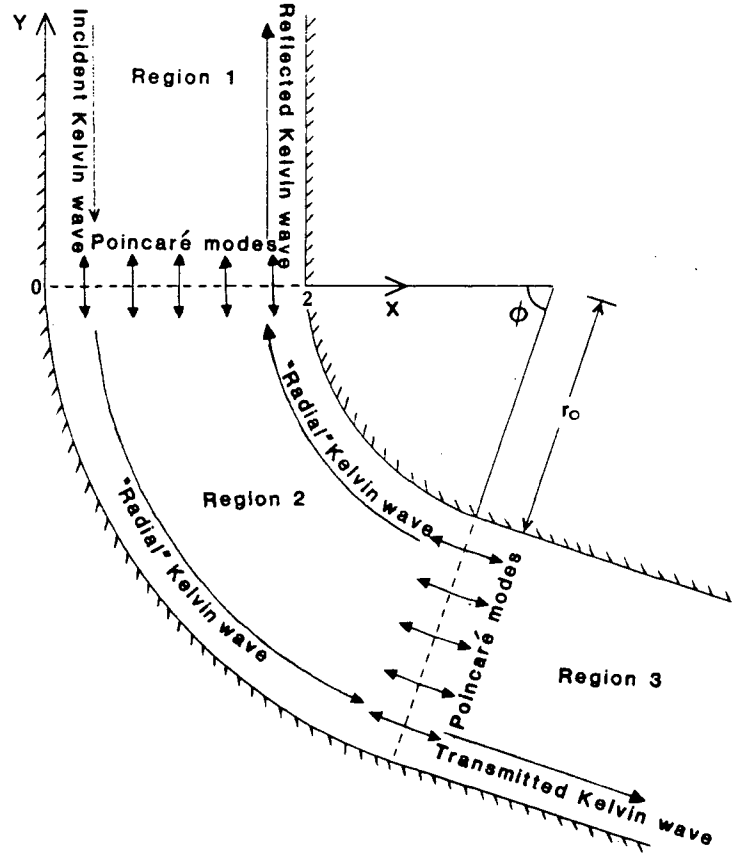

Figure 17 Schematic diagram of the "annular bend".

The boundary conditions of zero normal flow at the inner and outer radii of the annulus become

$$\mathcal{U}_r \equiv R' + \frac{\tau\nu}{r}R = 0 \qquad \text{at } r = r_0,\ r_0 + 2. \tag{2.32}$$

Equations 2.30 and 2.32 form an eigenvalue problem, whose eigenfunctions form a complete set. The corresponding expression for the velocity component parallel to the channel is

$$\mathcal{V}_\theta \equiv \frac{i\nu}{r}R + i\tau R'. \tag{2.33}$$

Equation 2.30 is Bessel's equation. For radial Kelvin waves, the eigenvalue ν is real, and the solution would be

$$R(r) = A\,J_\nu(kr) \ + \ B\,Y_\nu(kr), \tag{2.34}$$

where J_ν and Y_ν are Bessel functions of order ν, and A and B are undetermined complex coefficients. The boundary conditions at $r = r_0,\ r_0 + 2$ would determine these coefficients.

However, for evanescent radial Poincaré modes, ν is nearly imaginary (it is a complex number whose phase is close to 90° or 270° — see Section 2.8), and the solution of equation 2.30 would be in terms of Bessel functions of complex order. Because of the difficulty of computing such functions it was instead decided to solve the eigenvalue problem numerically.

A fourth order Runge-Kutta scheme was used with iterative refinement of the eigenvalue to satisfy the boundary condition at the endpoint of the integration (a "shooting" technique). This scheme was also used for the radial Kelvin waves, since no extra computer programming was required. The scheme was tested on an annulus with a very large inner radius compared to the width, and it was indeed found that the eigenvalues approached those of Kelvin waves and Poincaré modes in a straight channel (see Section 2.8).

The solution in the annulus was therefore expressed as a superposition of two radial Kelvin waves propagating in opposite directions around the annulus, and the two corresponding truncated sets of Poincaré modes, decaying in opposite directions. Again, the method of solution for the problem of an incident Kelvin wave of unit amplitude and zero phase was to solve for the $4(M+1)$ complex coefficients in two stages. Each stage involved inverting a square complex matrix of order $2(M+1)$.

The first stage is the matching of normal velocities across the boundaries between Regions 1 and 2, and between Regions 2 and 3, by the method of least squares at N locations along each boundary. For each of the $2M+3$ types of wave in the straight channels, the corresponding normal velocity was prescribed at the appropriate boundary of the annulus (zero on the opposite boundary), and the response of the annulus was calculated. The second stage is the matching of pressure, again by a least squares fit of the pressure anomalies for each of the $2M+3$ straight channel waves, to make the total pressure anomaly vanish.

2.8 Discussion of the Results of the Eigenvalue Problem in the Annulus

The eigenvalues ν_i for the radial Kelvin and Poincaré modes were found to be of the same order of magnitude as those in a straight channel of the same width. A value must be assigned to the radius when converting from polar coordinates to cartesian coordinates; this value was taken to be the average radius of the annulus ($r_0 + 1$). As the radius of the annulus tended to infinity, the eigenvalues ν_i tended to the eigenvalues in a straight channel, as expected.

The eigenvalues for Kelvin waves in a straight channel are real, and for evanescent Poincaré modes are imaginary. In both cases, the eigenvalues corresponding to waves propagating (or decaying) in the opposite direction are the negative of the original eigenvalues. However, in a bend, when there is rotation, a "splitting" occurs. As f is increased from zero, or as r_0 is decreased from infinity, the eigenvalue for a Kelvin wave propagating around a bend to the left increases slowly above its original value. The eigenvalue for a Kelvin wave propagating around a bend to the right decreases slowly below its original value. For sharp bends ($r_0 = 0.1$ say), this discrepancy between the eigenvalues for bends of opposite senses is large. This effect can be intuitively understood in terms of the difference in path lengths for a Kelvin wave bound tightly to the right-hand side of the channel. Such a wave propagating around a bend to the right will have a larger angular velocity than a wave propagating around a bend to the left for a given linear phase speed because of the shorter path length. Hence its angular wavenumber will be smaller.

The eigenvalues for Kelvin waves do, however, remain real. The cross-channel pressure distribution also stays real, and the along-channel velocity component is still imaginary (see equation 2.15). However, a small, real cross-channel velocity component is introduced. This quantity is small at first, but increases as r_0 decreases. The eigenvalues for the evanescent Poincaré modes are no longer imaginary, but a small real part is introduced as the sharpness of the bend is increased. It can be shown that the eigenvalue for a Poincaré mode decaying around a bend to the right is the negative of the complex conjugate of the eigenvalue for one decaying around a bend to the left. This small real part to the eigenvalues

is equivalent to a long wavelength oscillation which is quickly damped out by the presence of the imaginary part. The real part always has a sign such that the oscillation propagates around the bend in an anticyclonic direction (clockwise in the northern hemisphere).

2.9 Results for the Annular Bend

The following results were obtained using 10 Poincaré modes ($M = 10$), and doing a least squares fit at 20 points along each boundary ($N = 20$). It was found that it was not necessary to use such a high value for M as was used in the rectangular bend analysis (where $M = 15$) since energy conservation could be achieved with a lower number of Poincaré modes. Also N was reduced to the lowest number such that aliasing of the cross-channel structure of the highest Poincaré mode would not occur. These steps were taken to reduce computing costs. Again the approach was to vary one of the parameters while keeping the other three constant. The standard values were the same as in the rectangular bend, with the addition of $r_0 = 0.5$ and $\phi = +90°$ (a right-angled bend to the left).

2.9.1 Parameter Search 1: $\tau = 0.803$, $\phi = +90°$, $r_0 = 0.5$, *variable* k^2

Figure 18 shows a plot of the reflection coefficient $\mathcal{R}$ against k^2 for a right-angled bend to the left with constant τ and r_0. The shape of the curve is very similar to that in *Figure 7*, with a pronounced rise just before the cutoff. Again, the relationship is roughly linear for small k^2 ($k^2 < 0.025$), and the curve approaches the line $\mathcal{R} = 5.34\,k^2\,\%$ as $k^2 \to 0$. There is an order of magnitude difference in $\mathcal{R}$ between *Figure 18* and *Figure 7*; this difference can be attributed to the difference in sharpnesses of the two types of bend (see Subsection 2.9.5).

In all of the cases comprising *Figure 18* the current ellipses were observed to match very well, and no normal velocity component was observed at the boundaries. For example, in *Figures 21* and *23*, which correspond to *Figures 10* and *12*, the current ellipses match very well along the common boundaries between regions. The pattern of amphidromes in *Figure 11* is different from that in *Figure 22* because of the difference in reflection coefficients. Agreement between $\mathcal{R}$ and $100\% - \mathcal{T}$ was very good.

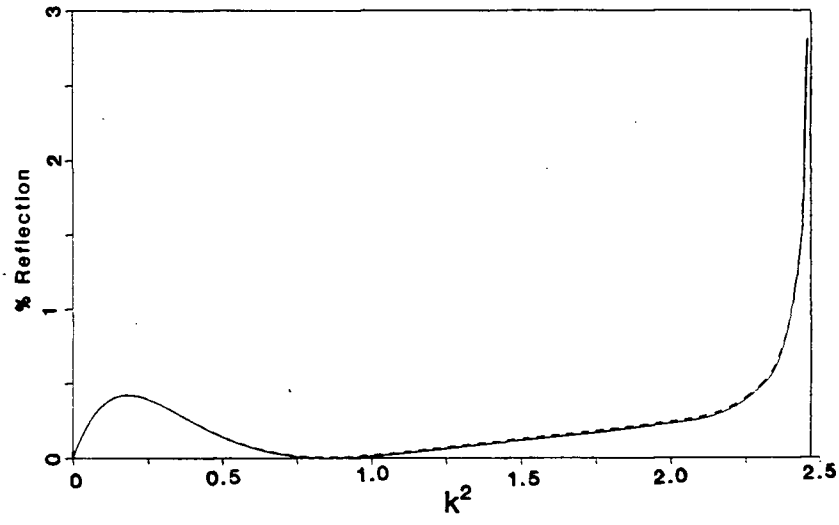

Figure 18 $\mathcal{R}$ vs k^2 for constant $\tau = 0.803$. $r_0 = 0.5$, $\phi = +90°$.
The value of k^2 for which the first Poincaré mode starts to propagate is shown by the right-hand border. Solid line = $\mathcal{R}$, dashed line = $100\% - \mathcal{T}$.

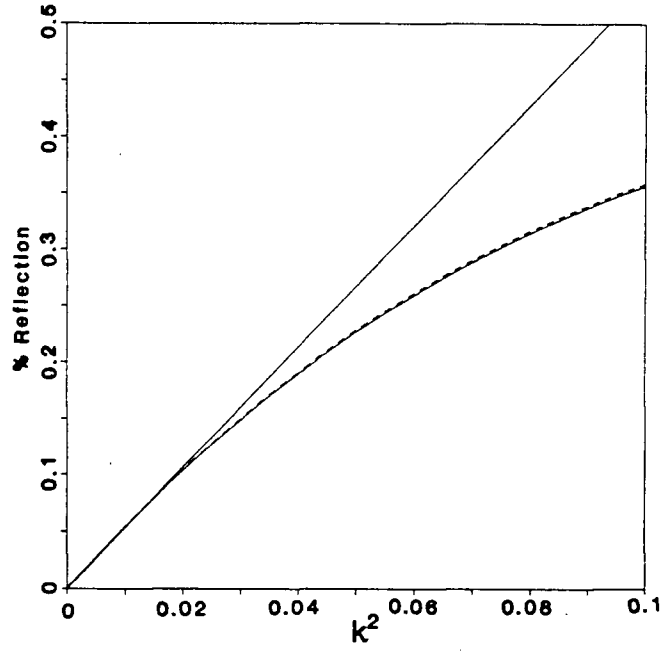

Figure 19 Blowup of *Figure 18* for small k^2.
The straight line is $\mathcal{R} = 5.34\,k^2\,\%$, which is the least squares fit for $k^2 < 0.025$.

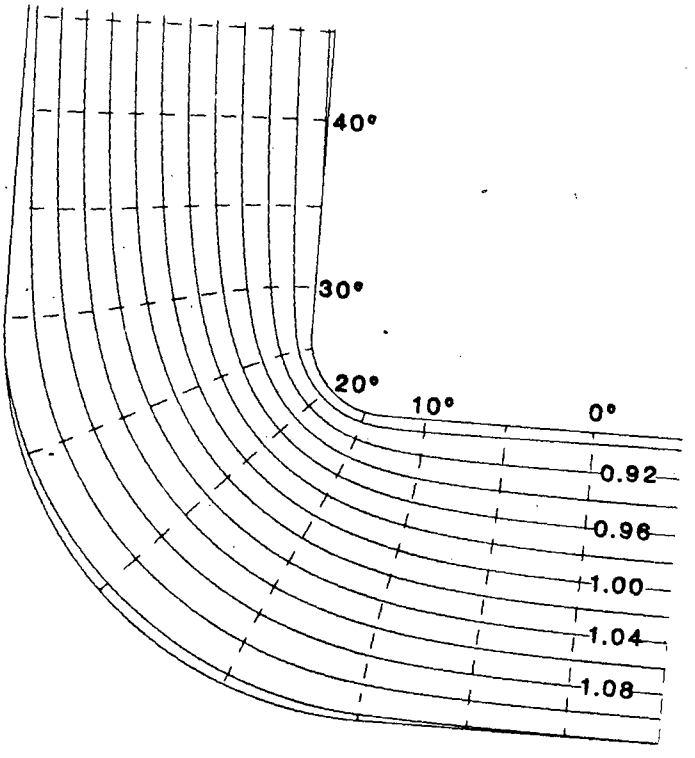

Figure 20 Pressure field for $k^2 = 7.02 \times 10^{-3}$, $\tau = 0.803$, $r_0 = 0.5$, $\phi = +90°$. Solid lines = $|P|$ contours, dashed lines = $Arg\, P$ contours. $\lambda = 44.7$, $R_n = 8.8$, $\mathcal{R} = 0.038\,\%$, $100\% - \mathcal{T} = 0.038\,\%$.

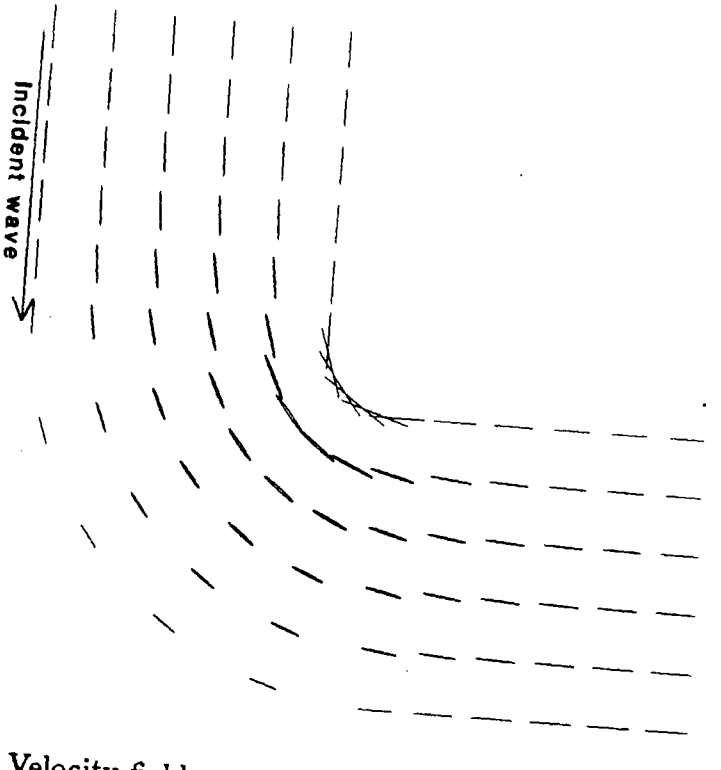

Figure 21 Velocity field corresponding to *Figure 20.*

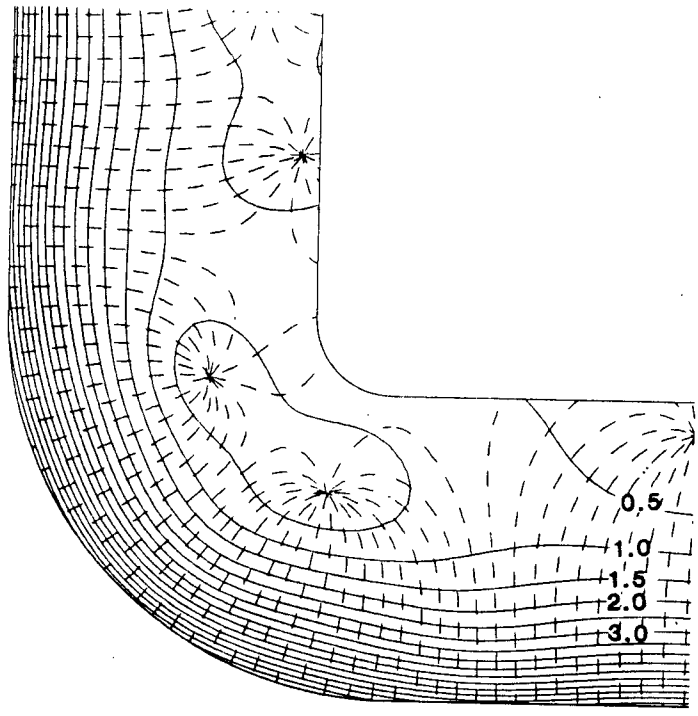

Figure 22 Pressure field for $k^2 = 2.25$, $\tau = 0.803$, $r_0 = 0.5$, $\phi = +90°$.
Solid lines = $|P|$ contours, dashed lines = $Arg\, P$ contours.
$\lambda = 2.5$, $R_n = 0.49$, $\mathcal{R} = 0.394\,\%$, $100\% - \mathcal{T} = 0.408\,\%$.

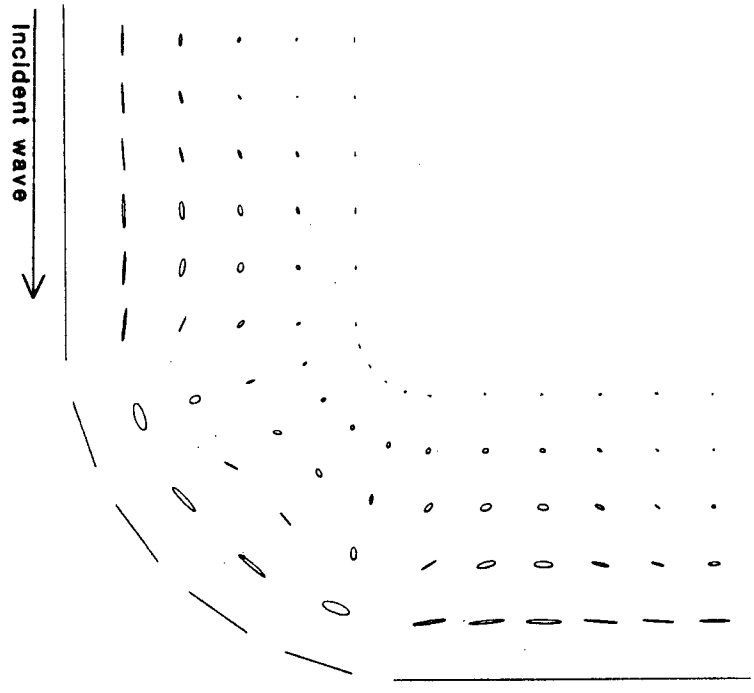

Figure 23 Velocity field corresponding to *Figure 22.*

2.9.2 Parameter Search 2: $\tau = 0.803$, $r_0 = 0.5$, *various* k^2, *variable* ϕ

Figure 24 shows the effect of varying the bend angle ϕ. Two statements can be made. The first is that there are certain angles for which there is zero reflection. The second is that there is no significant difference in reflection coefficient for a bend of a given angle to the left and a bend of the same angle to the right; i.e. *Figure 24* would be symmetrical about the $\mathcal{R}$-axis $\phi = 0$. Results for negative ϕ are not actually plotted because they are the mirror image of the values plotted. However, the results for negative ϕ would follow the $\mathcal{R}$ curve for positive ϕ as closely as the $100\% - \mathcal{T}$ curve does.

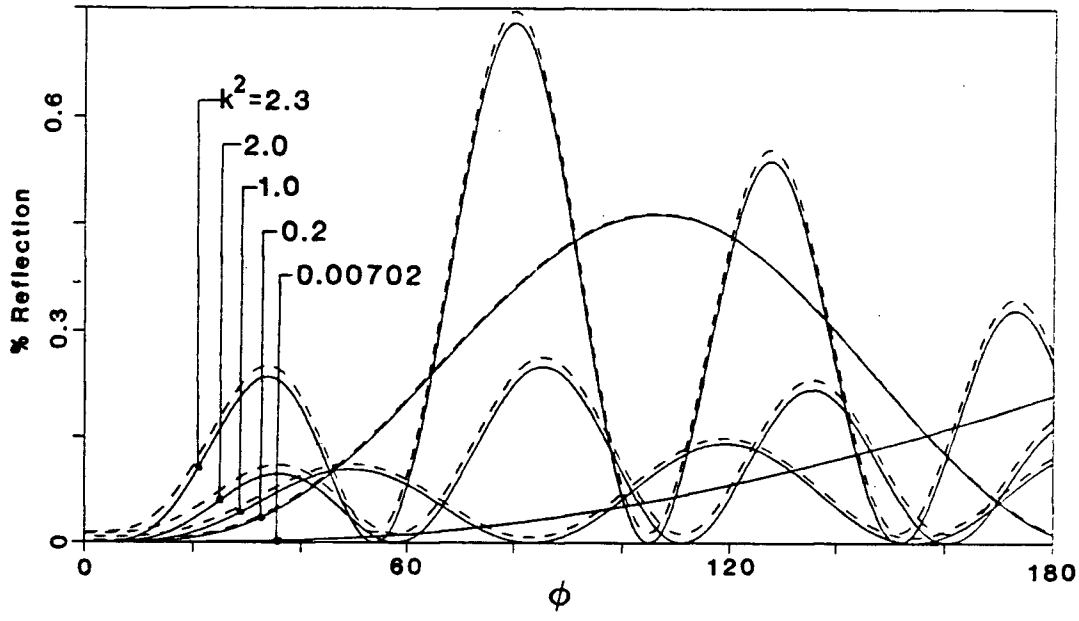

Figure 24 $\mathcal{R}$ vs ϕ for various values of k^2. $\tau = 0.803$, $r_0 = 0.5$.
Solid lines = $\mathcal{R}$, dashed lines = $100\% - \mathcal{T}$.

The effect of increasing k^2 is to compress the peaks laterally (i.e. make the zeros closer together), and to make them higher. The case $k^2 = 2.467$ was also calculated, but was not included in *Figure 24* because it would have gone off scale. It can be seen in *Figure 32* on different axes. Examination of *Figure 24* reveals why there is a dip in *Figure 18* at around $k^2 = 0.75$. *Figure 18* is a plot of $\mathcal{R}$ against k^2 for constant $\phi = 90°$, and *Figure 24* shows that the dip at $k^2 \approx 0.75$–1.00 is due to the passing of the first zero reflection over the value $\phi = 90°$. *Figures 25–28* illustrate the fact that a bend of 30° to the left and a bend

of 30° to the right have similar but not identical solutions, yet the captions show that they have the same reflection coefficient (36%). Energy is preserved, and the pressure and velocities match.

The value used for k^2 is 2.467, which is just before the cutoff value at which the first mode Poincaré wave propagates. This value was chosen to give a large $\mathcal{R}$. In fact, the e-folding length for the decay of the Poincaré mode is $50L$ (i.e. 25 times the channel width), and the solution is dominated by this mode (its amplitude is an order of magnitude higher than the Kelvin waves). This is the reason for the characteristic change in phase of the pressure in mid-channel by 180°, and the maximum in velocities in mid-channel in *Figures 25–28* (see equations 2.16 and 2.17 with very small k^2). There is no along-channel phase propagation because the Poincaré mode is evanescent. The Poincaré mode does not contribute any energy flux, but it does dominate the solution near the bend (within, say, $100L$ of the bend).

The generation of a large amplitude Poincaré mode seems to be associated with the occurrence of high reflection coefficients for the Kelvin wave and occurs when the Poincaré mode has a large decay scale (almost propagating). It is interesting to note that Brown (1973) found a similar result in his study of the reflection of a Kelvin wave from the end of a channel (the Taylor problem). He allowed the first Poincaré mode to propagate, so that any energy not reflected as a Kelvin wave was reflected as a Poincaré wave. He found that just above the critical frequency at which the first Poincaré mode starts to propagate (i.e. k^2 just above $(\frac{\pi}{2})^2$), this mode becomes the principal energy-reflection mechanism. The Poincaré mode rapidly asserts itself as the dominant reflection mechanism.

It therefore seems likely that soon after the first Poincaré mode starts to propagate it will rapidly become a dominant energy radiation mechanism in the bend too, although in which direction is open to speculation. The amplitude of the Poincaré mode has already been seen to become very large for k^2 just less than $(\frac{\pi}{2})^2$, although as long as the mode is evanescent it cannot contribute to the energy flux budget. However, as k^2 increases above

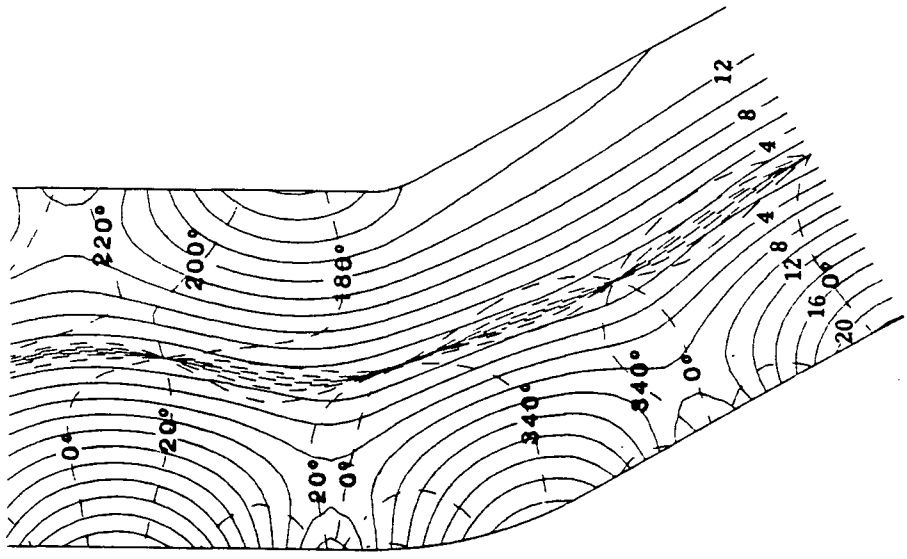

Figure 25 Pressure field for $k^2 = 2.467$, $\tau = 0.803$, $r_0 = 0.5$, $\phi = +30°$.
Solid lines = $|P|$ contours, dashed lines = $Arg\, P$ contours.
$\lambda = 2.4$, $R_n = 0.47$, $\mathcal{R} = 35.93\,\%$, $100\% - \mathcal{T} = 36.00\,\%$.

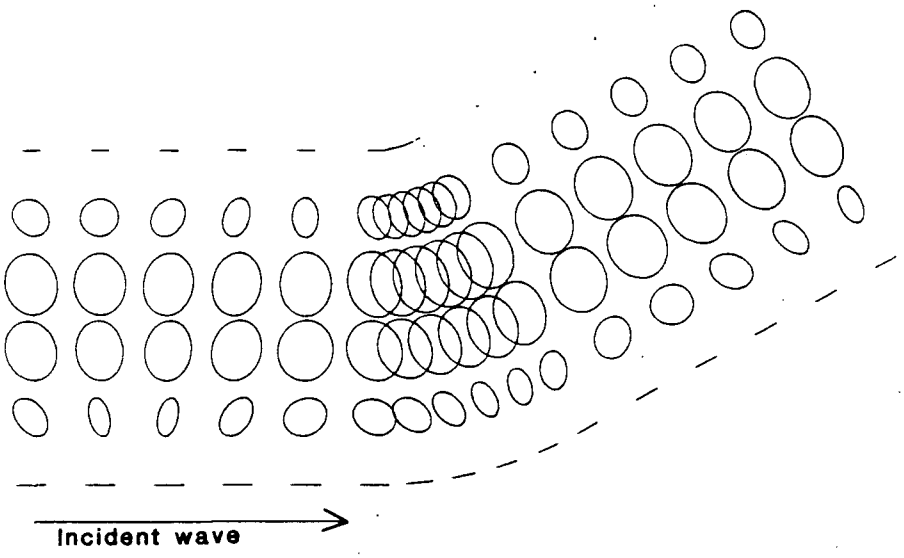

Figure 26 Velocity field corresponding to *Figure 25*. The curved line at the inside corner is a result of several short ellipses running into each other.

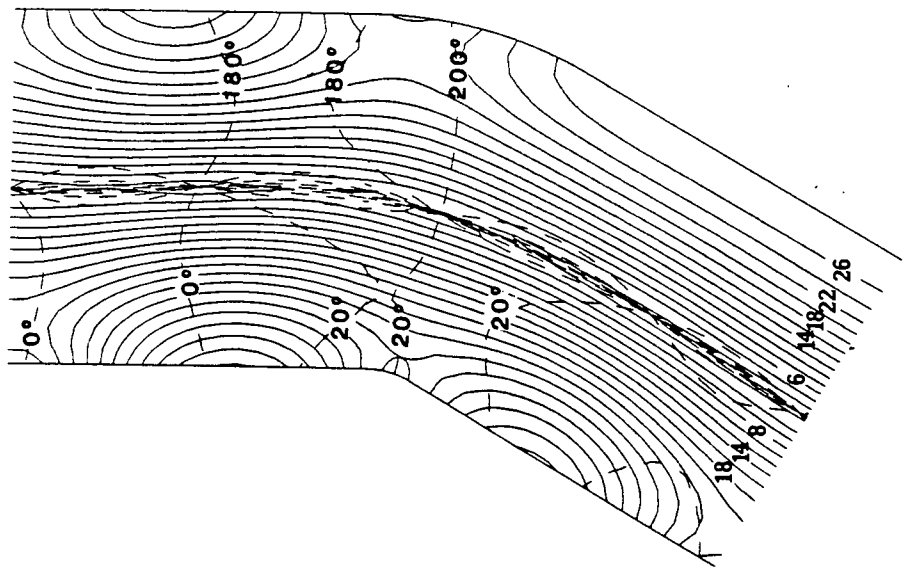

Figure 27 Pressure field for $k^2 = 2.467$, $\tau = 0.803$, $r_0 = 0.5$, $\phi = -30°$.
Solid lines = $|P|$ contours, dashed lines = $Arg\, P$ contours.
$\lambda = 2.4$, $R_n = 0.47$, $\mathcal{R} = 35.88\,\%$, $100\% - \mathcal{T} = 36.42\,\%$.

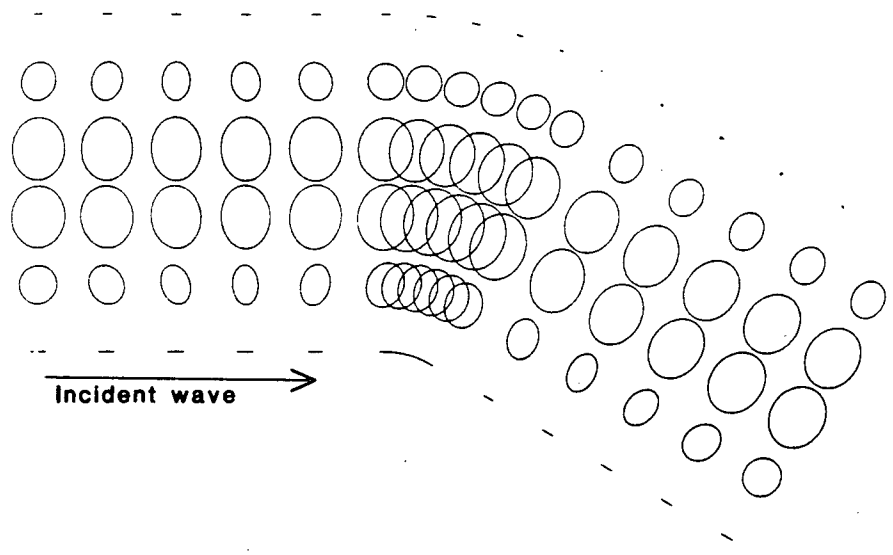

Figure 28 Velocity field corresponding to *Figure 27.*

$(\frac{\pi}{2})^2$, it is only necessary for the magnitude of that mode to remain large for the energy flux to increase rapidly, since the group velocity c_g will increase rapidly anyway. Brown showed that if $k^2 = (\frac{\pi}{2})^2(1+\delta)$, then $c_g = O(\delta^{\frac{1}{2}})$.

2.9.3 Parameter Search 3: $k^2 = 7.02 \times 10^{-3}$, $r_0 = 0.5$, $\phi = 90°$, *variable* τ

Figure 29 shows the effect of varying τ with a constant, small k^2 in a right-angled bend. Just as in the rectangular bend (*Figure 13*), there is good agreement with a curve of the form $\frac{1}{1-\tau^2}$, at least for $\tau < 1$. The constant of proportionality is 1.33×10^{-3} for the case $r_0 = 0.5$. This is equivalent to

$$\mathcal{R} = 0.191\, r^2\,\%, \tag{2.35}$$

where again r is the ratio of the channel width to the wavelength of the incident Kelvin wave. This result can be compared to $1.96\, r^2\,\%$ (equation 2.25) for the rectangular bend.

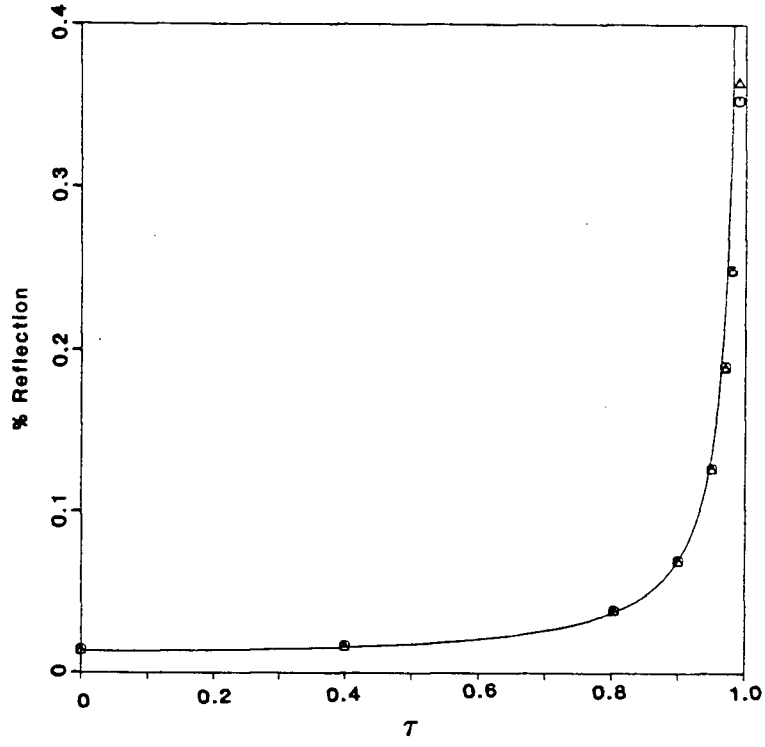

Figure 29 $\mathcal{R}$ vs τ for constant $k^2 = 7.02 \times 10^{-3}$ and $\phi = +90°$. $r_0 = 0.5$.
Circles = $\mathcal{R}$, triangles = $100\% - \mathcal{T}$.
The curve is $\mathcal{R} = \frac{1.33 \times 10^{-3}}{1-\tau^2}\,\%$, which is the least squares fit to a function of that form.

The method of solution breaks down for $\tau > 1$ (sub-inertial frequencies). For these

values of τ, k^2 was taken to be -7.02×10^{-3}. This choice preserves the wavelength of the Kelvin waves and the Rossby radius. Poincaré waves can never propagate at sub-inertial frequencies. There was found to be a large discrepancy between $\mathcal{R}$ and $100\% - \mathcal{T}$. Also, inspection of the current ellipses revealed that velocity matching was bad.

Figures 30 and *31* show the solution in the case $\tau = 0$, which corresponds to no rotation. The Rossby radius is infinite, and there is therefore no cross-channel decay of the Kelvin wave. The Kelvin wave becomes a regular gravity wave. There is very little variation in the amplitude of P in the whole domain; the solution is more or less a plane wave propagating directly around the bend with no reflection.

The current ellipses are almost linear, which is associated with the fact that the Poincaré modes are of very small amplitude and short decay scale (an e-folding length of $0.6L$). Kelvin waves have no cross-channel velocity in straight channels, and very little cross-channel velocity in annular bends. On the other hand, odd Poincaré modes have a maximum in the cross-channel velocity at the centre of the channel, which gives rise to round current ellipses there. The presence of large, slowly decaying Poincaré modes seems to be associated with large reflection coefficients for the Kelvin wave, which therefore correlates with round current ellipses.

2.9.4 Parameter Search 4: $r_0 = 0.5$, *various* k^2, *various* τ, *variable* ϕ

Figure 32 shows plots of $\mathcal{R}$ against bend angle ϕ for various values of k^2 and τ. For small k^2 (*Figure 32*a), larger values of τ lead to larger values of $\mathcal{R}$ for all angles. The system is in the $\frac{1}{1-\tau^2}$ regime. However, for large k^2 (*Figure 32c*), larger values of τ lead to smaller values of $\mathcal{R}$. For intermediate values of k^2 (*Figure 32b*), the curves seem to start off in the $\frac{1}{1-\tau^2}$ regime for small angles (say $\phi < 40°$), but move into the large k^2 regime for larger angles.

Figure 32c is in keeping with the results of Packham and Williams (1968). Their Figure 1 is presented in *Figure 34* on reversed axes to conform with *Figure 32c*. They investigated the propagation of a Kelvin wave around a wedge of variable angle. In their

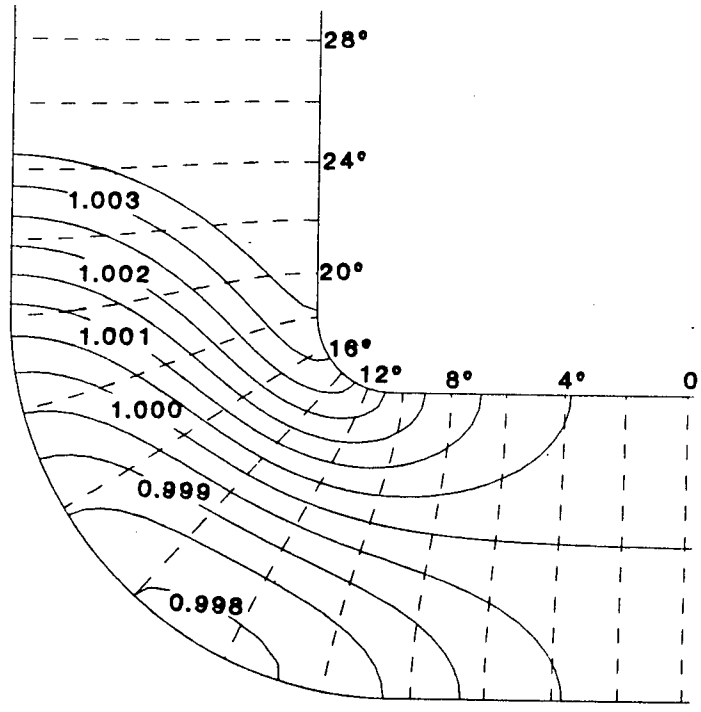

Figure 30 Pressure field for $k^2 = 7.02 \times 10^{-3}$, $r = 0$, $r_0 = 0.5$, $\phi = +90°$.
Solid lines = $|P|$ contours, dashed lines = $Arg\, P$ contours.
$\lambda = 75.0$, $R_n = \infty$, $\mathcal{R} = 0.141\,\%$, $100\% - \mathcal{T} = 0.144\,\%$.

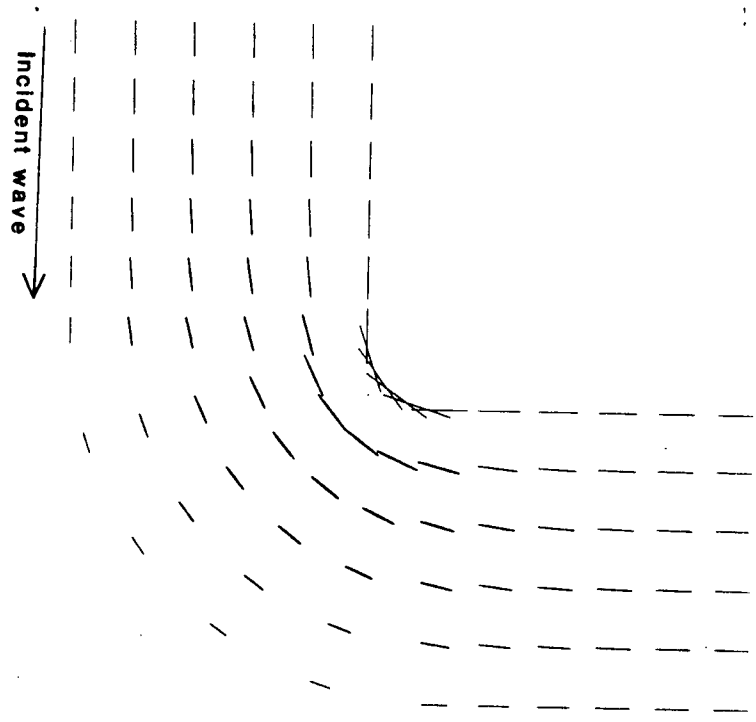

Figure 31 Velocity field corresponding to *Figure 30.*

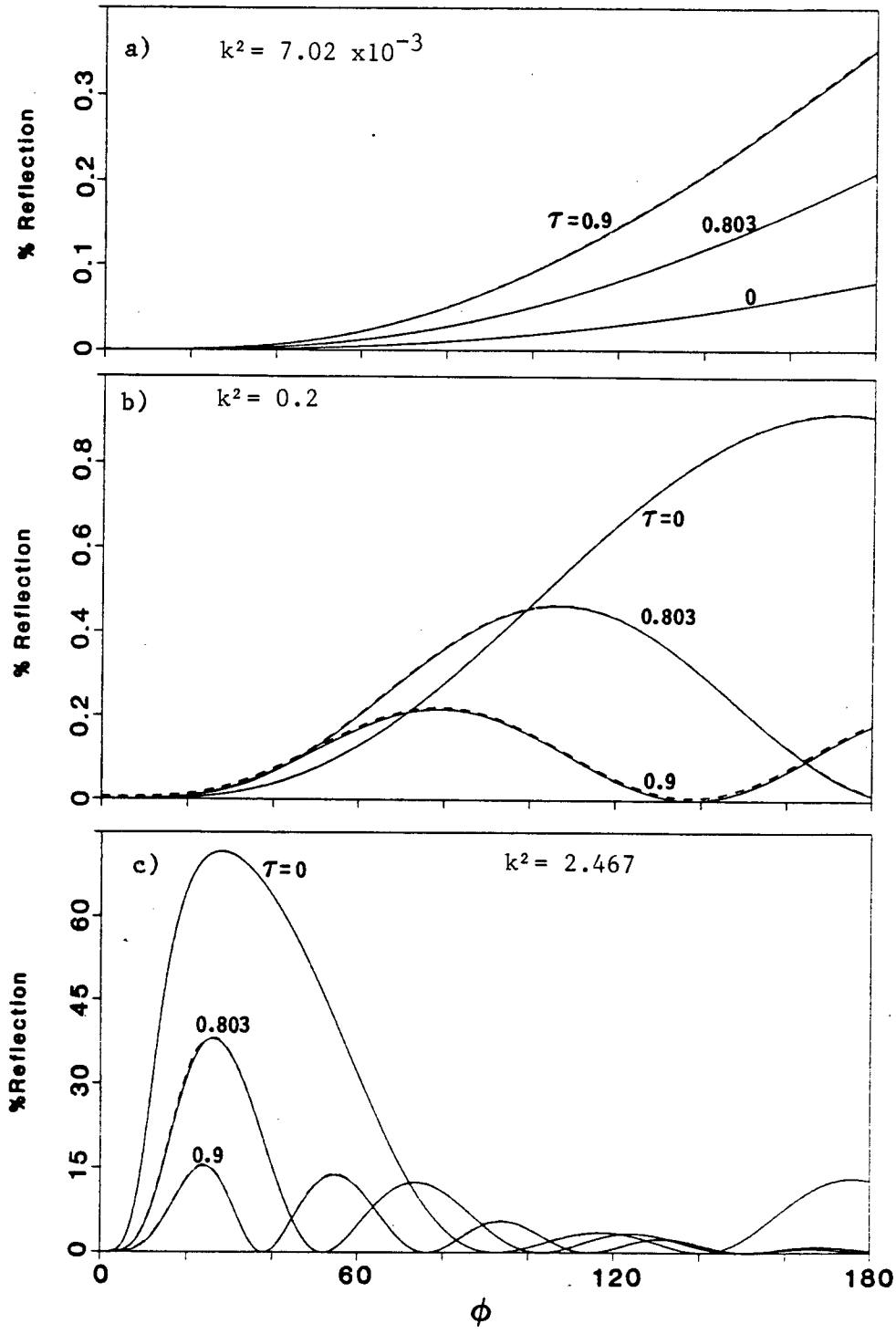

Figure 32 $\mathcal{R}$ vs ϕ for various values of k^2 and τ. $r_0 = 0.5$.

case no reflected Kelvin wave was possible. Energy that was not transmitted as an ongoing Kelvin wave was radiated as cylindrical Poincaré waves (see *Figure 33*). These Poincaré waves could propagate because the frequency was super-inertial, and there was no channel.

They also found angles at which there was complete transmission, and that larger values of τ gave lower values for $\mathcal{R}$. Their problem gives no meaning to k^2, since there is no natural length scale with which to non-dimensionalise the incident wavelength. However, large k^2 (as in *Figure 32c*) in the annular bend would be expected to correspond most closely with their problem, since then the Poinçaré modes are almost propagating, and they do have propagating Poincaré modes.

The observation that the peaks in *Figures 32* and *24* were compressed as k^2 increased led to the idea of plotting the first angle of complete transmission ϕ_0, against the incident wavelength λ. The result is shown in *Figure 35*, which includes results from various values of k^2 and τ. A remarkable linear relationship was found. This result means that the width of the "lobes" in the $\mathcal{R}$–ϕ plots is directly proportional to the incident wavelength. This result is also found in diffraction theory in other fields such as optics and electromagnetism (e.g. Hecht and Zajac 1974 Chapter 10). It suggests that perhaps a better way to represent the data would be to scale the ϕ-axes with λ, since then the angles of complete transmission would lie at the same position. Then only the amplitudes and shapes of the diffraction patterns would vary; some secondary lobes are bigger than the primary lobe.

This relationship between the width of the lobe and λ is also consistent with the linear relationship between $\mathcal{R}$ and λ^{-2} for large λ and fixed ϕ. The relationship between $\mathcal{R}$ and ϕ is almost quadratic for small ϕ (i.e. $\mathcal{R} \propto \phi^2$, see, for example *Figure 32a*), so scaling ϕ with λ is almost equivalent to scaling $\mathcal{R}$ with λ^2. This means that plots of $\mathcal{R}$ against $\lambda\phi$ for various values of k^2 and τ will be approximately the same for small $\lambda\phi$. After the initial portion of the curve, the plots will diverge according to their different peak values.

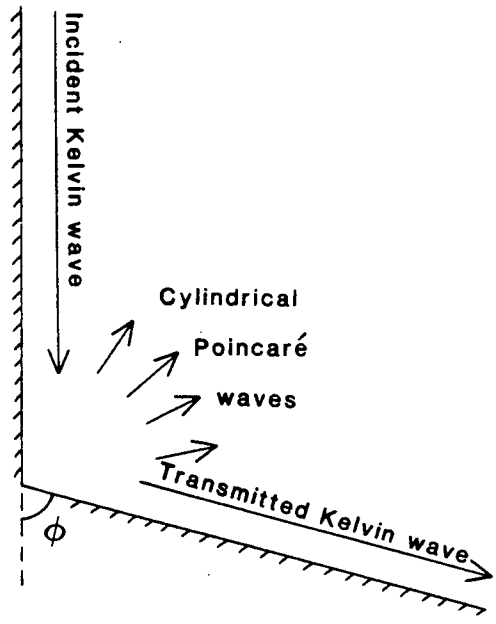

Figure 33 Bend in a straight coastline studied by Packham and Williams (1968).

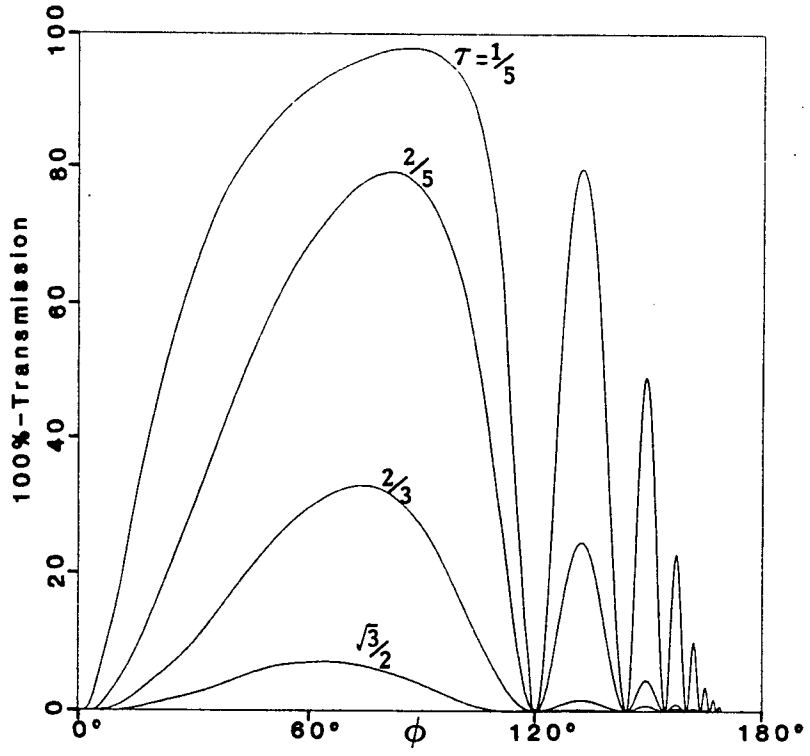

Figure 34 $100\% - \tau$ vs ϕ for Packham and Williams' bend.
(After Packham and Williams 1968.)

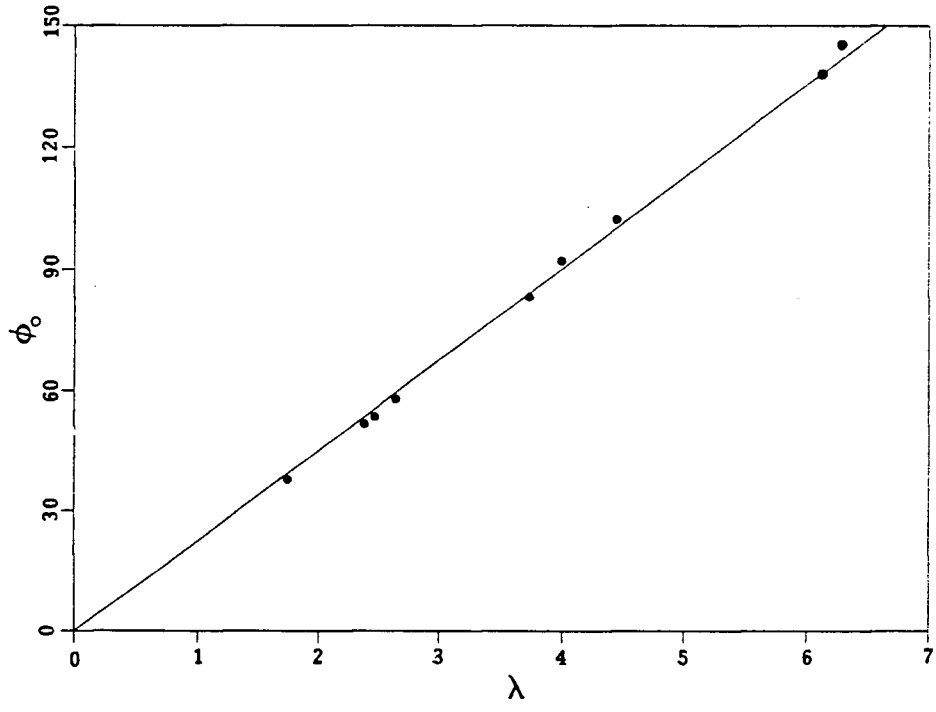

Figure 35 Angle of first zero reflection vs λ for $r_0 = 0.5$.
The straight line is the least squares fit.

2.9.5 Parameter Search 5: $\tau = 0.803$, *various* k^2, *various* r_0, *variable* ϕ

So far all the results for the annular bend have been for a fixed sharpness, $r_0 = 0.5$. *Figure 36* shows the effect of varying this inside radius for medium and large values of k^2. In both cases increasing the sharpness (decreasing r_0) gives rise to higher reflection coefficients. Not only are the peak values of the lobes increased but the constant of proportionality between the width of the lobe ϕ_0 and the incident wavelength λ is increased.

For very sharp bends ($r_0 = 0.1$) there is a significant discrepancy between $\mathcal{R}$ and $100\% - \mathcal{T}$ and the velocities fail to match precisely. Also there are large velocities in the region of the inside bend, especially for small k^2. In effect, all the problems encountered with the rectangular bend start to show.

Figures 37 and *38* show the solution in a gradual bend. The parameters are the same as in *Figures 25* and *26* except for the inside radius, which has been increased from 0.5 to 2.0. This change has caused the reflection coefficient to drop from 36% to 0.7%. The

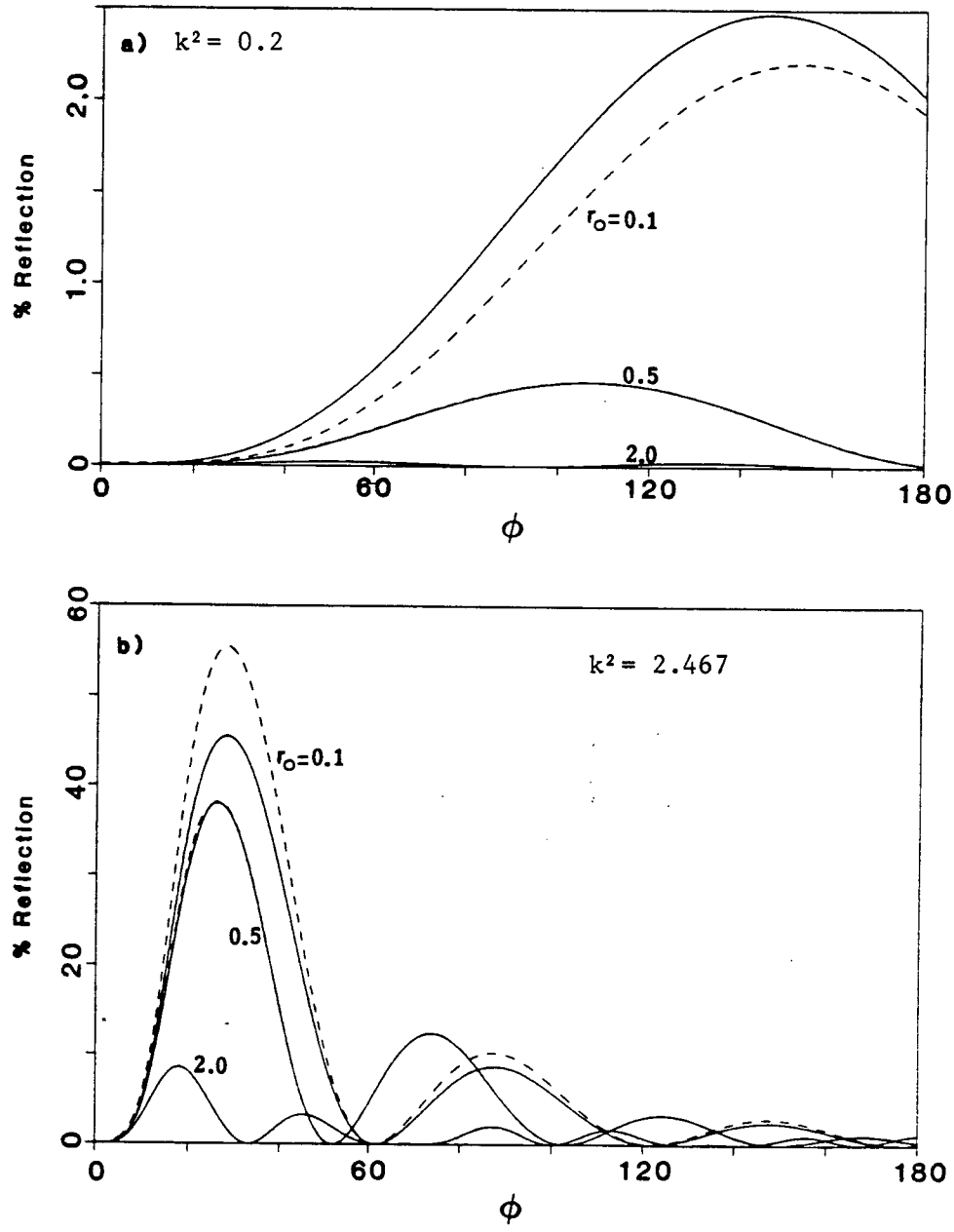

Figure 36 $\mathcal{R}$ vs ϕ for various values of r_0 and k^2. $\tau = 0.803$.
Solid lines = $\mathcal{R}$, dashed lines = $100\% - \mathcal{T}$.

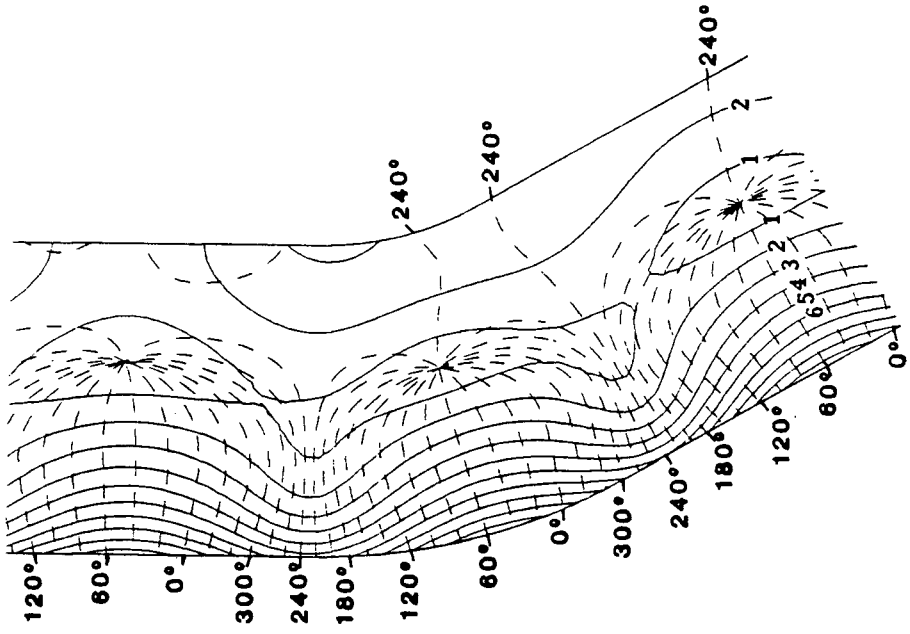

Figure 37 Pressure field for $k^2 = 2.467$, $\tau = 0.803$, $r_0 = 2.0$, $\phi = +30°$.
Solid lines = $|P|$ contours, dashed lines = $Arg\, P$ contours.
$\lambda = 2.4$, $R_n = 0.47$, $\mathcal{R} = 0.733\,\%$, $100\% - \mathcal{T} = 0.738\,\%$.

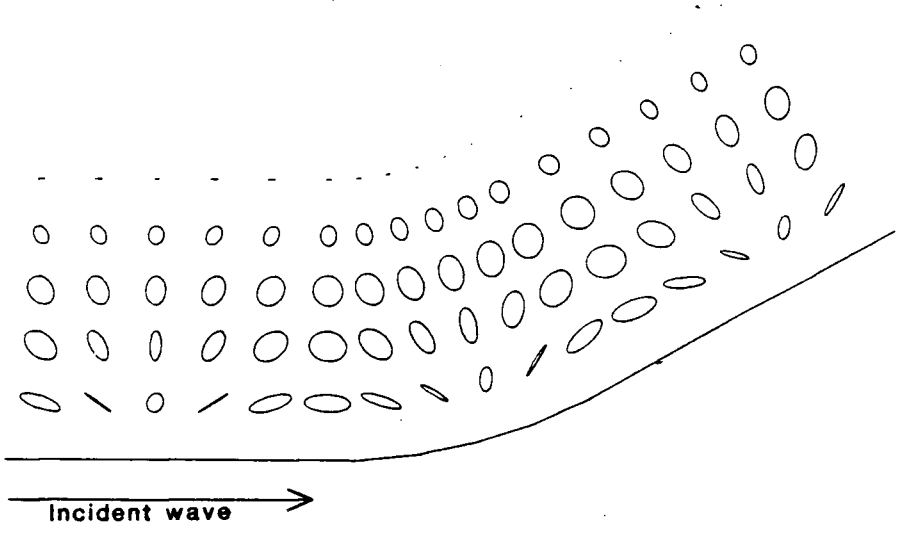

Figure 38 Velocity field corresponding to *Figure 37.*

solution is no longer dominated by Poincaré modes. It is remarkable that bends to the left and bends to the right of the same angle (e.g. *Figures 25–28*) have similar solutions and identical reflection coefficients, whereas changing the inside radius and leaving the angle alone (e.g. *Figures 37* and *38*) has a major impact upon the solution and reflection coefficient.

2.10 Conclusion

It was found that the method of solution did not work in a bend with an obtuse discontinuity in the direction of the boundary (i.e. the rectangular bend) because there is a singularity in the velocity field there. The method worked well in a bend with smooth sides (i.e. the annular bend). The bend acts as a "diffraction grating." For certain bend angles there is total transmission, and between these angles there are "lobes" of high reflection. These lobes form a diffraction pattern which spreads out as the incident wavelength increases. The width of the lobes is proportional to the wavelength, as in other types of waves in optics, electromagnetism etc. The constant of proportionality depends on the sharpness of the bend.

It was found that bends to the left give rise to the same reflection coefficient as bends to the right of the same angle, irrespective of the degree to which the incident Kelvin wave is trapped against one wall (as measured by the Rossby radius). For bends of fixed angle the reflection coefficient was found to be proportional to r^2 for small r, where r is the ratio of the channel width to the incident wavelength. (This result is similar to that of Buchwald (1971) for a Kelvin wave propagating past the mouth of a narrow channel (see Section 2.1).) The constant of proportionality increases as the bend becomes sharper. Just below the critical frequency at which Poincaré mode propagation becomes possible, this mode starts to dominate the solution, although while this mode is still evanescent it cannot contribute to the energy flux budget. This is consistent with Brown's (1973) result just above the critical frequency in a closed channel.

The method of solution breaks down inexplicably for sub-inertial frequency waves. The

method also breaks down as the inside radius of the annular bend tends to zero, because of the singularity in the velocity field near corners whose angular opening is greater than 180°, as shown by Pnueli and Pekeris (1967). To solve the problem correctly in a geometry that has such a corner, the form of the solution must be capable of expressing a singularity.

The reflection coefficient of the internal tide in Knight Inlet at the 90° bend was found to be very small. It would be much less than 1% even for modes of order 4 or 5. However, the results of this chapter are equally applicable to a bend in any channel, and to barotropic tides.

3. Observations of the Internal Tide in Knight Inlet

3.1 Introduction

In this Chapter data taken from Knight Inlet in the summers of 1981 and 1983 will be used to try to determine how much of the internal tide propagating up-inlet from the sill is reflected by the first bend, and how much is transmitted. The first few theoretical normal modes for a flat-bottomed ocean (calculated using measured N^2-profiles) are fitted to the vertical profiles of amplitude and phase of the M_2 constituent of longitudinal velocity and density oscillations. In this way the amplitude and phase of the first few normal modes can be estimated at each station, for waves propagating both up-inlet and down-inlet. The results of this analysis at the station just before the bend should, in theory, give a reflection coefficient for each mode.

Sections 3.2–3.3 describe the data and give the results of the harmonic analysis. The amplitude and phase of *each* constituent are included for completeness, although only those of the M_2 constituent will be used in the subsequent analysis. Sections 3.4–3.7 give the theory of normal modes and normal mode fitting, including the treatment of the barotropic mode. Section 3.8 describes how the amplitude af the various modes can be converted into energy flux estimates for each mode. The actual normal modes used in the fitting are presented in Section 3.9, and a discussion of how they differ from Farmer and Smith's (1980) modes given in Section 3.10. Finally, the results of the fitting are presented in Section 3.11. In Section 3.12 the energetics of Knight Inlet are discussed, with reference to the work of Stacey (1985) and Freeland and Farmer (1980). The Chapter is concluded in Section 3.13.

3.2 Description of the Data

In an attempt to study the internal tide in Knight Inlet, four cyclesonde current meters were deployed in the summers of 1981 and 1983. In total they produced 11 time series: three 12-day records from 30th July – 11th Aug 1981 (Julian days 211 – 223), four 32-day records from 20th July – 21st Aug 1983 (Julian days 201 – 233) and four 26-day records from 1st Sept – 27th Sept 1983 (Julian days 244–270).

The positions of the stations are shown in *Figure 1.* In 1981 the instruments were located at Protection Point (towards the mouth of Knight Inlet), Lull Bay (2 km seaward of the sill), and at Tomakstum Island (8 km seaward of the first big bend). In July 1983 an additional instrument was deployed off Adeane Point (3 km landward of the bend). All these stations were in mid-channel. However, in September 1983 the mooring at Lull Bay was replaced by a second mooring at Tomakstum Island. The two moorings at Tomakstum Island were placed on either side of the channel, each approximately 500 m from the centreline of the channel. The locations of these two stations are shown in *Figure 39.*

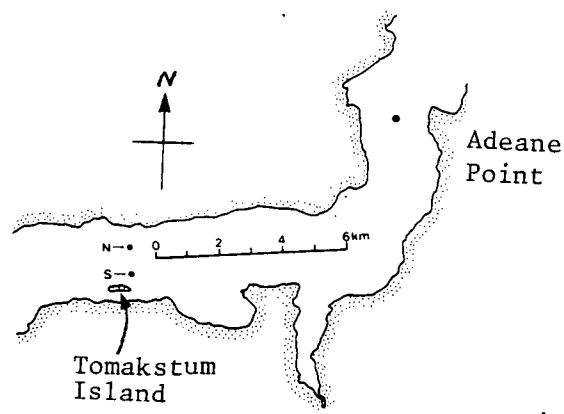

Figure 39 Detailed map of the first bend in Knight Inlet.

The cyclesondes are automatic-profiling current meters (Van Leer et al., 1974). Built into the body of the instrument is an inflatable bladder and a helium tank. The valve to inflate and deflate the bladder with helium is under electronic control. When the bladder is inflated the instrument has a positive buoyancy of about 500 g, whereas when it is deflated

it has a similar negative buoyancy. Ballast can be added to or removed from the instrument before each deployment to compensate for an operating environment of different density from its previous deployment. The cyclesonde moves up and down a plastic coated steel wire, which passes through a block in the body of the instrument, under its own buoyancy. The wire is attached to a railway wheel at the bottom, and is kept tight by a subsurface buoy at a depth of approximately $10\,m$. The vertical travel of the instrument is constrained by two bumpers, the upper one at around $12-17\,m$, depending on the state of the tide, and the lower one at no more than $200\,m$ for these deployments. Sometimes the instrument did not reach the upper bumper if the pycnocline was relatively deep, because of insufficient buoyancy.

The current is measured by two Savonius rotors which provide independent information on the speed of the water relative to the instrument. In addition there is an internal compass, and temperature, conductivity, pressure and pitch sensors. Salinity and density can be calculated from the conductivity and temperature data. In 1981 the profiles were set to commence every $1\frac{1}{2}$ hours at Tomakstum Island and Protection Point, and every 1 hour at Lull Bay. The sampling interval, that is the interval over which revolutions of the rotors are counted and data recorded on cassette tape, was set to be 1 minute. However, in 1983 the profiles were set to occur every 3 hours at all stations, and a variable sampling rate was used. In the variable rate mode, the data were recorded every minute for one hour during the profile, and every 5 minutes for the next 2 hours while the instrument was sitting against the top or bottom bumper. This mode is more efficient on tape usage than the fixed rate mode by not wasting tape when not profiling. Each profile took approximately 30–45 minutes, depending on the depth of the bottom bumper and on the weight of helium remaining in the tank.

The data were transferred back in the laboratory from cassette tape to computer tape, so that the processing could be done on the mainframe computer. After the data had been converted into physical units they were edited on the terminal. Suspect features such as spikes in the conductivity record (which could be caused by organisms swimming

in the conductivity cell) or in the heading (which could be caused by a faulty reading from the compass) were listed and looked at, with the option of replacing the values with interpolated values based on previous and succeeding points.

The average water speed past the instrument over the one-minute period was calculated from the number of revolutions of the rotors over that period. If the two rotors did not differ by more than $3\,cm/s$ the average of the two was used, otherwise the higher value was used on the assumption that the other rotor had become stuck for some time. The vertical component of the velocity due to rising or falling of the instrument was calculated from the rate of change of depth (given by the pressure sensor), and the square of this vertical component was subtracted from the square of the speed of water past the intrument. The absolute vertical component of velocity of the water was assumed to be small enough to be ignored, since according to theory the vertical component of velocity for the internal tide is at most $\frac{1}{100}$ times the horizontal component (see *Figures 75–76*). Average values for the northwards and eastwards components of the horizontal velocity for that minute were then calculated by assuming that the heading varied linearly with time from the beginning of the interval to the end. These velocities were vector-averaged over intervals of a little less than the standard depth interval (10 or $15\,m$) and then interpolated to standard depths. *Table 1* lists the standard depths for each station.

Table 1
Standard depths at each station

station	*bottom depth (m)*	*shallowest standard depth (m)*	*standard depth interval (m)*	*deepest standard depth (m)*
Protection Point	180	20	15	155
Lull Bay	164	25	10	125
Tomakstum Island	340	20	15	170
Adeane Point	530	20	15	170

These standard depths were chosen so that the profiles usually reached the upper and lower depths. The principal axes of the velocities at each standard depth were then calculated, and their average orientation over the water column used to resolve the velocities

into along-channel (longitudinal) and cross-channel (transverse) components. In practice, the principal axes at Protection Point, Lull Bay and Tomakstum Island were all within 5° of true east, and those at Adeane Point were all within 5° of true north. *Figures 40* and *41* show the longitudinal and transverse components of the velocity at Tom-N in September 1983 at the standard depths. The dominant signal is the M_2 tide , with a period of 12.42 hours. The signal is modulated at a fortnightly frequency. This springs to neaps cycle can be thought of as a beating of the M_2 signal with the S_2 signal which has a period of 12.00 hours.

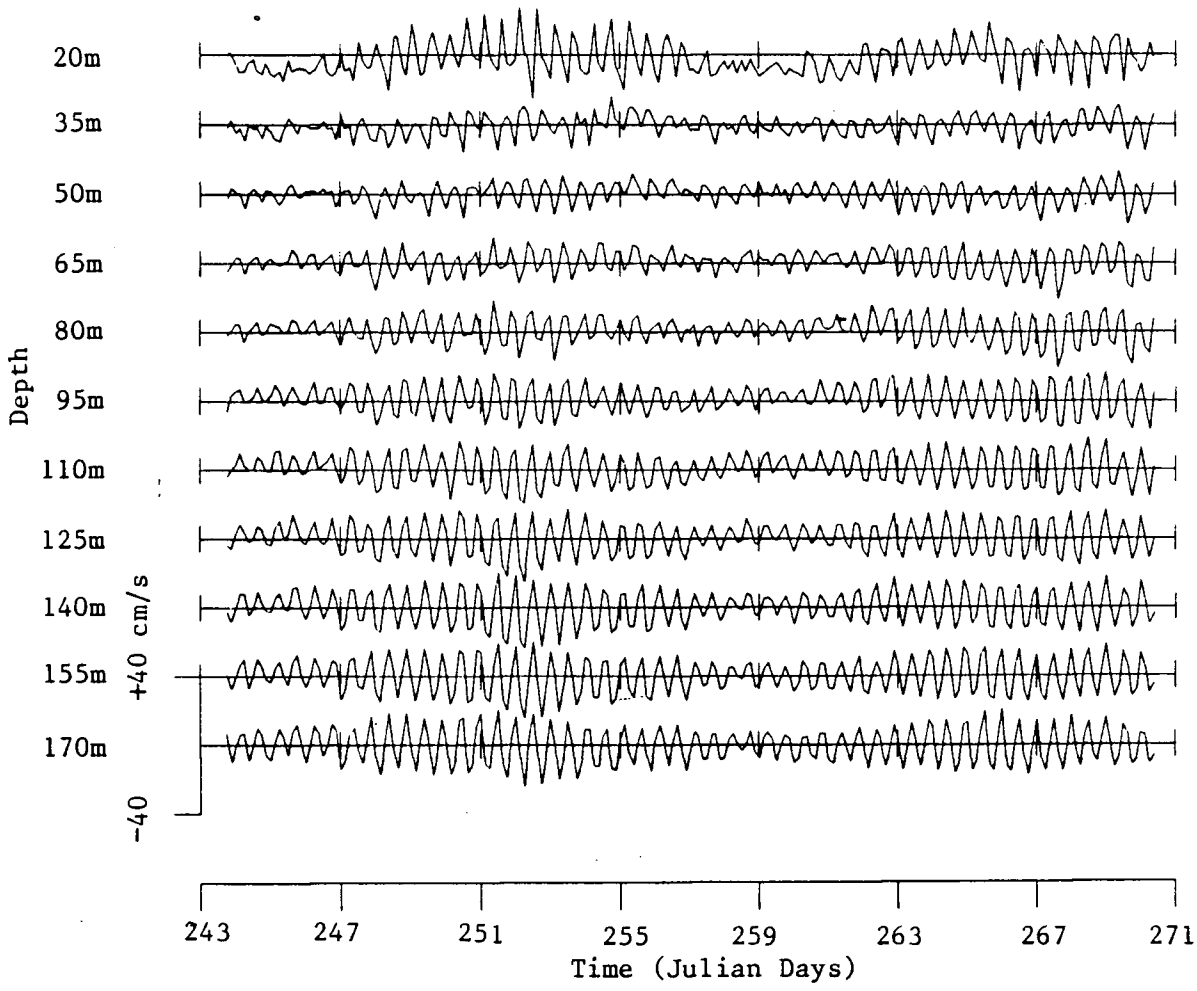

Figure 40 Longitudinal velocity vs time at Tom-N. September 1983.
Positive is up-inlet (eastwards).

The density was calculated from the conductivity and temperature data, assuming

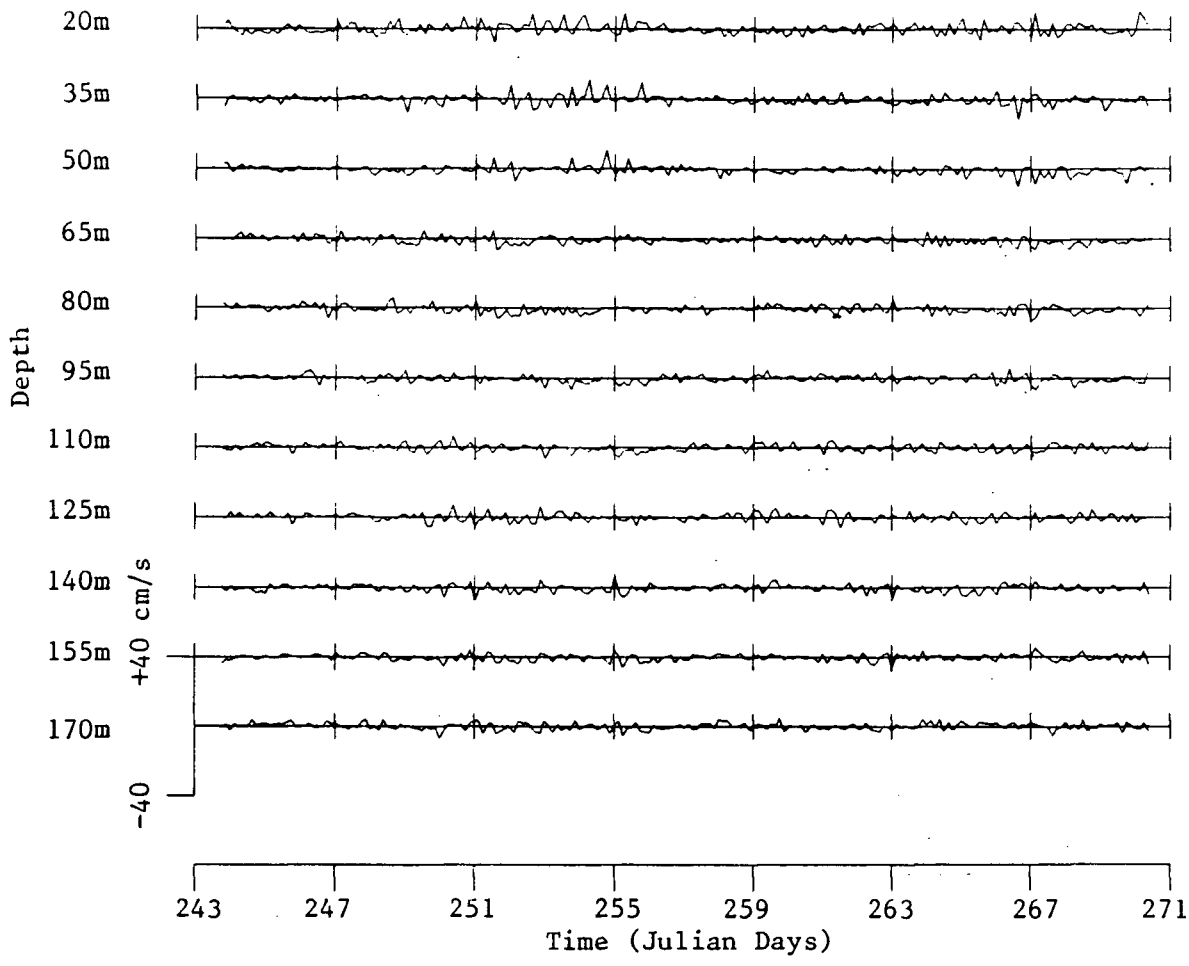

Figure 41 Transverse velocity vs time at Tom-N. September 1983.
Positive is northwards.

that both sensors provided intantaneous readings. This assumption is satisfactory for the temperature, where the thermistor was well ventilated, but not so good for the conductivity, because the conductivity cell did not flush well at low water speeds. However, the velocities in Knight Inlet are large enough that the cell should be sufficiently well flushed. In coastal waters such as these, salinity rather than temperature dominates density variations. *Figure 42* shows the isopycnals in the time-depth plane at Tom-N in September 1983. Again the signal is dominated by an oscillation at M_2 period with a very large amplitude (sometimes a $50\,m$ peak-to-peak isopycnal displacement). Large amplitude oscillations in isopycnal depth at tidal period like these are charateristic of an internal tide. *Figure 43* shows the same data in a different form — it shows the density as a function of time at

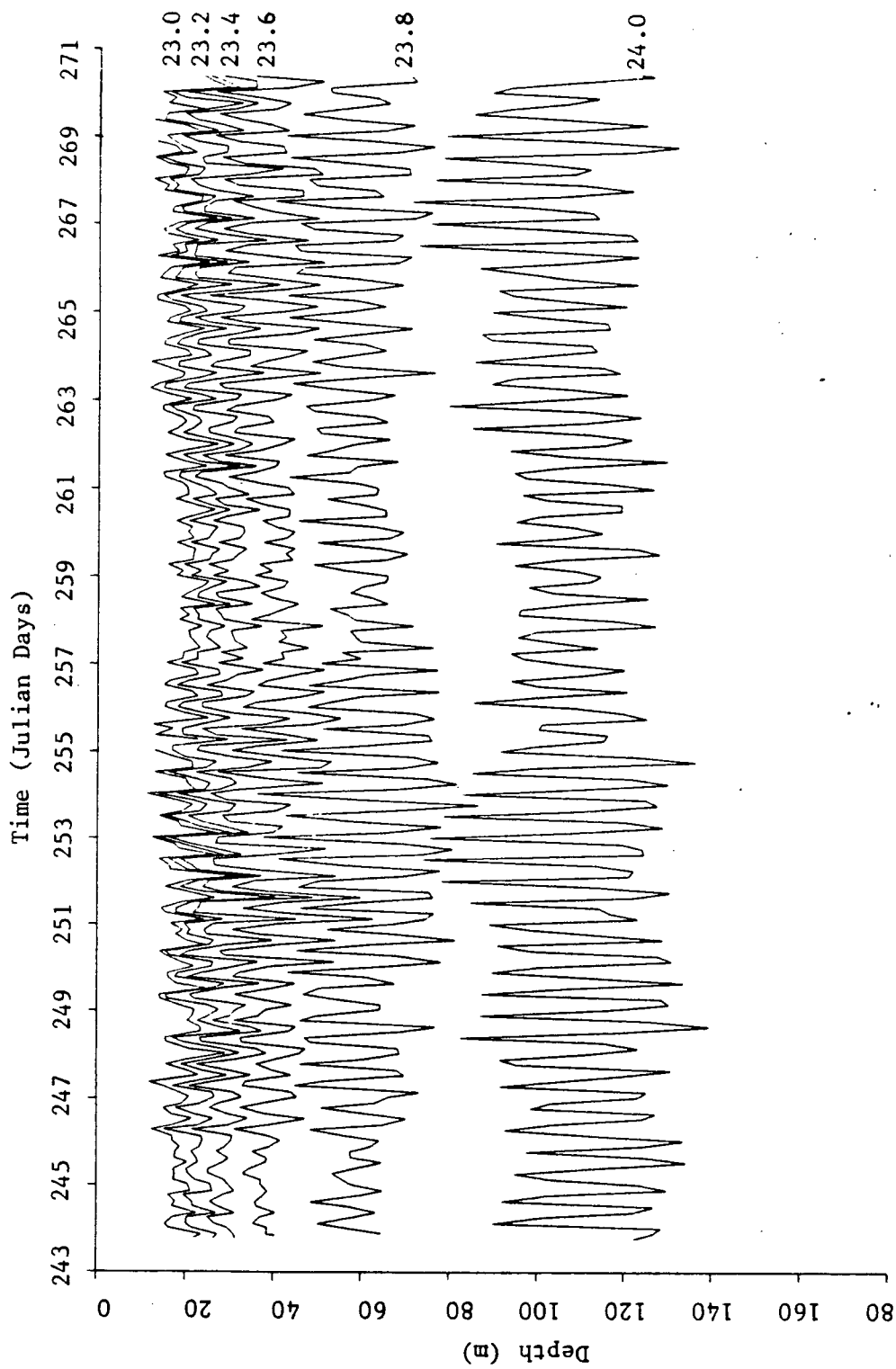

Figure 42 Isopycnals in the time-depth plane at Tom-N. September 1983.

each standard depth. The average density at each depth is given on the right-hand side of the plot. There is a small offset in the conductivity values due to calibration drift, so these average density values can not be compared between records.

The cyclesondes also give information on surface elevation variations due to the tide in 1983, because for over two hours out of every six they were resting against the bottom bumper. The bottom bumper is a fixed distance from the bottom, so that any variations in the depth of the instrument as calculated from pressure sensor data are due to variations in surface elevation. The pressure sensor is $2\,m$ from the block, so that the depth data must be corrected for the pitch of the instrument, which varies by as much as $\pm 10°$. *Figure 44* shows the depth of the bottom bumper as a function of time at Tom-N in September 1983. The dots are data points from the pressure sensor, and the solid line is the reconstructed signal after a harmonic analysis was done on the data (see Section 3.3.3).

In addition to the cyclesonde density information from $20\,m$ or below, CTD data were also available for this study. CTD casts were done at each station at each deployment and retrieval of the cyclesondes. Unfortunately the timing of these casts was somewhat sporadic due to the limitations of ship time. What the CTDs gain in terms of depth coverage the cyclesondes make up for in temporal coverage.

3.3 Harmonic Analysis of the Data

Harmonic analysis was done on the longitudinal velocity and density data at the standard depths, and on the surface elevation data. Nine constituents were included in the analysis, as listed in *Table 2.*

These components were chosen to be the smallest set that could be reasonably be expected to describe the data. With short records only a few constituents should be included in the analysis. Foreman's (1977, Tables 1–3) guidelines on which constituents should be included for a given record length were followed. In practice the number of constituents included was not found to affect the phase and amplitude of the M_2 constituent, and this component is the one of primary interest in this study because it contains the most energy.

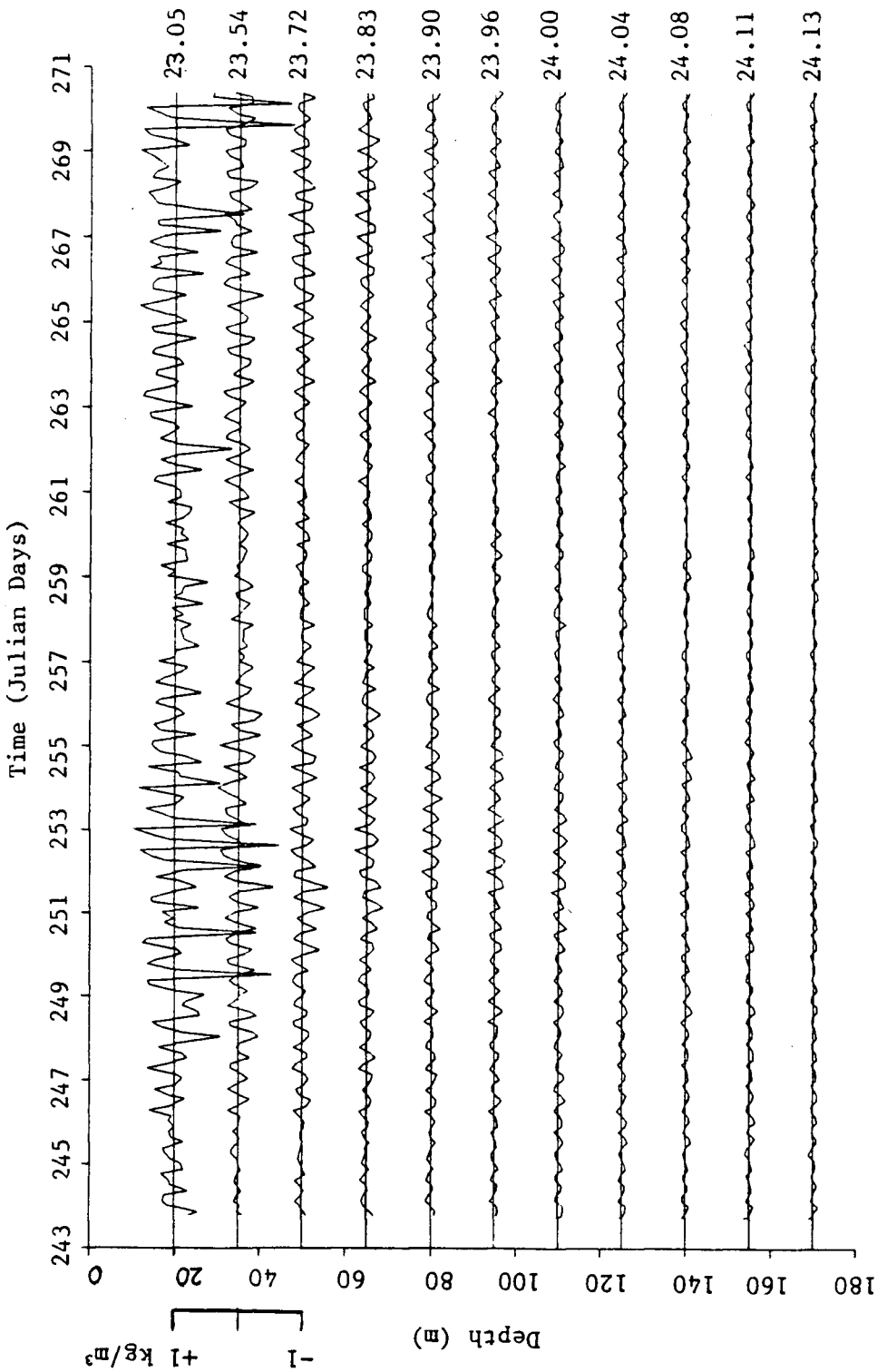

Figure 43 Density at the standard depths vs time at Tom-N. September 1983.

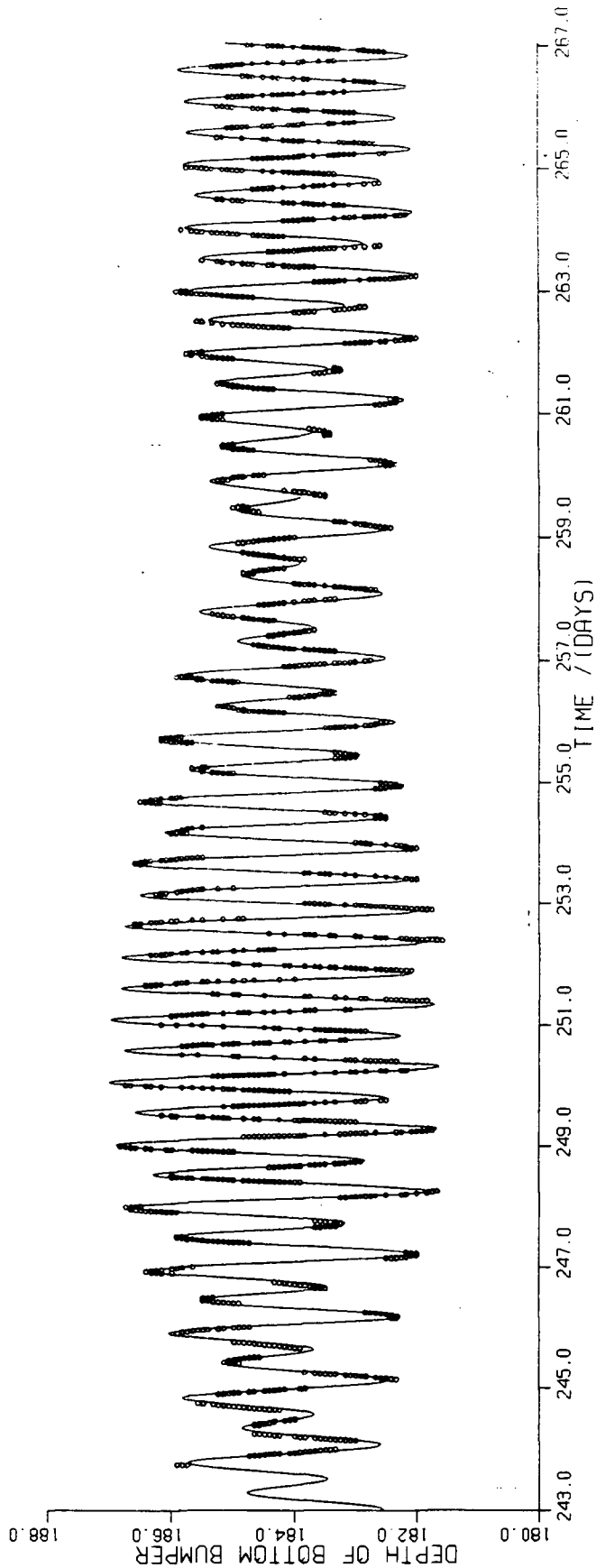

Figure 44 Depth of the bottom bumper vs time at Tom-N. September 1983.

Table 2
Tidal constituents used in the harmonic analysis

tidal harmonic	*Darwin name*	*period (hours)*	
Shallow water constituents			
	M_4	6.21	
	MK_3	8.18	
Semi-diurnal			
Principal solar	S_2	12.00	
Principal lunar	M_2	12.42	
Longer lunar elliptic	N_2	12.66	(Not in 1981)
Diurnal			
Soli-lunar declinational	K_1	23.93	
Main lunar	O_1	25.82	
Long period			
Luni-solar fortnightly	MSf	354.4	(Not in 1981)
Mean	Z_0	∞	

The basic criterion was whether the M_2 signal could be separated from the S_2 signal. The Rayleigh criterion requires the record length to be greater than the reciprocal of the difference of their frequencies. In other words, the record must be at least as long as the period of the beat frequency (14.76 days — the MSf tide). This was certainly true in 1983, and almost true in 1981. The N_2 constituent could not be included in the analysis of the 1981 data because the frequency is too close to that of the M_2 constituent. It was found that between 60% and 80% of the total variance of the longitudinal velocity signal was at the M_2 frequency, and that the amplitude of the M_2 constituent was always at least twice that of the S_2 constituent, which was the next largest.

Two shallow water constituents were included in the analysis. These constituents arise from the non-linear terms in the hydrodynamic equations, and are products of the interactions between the main constituents. Only two shallow water constituents were included because the sampling interval was $3\,hrs$ in 1983, and constituents whose periods are shorter than twice that value cannot be resolved without aliasing (the Nyquist criterion). M_4 arises from the interaction of M_2 with itself, and MK_3 from the interaction of M_2 with K_1.

3.3.1 Harmonic Analysis of Velocity Data

Figures 45–68 show the results of the harmonic analysis of the longitudinal velocity at the various standard depths at each station. The Greenwich phase and nodally corrected amplitudes of the various constituents at each depth are plotted in the complex plane. If ϕ is the Greenwich phase and r is the nodally corrected amplitude at a particular depth, then these values are plotted at the point (r, ϕ) in polar coordinates. The Greenwich phase is the phase relative to the passage of the sun or the moon (depending on the constituent under consideration) over the Greenwich meridian, and is therefore a standard reference for the three different time periods. The nodally corrected amplitude is corrected for long period modulations in the tide-generating force due to other astronomical cycles. This nodal correction is an attempt to standardise the amplitude of the response of the inlet in a situation where the amplitude of the tide-generating force at a particular frequency is not the same for the two years 1981 and 1983. However, this small correction makes the implicit assumption that the amplitude of the response of the inlet at that frequency is linear in the amplitude of the tide-generating force.

Figures 45–68 show the loci of these (r, ϕ) points at the standard depths ($10\,m$ intervals for Lull Bay, $15\,m$ for the others). The point corresponding to the shallowest standard depth ($25\,m$ for Lull Bay, $20\,m$ for the others) is marked by a larger symbol. The constituents are arranged in decreasing order as in *Table 2*, except that the complex amplitudes (i.e. amplitudes and phases) of the MK_3 constituent are not given because they were always small ($< 2\,cm/s$). The corresponding plots for the MSf constituent appear later in Chapter 4 (*Figures 107–110*). The scale factors used in the figures were allowed to vary so that the loci could be distinguished from each other, although each of the four figures for a particular constituent were plotted on the same scale for comparison.

These loci have strikingly similar shapes for the three time periods at a given station, whereas different stations have quite different loci. The repeatability of the loci at any given station provides motivation to understand why they have their characteristic shapes, and shows that they are not simply random patterns. Even the shapes of the loci for the

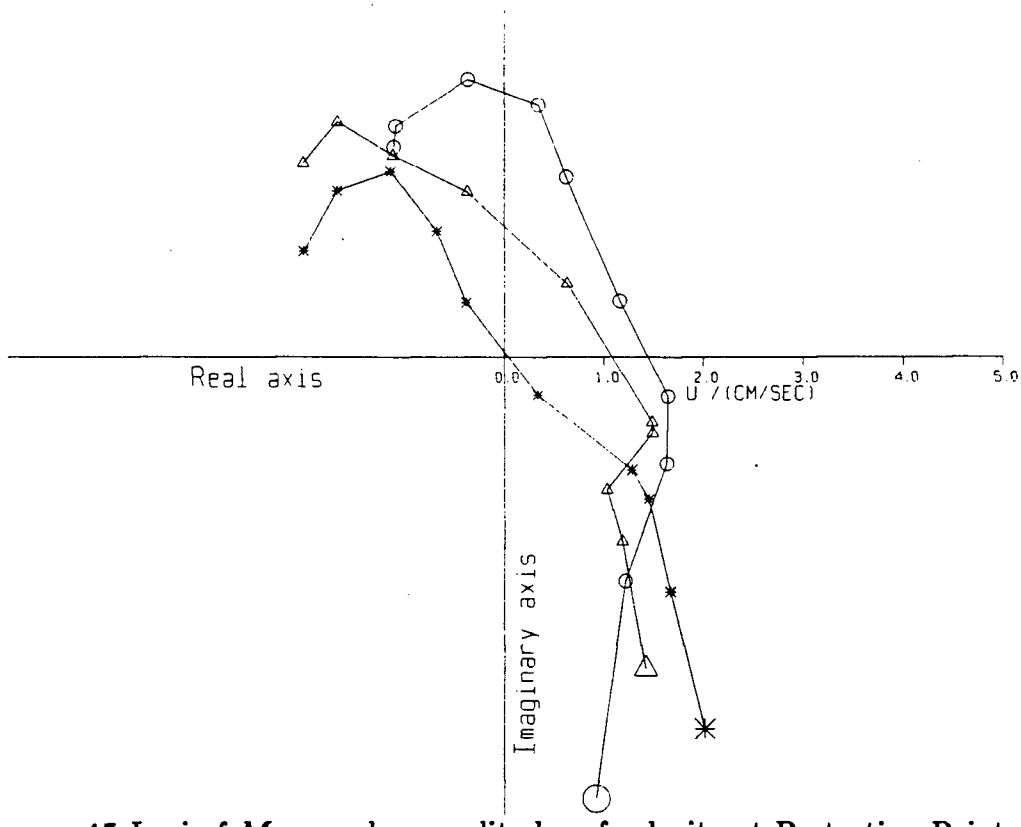

Figure 45 Loci of M_4 complex amplitudes of velocity at Protection Point.
o July 1983, △ September 1983, * July 1981.
The shallowest standard depth is marked by a larger symbol.

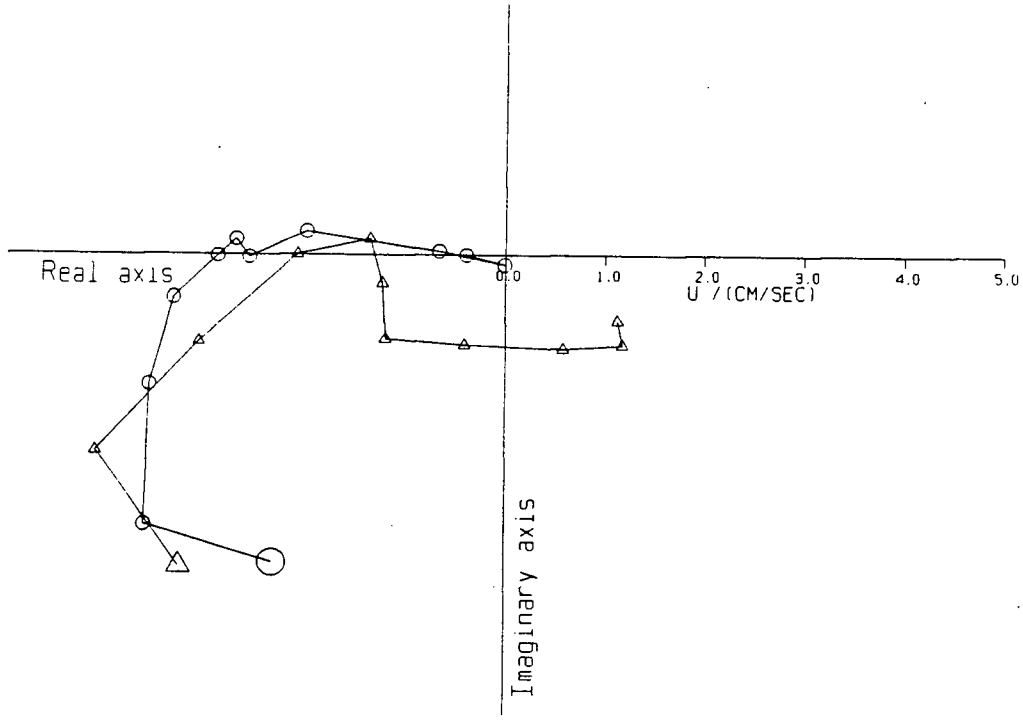

Figure 46 Loci of M_4 complex amplitudes of velocity at Lull Bay.
o July 1983, △ July 1981.

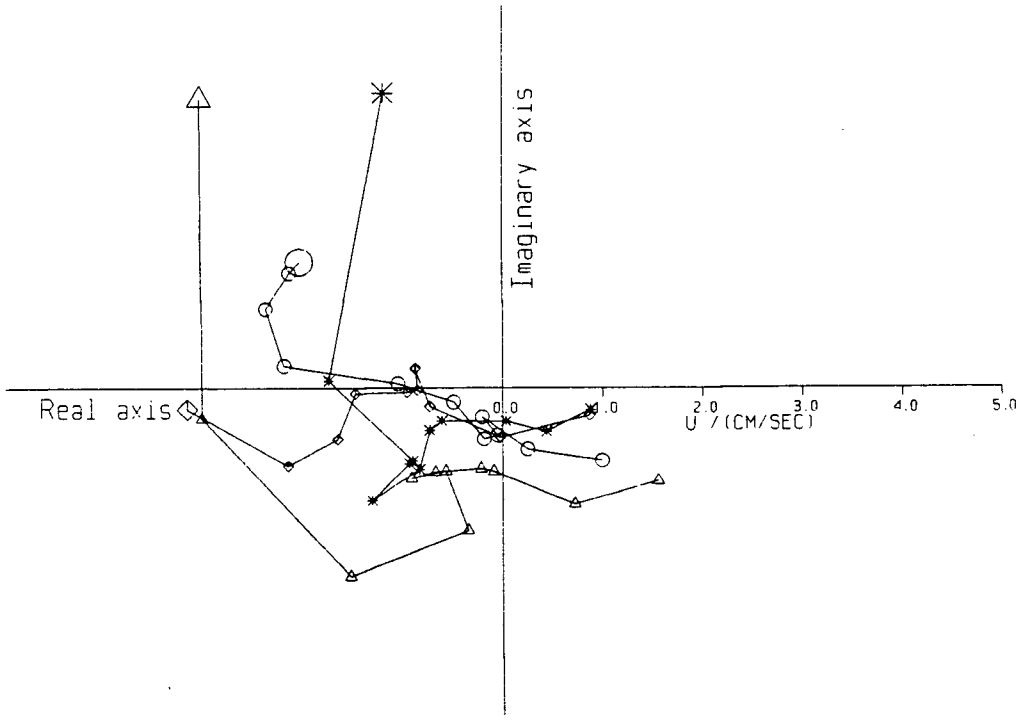

Figure 47 Loci of M_4 complex amplitudes of velocity at Tomakstum Island. ○ July 1983, △ Tom-S September 1983, ∗ Tom-N September 1983, ◇ July 1981. The shallowest standard depth is marked by a larger symbol.

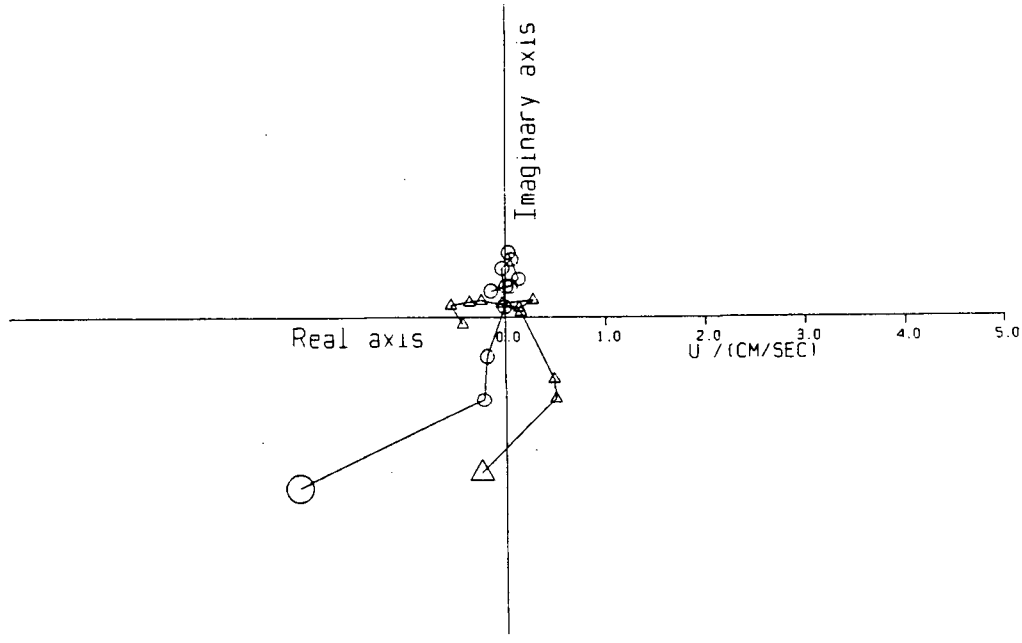

Figure 48 Loci of M_4 complex amplitudes of velocity at Adeane Point. ○ July 1983, △ September 1983.

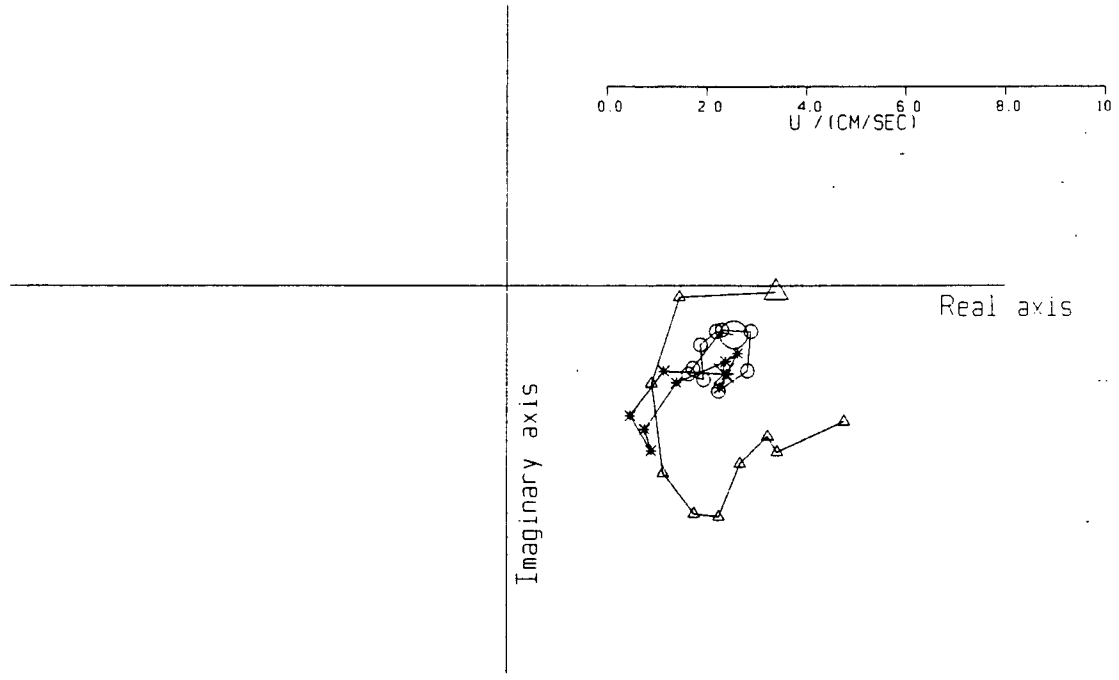

Figure 49 Loci of S_2 complex amplitudes of velocity at Protection Point.
∘ July 1983, △ September 1983, ∗ July 1981.
The shallowest standard depth is marked by a larger symbol.

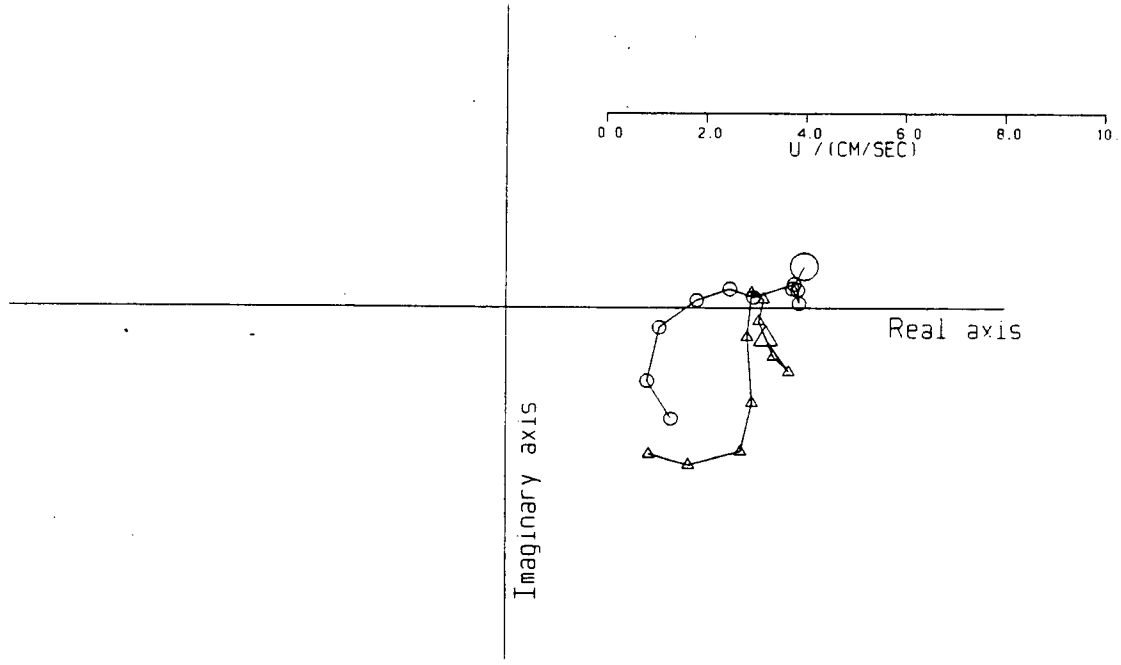

Figure 50 Loci of S_2 complex amplitudes of velocity at Lull Bay.
∘ July 1983, △ July 1981.

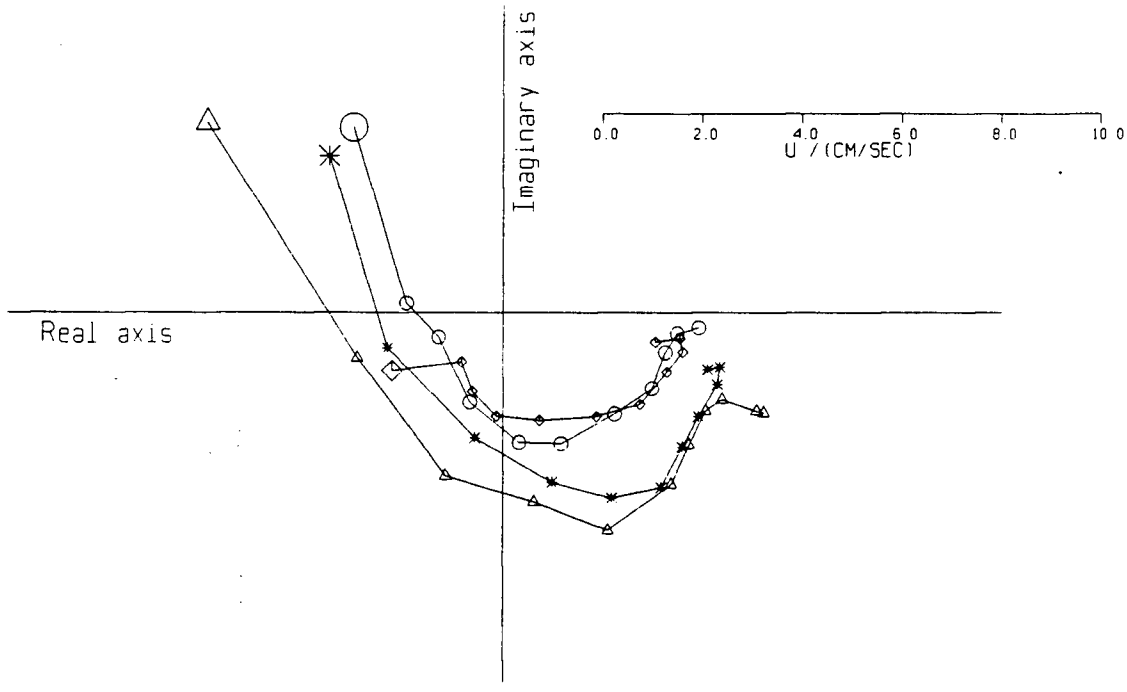

Figure 51 Loci of S_2 complex amplitudes of velocity at Tomakstum Island.
o July 1983, △ Tom-S September 1983, * Tom-N September 1983, ◇ July 1981.
The shallowest standard depth is marked by a larger symbol.

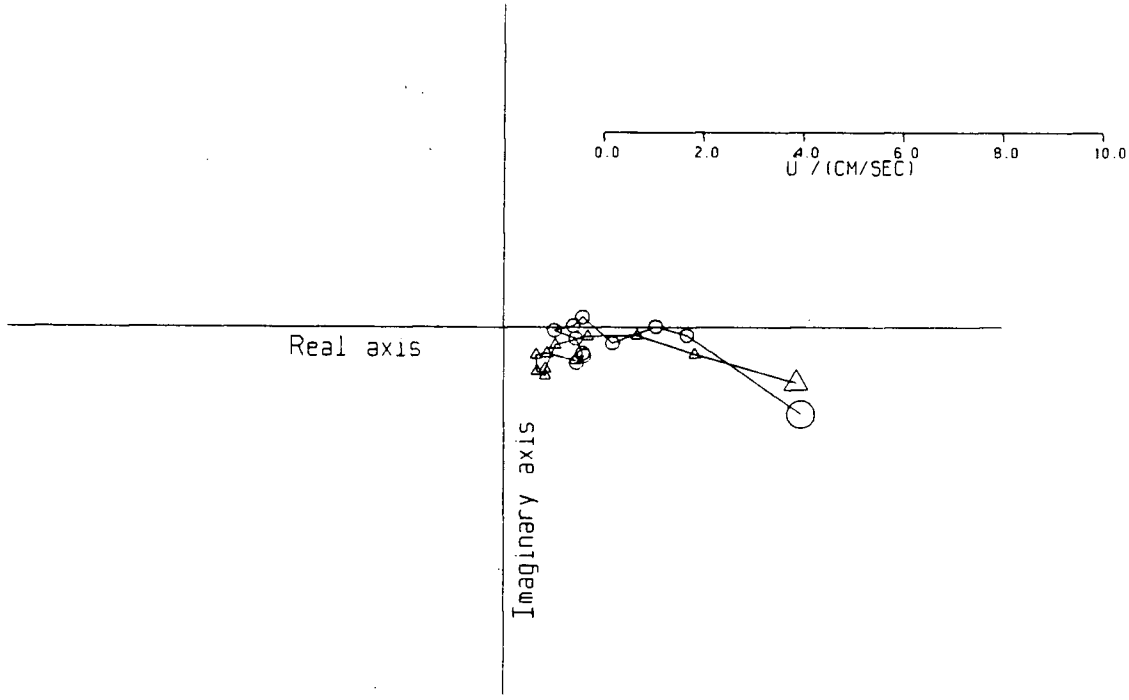

Figure 52 Loci of S_2 complex amplitudes of velocity at Adeane Point.
o July 1983, △ September 1983.

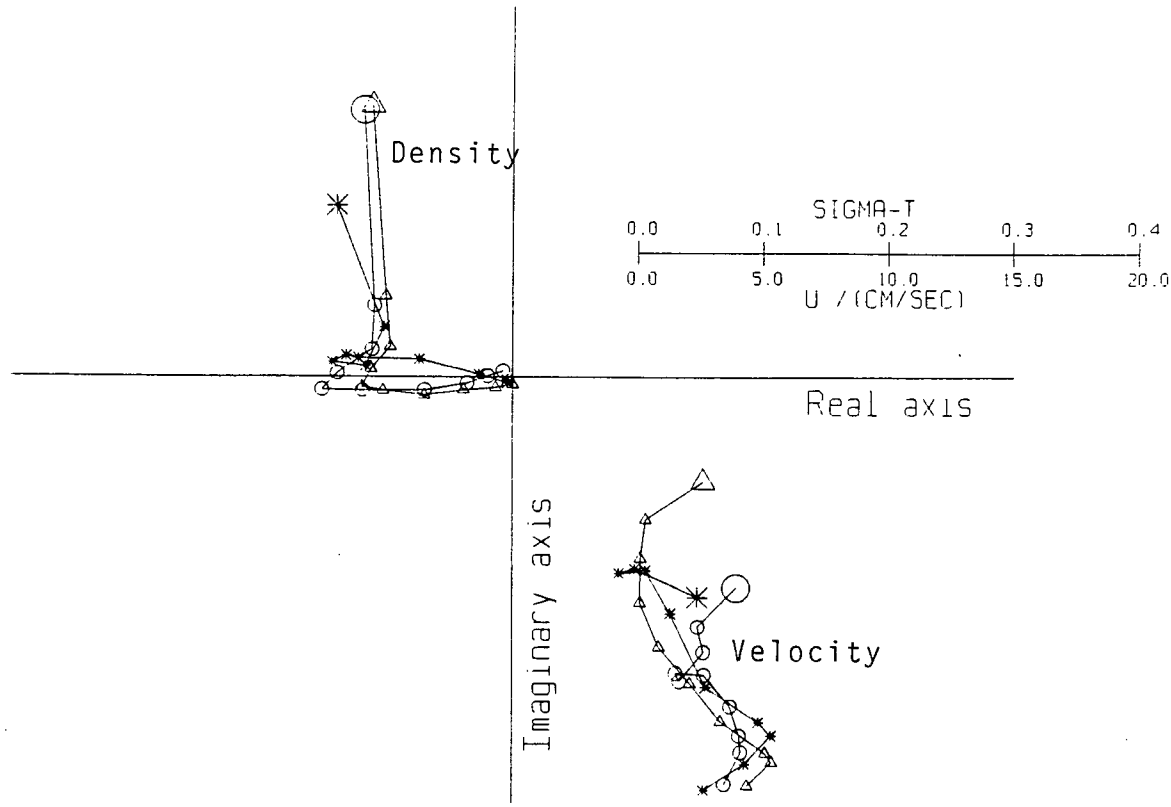

Figure 53 Loci of M_2 complex amplitudes of velocity and density at Protection Point.
∘ July 1983, △ September 1983, ∗ July 1981.
The shallowest standard depth is marked by a larger symbol.

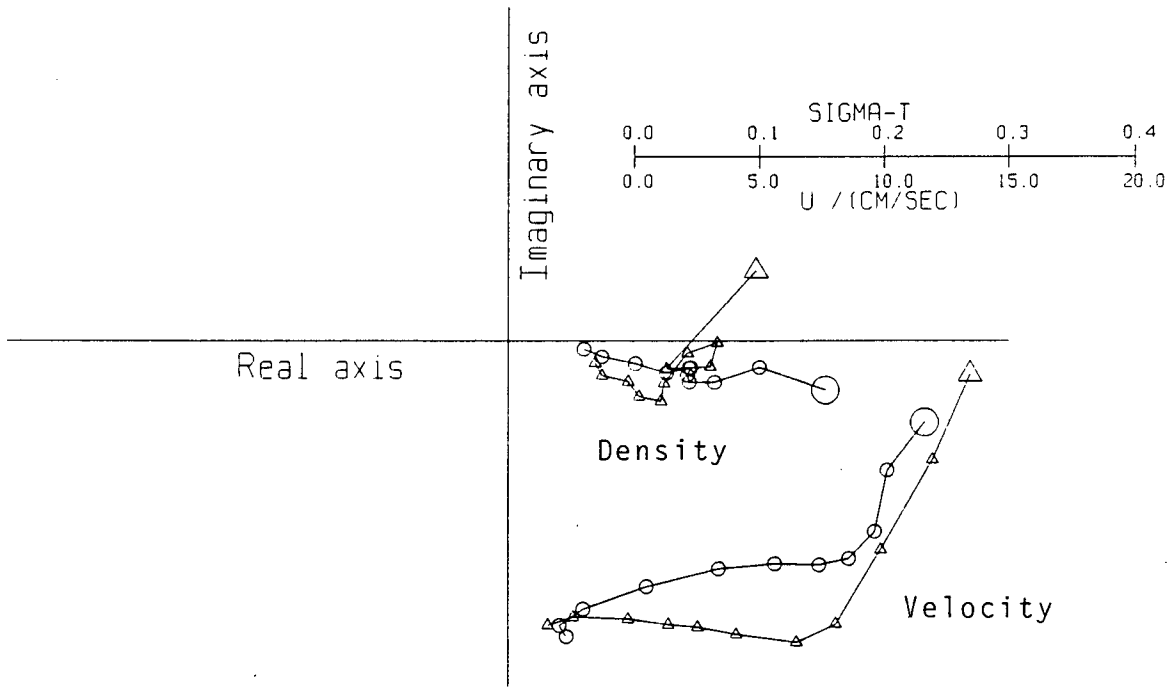

Figure 54 Loci of M_2 complex amplitudes of velocity and density at Lull Bay.
∘ July 1983, △ July 1981.

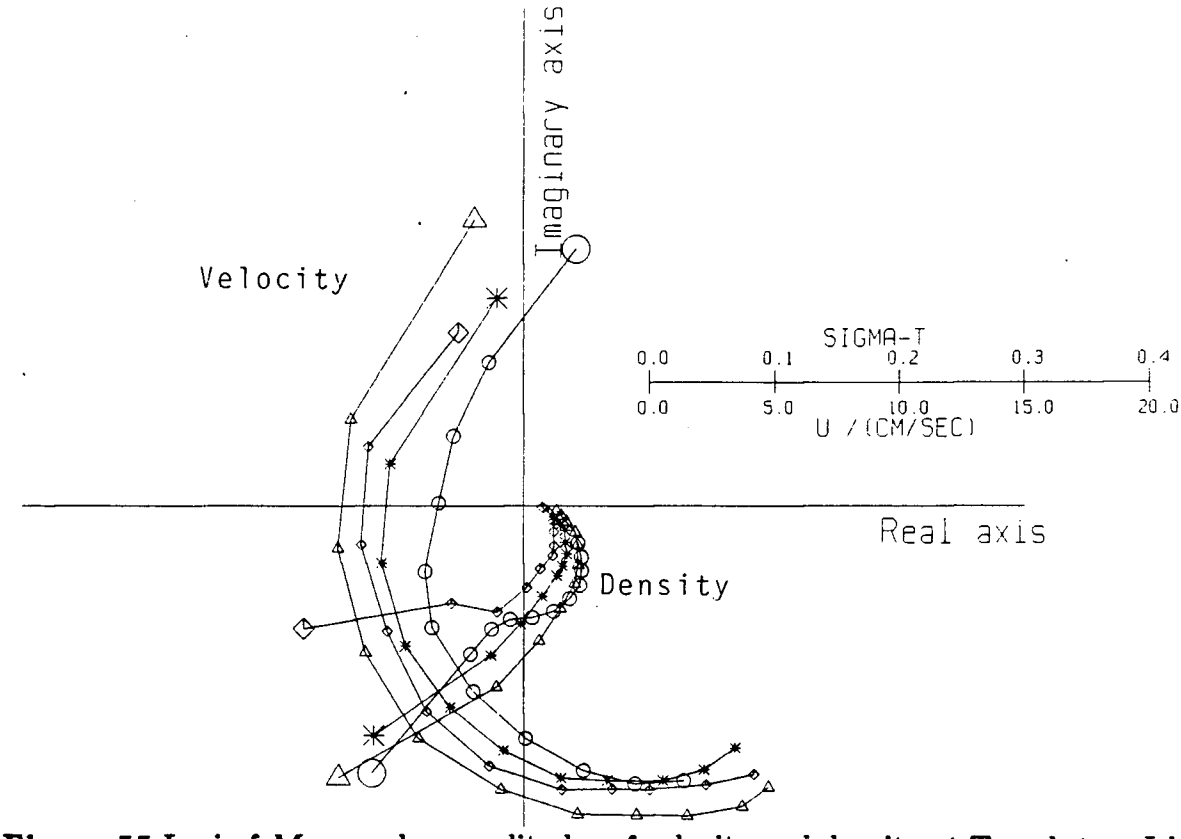

Figure 55 Loci of M_2 complex amplitudes of velocity and density at Tomakstum Island. ○ July 1983, △ Tom-S September 1983, ∗ Tom-N September 1983, ◇ July 1981. The shallowest standard depth is marked by a larger symbol.

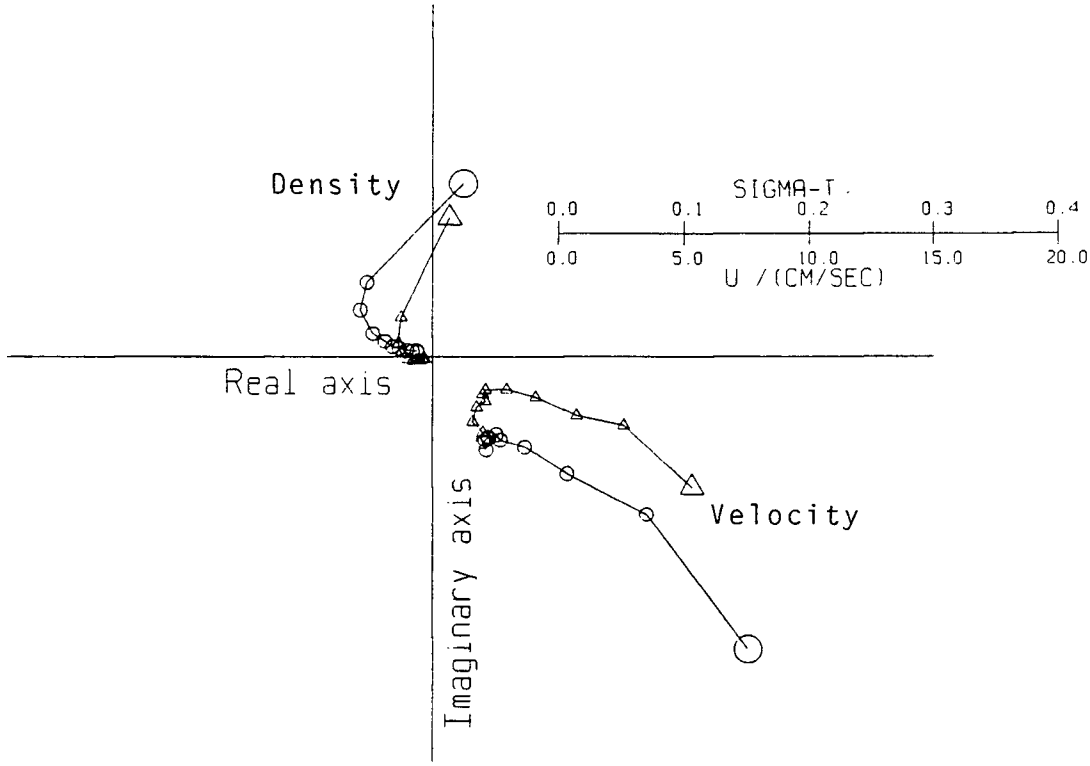

Figure 56 Loci of M_2 complex amplitudes of velocity and density at Adeane Point. ○ July 1983, △ September 1983.

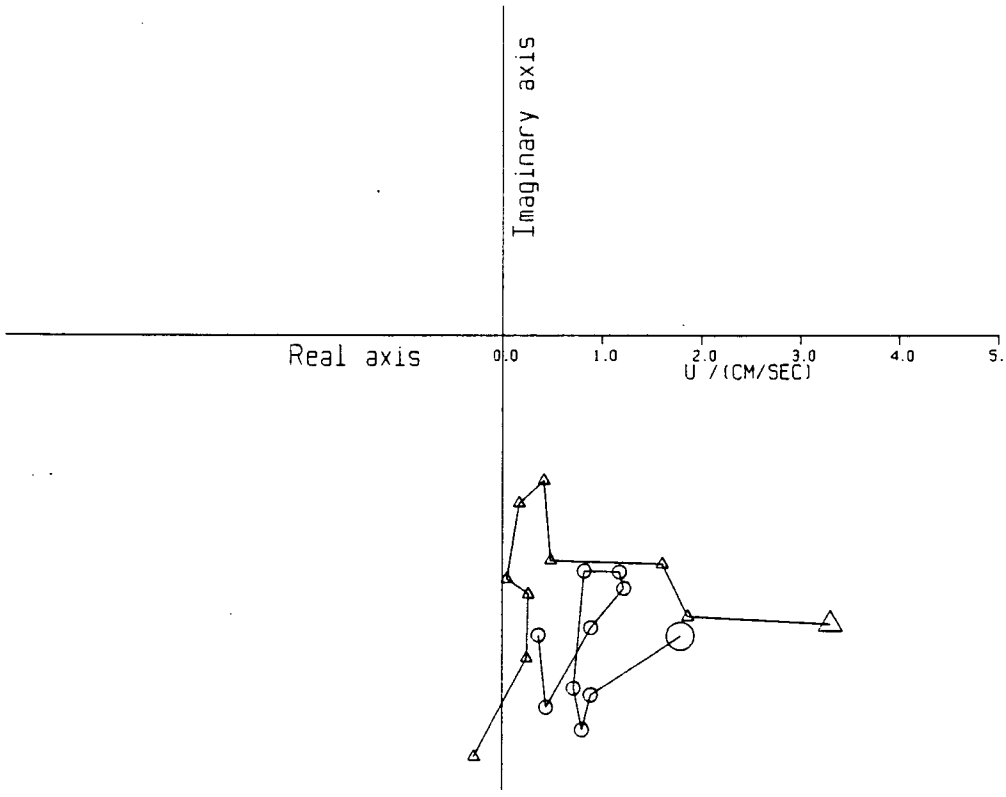

Figure 57 Loci of N_2 complex amplitudes of velocity at Protection Point.
o July 1983, △ September 1983.
The shallowest standard depth is marked by a larger symbol.

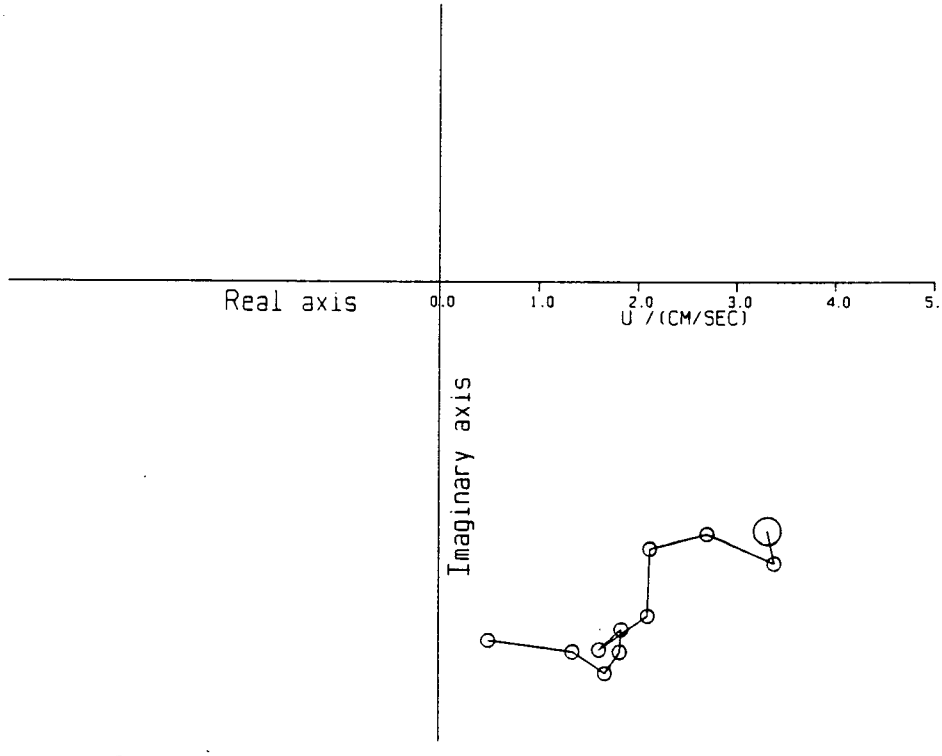

Figure 58 Locus of N_2 complex amplitudes of velocity at Lull Bay. o July 1983.

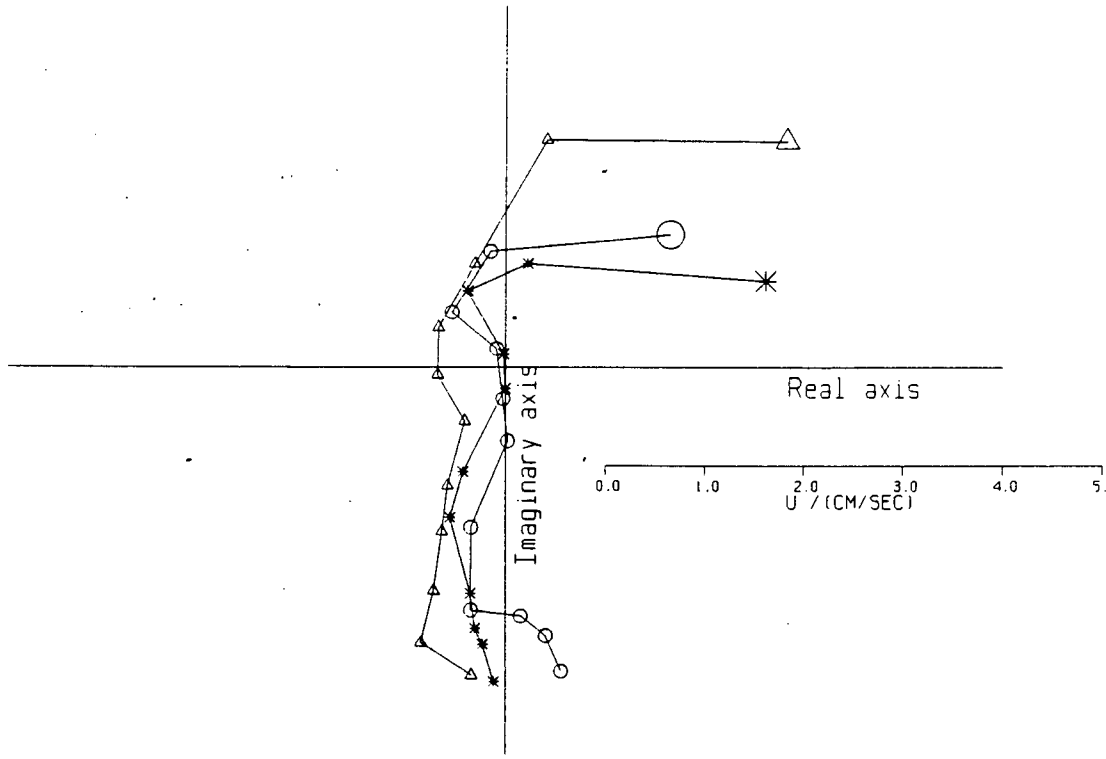

Figure 59 Loci of N_2 complex amplitudes of velocity at Tomakstum Island.
o July 1983, △ Tom-S September 1983, * Tom-N September 1983.
The shallowest standard depth is marked by a larger symbol.

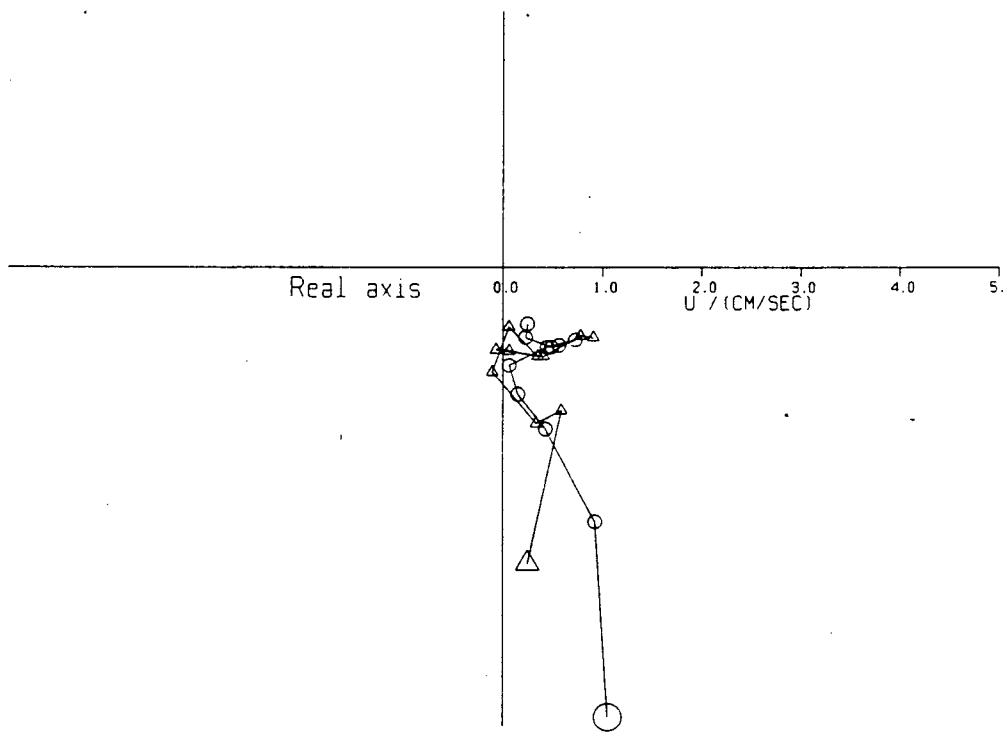

Figure 60 Loci of N_2 complex amplitudes of velocity at Adeane Point.
o July 1983, △ September 1983.

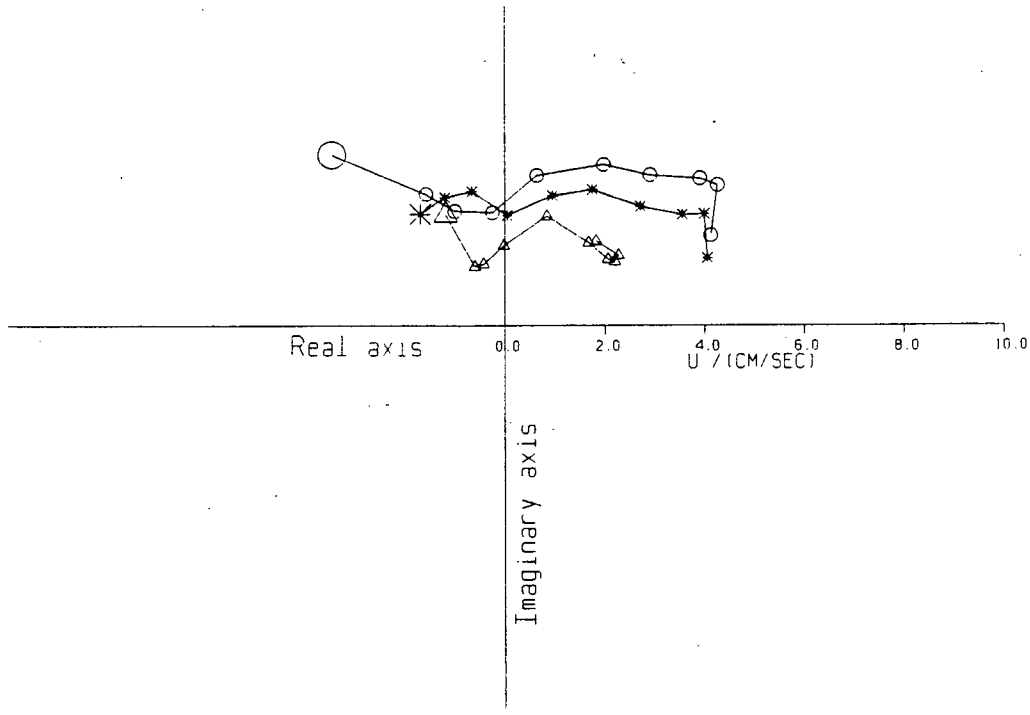

Figure 61 Loci of K_1 complex amplitudes of velocity at Protection Point.
∘ July 1983, △ September 1983, ∗ July 1981.
The shallowest standard depth is marked by a larger symbol.

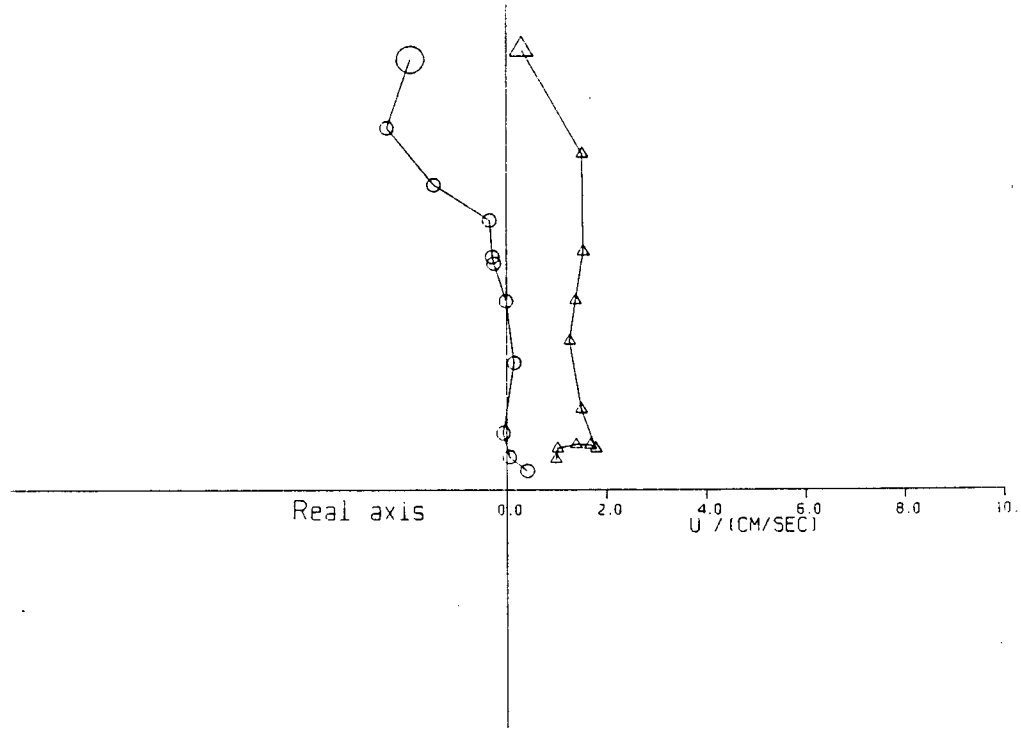

Figure 62 Loci of K_1 complex amplitudes of velocity at Lull Bay.
∘ July 1983, △ July 1981.

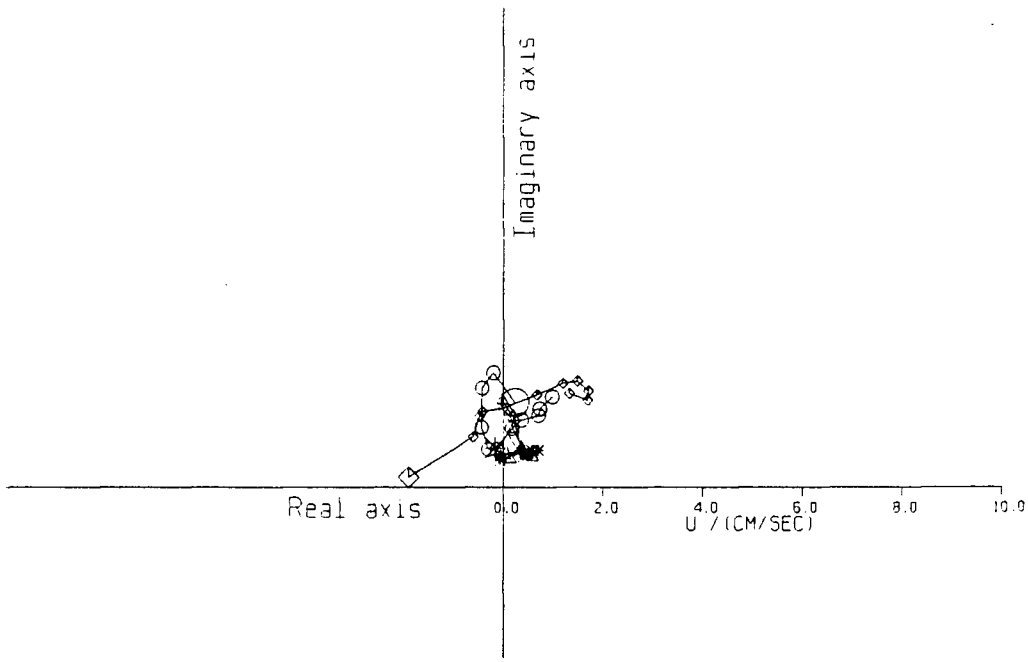

Figure 63 Loci of K_1 complex amplitudes of velocity at Tomakstum Island. ∘ July 1983, △ Tom-S September 1983, ∗ Tom-N September 1983, ⋄ July 1981. The shallowest standard depth is marked by a larger symbol.

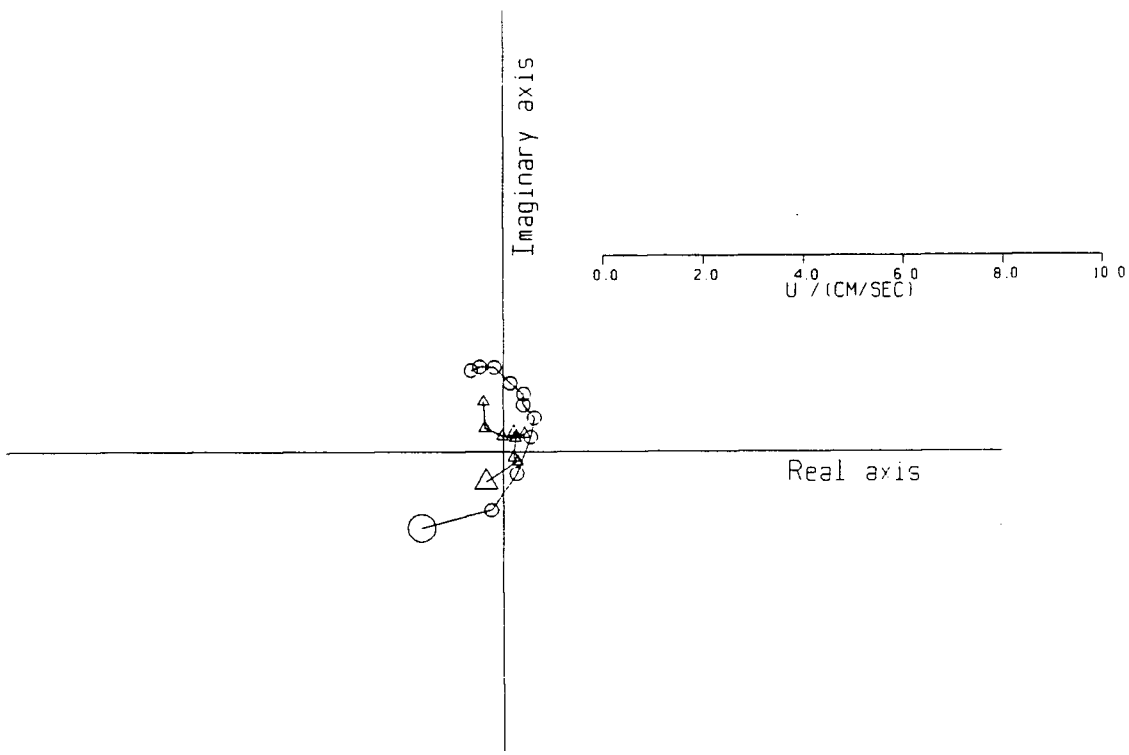

Figure 64 Loci of K_1 complex amplitudes of velocity at Adeane Point. ∘ July 1983, △ September 1983.

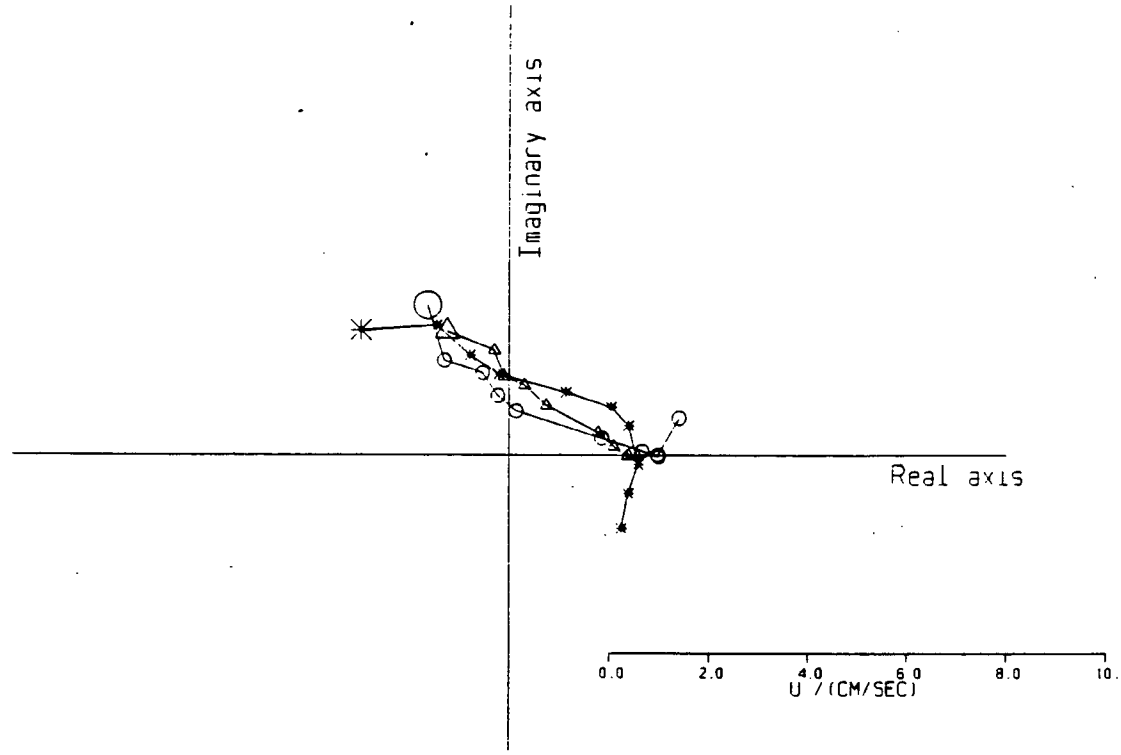

Figure 65 Loci of O_1 complex amplitudes of velocity at Protection Point.
o July 1983, △ September 1983, * July 1981.
The shallowest standard depth is marked by a larger symbol.

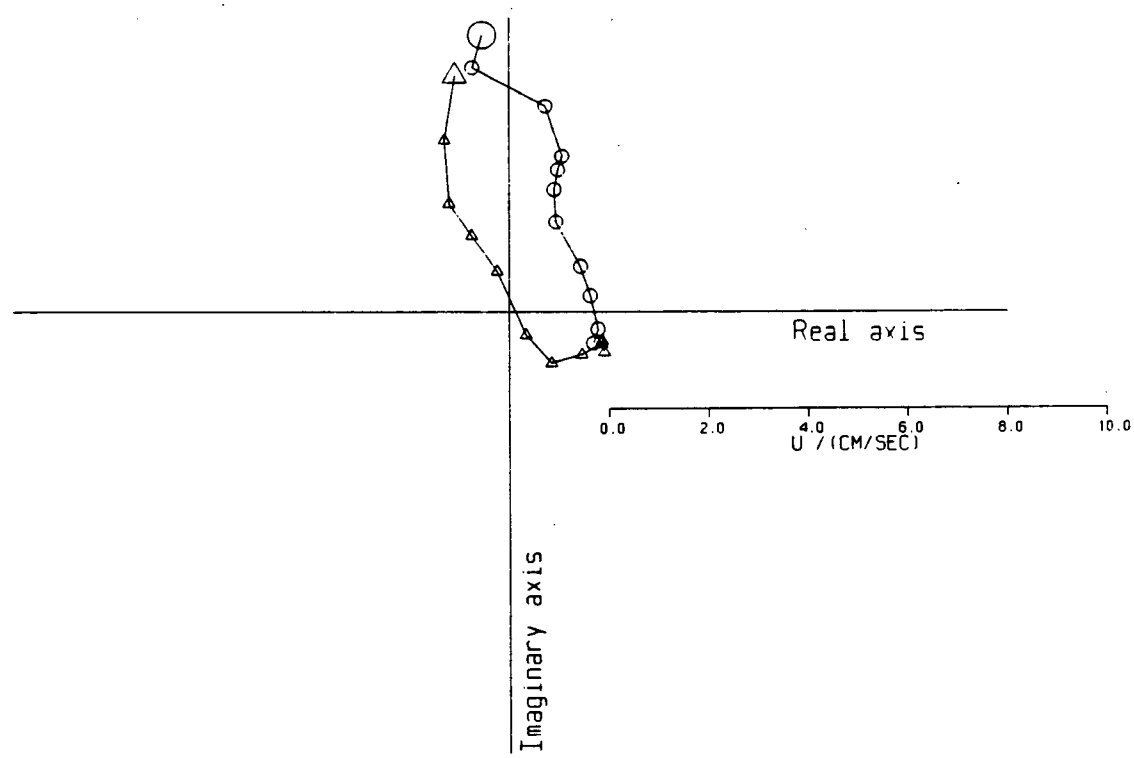

Figure 66 Loci of O_1 complex amplitudes of velocity at Lull Bay.
o July 1983, △ July 1981.

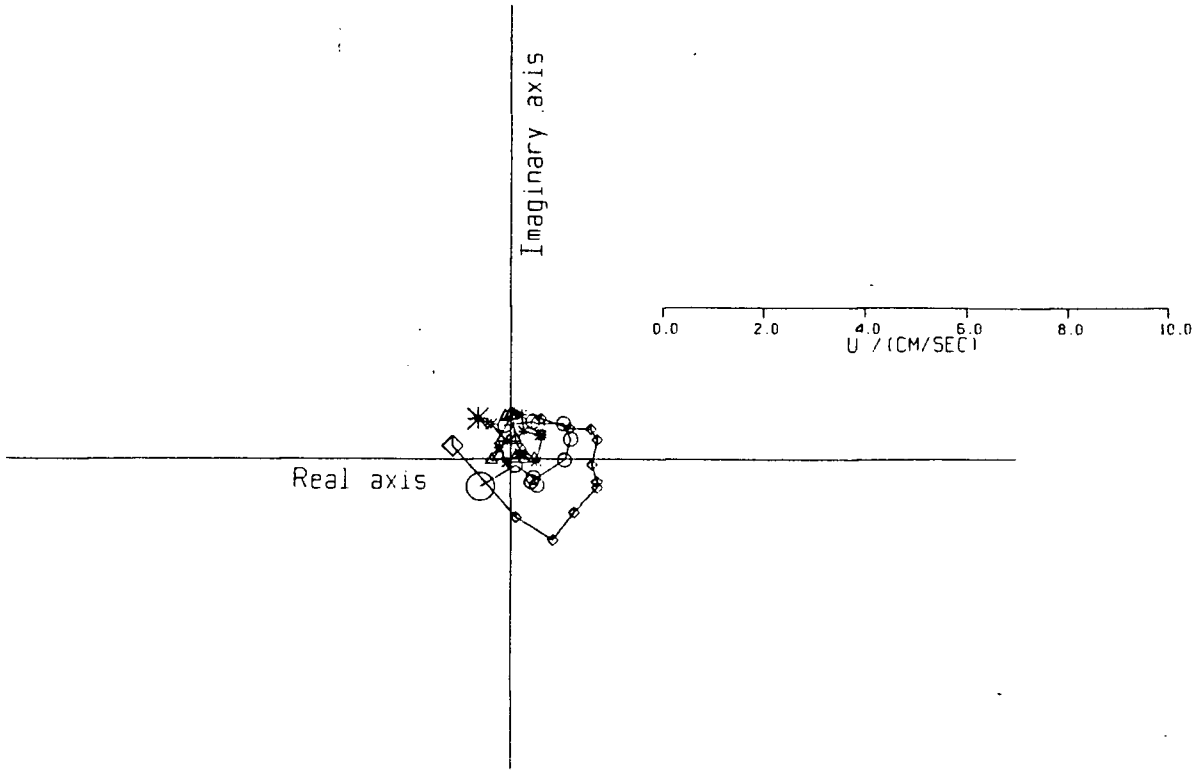

Figure 67 Loci of O_1 complex amplitudes of velocity at Tomakstum Island. ∘ July 1983, △ Tom-S September 1983, ∗ Tom-N September 1983, ⋄ July 1981. The shallowest standard depth is marked by a larger symbol.

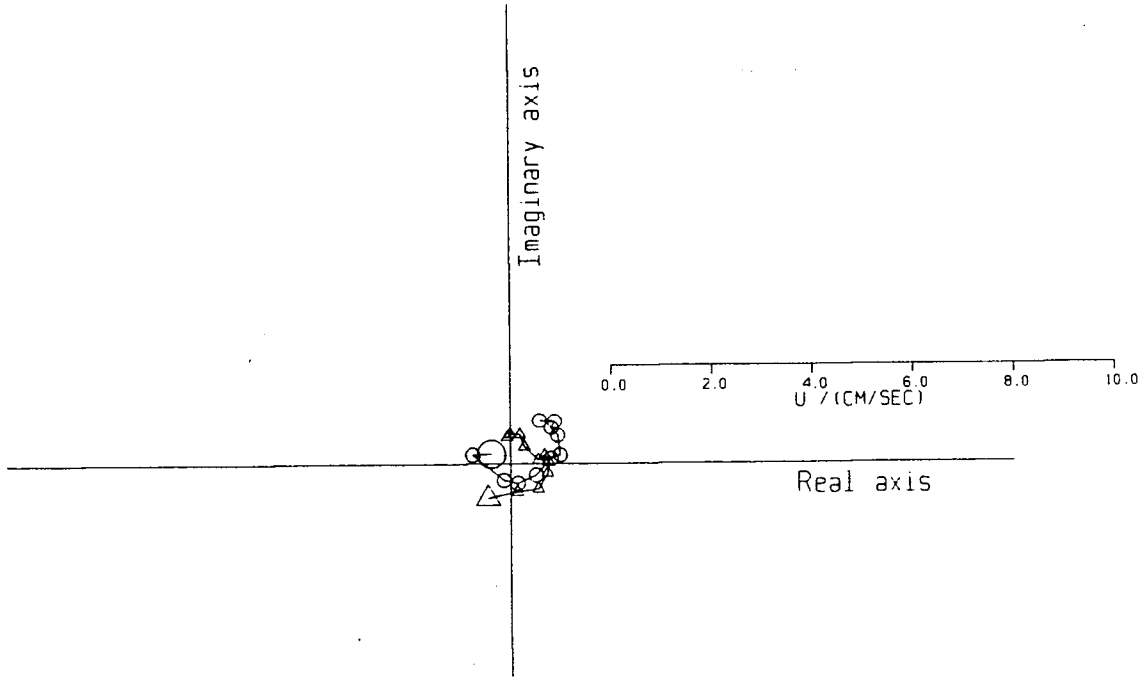

Figure 68 Loci of O_1 complex amplitudes of velocity at Adeane Point. ∘ July 1983, △ September 1983.

M_4 constituent are repeatable from month to month, especially at Protection Point and Lull Bay. The amplitude of this shallow water constituent is as large as that of the diurnal constituents at Tomakstum Island and Adeane Point, or that of the N_2 constituent at all stations. The next larger group consists of the diurnal constituents at Protection Point and Lull Bay, and the S_2 constituent. However, the M_2 constituent is by far the largest of all.

The loci at a particular station for a particular constituent are also quite similar in shape to the loci at the same station for a different constituent, as long as the two constituents are in the same band (i.e. diurnal or semi-diurnal). For example, the loci in *Figures 51, 55* and *59* all have similar shapes, as do those in *Figures 62* and *66*, and in *Figures 61* and *65*. This property indicates that the inlet is far from resonance at these frequencies, because the transfer function is almost the same at two very close frequencies.

3.3.2 Harmonic Analysis of Density Data

The oscillations of density values also give valuable information on the internal tide, so *Figures 53–56* also show the loci of the M_2 constituent of density oscillations as the depth varies. An example of the original data that were used in this analysis was shown in *Figure 43*. The small offset in density values will not affect this analysis because only the M_2 constituent of the density signal is of interest. Later, the vertical gradient of the average density values will be used, but this is also unaffected by the offset.

The foregoing comments on the repeatability of the loci of the M_2 constituent of the longitudinal velocities apply equally well to those of density. The density oscillations are caused by oscillations in the vertical component of velocity w, so a harmonic analysis of density variations gives information on the phase and magnitude of the w-oscillation, as will be discussed quantitatively in Section 3.5.

3.3.3 Harmonic Analysis of Surface Elevations

The third variable for which continuous data exist is surface elevation. It gives information on the barotropic component of the tide, since the baroclinic modes have very little influence on the surface elevation. *Figure 69* shows the phase and magnitude, in the complex plane, of the M_2 constituent of the surface elevation oscillation for each record. Again, Greenwich phases and nodally corrected amplitudes are used. Only a small sector of the complex plane is plotted because the surface elevation phases and amplitudes are almost constant throughout the inlet. The surface of the inlet rises and falls almost in unison because the wavelength of the Kelvin wave associated with the barotropic tide is so large ($\lambda = T\sqrt{gH} \approx 2500\,km$ when $H = 300\,m$ and $T = 12.42\,hours$). In fact, the time series of surface elevations (as in *Figure 44*) from the different stations are nearly identical. The barotropic tide is a standing wave, because it is a superposition of an incoming wave and a reflected wave, with complete reflection occurring at the head. In a straight, flat-bottomed channel with rectangular cross-section, the shape of the surface would be a cosine curve whose peak would occur at the head of the inlet and whose first zero-crossing (or *node*) would occur at a distance of $\lambda/4$ from the head. Knight Inlet is much shorter than $\lambda/4$, so no node occurrs. However, the amplitude of the oscillation at $50\,km$ should be 99.2% of the amplitude at the head, and the amplitude at $100\,km$ should be 96.7% of that at the head, assuming that $H = 300\,m$. The difference between them, 2.5%, is consistent with the drop in amplitude from $\approx 1.54\,m$ at Adeane Point and Tomakstum Island to $\approx 1.51\,m$ at Lull Bay and Protection Point (a drop of 1.9%).

However, the change in phase by 2–3° from Protection Point to Tomakstum Island cannot be explained by this simple frictionless model, because the model predicts a constant phase along the channel with 180° jumps at nodes. This change in phase is caused by energy dissipation due to transfer of energy to the internal tide and due to friction. Freeland and Farmer (1980) concluded that about 95% of the energy dissipation rate of the barotropic tide in Knight Inlet could be accounted for by internal wave and hydraulic jump generation, and that the remaining 5% is lost to bottom and side friction. They obtained phase

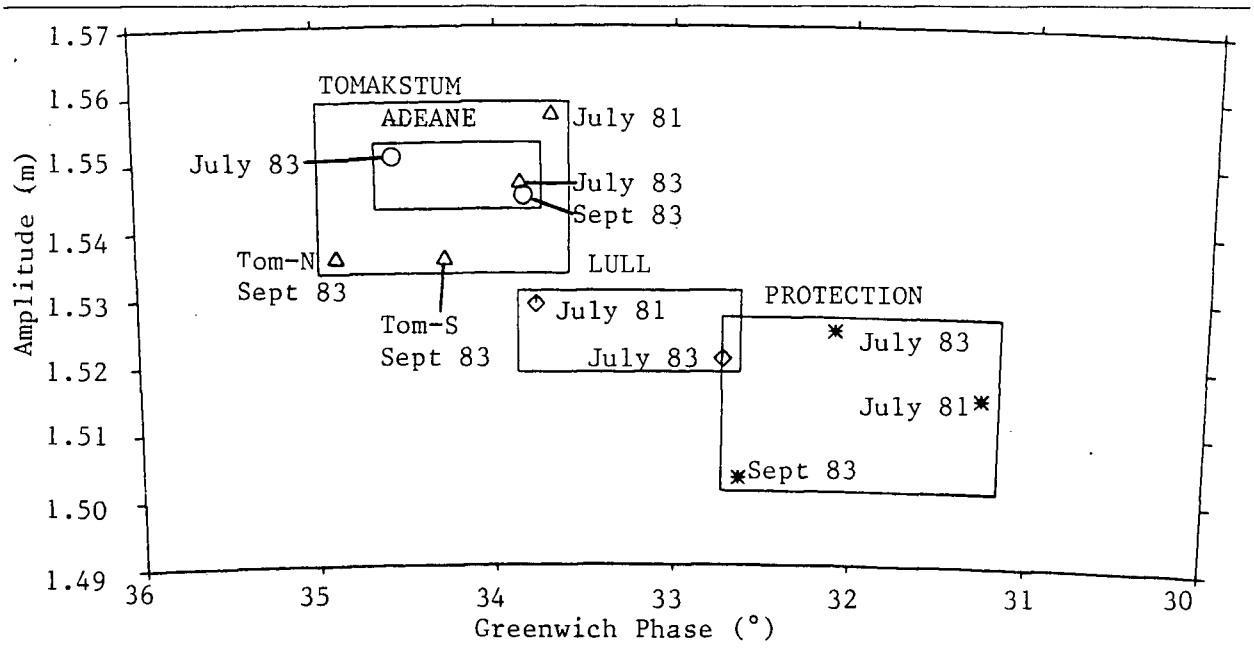

Figure 69 M_2 complex amplitudes of surface elevation.
○ Adeane Point, △ Tomakstum Island, ◇ Lull Bay, ∗ Protection Point.

differences of around 1.5° between Tomakstum Island and Protection Point (see Freeland and Farmer 1980 Figure 7a) using 29-day blocks of data, compared to the cyclesonde value of 2–3°.

The bottom bumpers at Tomakstum Island and Adeane Point were much further from the bottom than at the other two stations, so that the drag assosciated with oscillating baroclinic currents at M_2 frequency could pull them down. This effect could change the calculated amplitude and phase of the surface elevation. However, the currents at depth and therefore the associated drag are not likely to be large.

3.4 Normal Modes — Theory

In a flat-bottomed ocean with vertical side-walls the solutions to the linearised (i.e. infinitesimally small disturbances from the mean state) equations of motion can be separated into a vertical dependency and a horizontal dependency. A harmonic time dependency of $e^{-i\omega t}$ is assumed, so that waves propagate in the direction of increasing phase. This sign convention was chosen so as to be consistent with the harmonic analysis program of Foreman (1979), and with LeBlond and Mysak (1978). The opposite sign convention was used in Chapter 2 so as to be consistent with Taylor (1920), Packham and Williams (1968), Buchwald (1968), Brown (1972) and Pnueli and Pekeris (1968). With the Boussinesq approximation, the horizontal equations are:

$$i\omega\vec{\mathbf{U}}^h - 2\vec{\Omega} \times \vec{\mathbf{U}}^h = \vec{\nabla}\mathbf{P}, \tag{3.1}$$

$$\vec{\nabla}.\vec{\mathbf{U}}^h = \frac{i\omega}{gh_n}\mathbf{P}, \tag{3.2}$$

and the vertical equation is

$$\frac{d^2Z}{d^2z} + \frac{N^2 - \omega^2}{gh_n}Z = 0, \tag{3.3}$$

with the bottom boundary condition

$$Z(0) = 0, \tag{3.4}$$

and the surface boundary condition

$$\frac{dZ}{dz} - \frac{Z}{h_n} = 0 \qquad \text{at} \qquad z = H. \tag{3.5}$$

(LeBlond and Mysak equations 10.39–10.42)

The horizontal velocity is given by

$$\vec{\mathbf{u}}^h(x,y,z) = -h_n \frac{dZ}{dz}(z)\,\vec{\mathbf{U}}^h(x,y), \tag{3.6}$$

the vertical velocity by

$$\mathrm{w}(x,y,z) = \frac{i\omega}{g}\,Z(z)\,\mathbf{P}(x,y), \tag{3.7}$$

and the pressure by

$$\mathbf{p}(x,y,z) = -\rho_0 h_n \frac{dZ}{dz}(z)\,\mathbf{P}(x,y), \tag{3.8}$$

where

$$2\vec{\Omega} \equiv (0, 0, f), \tag{3.9}$$

and

$$N^2(z) \equiv -\frac{g}{\bar{\rho}_0}\frac{d\rho_0}{dz}. \tag{3.10}$$

Equations 3.3–3.5 form an eigenvalue problem which determines the vertical structure of the solution. The eigenvalue problem has an infinite set of solutions (*eigenfunctions* or *vertical modes*) $Z_n(z)$ and corresponding *eigenvalues* h_n (or *equivalent depths*). The gravest mode is the barotropic mode, and is called mode 0 because the vertical structure of the horizontal velocity does not have a zero crossing. In this mode the second term of equation 3.3 becomes negligible because h_n is so large, so equation 3.3 becomes $Z'' = 0$. The solution to this problem is $Z_0(z) = z$ with $h_0 = H$. The vertical strucure of w is linear with w = 0 at the bottom, and the vertical structure of $\vec{u}^h$ is a constant function. The equivalent depth h_0 is equal to the total depth H. The reason for the name *equivalent depth* is that it is the depth of water h_n that would give the same phase speed for the barotropic mode as for a higher mode n in water of depth H. It will be seen later that the phase speed of Kelvin waves for mode n is $\sqrt{gh_n}$. For the barotropic mode, this is the familiar expression for gravity waves in shallow water.

If the eigenvalues of the higher modes are arranged in order of decreasing size , then the n^{th} mode has n zero crossings in the u-eigenfunction. The first term of the boundary condition 3.5 can be discarded for the higher modes, although it is of paramount importance for mode 0.

Density perturbations $\rho'(x, y, z, t)$ are related to w perturbations by

$$\frac{\partial \rho'}{\partial t} + \mathrm{w}\frac{d\rho_0}{dz} = 0. \tag{3.11}$$

(LeBlond and Mysak equation 8.2)

Therefore

$$\begin{aligned}\rho'(x, y, z) &= -\frac{\bar{\rho}_0}{i\omega g} N^2(z)\, \mathrm{w}(x, y, z) \\ &= -\frac{\bar{\rho}_0}{g^2} N^2(z)\, Z(z)\, \mathbf{P}(x, y).\end{aligned} \tag{3.12}$$

The procedure for calculating the vertical structure of the normal modes is therefore as follows:

(i) Calculate a "mean" density profile $\rho_0(z)$ from either several CTD casts, or a cyclesonde record.

(ii) Calculate the N^2-profile (Brunt-Väisälä frequency squared) using definition 3.10.

(iii) Solve the eigenvalue problem given by equations 3.3–3.5 to give a series of eigenvalues h_n and eigenfunctions $Z_n(z)$.

(iv) Calculate the u-eigenfunctions using equation 3.6 and the ρ-eigenfunctions using equation 3.12 for each mode. The former is proportional to the vertical gradient of $Z(z)$, and the latter is proportional to $N^2(z)$ times $Z(z)$.

Any small oscillation of a fluid in a flat-bottomed ocean can then be expressed as a superposition of these modes. The coefficients of each mode will be complex, because an $e^{-i\omega t}$ time dependancy has been assumed.

The horizontal problem consists of equations 3.1–3.2 along with boundary conditions of zero normal flow at the coast and matching conditions at open boundaries. A special solution in a straight channel is the Kelvin wave. In fact, this is the way the barotropic and internal tides in Knight Inlet propagate, because this solution is the only propagating wave that can exist in such a narrow channel. The effect of the evanescent Poincaré modes generated at the bend is negligible, because the e-folding length scale of the first cross-channel mode is approximately $600\,m$, and shorter for the higher modes. The expressions for $\mathbf{P}$ and $\vec{\mathbf{U}}^h = (\mathbf{U}, \mathbf{V})$ for the Kelvin wave solution are:

$$\mathbf{U}(x,y) = U_0\, e^{(i\omega x - fy)/c_n} \tag{3.13}$$

$$\mathbf{V}(x,y) = \mathbf{0} \tag{3.14}$$

$$\mathbf{P}(x,y) = U_0\, c_n\, e^{(i\omega x - fy)/c_n} \tag{3.15}$$

where $c_n = \sqrt{gh_n}$, and x and y are the longitudinal and transverse co-ordinates respectively. U_0 is an arbitrary scaling constant. The Kelvin wave decays exponentially away

from the wall to the right of the direction of propagation with a decay scale given by $R_n = c_n/f$ (the *Rossby radius*).

Upon substitution into equations 3.6 and 3.12 one obtains:

$$\mathbf{u}(x,y,z) = -U_0\, h_n \frac{dZ}{dz}(z)\, e^{(i\omega x - fy)/c_n} \tag{3.16}$$

$$\mathbf{v}(x,y,z) = \mathbf{0} \tag{3.17}$$

$$\rho'(x,y,z) = -\frac{U_0\, c_n \bar{\rho}_0}{g^2} N^2(z)\, Z(z)\, e^{(i\omega x - fy)/c_n}, \tag{3.18}$$

where $\vec{\mathbf{u}}^h = (\mathbf{u}, \mathbf{v})$.

The use of theoretical modes for a flat-bottomed ocean in an inlet where the bottom is not flat must be justified. In a flat-bottomed ocean the normal modes approach is equivalent to the ray-tracing approach, with rays being reflected from the surface and the bottom. The upward propagating rays interfere with the downward propagating rays. However, when the bottom is not flat, it is necessary for the rays to be steeper than the bottom slope if the normal mode approach is to be retained, otherwise the rays will be reflected about the horizontal rather than the vertical (see LeBlond and Mysak 1978 p55). The ray slope is given by the ratio $\sqrt{N^2 - \omega^2} : \sqrt{\omega^2 - f^2}$. Taking a typical value of $log_{10} N^2 = -5.5$ at the bottom (see *Figures 71–74* in Section 3.9), the slope of the rays near the bottom at M_2 frequency can be calculated to be approximately 1 in 21. Hence the bottom slope must be less than this value for the normal mode approach to be used. *Figure 1* shows that on average, apart from irregularities in the topography, the longitudinal bottom slope does not exceed $100\,m$ in $10\,km$ (1 in 100) except on the flanks of the sill. Therefore the rays will usually be reflected about the vertical, as required by normal mode theory.

In addition, as the waves propagate along the inlet, it is necessary for the length scale over which the depth varies ($\frac{H}{\nabla H} \approx 40\,km$ if $H = 400\,m$) to be greater than the wavelength of those waves if a WKB approximation is to be valid. Typical wavelengths for the internal tide are around $36\,km$ for the first mode and $20\,km$ for the second mode, so this criterion is in fact barely met.

3.5 Modal Decomposition

The observed profiles of the M_2 amplitude and phase of longitudinal current and density will be decomposed into a superposition of normal modes. Moreover,a distinction between waves propagating up-inlet and waves propagating down-inlet is also desirable, so that the reflection coefficient at the bend for each mode can be estimated. To make this distinction, the phase relationship between density oscillations and longitudinal velocity oscillations will be exploited. It can be seen from equations 3.16 and 3.18 that these two quantities are in phase. However, for a wave propagating in the negative x-direction, the corresponding expressions can be obtained by replacing c_n by $-c_n$. Thus the expression for density oscillations changes sign, which is equivalent to a 180° phase change. This phase relationship can be used to resolve the waves going up-inlet from those going down-inlet.

Another way of resolving the direction of the waves is to make use of the cross channel decay of Kelvin waves, since higher amplitude oscillations will occur to the right of the direction of propagation of a single Kelvin wave in the northern hemisphere. This method can be used without a density record — velocity data from two stations across the channel and a few CTD casts are sufficient.

In fact, this was the method used by Freeland (1984) in his analysis of current meter records from Knight Inlet. He had a total of four current meters at Tom-N and Tom-S at depths of $75\,m$ and $300\,m$. Unfortunately, with current meters at only two depths, he was forced to assume that there was only one significant internal mode besides the barotropic mode. Farmer and Freeland (1983) assumed that this mode was the first mode, whereas Freeland (1984) modified the analysis by assuming that the dominant mode was the second.

When only the barotropic mode is present, the locus of the complex amplitude (i.e. amplitude and phase) of the longitudinal velocity as the depth varies is a single point in the complex plane. However, when a single internal mode (the n^{th} mode) is also present, this locus becomes a straight line. This line passes through the point corresponding to

the barotropic tide, because the additional velocity component due to the internal mode is zero at depths where the u-eigenfunction has a zero crossing. The point corresponding to the barotropic tide should be the same for both stations, because the cross-channel decay of the barotropic tide is very small (since the external Rossby radius R_0 is very large, about $2000\,km$), and it is assumed that the barotropic current is laterally homogeneous (i.e. negligible topographic effects, and negligible inertial and centrifugal forces associated with the bend). Therefore, the loci at the two stations should intersect at this point in the complex plane.

If a_n^{up} and ϕ_n^{up} are the non-dimensional magnitude and phase of the up-inlet internal wave, a_n^{down} and ϕ_n^{down} are the corresponding values for the down-inlet internal wave, and u_{bt} and ϕ_{bt} are the velocity and phase of the barotropic component, then the complex amplitude of the longitudinal velocity at the northern station is given by:

$$u_{bt}\, e^{i\phi_{bt}} \quad + \quad (a_n^{up}\, e^{-sf/c_n + i\phi_n^{up}} + a_n^{down}\, e^{+sf/c_n + i\phi_n^{down}})\, u_n(z) \tag{3.19}$$

whereas that at the southern station is:

$$u_{bt}\, e^{i\phi_{bt}} \quad + \quad (a_n^{up}\, e^{+sf/c_n + i\phi_n^{up}} + a_n^{down}\, e^{-sf/c_n + i\phi_n^{down}})\, u_n(z), \tag{3.20}$$

where s is the distance of the two stations from the centre of the channel (assumed to be equidistant from the centre), and

$$u_n(z) \equiv U_0\, h_n\, \frac{dZ}{dz}(z) \tag{3.21}$$

is the dimensional u-eigenvalue. U_0 is fixed by some normalisation criterion, such as $\max u_n(z) = 1\,m/sec$.

The two expressions in brackets in equations 3.19–3.20 will not in general be the same complex number. The fact that they have a different phase means that the slopes of the two loci in the complex plane are different. The quotient of the two numbers in brackets can be determined by plotting the four complex amplitudes in the complex plane; the angle between the two lines joining the $75\,m$-points to the $300\,m$-points gives the phase

of the quotient, and the ratio of the length of these two lines gives the magnitude of the quotient. The reflection coefficient $\varphi = a_n^{down}/a_n^{up}$ can be determined from this complex quotient (see Freeland 1984 equation 3).

Freeland (1984) obtained a value of $\varphi = 0.70 \pm 0.07$ using the second mode, whereas Freeland and Farmer (1983) had obtained a value of $\varphi = 0.93$ using the first mode. These vales of φ correspond to energy reflection coefficients of $\mathcal{R} = 49\%$ and $\mathcal{R} = 86\%$ respectively after squaring.

However, the fact that the loci of the complex amplitudes of longitudinal velocity are *not* straight lines (e.g. see *Figure 55*) conflicts with their assumption of a *single* dominant mode, and puts their values for the reflection coefficient into doubt. One argument in support of their assumption is that the calculated phase and magnitude of the barotropic current agrees very well with the theoretical values based on the phase and magnitude of the surface elevation. However, this agreement could be coincidental.

Looking at the loci of the longitudinal velocity at Tom-S and Tom-N in *Figure 55*, it might be tempting to deduce that the internal tide *must* be propagating predominantly up-inlet because the magnitude of the oscillation is always greater on the south side than on the north side, just as it would be for a single Kelvin wave propagating up a straight inlet. However, this argument is not valid, because it is possible to construct a counterexample where a single second mode internal tide propagating down-inlet combines with the barotropic tide to produce stronger currents on the south side than on the north side.

Consider a barotropic tidal current of phase 0° and magnitude $10\,cm/s$ at Tomakstum Island. On top of this current superimpose a second mode velocity profile that decreases monotonically from a magnitude of $6\,cm/s$ (for example) at $20\,m$ to $3\,cm/s$ at $120\,m$ (see *Figure 76* for an illustration of a u-eigenfunction of this form), with a phase of 180°. This internal wave is propagating down-inlet, so that its magnitude might be $6.6\,cm/s$ (at $20\,m$) and $3.3\,cm/s$ (at $120\,m$) at Tom-N, and $5.4\,cm/s$ (at $20\,m$) and $2.7\,cm/s$ (at $120\,m$) at Tom-S. However, the internal mode currents are 180° out of phase with the barotropic

currents, so the net currents are $3.4\,cm/s$ (at $20\,m$) and $6.7\,cm/s$ (at $120\,m$) at Tom-N, and $4.6\,cm/s$ (at $20\,m$) and $7.3\,cm/s$ (at $120\,m$) at Tom-S. The currents are now stronger at Tom-S than at Tom-N, even though the internal wave is propagating down-inlet!

Moreover, the larger currents at Tom-S might be solely due to the inertia of the water as it flows from the bend on an ebb tide, and have nothing to do with the cross-channel decay of Kelvin waves at all. However, the tidal excursion is only of the order of 1 or 2 km, and Tomakstum Island is about $6\,km$ from the bend, so hopefully it is justifiable to ignore this effect.

3.6 Normal Mode Fitting — Theory

It is assumed that the longitudinal velocity and density oscillations at a particular station can be represented by a superposition of normal modes as follows:

$$\mathbf{u}(y,z) = \sum_{n=0}^{\infty} u_n(z)\left(a_n^{up}\, e^{-yf/c_n + i\phi_n^{up}} + a_n^{down}\, e^{+yf/c_n + i\phi_n^{down}}\right) \tag{3.22}$$

$$\rho'(y,z) = \sum_{n=0}^{\infty} \rho_n(z)\left(a_n^{up}\, e^{-yf/c_n + i\phi_n^{up}} - a_n^{down}\, e^{+yf/c_n + i\phi_n^{down}}\right) \tag{3.23}$$

where y is the cross-channel co-ordinate ($y = 0$ at mid-channel, $y = +500\,m$ at Tom-N and $y = -500\,m$ at Tom-S), and $\rho_n(z)$ is the dimensional ρ-eigenfunction for the n^{th} mode defined by

$$\rho_n(z) \equiv U_0\,\frac{\bar{\rho}_0 c_n}{g^2}\,N^2(z)\,Z_n(z). \tag{3.24}$$

$u_n(z)$ is the dimensional u-eigenfunction, previously defined in equation 3.21. The dimensions of $\rho_n(z)$ are those of density, and the dimensions of $u_n(z)$ are those of velocity. The minus sign in equation 3.23 arises because equation 3.18 must be modified for down-inlet propagating waves (i.e. waves propagating in the negative x-direction) by replacing c_n by $-c_n$, as was stated earlier.

For stations in the centre of the channel (that is, all stations except Tom-N and Tom-S), y must be set to 0, and 3.22 and 3.23 reduce to

$$\mathbf{u}(z) = \sum_{n=0}^{\infty} u_n(z)\left(\mathbf{A}_n^{up} + \mathbf{A}_n^{down}\right) \tag{3.25}$$

$$\rho'(z) = \sum_{n=0}^{\infty} \rho_n(z) \left(\mathbf{A}_n^{up} - \mathbf{A}_n^{down} \right), \tag{3.26}$$

where

$$\mathbf{A}_n^{up} = a_n^{up} \, e^{i\phi_n^{up}} \tag{3.27}$$

and

$$\mathbf{A}_n^{down} = a_n^{down} \, e^{i\phi_n^{down}} \tag{3.28}$$

are the complex amplitudes of the up- and down-inlet propagating waves.

3.6.1 Least Squares Fitting at a Single Station in Mid-Channel

The statistical model can be formally defined by

$$\mathbf{u}_{obs}(z) = \sum_{n=0}^{N} u_n(z) \left(\mathbf{A}_n^{up} + \mathbf{A}_n^{down} \right) \quad + \quad \varepsilon^u(z) \tag{3.29}$$

$$\rho_{obs}(z) = \sum_{n=0}^{N} \rho_n(z) \left(\mathbf{A}_n^{up} - \mathbf{A}_n^{down} \right) \quad + \quad \varepsilon^\rho(z). \tag{3.30}$$

The ε's are error terms, and $\mathbf{u}_{obs}(z)$ and $\rho_{obs}(z)$ are the complex amplitudes of longitudinal velocity and density oscillations from a harmonic analysis of the data. In practice the infinite series must be truncated after a finite number of terms N; this was usually two or three (see Section 3.10).

In the case of a station in mid-channel, the least squares fit can be done independently for each of the following four quantities:

(i) $\Re(\mathbf{u}_{obs})$ to yield $\Re(\mathbf{A}_n^{up} + \mathbf{A}_n^{down})$

(ii) $\Im(\mathbf{u}_{obs})$ to yield $\Im(\mathbf{A}_n^{up} + \mathbf{A}_n^{down})$

(iii) $\Re(\rho_{obs})$ to yield $\Re(\mathbf{A}_n^{up} - \mathbf{A}_n^{down})$

(iv) $\Im(\rho_{obs})$ to yield $\Im(\mathbf{A}_n^{up} - \mathbf{A}_n^{down})$.

This decomposition is possible because the u_n's and ρ_n's are all real. It can be seen that a fit of the u-eigenfunctions to the observed u-profiles yields $(\mathbf{A}_n^{up} + \mathbf{A}_n^{down})$, whereas a fit of the ρ-eigenfunctions to the observed ρ-profiles yields $(\mathbf{A}_n^{up} - \mathbf{A}_n^{down})$. The sum of these two complex numbers then gives $2\mathbf{A}_n^{up}$, and the difference gives $2\mathbf{A}_n^{down}$.

3.6.2 Least Squares Fitting at Two Stations on Opposite Sides of the Channel

However, when simultaneous data are available from both sides of the channel, as at Tomakstum Island in September 1983, the four fits described above cannot be done independently if the information on the cross-channel decay of Kelvin waves is to be used.

The statistical model is now

$$\mathbf{u}_{obs}(y,z) = \sum_{n=0}^{N} u_n(z)\left(\mathbf{A}_n^{up} e^{-yf/c_n} + \mathbf{A}_n^{down} e^{+yf/c_n}\right) \quad + \quad \varepsilon^u(y,z) \tag{3.31}$$

$$\rho_{obs}(y,z) = \sum_{n=0}^{N} \rho_n(z)\left(\mathbf{A}_n^{up} e^{-yf/c_n} - \mathbf{A}_n^{down} e^{+yf/c_n}\right) \quad + \quad \varepsilon^\rho(y,z). \tag{3.32}$$

At Tom-S, $y = +s$, and these two equations become

$$\mathbf{u}_{obs}(+s,z) = \sum_{n=0}^{N} u_n(z)\left(\mathbf{A}_n^{up} e^{-sf/c_n} + \mathbf{A}_n^{down} e^{+sf/c_n}\right) \quad + \quad \varepsilon^u(+s,z) \tag{3.33}$$

$$\rho_{obs}(+s,z) = \sum_{n=0}^{N} \rho_n(z)\left(\mathbf{A}_n^{up} e^{-sf/c_n} - \mathbf{A}_n^{down} e^{+sf/c_n}\right) \quad + \quad \varepsilon^\rho(+s,z). \tag{3.34}$$

At Tom-N, $y = -s$, giving

$$\mathbf{u}_{obs}(-s,z) = \sum_{n=0}^{N} u_n(z)\left(\mathbf{A}_n^{up} e^{+sf/c_n} + \mathbf{A}_n^{down} e^{-sf/c_n}\right) \quad + \quad \varepsilon^u(-s,z) \tag{3.35}$$

$$\rho_{obs}(-s,z) = \sum_{n=0}^{N} \rho_n(z)\left(\mathbf{A}_n^{up} e^{+sf/c_n} - \mathbf{A}_n^{down} e^{-sf/c_n}\right) \quad + \quad \varepsilon^\rho(-s,z). \tag{3.36}$$

These equations can then be solved simultaneously by least squares, using information from both stations, to give estimates for $\mathbf{A}_n^{up}$ and $\mathbf{A}_n^{down}$. The advantage of using both stations simultaneously is that there is twice the amount of data to fit to, and information on the cross-channel decay of Kelvin waves is used as well as information on the phase of ρ-oscillations relative to u-oscillations.

3.7 The Estimation of the Barotropic Component

The component of the u- and ρ-oscillations due to the barotropic tide can be estimated from a harmonic analysis of the surface elevation data and a knowledge of the geometry of the inlet. As previously described, the surface tide in an inlet is classically described as a standing wave, where the whole surface of the inlet rises and falls together. A standing wave can be thought of as a superposition of an incident wave and a reflected wave of equal magnitude. At the head, the longitudinal velocity due to the incident wave is precisely 180° out of phase with the longitudinal velocity due to the reflected wave. In this way the longitudinal velocity cancels out there as required.

As *Figure 69* shows, the surface elevation phases are indeed roughly constant along Knight Inlet. This observation implies a standing wave pair, in which the amplitude of the up-inlet wave equals that of the down-inlet wave at each station i.e.:

$$a^0_{up} = a^0_{down}. \tag{3.37}$$

It will be seen later in Section 3.10 that only about 1% ($= 7\,MW \div 700\,MW$) of the up-inlet or down-inlet barotropic energy flux is lost through friction and non-linear processes in the straight section, so that this assumption (3.37) can be justified *a posteriori*. The phase of the barotropic component of the longitudinal velocity will lead the phase of the surface elevation by 90°. Therefore, if the phase of the surface elevation is taken to be 33° (see *Figure 69*), then that of velocity will be 303° ($= \phi_{bt}$ in equations 3.19–3.20). In addition, the magnitude of the barotropic component of the velocity u_{bt} can be estimated from the magnitude η_0 of the surface elevation oscillation, the cross-sectional area $S$of the inlet at a particular section, and the surface area A of the inlet landward of that section. The magnitude of the barotropic velocity will be given by

$$u_{bt} = \frac{\eta_0 \omega A}{S}, \tag{3.38}$$

where ω is the frequency of the M_2 tide.

Then

$$U_0(\mathbf{A}_0^{up} + \mathbf{A}_0^{down}) = u_{bt} e^{i\phi_{bt}}, \tag{3.39}$$

where it is assumed that the normalisation constant U_0 is such that $u_0(z) = 1\,m/sec$ for all z.

There is one more piece of information that enables the unique determination of $\mathbf{A}_0^{up}$ and $\mathbf{A}_0^{down}$ at any particular section in the inlet, namely the barotropic phase speed c_0. Temporarily assuming this to be a constant, the phase of the u-oscillation due to the up-inlet wave will be given by $(\phi_0^{up} + \frac{d\omega}{c_0})$ at the head, where d is the distance from the section of interest to the head, and ϕ_0^{up} is the phase of the up-inlet wave at that section. Similarly, the phase of the u-oscillation due to the down-inlet wave will be $(\phi_0^{down} - \frac{d\omega}{c_0})$ at the head. These two quantities must be 180° out of phase there, so

$$\phi_0^{up} + \frac{d\omega}{c_0} = \phi_0^{down} - \frac{d\omega}{c_0} + \pi. \tag{3.40}$$

Equation 3.39 now becomes

$$\begin{aligned} \underbrace{u_{bt}\, e^{i\phi_{bt}}}_{known} &= a_0^{up} U_0 \left(e^{i\phi_0^{up}} + e^{i[\phi_0^{up} + 2d\omega/c_0 - \pi]} \right) \\ &= 2\, a_0^{up} U_0 \sin\left(\frac{d\omega}{c_0}\right) e^{i[\phi_0^{up} + d\omega/c_0 - \pi/2]}. \end{aligned} \tag{3.41}$$

Therefore,

$$a_0^{up} = a_0^{down} = \frac{u_{bt}}{2U_0} \operatorname{cosec}\left(\frac{d\omega}{c_0}\right), \tag{3.42}$$

$$\phi_0^{up} = \phi_{bt} - \frac{d\omega}{c_0} + \frac{\pi}{2}, \tag{3.43}$$

and

$$\phi_0^{down} = \phi_{bt} + \frac{d\omega}{c_0} - \frac{\pi}{2}. \tag{3.44}$$

In the case of c_0 varying slowly along the length of the inlet, as occurs in reality, $\frac{d\omega}{c_0}$ must be replaced by a WKB approximation to the phase difference between the section of interest and the head of the inlet

$$\Delta\phi = \int_{section}^{head} \frac{\omega}{c_0(x)}\, dx. \tag{3.45}$$

Since $c_0^2(x) = g\,H(x)$, this amounts to calculating the average value of $H^{-\frac{1}{2}}$ between the section of interest and the head of the inlet. This calculation was done by taking the depths

from the chart, which are given every kilometer or so, and calculating average values of $H^{-\frac{1}{2}}$ between the four stations and the head.

Table 3 gives the calculated values of $\Delta\phi$ between each station and the head. They range from 7.3° at Adeane Point to 13.2° at Protection Point. *Table 3* also gives values of A and S, as estimated from the chart. Assuming that $\eta_0 = 1.52\,m$, equations 3.42–3.44 were used to calculate a_0^{up} (which $= a_0^{down}$), ϕ_0^{up} and ϕ_0^{down}.

Table 3
Estimates of the barotropic tidal currents at each station

station	$\Delta\phi$ (°)	A (km^2)	S (km^2)	u_{bt} (cm/s)	$U_0\,a_0^{up}$ (cm/s)	ϕ_0^{up} (°)	ϕ_0^{down} (°)
Protection Point	13.2	234	0.41	11.9	26.0	20	226
Lull Bay	11.0	195	0.36	11.4	29.9	22	224
Tomakstum Island	9.0	156	0.50	6.7	21.4	24	222
Adeane Point	7.3	130	0.76	3.6	14.2	26	220

In the case of the barotropic mode, the Rossby radius is so large ($\approx 2000\,km$) that the Kelvin wave has insignificant cross-channel decay, so it is not necessary to consider this at Tom-N and Tom-S.

There is considerable error involved in these estimates, especially in u_{bt} because it depends on the reciprocal of S, and in a_0^{up} (and a_0^{down}) because it depends on cosec $\Delta\phi$. The second of these is not too important, because a knowledge of a_0^{up} is only necessary for the calculation of the contribution of the barotropic mode to ρ-oscillations (proportional to $(\mathbf{A}_0^{up} - \mathbf{A}_0^{down}) = 2\,a_0^{up}\,\cos\Delta\phi\,e^{i[\phi_{bt}+\pi/2]}$), which is small compared to the contribution from other modes. An error in the estimation of the magnitude of this small contribution will not affect the results of fitting the internal modes to the residual. Note that the phase of this barotropic contribution to ρ-oscillations can be accurately determined — it is $[\phi_{bt} + \pi/2]$.

However, the first of the two errors, namely that of estimating u_{bt}, *is* important because the contribution of the barotropic mode to u-oscillations is considerable. All that can be done is to make the most careful estimate possible of u_{bt} given the existing data on the

geometry of Knight Inlet. It is still worth incorporating this information into the fitting process, even though it is of poor quality. Note that the phase ϕ_{bt} of the barotropic component of u-oscillations can be accurately estimated — it is the phase of the surface elevation oscillation minus $\frac{\pi}{2}$.

Knowledge of $\mathbf{A}_0^{up}$ and $\mathbf{A}_0^{down}$ was incorporated into the fitting procedure by subtracting the $n = 0$ terms on the right-hand sides of equations 3.29–3.30 (or equations 3.33–3.36) from the observed complex amplitude profiles on the left-hand sides, and fitting the internal modes to the residual.

3.8 Energy Fluxes

The *energy density* E of an internal wave is defined as the mean perturbation energy per unit volume:

$$E = \tfrac{1}{2}\rho_0 \overline{(u^2 + v^2 + w^2)} \quad + \quad \frac{g^2 \overline{\rho'^2}}{2\,\rho_0\, N^2}. \tag{3.46}$$

(Gill 6.7.6)

Assuming a flat-bottomed channel, and using the expressions 3.16–3.18 for a Kelvin wave, the following expression is obtained for the vertically and laterally integrated energy density E' per unit length of channel for the n^{th} mode:

$$E' = \frac{\bar{\rho_0}\, U_0^2\, c_n^2\, W\, F}{4\, g^2} \int_0^H \left(c_n^2 \left(\frac{dZ}{dz}\right)^2 \quad + \quad \omega^2\, Z^2 \quad + \quad N^2\, Z^2 \right) dz, \tag{3.47}$$

where W is the channel width and

$$F = \frac{R_n}{W} \sinh\left(\frac{W}{R_n}\right) \tag{3.48}$$

$$= 1 + \frac{1}{6}\left(\frac{W}{R_n}\right)^2 + O\left(\left(\frac{W}{R_n}\right)^4\right). \tag{3.49}$$

The first term inside the integral is the kinetic energy due to longitudinal velocity, the second term is the kinetic energy due to vertical velocity, and the third term is the potential energy associated with the displacement of isopycnals. The second term is negligible compared to the third because $\omega^2 \ll N^2$. It will be seen in the next Section that $log_{10}N^2$ varies from -1.5 near the surface to -5.5 at depth when N is measured in units of rad/s, whereas $log_{10}\omega^2 = -7.7$ for the M_2 constituent.

For internal waves there is an equipartition between the kinetic energy and the potential energy associated with the displacement of isopycnals. This was checked by direct calculation of the three terms in equation 3.47 using the numerical solutions of the eigenvalue problem (see Section 3.8). It was found that the first term comprised 50–52% of the total, the second comprised around 0.001%, and the third comprised 48–50%.

A fourth component becomes significant for the barotropic mode, namely the potential energy associated with the displacement of the free surface. The energy density of this component is given by:

$$E' = \frac{1}{4}\bar{\rho}_0\, g\, \eta_0^2\, F\, W, \tag{3.50}$$

where η_0 is the amplitude of the surface oscillation. This component is insignificant for the internal modes, but for the barotropic mode it becomes equal in magnitude to the kinetic energy density. Again there is equipartition of energy between kinetic and potential energy, but for the surface wave the potential energy is associated with the free surface displacement, whereas for internal modes the potential energy is associated with isopycnal displacements. The third term in equation 3.47 drops to around 1–2% of the total for the barotropic mode.

The factor F takes account of the cross-channel decay of Kelvin waves. For large Rossby radii compared to the width (e.g. for the surface wave), this factor is practically equal to unity. For the first internal mode, which has a Rossby radius of roughly $7\,km$, $F \approx 1.01$. Even for the fourth internal mode, which has a Rossby radius of the order of $1.6\,km$, this factor is still only 1.28. Even though this factor was incorporated into the calculation of the energy flux, it is a minor factor compared to the inaccuracy involved in obtaining a value for W. W is the width of a channel of rectangular cross-section that would have the same energy flux as Knight Inlet, which has a trapezoidal or U-shaped cross-section (see Pickard 1961).

The energy *flux* associated with each mode can easily be calculated from the energy density E' by multiplying by the group velocity, which in the case of Kelvin waves is equal

to the phase velocity c_n. The units of E' are J/m, and those of energy flux are J/sec. In the case of up-inlet waves $a_n^{up}U_0$ was used for U_0 in equation 3.47, and in the case of down-inlet waves $a_n^{down}U_0$ was used for U_0. In this way the non-dimensional amplitudes of the various modes were used to calculate the corresponding energy fluxes.

3.9 The Calculation of the Normal Modes

The eigenvalue problem for the normal modes (equations 3.3–3.5) was solved numerically for observed N^2-profiles. As in Section 2.7, the numerical scheme used was a 4^{th}-order Runge-Kutta scheme with iterative refinement of the eigenvalue to satisfy the boundary condition at the surface (a "shooting" technique). The biggest problem in calculating the normal modes was in knowing what to use for the N^2-profile. The linear theory requires the use of the vertical gradient of the average density. Here, average means over many tidal cycles, but not too many since the average density itself will change over the course of a year . A one-month mean would be desirable. Unfortunately, the cyclesondes only have a limited profile range, usually $20\,m$ to around $170\,m$. They can provide good estimates of the monthly averaged N^2-profile over that depth range, but lack vital information on the upper $20\,m$. This information is contained in the CTD casts, but they were only taken before deployment and after retrieval of each cyclesonde, so some aliasing will be introduced because of the different phases of the tide.

A combination N^2-profile was eventually used, taking cyclesonde data wherever available, and CTD data for the upper $20\,m$ or so. There are two ways of taking averages of the various CTD casts: (i) calculate the normal modes using the average of all CTD profiles at a particular station, or (ii) calculate the normal modes using single CTD profiles, and then take the average of these normal modes. Both methods were used, and compared.

Figure 70 shows all the density profiles from CTD casts at the Tomakstum Island stations (including Tom-N and Tom-S). The dashed profiles were taken at the end of September, and a weakening of the fresh surface layer is evident due to a reduction in river runoff. The density structure of the inlet is in a transition from summer stratification

(with a strong pycnocline) to winter stratification (with no fresh surface layer). Because this winter stratification is not typical of the period July–September, all CTD data from the end of September will henceforth be ignored.

Figures 71–74 show log-plots of N^2-profiles at the various stations. In each plot, the dashed line is the mean N^2-profile of all CTD profiles (except the end of September)at that station. The solid lines are N^2-profiles calculated from monthly averages of cyclesonde density data from 1983. The triangles on these lines indicate the deepest standard depth. The cyclesonde N^2-profiles were linearly extrapolated in log space to the bottom using a best straight line fit to the last five standard depths, since none of the CTD casts went further than $200\,m$ either. This extrapolation was chosen because the $log_{10}N^2$ profiles seemed to be reasonably linear below $60\,m$. The cyclesonde profiles and the CTD profiles agree well.

Figures 75 and *76* show a set of five normal modes at Tomakstum Island, calculated using the average of all CTD data (except the end of September) in the upper $20\,m$, and using the average of all three appropriate records of cyclesonde density data. The modes in these figures are normalised so that the maximum value attained by the horizontal velocity eigenfunction is $1\,m/sec$. Most of the structure of these functions is in the upper $20\,m$, which is a pity because that is precisely where there are no cyclesonde data. Some of these eigenfunctions look very similar if their shape above $20\,m$ is ignored.

If there *were* data from the upper $20\,m$, then the least squares fitting procedure could be replaced by a method which takes the dot product of the observed velocity profiles with each of the normal modes to obtain the coefficients of each mode; i.e. exploiting the orthogonality property of the normal modes:

$$\int_0^H u_m(z)\,u_n(z)\,dz \quad \propto \quad \delta_{mn} \tag{3.51}$$

and

$$\int_0^H \mathrm{w}_m(z)\,\mathrm{w}_n(z)\left(N^2(z)-\omega^2\right)dz \quad \propto \quad \delta_{mn}. \tag{3.52}$$

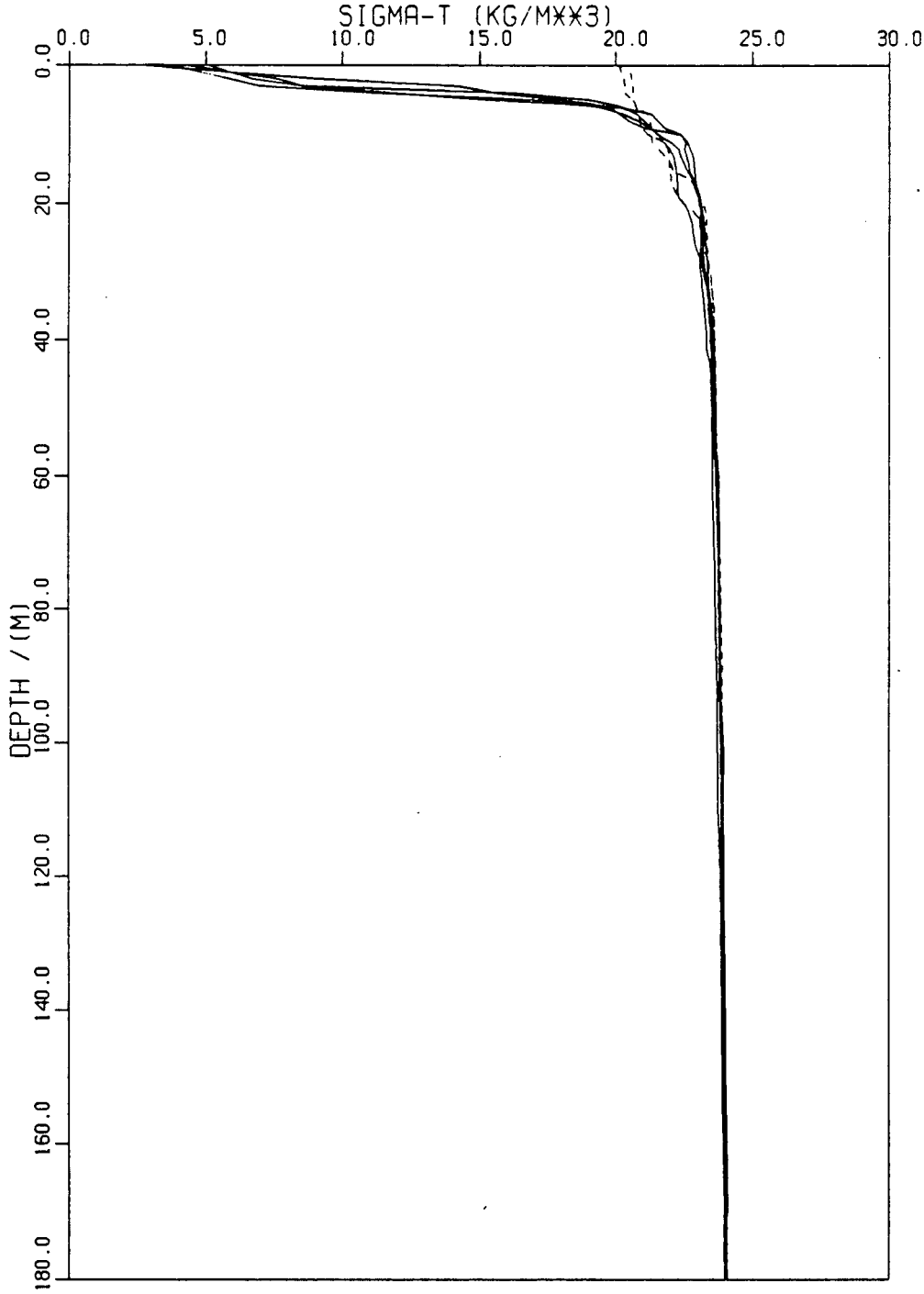

Figure 70 CTD density profiles at Tomakstum Island in 1983.
Solid lines = July and August, dashed lines = end of September.

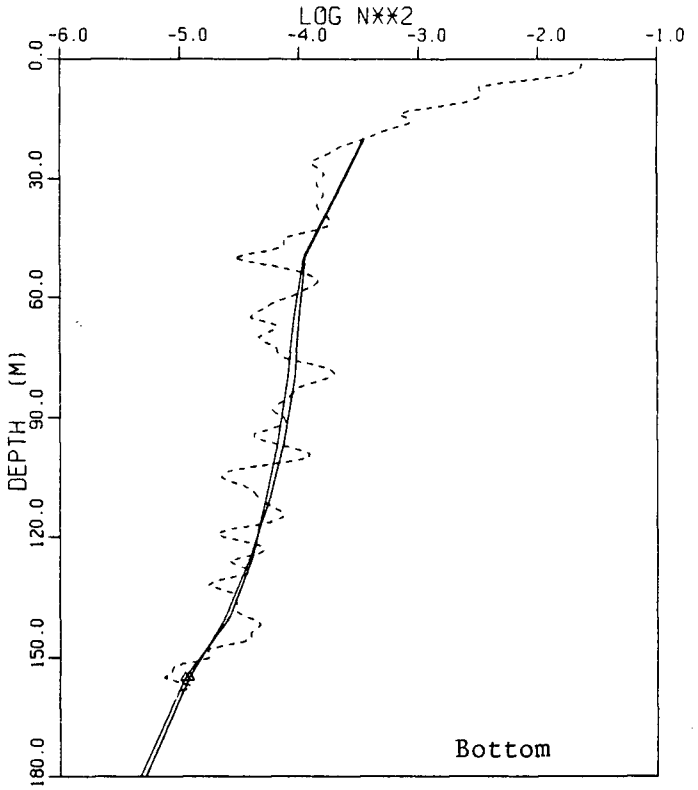

Figure 71 $log_{10}N^2$ vs depth at Protection Point.
Dashed line = CTD data, solid lines = cyclesonde data.

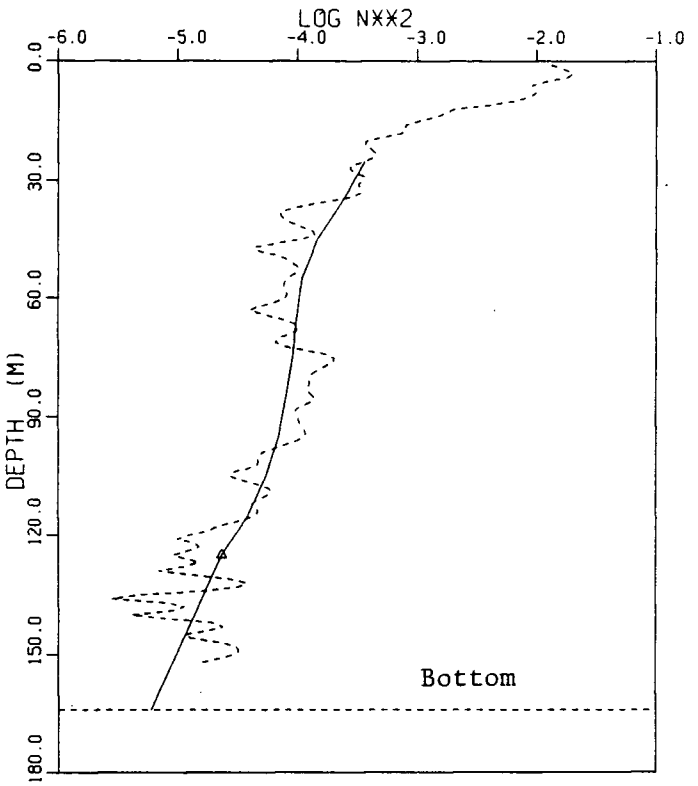

Figure 72 $log_{10}N^2$ vs depth at Lull Bay.
Dashed line = CTD data, solid line = cyclesonde data.

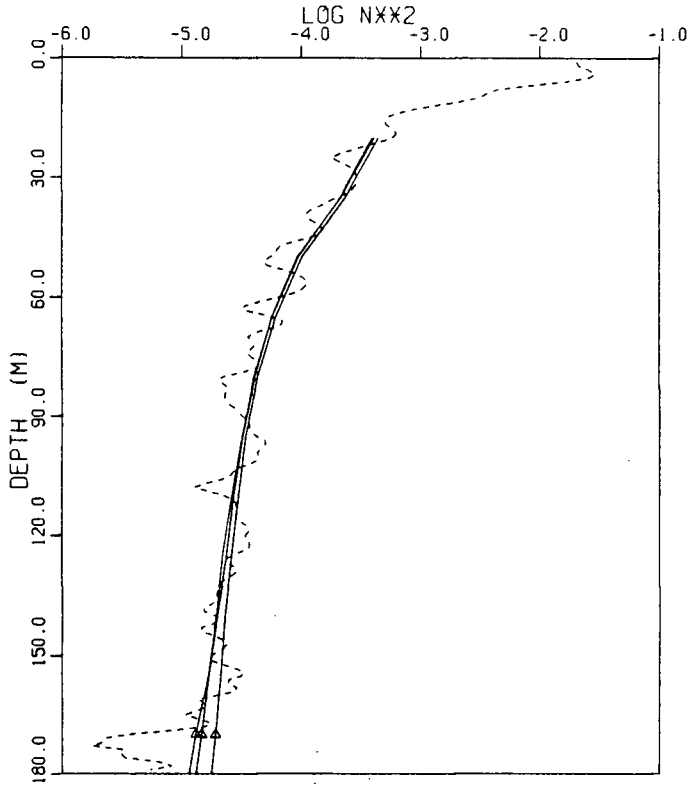

Figure 73 $log_{10}N^2$ vs depth at Tomakstum Island.
Dashed line = CTD data, solid lines = cyclesonde data. $H = 340\,m$.

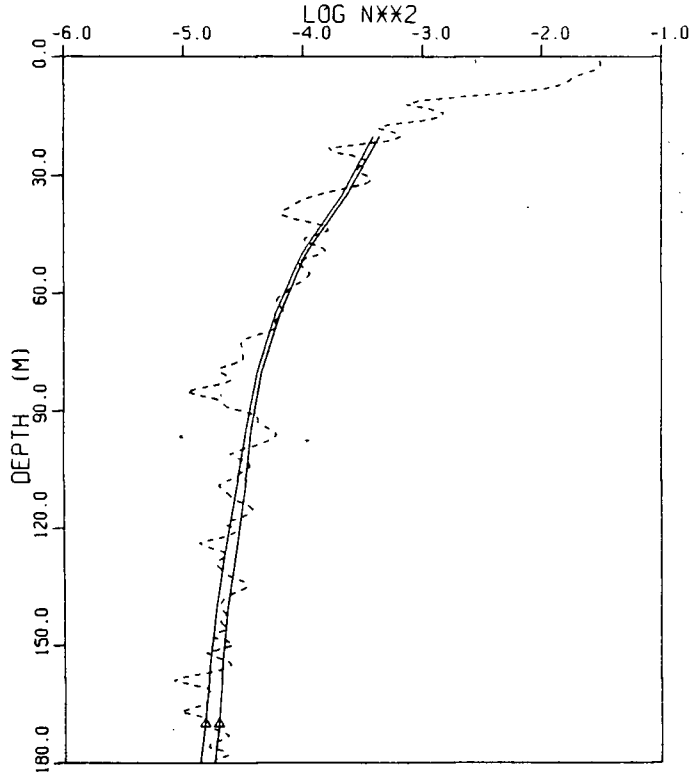

Figure 74 $log_{10}N^2$ vs depth at Adeane Point.
Dashed line = CTD data, solid lines = cyclesonde data. $H = 540\,m$.

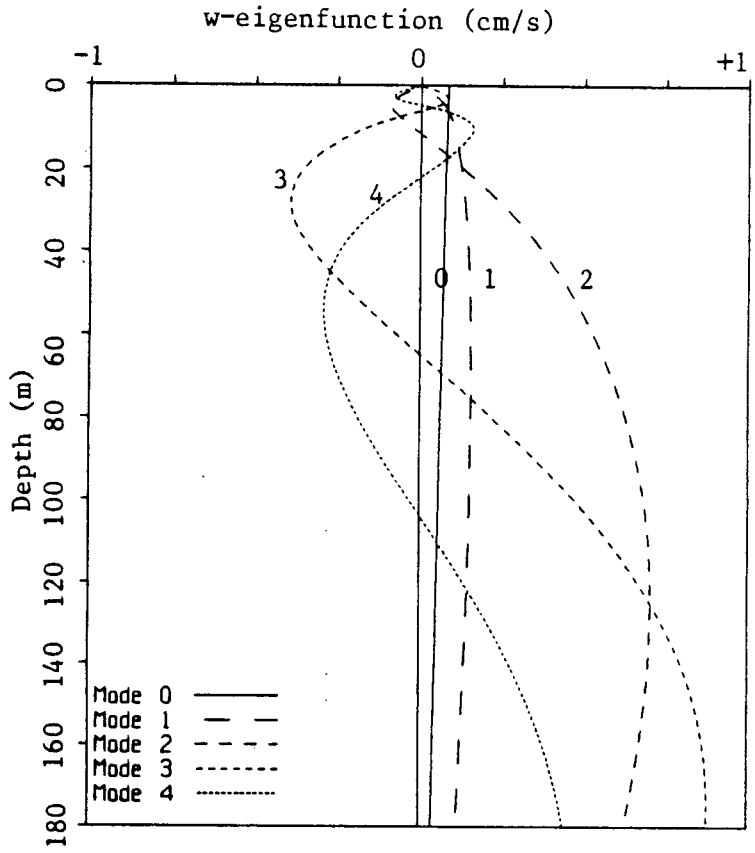

Figure 75 w-eigenfunctions at Tomakstum Island including upper 20 m. $H = 340\,m$.

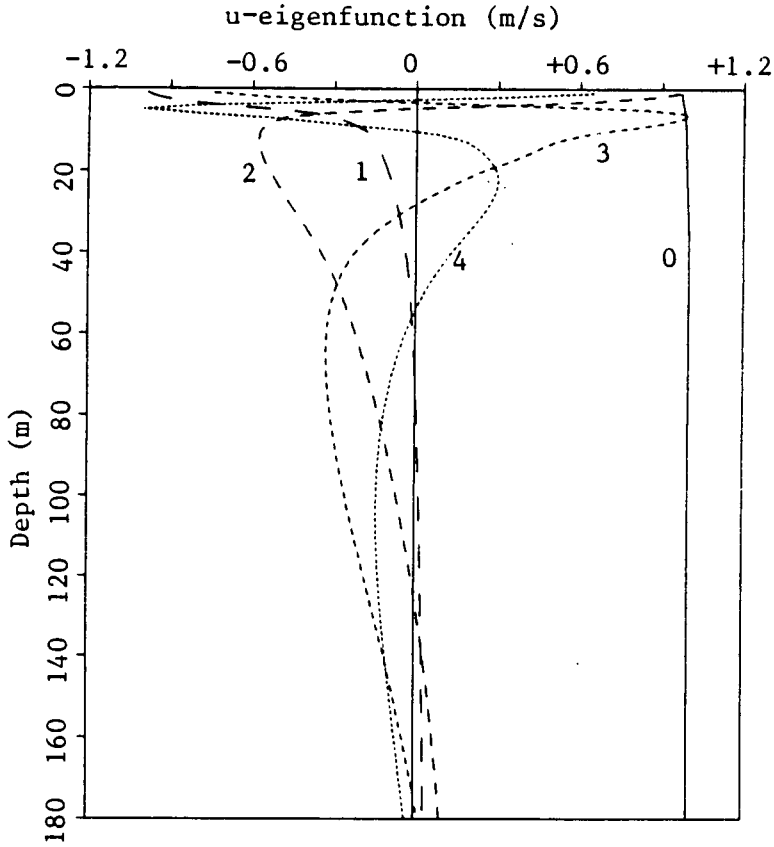

Figure 76 u-eigenfunctions corresponding to *Figure 75.*

Unfortunately there is no orthogonality condition which uses only the portion of the normal mode profiles below $20\,m$, so a least squares fitting approach must be taken.

The solid lines in *Figures 81–82* show the same set of normal modes as in *Figures 75–76* (using an average N^2-profile from CTD casts in the upper $20\,m$, and from cyclesonde density profiles below $20\,m$). However, in *Figures 77–84* the profiles were plotted below $20\,m$ ($25\,m$ at Lull Bay) only, and the modes were normalised so that each mode had the same energy density E' as given by equation 3.47. The ρ-eigenfunctions were calculated using equation 3.24, and are plotted at the standard depths with straight line segments joining them. The two dashed lines for each mode are ± 1 standard deviation from the mean of profiles calculated using a single CTD cast above $20\,m$ and a single cyclesonde profile below $20\,m$. Each CTD cast (M_{CTD} of them) was combined with a cyclesonde profile (M_{cy} of them) to produce $M_{CTD} \times M_{cy}$ different N^2-profiles. These profiles were then used in turn to calculate $M_{CTD} \times M_{cy}$ sets of normal modes, which were then averaged to give the dashed lines shown in *Figures 77–84*. The mean phase speeds in m/s are also given, along with the ± 1 standard deviation values. In all cases there is good agreement between the eigenfunctions calculated using the mean composite N^2-profiles and the mean eigenfunctions calculated using single composite N^2-profiles. In the fitting stage discussed later in Section 3.10 it was the former (eigenfunctions calculated using mean composite N^2-profiles) that were actually used.

3.10 Comparison with Farmer and Smith's Normal Modes

Figure 85 is a reproduction of the density profiles and corresponding normal modes used by Farmer and Smith (1980a). This CTD cast was taken on August 13, 1977 "a few kilometers up-inlet of the sill." Given a bottom depth of $320\,m$, their location would correspond most closely with the Tomakstum Island station. Farmer and Smith argue that because their w-eigenfunction has a maximum at around $24\,m$ for mode 1, and at around $136\,m$ (and $4\,m$) for mode 2, a large disturbance at depth, such as flow over a sill, might be expected to excite mode 2 oscillations in the summer. In the winter the surface fresh layer is much weaker, and the mode 1 eigenfunction in the winter looks very similar to the

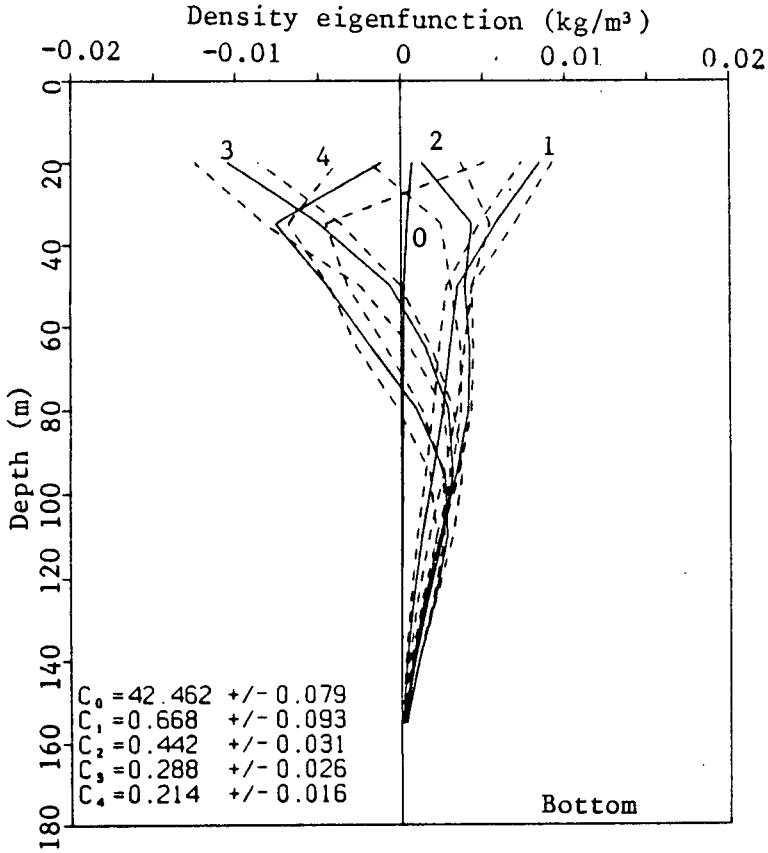

Figure 77 ρ-eigenfunctions at Protection Point excluding upper 20 m.

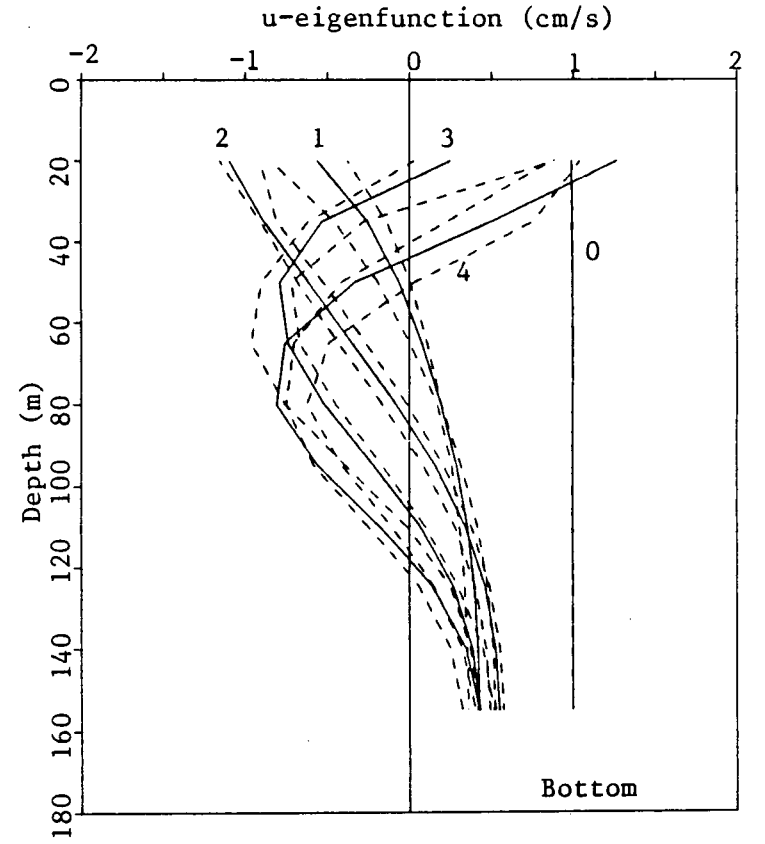

Figure 78 u-eigenfunctions corresponding to *Figure 77*. $M_{CTD} = 4$, $M_{cy} = 2$.

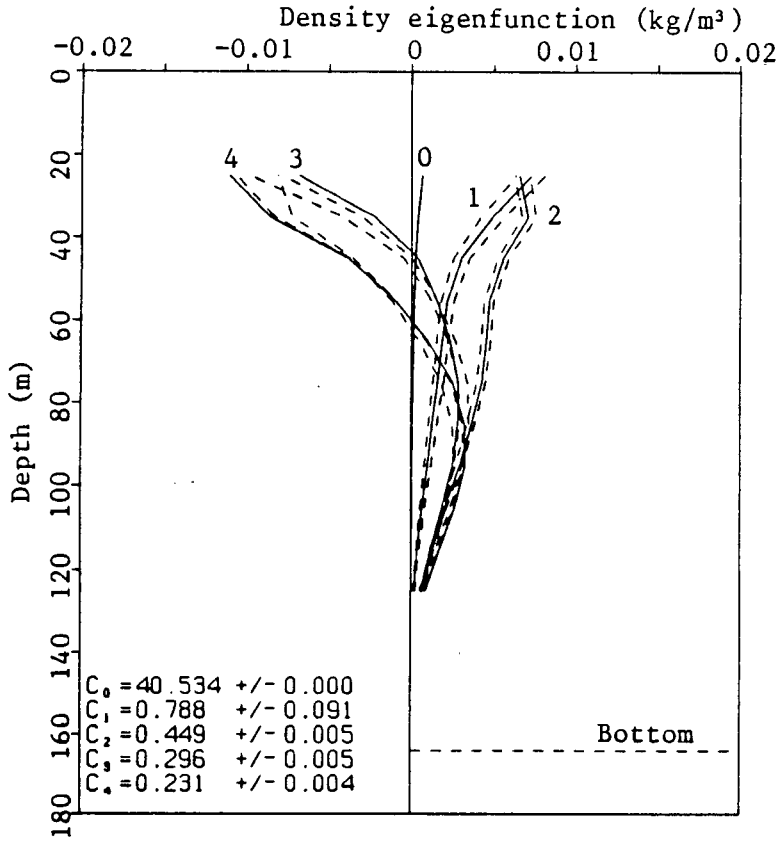

Figure 79 ρ-eigenfunctions at Lull Bay excluding upper 25 m.

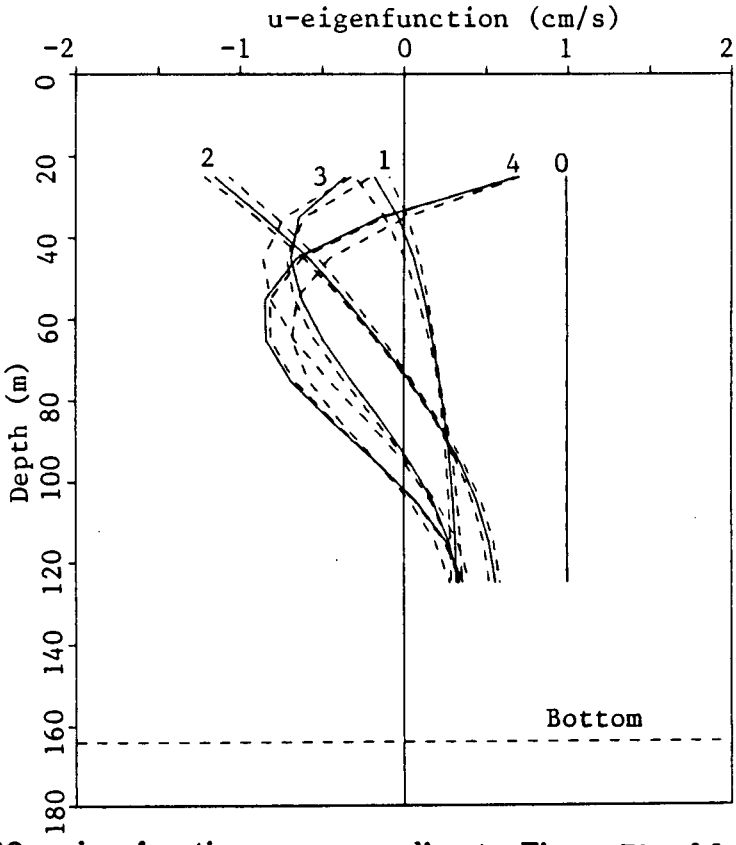

Figure 80 u-eigenfunctions corresponding to *Figure 79*. $M_{CTD} = 3$, $M_{cy} = 1$.

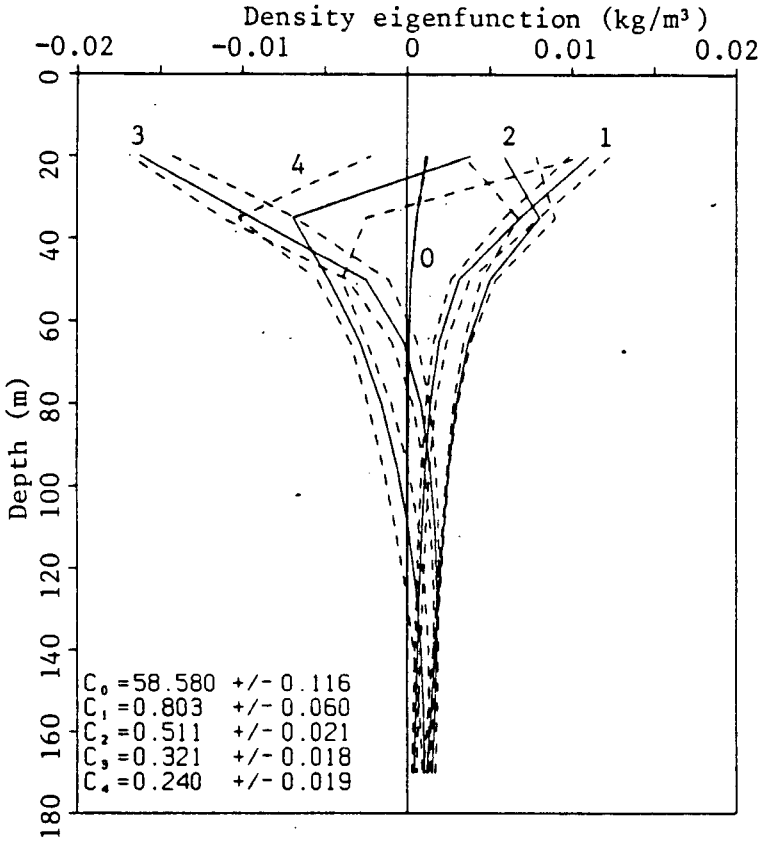

Figure 81 ρ-eigenfunctions at Tomakstum Island excluding upper 20 m. $H = 340\,m$.

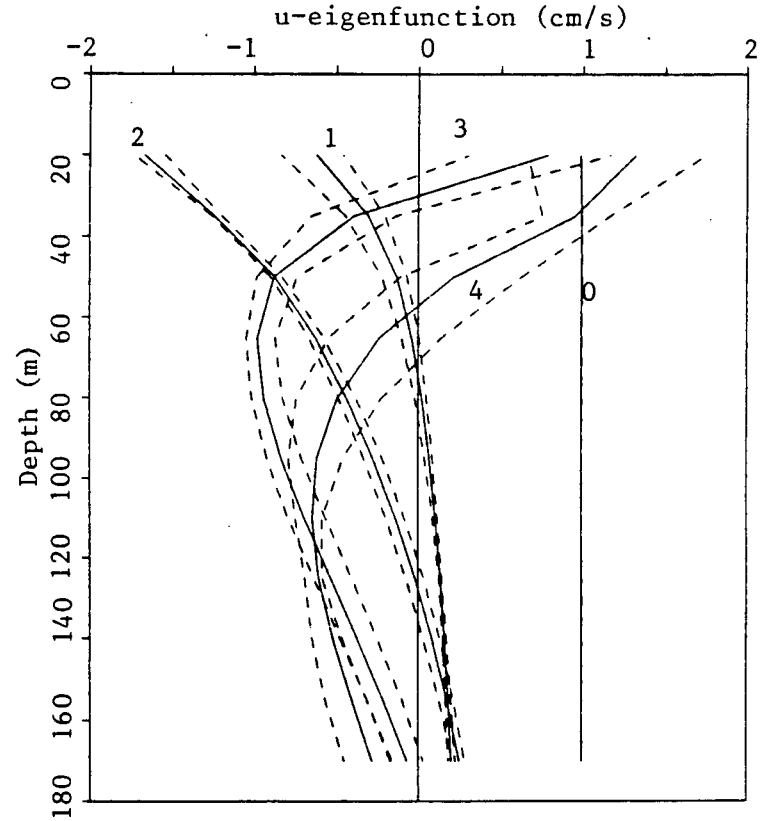

Figure 82 u-eigenfunctions corresponding to *Figure 81*. $M_{CTD} = 5$, $M_{cy} = 3$.

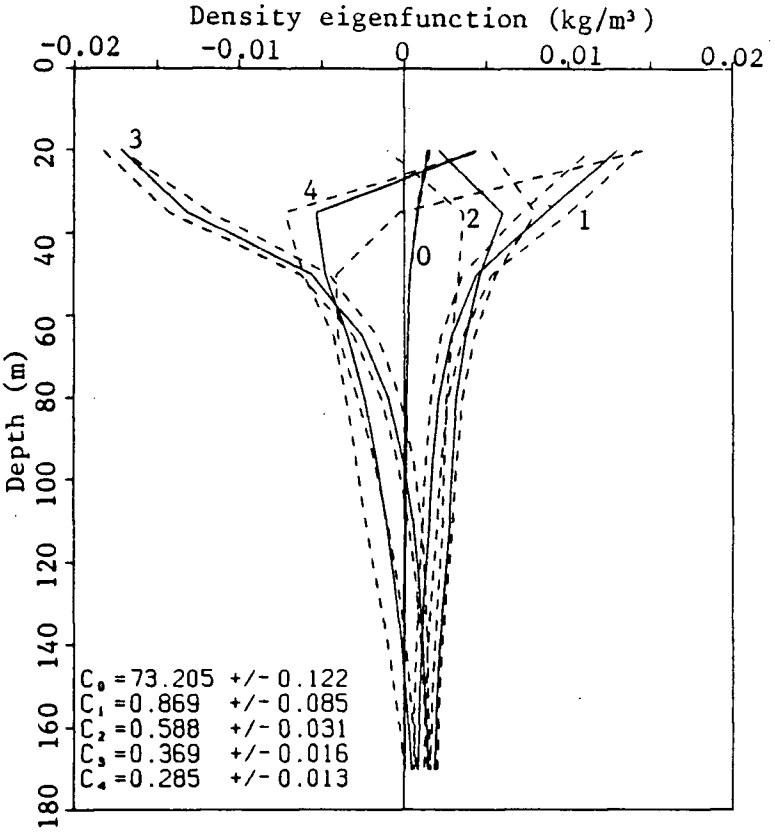

Figure 83 ρ-eigenfunctions at Adeane Point excluding upper $20\,m$. $H = 540\,m$.

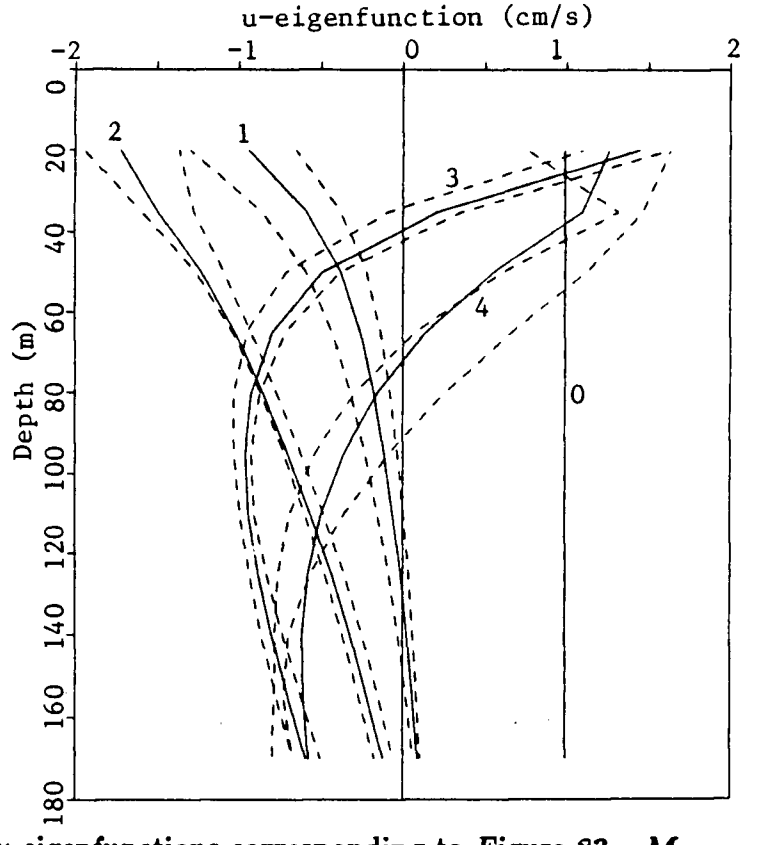

Figure 84 u-eigenfunctions corresponding to *Figure 83*. $M_{CTD} = 3$, $M_{cy} = 2$.

mode 2 eigenfuntion in the summer, with a maximum at 127 m. Mode 1 should therefore be excited by the sill in winter.

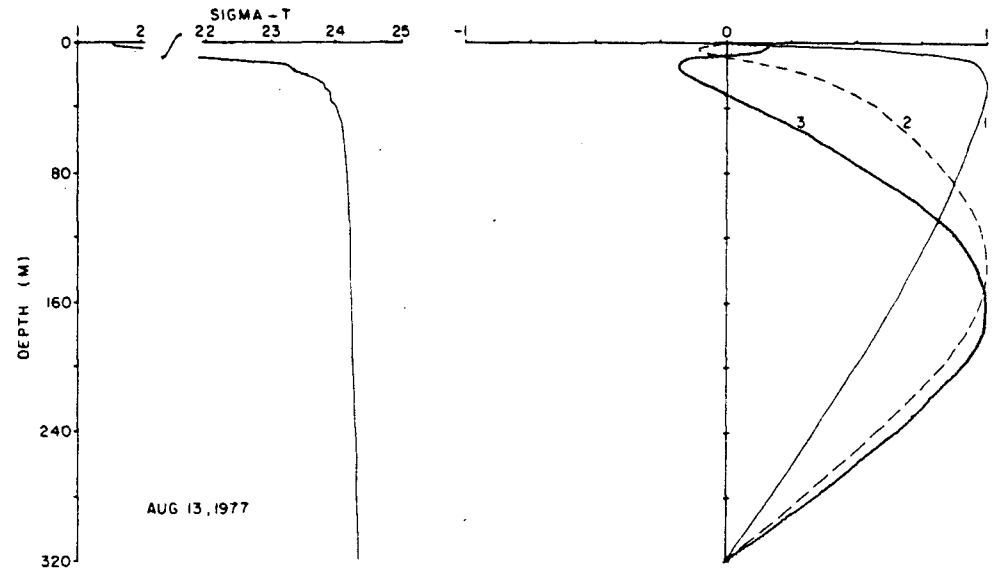

Figure 85 Farmer and Smith's density profile and w-eigenfunctions.
Phase speeds: $c_1 = 98\,cm/s$, $c_2 = 41\,cm/s$, $c_3 = 33\,cm/s$. (From Farmer and Smith 1980.)

Blackford (1984) also proposes the same argument in favour of a predominantly mode 2 response, based upon the same normal modes. He also cites the zero crossing in the mode 2 u-eigenfunction at 136 m as an explanation for the 180° phase shift in the baroclinic component of the longitudinal velocity between 75 m and 300 m found by Farmer and Freeland (1983). A predominantly mode 1 response would not produce this 180° phase shift, because the mode 1 u-eigenfunction has a zero crossing at 24 m. (Note that extrema in the w-eigenfunctions correspond to zero crossings in the u-eigenfunctions.)

However, inspection of *Figure 76* reveals zero crossings in the u-eigenfunctions at 75 m for mode 1, and at 126 m and 4 m for mode 2. This change of the shape would partially invalidate the preceding arguments, because the sill crest would now be at the same depth as the mode 1 maximum in w-eigenfunction, and because a mode 1 with a u-eigenfunction zero crossing below 75m is capable of producing the 180° phase shift between 75m and 300m on its own. How can the deepening of the mode 1 zero crossing from Farmer and

Smith's 24 m to this value of 75 m be explained? The obvious answer is that the N^2-profile taken in 1977 used by Farmer and Smith is different from the one taken in 1983 by the cyclesonde.

In an attempt to understand how the N^2-profile affects the shape of the normal modes, two simple models were investigated. The first model consisted of two layers of constant N^2 so that the density profile was made up of two linear segments which matched at the interface. The upper layer was of thickness h_1 with $N = N_1$, and the lower layer was of thickness h_2 with $N = N_2$. The second model consisted of a well mixed surface layer of constant density (so that $N = 0$), overlying the remainder of the water column which had a constant N value. There was a density jump of $\Delta\rho$ at the interface. In both models an asymptotic expansion was used, assuming that the ratio ε of the lower layer N value to the mean upper layer N value (including any density jump at the interface) was small.

The details of the theory are presented in Appendices A1 and A2. In the first model the eigenfunctions could be categorized into so-called α-modes and β-modes. α can be any non-negative integer, and β can be any positive integer. β-modes are due to the lower layer stratification, since their $O(1)$ phase speed $c^0 = \frac{N_2 h_2}{\beta\pi}$ only depends on $N_2 h_2$. α-modes are associated with the upper layer stratification, since their $O(1)$ phase speed $c^0 = \frac{N_1 h_1}{(\alpha+\frac{1}{2})\pi}$ only depends on $N_1 h_1$. The n^{th} mode can be either an α-mode or a β-mode, since its phase speed is the n^{th} element of the ranked series of the two sets of phase speeds. In the second model the α-modes are replaced by a single surface mode. The surface mode is associated with the density jump at the interface, and to $O(1)$ has a phase speed of $\sqrt{g' h_1}$, where $g' \equiv g\Delta\rho_0/\bar{\rho}_0$ is the reduced gravity. As before, the n^{th} mode could either be one of the β-modes or the surface mode. However, in the summer the first mode is most likely to be the surface mode or the $\alpha = 0$ mode.

The phase speeds and zero crossing depths of Farmer and Smith's normal modes and those shown in *Figure 76* can be interpreted in terms of the model profiles described in Appendices A1 and A2. Farmer and Smith obtained phase speeds of 0.98, 0.41 and

$0.33\,m/sec$ for the first three modes. The fact that $0.98 \approx 3 \times 0.33$ is entirely consistent with the first and third modes being $\alpha = 0$ and $\alpha = 1$ modes respectively, for which the $O(1)$ phase speeds are $\frac{2N_1h_1}{\pi}$ and $\frac{2N_1h_1}{3\pi}$. This gives a value of $N_1h_1 = 1.54\,m/sec$. The second mode must therefore be the $\beta = 1$ mode, which has a $O(1)$ phase speed of $\frac{N_2h_2}{\pi}$, giving $N_2h_2 = 1.29\,m/sec$. Given a total density drop of $\Delta\rho = 22\,kg/m^3$ across the upper layer (from $\sigma_t = 24$ below the surface layer to $\sigma_t \approx 2$ at the surface), values of $h_1 = 11\,m$, $h_2 = 309\,m$, $N_1 = 0.14\,s^{-1}$, and $N_2 = 0.0042\,s^{-1}$ can then be deduced for the individual parameters.

The same procedure can then be applied to the normal modes in *Figure 76*, where the phase speeds are 0.80, 0.51 and $0.32\,m/sec$. It is less obvious this time which modes are α-modes, because neither $0.80 = 3 \times 0.32$ (if the first and third modes were α-modes) nor $0.51 = 2 \times 0.32$ (if the second and third modes were β-modes). However, assuming the first mode to be the $\alpha = 0$ mode, $N_1h_1 = 1.26\,m/sec$ is obtained, and assuming the second mode to be the $\beta = 1$ mode, $N_2h_2 = 1.60\,m/sec$ is obtained. Again $\Delta\sigma_t = 22$, gives $h_1 = 7.5\,m$, $h_2 = 312.5\,m$, $N_1 = 0.16\,s^{-1}$, and $N_2 = 0.0052\,s^{-1}$. However, if the third mode is used to calculate N_1h_1 assuming it to be the $\alpha = 1$ mode, then $N_1h_1 = 1.51m/sec$, $h_1 = 11\,m$ and $N_1 = 0.14\,s^{-1}$ are obtained, which are the same as calculated for Farmer and Smith.

It was therefore hypothesised that the most important difference between Farmer and Smith's profile and the *Figure 76* profile was in the lower layer stratification. *Figures 86–88* show plots of the phase speeds and zero crossing depths as a function of N_2 for the first three modes, keeping $h_1 = 11\,m$, $h_2 = 309\,m$, and $N_1 = 0.14\,s^{-1}$ constant. The vertical dashed lines indicate transitions from α-modes to β-modes; for example, mode 2 could either be the $\alpha = 1$ mode or the $\beta = 1$ mode depending on the value of N_2. The horizontal dashed line indicates the depth of the interface between the two layers. The solid curves are solutions to the full non-linear dispersion relation (equation A4), whereas the short dashed curves are the $O(1)$ terms in the asymptotic expansion. (Note that the classification of modes into α-modes and β-modes is not possible without the asymptotic

expansion.) The phase speeds and zero crossing depths are marked by circles for Farmer and Smith's profile, and by triangles for the *Figure 76* profile.

This simple model explains the main differences between the Farmer and Smith modes and the *Figure 76* modes well:

(i) The mode 1 zero crossing is deeper in *Figure 76* ($75\,m$) than in the Farmer and Smith mode 1 ($24\,m$) because the former has a stronger lower layer stratification (i.e. larger N_2). The zero crossing is pulled down below the interface to a value of $z = \frac{N_1 h_1}{N_2}$ when $\frac{N_2 h_2}{N_1 h_1} > 1$ (see *Figure 116*). This also occurs in model 2 when $\frac{2N_2 h_2}{\pi\sqrt{g' h_1}} > 1$ (see *Figure 119*). Therefore in *both* models, the criterion for the mode 1 zero crossing to be pulled down below the interface is $\frac{2c_2}{c_1} > 1$. For Farmer and Smith this ratio is 0.84, whereas in *Figure 76* it is 1.27.

(ii) The mode 2 phase speed is smaller for Farmer and Smith because of their weaker lower layer stratification. Mode 2 is the $\beta = 1$ mode, for which the $O(1)$ phase speed is given by $\frac{N_2 h_2}{\pi}$. This argument also applies for model 2.

(iii) The higher mode 1 phase speed for Farmer and Smith can only be explained by a stronger surface layer stratification. This phase speed is given by $\frac{2N_1 h_1}{\pi}$ for model 1, or $\sqrt{g' h_1}$ for model 2.

The weaker lower layer statification used by Farmer and Smith can be seen by comparing the density gradients at depth from the density profiles. In Farmer and Smith's profile, the density changes by $0.55\,kg/m^3$ between $20\,m$ and $170\,m$ (an average N value of $0.0059\,s^{-1}$), whereas in the profiles in *Figure 70* the corresponding density change is $1.07\,kg/m^3$ (an average N value of $0.0083\,s^{-1}$).

These simple models of the stratification help to conceptualise statements like "a mode 2 eigenfunction for the summer is very similar to a mode 1 eigenfunction for November below the top few meters" (Farmer and Smith 1980a, p240), because with the disappearance of the fresh surface layer in the winter, the phase speed of the "surface mode" (model 2),

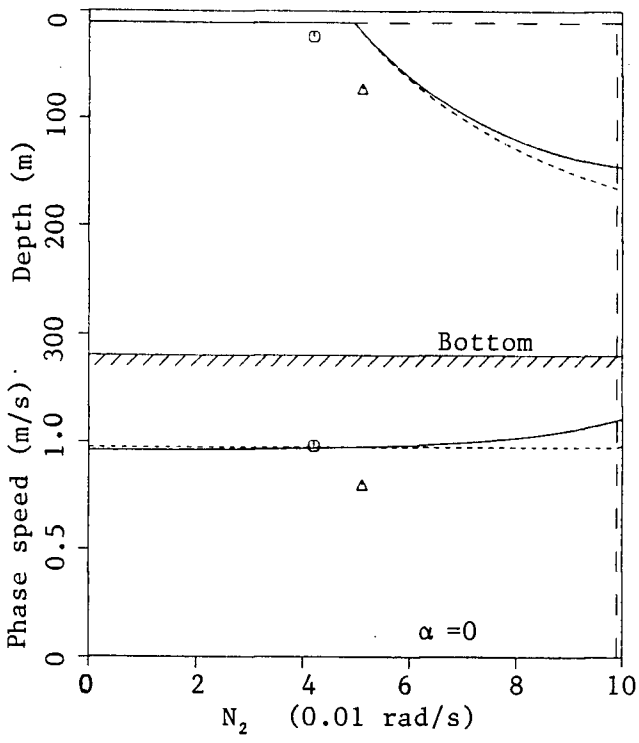

Figure 86 Mode 1 phase speed and zero crossing depth vs N_2. See text for explanation.

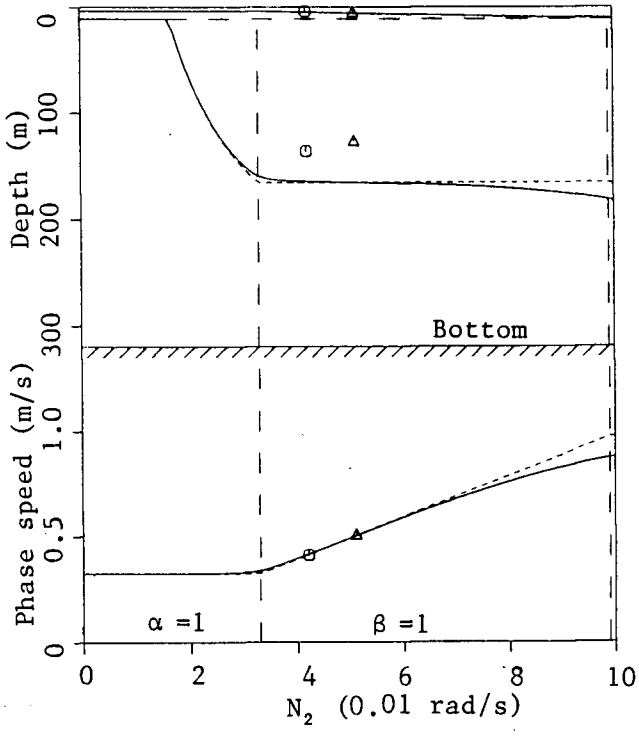

Figure 87 Mode 2 phase speed and zero crossing depths vs N_2.

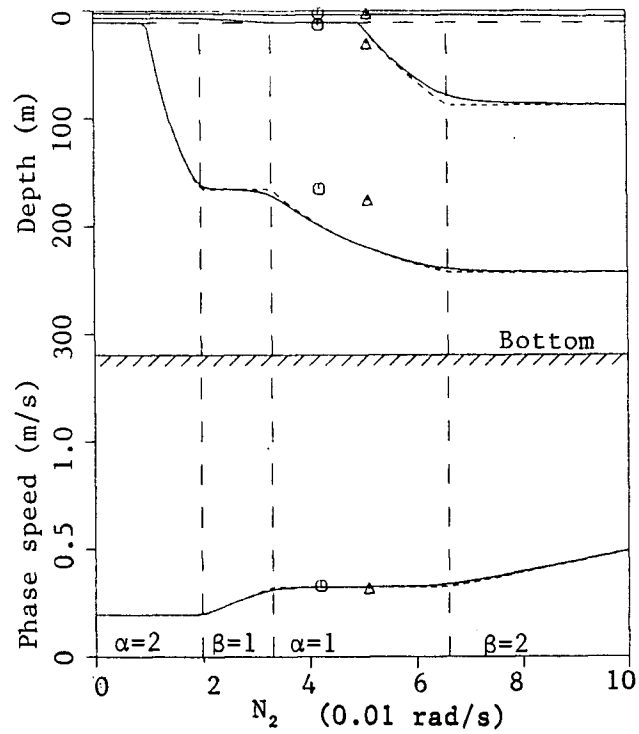

Figure 88 Mode 3 phase speed and zero crossing depths vs N_2.

or the $\alpha = 0$ mode (model 1), drops off to a value that is lower than the phase speed of the first "lower layer mode" $\beta = 1$, causing this mode to become mode 1. Hence the $\beta = 1$ mode is mode 1 in the winter, yet it is mode 2 in the summer.

It is obvious from this discussion that small values of N at depth cannot be neglected when calculating normal modes, for it is the depth-integrated value $N_2 h_2$ that is important, not N_2 itself. N_2 may be very small compared to the surface value of N, but it maintains this small value over a great depth range, and $N_2 h_2$ is *not* small. Therefore when taking CTD casts it is preferable to lower the instrument to the bottom rather than assuming that the density changes at great depth are so small that it is not worth the time to go that far. This error was made in our CTD casts in Knight Inlet, where the instrument was never lowered any further than $200\,m$. To make up for this missing data, a linear extrapolation of $log_{10} N^2$ had to be made to the bottom.

To summarise this section, it has been shown that the differences between the normal modes of Farmer and Smith (1980a) and those in *Figure 76* can be explained by the

differences in the N^2-profile used; specifically Farmer and Smith used a stronger upper layer stratification and a weaker deep-water stratification. In the mode fitting that follows, the normal modes shown in *Figures 77-84* will be used, since they were calculated using 1983 data.

3.11 Results of the Normal Mode Fitting

Having gained some confidence in the correctness of the calculated normal modes, the results of fitting them to the observed profiles of complex amplitudes of u- and ρ-oscillations can be discussed. The statistical model described by equations 3.33–3.36 was used at the Tomakstum Island stations, and that described by equations 3.29–3.30 at the remaining stations. In both cases, a pre-programmed least-squares fitting routine was used to yield estimates of $\mathbf{A}_n^{up}$ and $\mathbf{A}_n^{down}$ for each of the modes. The pre-programmed subroutine fitted real functions to real functions, so the real and imaginary parts of $\mathbf{A}_n^{up}$ and $\mathbf{A}_n^{down}$ were solved for simultaneously as real numbers. The complex amplitude profiles from the month of September 1983 were used at each station, because there were data from both sides of the channel at Tomakstum Island, and that month was representative of the other months at the other stations. However, the July 1983 data was used at Lull Bay because there were no data from that station in September 1983.

Mode 1 strongly resembles mode 2 below 20 m. Except for the fact that mode 1 has a zero crossing in the u-eigenfunction at around 75 m and that mode 2 has a zero crossing at around 125 m their shapes are very similar. It is therefore very difficult for the fitting routine to separate mode 1 from mode 2. Likewise, modes 0 and 1 have a similar ρ-eigenfunction shape, although this is not such a problem because the amplitude and phase of the barotropic component are fixed by other considerations (see Section 3.6). *Table 4* gives the correlations

$$r_{mn}^{u} = \frac{\int_0^{H-20m} \hat{u}_m(z)\,\hat{u}_n(z)\,dz}{\sqrt{\left\{\int_0^{H-20m} \hat{u}_m^2(z)\,dz\right\}\,\left\{\int_0^{H-20m} \hat{u}_n^2(z)\,dz\right\}}} \tag{3.53}$$

where

$$\hat{u}_n(z) = u_n(z) - \frac{1}{H - 20m} \int_0^{H-20m} u_n(\xi)\, d\xi, \tag{3.54}$$

and r^{ρ}_{mn} (defined similarly) between the eigenfunctions at each of the stations. The correlation between the mode 1 and mode 2 u-eigenfunctions is always at least 0.96!

Table 4
Correlations between the modes below 20 m at each station

	u-eigenfunctions					ρ-eigenfunctions			
Mode	1	2	3	4	*Mode*	1	2	3	4
Protection Point									
0	0.881	0.772	-0.080	-0.734	0	0.979	0.112	-0.937	-0.501
1	1.000	0.975	0.338	-0.451	1	1.000	0.312	-0.873	-0.596
2		1.000	0.537	-0.268	2		1.000	0.141	-0.476
3			1.000	0.625	3			1.000	0.549
Lull Bay									
0	0.859	0.810	0.456	-0.346	0	0.996	0.816	-0.918	-0.945
1	1.000	0.986	0.715	-0.124	1	1.000	0.862	-0.886	-0.943
2		1.000	0.822	0.039	2		1.000	-0.542	-0.760
3			1.000	0.596	3			1.000	0.930
Tomakstum Island									
0	0.816	0.690	-0.801	-0.742	0	0.995	0.766	-0.993	0.082
1	1.000	0.978	-0.508	-0.934	1	1.000	0.833	-0.998	-0.020
2		1.000	-0.318	-0.892	2		1.000	-0.828	-0.574
3			1.000	0.620	3			1.000	0.022
Adeane Point									
0	0.598	0.452	-0.682	-0.478	0	0.993	0.230	-0.970	0.313
1	1.000	0.964	-0.881	-0.968	1	1.000	0.343	-0.992	0.200
2		1.000	-0.729	-0.966	2		1.000	-0.460	-0.846
3			1.000	0.832	3			1.000	-0.074

As was shown in Section 3.5.1, the fitting of u-eigenfunctions to observed profiles for mid-channel stations yields the sum $(\mathbf{A}_n^{up} + \mathbf{A}_n^{down})$, whereas the fitting of ρ-eigenfunctions yields the difference $(\mathbf{A}_n^{up} - \mathbf{A}_n^{down})$. If both mode 1 and mode 2 were included in the fit, the coefficients $(\mathbf{A}_n^{up} + \mathbf{A}_n^{down})$ of the u-eigenfunctions would be expected to be very large and differing by 180° in phase, so that the mode 1 and mode 2 u-eigenfunctions would almost cancel each other out (analogous to including two constituents in a harmonic analysis that are too close together in frequency). If the ρ-eigenfunction fit yields reasonably small values for $(\mathbf{A}_n^{up} - \mathbf{A}_n^{down})$, then this leads to very large magnitudes for $\mathbf{A}_n^{up}$ and $\mathbf{A}_n^{down}$,

with $\mathbf{A}_n^{up} \approx \mathbf{A}_n^{down}$.

This was, in fact, observed to happen whenever both mode 1 and mode 2 were included in the fit, even at Tomakstum Island where information on the cross-channel structure could be incorporated. *Tables 5–7* show the results of a series of fits at each station. The different fits arise by excluding various combinations of modes from the analysis by deleting those modes from the set of basis functions to be fitted to the observations. A blank entry in any table means that the corresponding mode was excluded from the set of basis functions, so that its amplitude can be taken to be zero. *Table 5* gives the amplitudes a_n^{up} and a_n^{down}, and *Table 6* gives the phases ϕ_n^{up} and ϕ_n^{down} of the fitted waves. The normalisation constant U_0 for each eigenfunction was such that the a_n values are amplitudes of the dimensional eigenfunctions given in *Figures 77-84*. The energy density E' of equation 3.47 is the same for each mode in those figures. *Table 7* gives the energy fluxes in Megawatts as calculated using equation 3.47, integrating over the whole water column (note: $Flux = E' c_n$). It should be noted that the fluxes are only the M_2 component of the total flux of the internal tide, and that there will be a small but significant S_2 component.

What are considered to be the most accurate and consistent estimates from the various fits are italicised in *Tables 5–7*. The values in italics were then averaged to give best estimates of the values in each mode at the various stations. These best estimates are given in the last column of the tables.

The rows in *Table 7* labelled "Residual sum sqs" contain estimates of the residual errors. They are the sum of squares of the residuals divided by the number of equations minus the number of unknowns, i.e. they are the mean squared distance of the observed points in the complex plane from the fitted points. It was necessary to assign an equivalency between "velocity distances" and "density distances", which is the same as assigning a weight to u-observations relative to ρ-observations. This equivalency was chosen so that $20\,cm/s$ of "velocity distance" is the same as $0.4\,kg\,m^{-3}$ of "density distance". This equivalency was used in *Figures 53–56*.

The inclusion of more basis functions in the fit leads to a smaller residual sum of squares, but also increases the possibility of meaningless results because of degenerate basis functions. Thus there is a trade-off between goodness-of-fit and robustness in the derived coefficients. The approach used was to find the smallest set of modes that was sufficient to give an acceptable fit to the data.

Table 5
Results of the fitting — non-dimensional amplitudes a_n^{up} and a_n^{down}

Fit #	1	2	3	4	5	6	7*	*Best estimate*
Protection Point								
Up-inlet mode 0	26.04	26.04	26.04	26.04	26.04	26.04		26.0
1	5.05	–	–	–	–	–		?
2	5.42	–	7.95	*8.04*	–	–		8.0
3	1.47	–	1.64	*4.56*	–	–		4.6
4	–	–	0.94	–	–	–		?
Down-inlet mode 0	26.04	26.04	26.04	26.04	26.04	26.04		26.0
1	19.17	20.01	–	–	–	–		?
2	6.40	7.25	13.43	*9.59*	8.81	13.57		9.6
3	6.59	6.09	9.13	*3.84*	3.91	10.65		3.8
4	–	–	5.98	–	–	7.82		?
Lull Bay								
Up-inlet mode 0	29.90	29.90	29.90	29.90	29.90	29.90		29.9
1	27.11	–	–	–	–	–		?
2	10.93	–	10.10	*6.91*	–	–		6.9
3	7.66	–	13.56	*3.93*	–	–		3.9
4	–	–	6.22	–	–	–		?
Down-inlet mode 0	29.90	29.90	29.90	29.90	29.90	29.90		29.9
1	21.64	9.05	–	–	–	–		?
2	6.41	12.02	9.71	*9.04*	10.39	16.09		9.0
3	14.54	2.59	5.12	*6.26*	4.58	15.69		6.3
4	–	–	3.68	–	–	9.82		?
Tomakstum Island								
Up-inlet mode 0	21.41	21.41	21.41	21.41	21.41	21.41	21.41	21.4
1	27.82	*7.94*	–	–	–	–	–	7.9
2	0.46	*10.54*	6.43	9.33	*9.08*	*6.96*	*6.98*	8.8
3	7.21	*5.91*	7.16	7.33	*7.90*	*8.46*	*8.37*	7.7
4	–	–	4.61	–	–	*4.73*	*4.52*	4.6
Down-inlet mode 0	21.41	21.41	21.41	21.41	21.41	21.41	21.41	21.4
1	29.30	–	–	–	–	–	–	0
2	7.80	–	3.67	2.09	–	–	–	0
3	4.32	–	1.37	1.84	–	–	–	0
4	–	–	4.82	–	–	–	–	0
Adeane Point								
Up-inlet mode 0	14.16	14.16	14.16	14.16	14.16	14.16	14.16	14.2
1	8.30	*1.41*	–	–	–	–	–	1.4
2	6.26	*3.99*	3.59	3.55	*3.41*	*3.21*	*1.04*	2.9
3	2.90	*2.25*	2.23	2.10	*1.98*	*2.05*	*1.95*	2.0
4	–	–	1.61	–	–	*0.87*	*0.00*	0.4
Down-inlet mode 0	14.16	14.16	14.16	14.16	14.16	14.16	14.16	14.2
1	11.50	–	–	–	–	–	–	0
2	5.07	–	0.18	0.77	–	–	–	0
3	2.94	–	0.50	0.38	–	–	–	0
4	–	–	0.58	–	–	–	–	0

* Phase differences fixed.

Table 6
Results of the fitting — phases ϕ_n^{up} and ϕ_n^{down} in degrees

Fit #	1	2	3	4	5	6	7*	*Best estimate*
Protection Point								
Up-inlet mode 0	20	20	20	20	20	20		20
1	169	–	–	–	–	–		?
2	254	–	211	*198*	–	–		198
3	216	–	342	*315*	–	–		315
4	–	–	238	–	–	–		?
Down-inlet mode 0	226	226	226	226	226	226		226
1	320	332	–	–	–	–		?
2	122	178	328	*334*	311	317		334
3	344	349	120	*102*	124	139		102
4	–	–	317	–	–	327		?
Lull Bay								
Up-inlet mode 0	22	22	22	22	22	22		22
1	350	–	–	–	–	–		?
2	186	–	337	*320*	–	–		320
3	351	–	179	*171*	–	–		171
4	–	–	359	–	–	–		?
Down-inlet mode 0	224	224	224	224	224	224		224
1	156	83	–	–	–	–		?
2	303	203	170	*180*	179	163		180
3	166	155	234	*183*	230	302		183
4	–	–	141	–	–	139		?
Tomakstum Island								
Up-inlet mode 0	24	24	24	24	24	24	24	24
1	306	*192*	–	–	–	–	–	192
2	299	*320*	287	297	*302*	*294*	*298*	303
3	0	*55*	17	43	*42*	*31*	*32*	40
4	–	–	140	–	–	*147*	*144*	145
Down-inlet mode 0	222	222	222	222	222	222	222	222
1	332	–	–	–	–	–	–	
2	151	–	71	7	–	–	–	
3	357	–	292	133	–	–	–	
4	–	–	102	–	–	–	–	
Adeane Point								
Up-inlet mode 0	26	26	26	26	26	26	26	26
1	332	*20*	–	–	–	–	–	20
2	175	*186*	176	193	*183*	*178*	*111*	164
3	331	*328*	307	311	*316*	*307*	*306*	314
4	–	–	96	–	–	*53*		53
Down-inlet mode 0	220	220	220	220	220	220	220	220
1	316	–	–	–	–	–	–	
2	129	–	70	95	–	–	–	
3	313	–	318	25	–	–	–	
4	–	–	286	–	–	–	–	

* Phase differences fixed.

Table 7
Results of the fitting — energy fluxes in MW

Fit #	1	2	3	4	5	6	7*	*Best estimate*
Protection Point								
Up-inlet mode 0	610.3	610.3	610.3	610.3	610.3	610.3		610
1	0.181	–	–	–	–	–		?
2	0.143	–	0.310	*0.317*	–	–		0.32
3	0.007	–	0.009	*0.070*	–	–		0.07
4	–	–	0.002	–	–	–		?
Down-inlet mode 0	610.3	610.3	610.3	610.3	610.3	610.3		610
1	2.655	2.893	–	–	–	–		?
2	0.200	0.258	0.884	*0.451*	0.380	0.902		0.45
3	0.146	0.125	0.281	*0.050*	0.051	0.381		0.05
4	–	–	0.096	–	–	0.167		?
Residual sum sqs.	0.112	4.134	1.384	2.435	8.305	5.366		
Lull Bay								
Up-inlet mode 0	667.9	667.9	667.9	667.9	667.9	667.9		668
1	5.412	–	–	–	–	–		?
2	0.489	–	0.440	*0.206*	–	–		0.21
3	0.175	–	0.551	*0.046*	–	–		0.05
4	–	–	0.096	–	–	–		?
Down-inlet mode 0	667.9	667.9	667.9	667.9	667.9	667.9		668
1	3.449	0.603	–	–	–	–		?
2	0.178	0.623	0.396	*0.352*	0.466	1.117		0.35
3	0.633	0.020	0.078	*0.117*	0.063	0.738		0.12
4	–	–	0.034	–	–	0.239		?
Residual sum sqs.	0.512	5.101	0.700	1.125	5.272	3.748		
Tomakstum Island								
Up-inlet mode 0	682.7	682.7	677.6	677.6	677.6	677.6	677.6	680
1	8.062	*0.656*	–	–	–	–	–	0.66
2	0.001	*0.748*	0.278	0.355	*0.554*	*0.325*	*0.327*	0.49
3	0.231	*0.155*	0.227	0.238	*0.276*	*0.317*	*0.310*	0.26
4	–	–	0.075	–	–	*0.079*	*0.072*	0.08
Down-inlet mode 0	682.7	682.7	677.6	677.6	677.6	677.6	677.6	680
1	8.938	–	–	–	–	–	–	0
2	0.410	–	0.090	0.029	–	–	–	0
3	0.083	–	0.008	0.015	–	–	–	0
4	–	–	0.082	–	–	–	–	0
Residual sum sqs.	1.091	4.665	2.137	3.681	4.867	3.255	3.256	
Adeane Point								
Up-inlet mode 0	568.0	568.0	565.1	565.1	565.1	565.1	565.1	566
1	1.182	*0.034*	–	–	–	–	–	0.03
2	0.459	*0.187*	0.151	0.147	*0.136*	*0.121*	*0.013*	0.11
3	0.064	*0.039*	0.038	0.033	*0.030*	*0.032*	*0.029*	0.03
4	–	–	0.016	–	–	*0.004*	*0.000*	0.00
Down-inlet mode 0	568.0	568.0	565.1	565.1	565.1	565.1	565.1	566
1	2.268	–	–	–	–	–	–	0
2	0.301	–	0.001	0.007	–	–	–	0
3	0.066	–	0.002	0.001	–	–	–	0
4	–	–	0.002	–	–	–	–	0
Residual sum sqs.	0.065	0.193	0.087	0.147	0.214	0.176	0.183	

3.11.1 Results of the Fitting at Stations Up-inlet of the Sill

The first column in each table refers to Fit #1, where the first three internal modes in both directions were included. As expected, mode 1 has a very large amplitude both up-inlet and down-inlet, and the up-inlet wave is often in phase with the down-inlet wave. This is a symptom of degenerate basis functions. It was therefore necessary to remove either mode 1 or mode 2 from the fit, or to introduce more information in the form of phase speeds in order to resolve them.

In an attempt to exploit the difference in phase speeds between the two modes, the least squares fit was done simultaneously at Tomakstum Island and Adeane Point, and the phase difference of the up-inlet wave between the two stations was constrained to be $d\omega/\bar{c}_n$, where $d = 11.2\,km$ is the distance between the two stations and $1/\bar{c}_n$ is the average inverse phase speed of the n^{th} mode over the two stations (a crude WKB approximation). For $\bar{c}_1 = 83\,cm/s$ this phase difference is 108°, whereas for $\bar{c}_2 = 50\,cm/s$ it is 188°. The same procedure could not be applied to the down-inlet waves, because it is not known *a priori* how much of the up-inlet wave is reflected by the bend which is half-way between the two stations, so some of the down-inlet wave at Tomakstum Island could be a reflection from the bend and some could have propagated around the bend from Adeane Point. It is not even clear how the phases of the up-inlet waves are affected by passage around the bend unless the results of Chapter 2 are accepted. Despite this objection, the procedure was attempted on the up-inlet waves using a sophisticated least-squares fitting routine with non-linear constraints. Unfortunately, this additional information was insufficient to resolve the two modes, and similar results to Fit #1 were obtained.

Following these two failures, it was decided to exclude mode 1 from the fit in order to try to remove the degeneracy between modes 1 and 2. This step can be justified by assuming that mode 1 is mostly a surface phenomenon due to the fresh upper layer, and it does not manifest itself a great deal below $20\,m$. To illustrate this point, *Figure 76* shows that if the surface peak in the mode 1 u-eigenfunction takes a value of $1\,m/sec$, then the function has dropped to $10\,cm/s$ at $20\,m$. However, if the surface peak in the mode 2

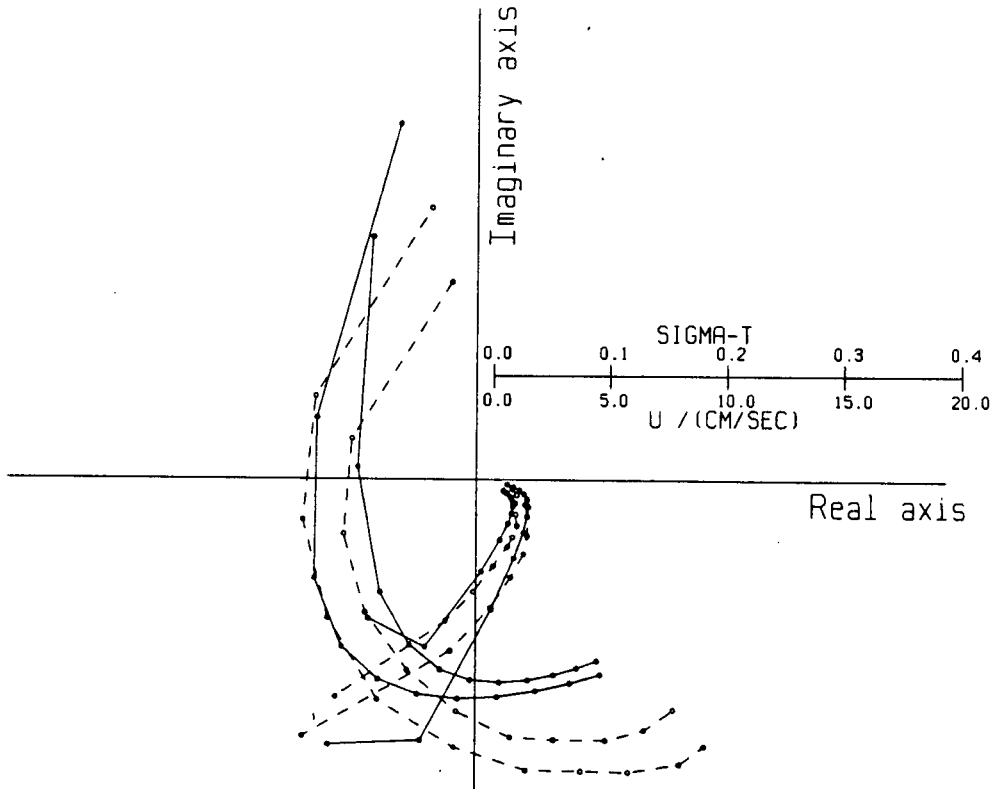

Figure 89 Results of Fit #6 at Tomakstum Island.
Dashed lines = observed, solid lines = fitted. (c.f. *Figure 55.*)

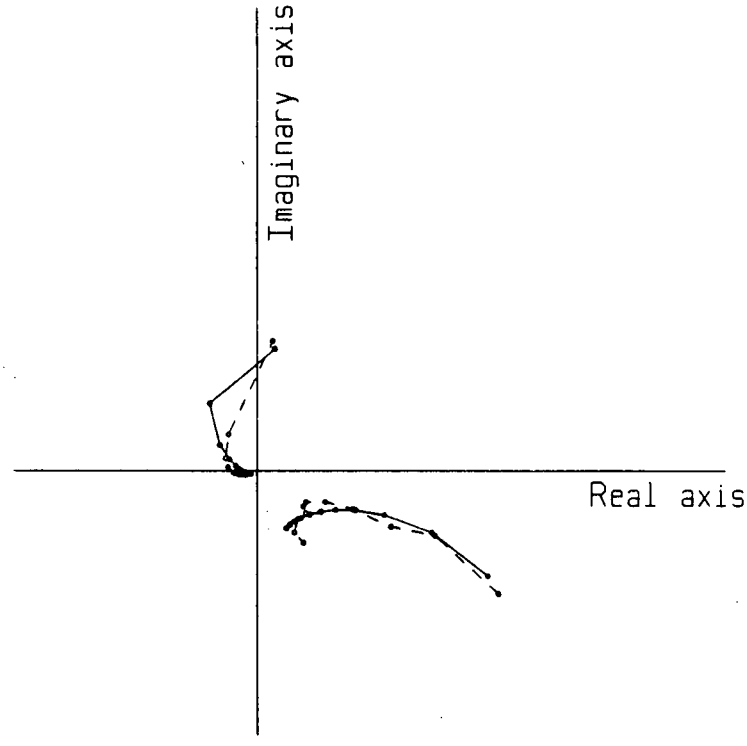

Figure 90 Results of Fit #6 at Adeane Point. (c.f. *Figure 56.*)

u-eigenfunction has the same amplitude, then the function has only dropped to $60\,cm/s$ at $20\,m$. In other words, currents at the surface are 10 times the currents at $20\,m$ for mode 1, whereas they are only twice as big for mode 2. If the total surface current is to be kept to a reasonable value, say $< 1\,m/sec$ (Pickard and Rogers 1959), then the mode 1 currents at $20\,m$ and below must be small. Farmer and Smith also argue in favour of mode 2 dominating mode 1, as does Blackford. However, their arguments are based on the shapes of the eigenfunctions in 1977, which have been shown to be different in 1983. This assumption of mode 1 having a negligible manifestation below $20\,m$ is compatible with the existence of a significant mode 1 energy flux, which would be mostly in the upper layer.

The results obtained by excluding mode 1 from a bi-directional fit are much improved over the full bi-directional fit. The amplitudes of the various waves are more reasonable, and the energy fluxes are in the correct direction — for example, there are no longer greater down-inlet fluxes than up-inlet fluxes as there were in Fit #1. These results are given under columns #3 and #4. Fit #3 includes modes 2, 3 and 4, whereas Fit #4 only includes modes 2 and 3. They show that there is indeed a much greater up-inlet flux at Tomakstum Island than down-inlet flux, which is consistent with the very low reflection coefficients found in Chapter 2.

To obtain more accurate estimates of the up-inlet energy fluxes at Tomakstum Island and Adeane Point, the down-inlet waves were specifically excluded from the fit (as in Fits #2, #5, #6 and #7), now that the reflection coefficient at the bend can be taken to be small. In Fit #2 modes 1, 2 and 3 were included, in Fit #5 modes 2 and 3 were included, and in Fit #6 modes 2, 3 and 4 were included. The fits were acceptable in all three cases. In Fit #2 modes 1 and 2 were successfully resolved by their different ρ-eigenfunctions. This was not possible in the bi-directional fit because the density information was being used to resolve the direction of propagation. Fit #2 gives supporting evidence for a dominantly mode 2 response, since the amplitude of the mode 2 up-inlet wave is greater than the mode 1 up-inlet wave. *Figures 89* and *90* show that it is possible to obtain adequate fits using only up-inlet propagating modes 2, 3 and 4. The fit is only marginally worse when mode

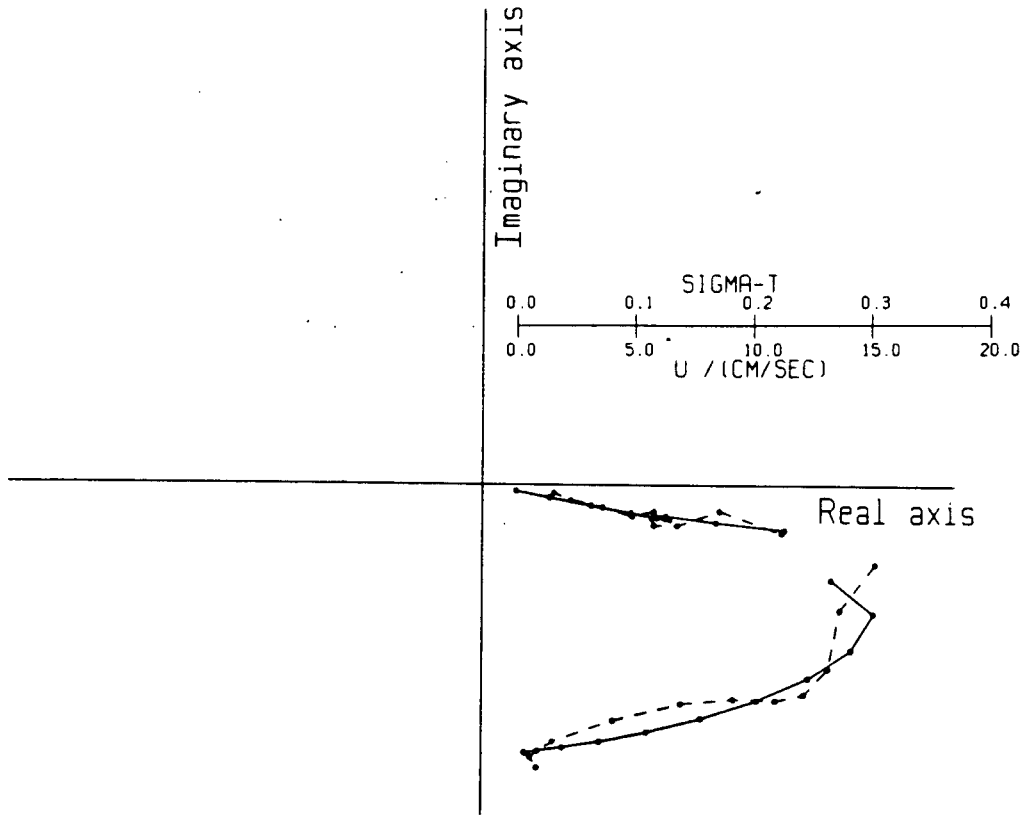

Figure 91 Results of Fit #4 at Lull Bay.
Dashed lines = observed, solid lines = fitted. (c.f. *Figure 54.*)

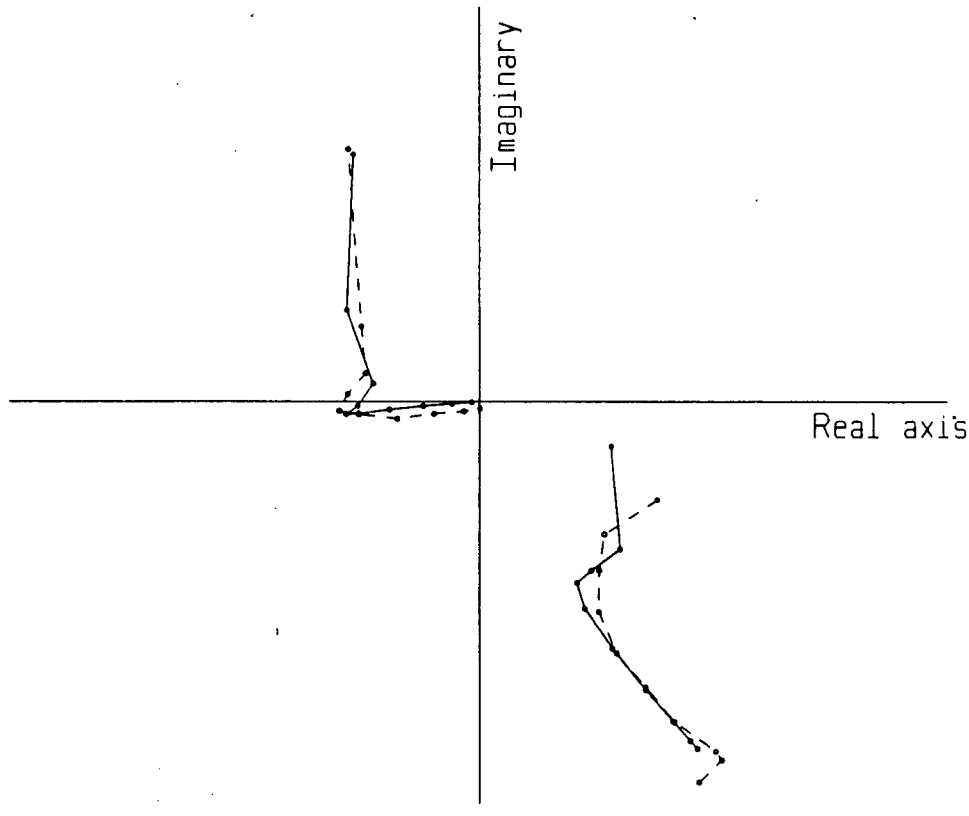

Figure 92 Results of Fit #4 at Protection Point. (c.f. *Figure 53.*)

4 is dropped. In Fit #7 the phase difference constraint described earlier was also imposed without much loss of goodness-of-fit. These four fits show that the data are compatible with the idea of zero reflection from the bend.

3.11.2 Results of the Fitting at Stations Down-inlet of the Sill

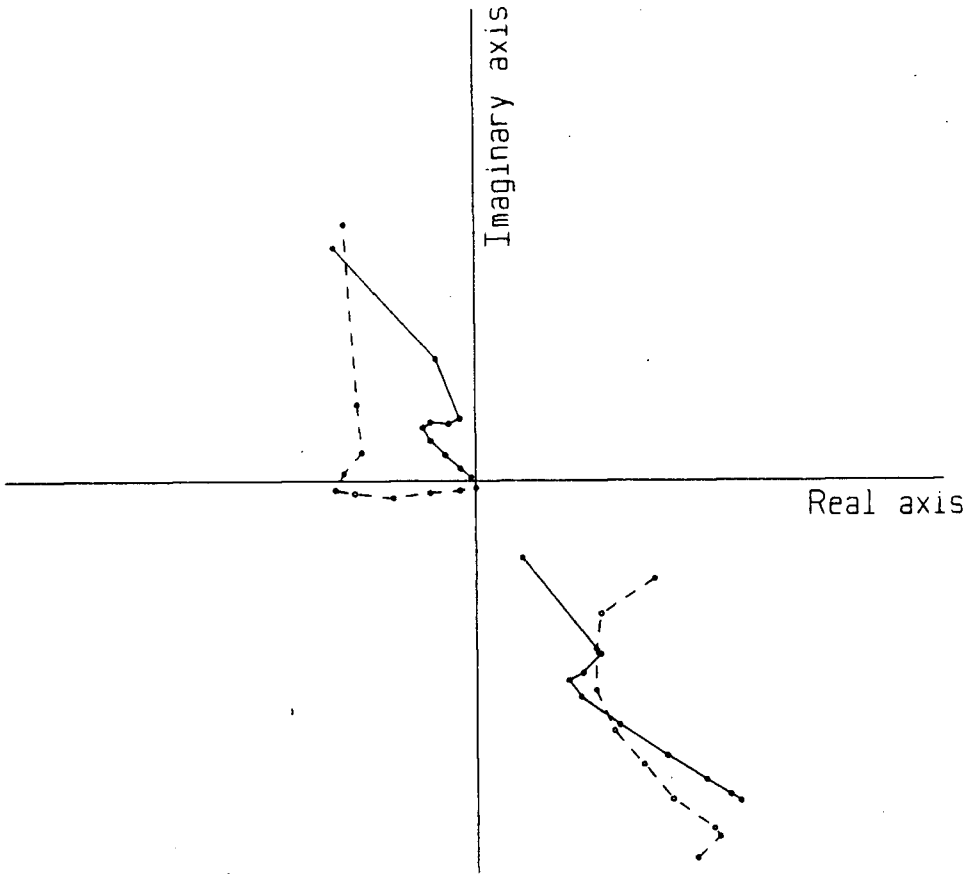

Figure 93 Results of Fit #6 at Protection Point.
Dashed lines = observed, solid lines = fitted. (c.f. *Figure 53.*)

Again, Fit #1 gives unacceptable results, with unreasonably large coefficients (although the fits are good). The exclusion of mode 1, as in Fits #3 and #4, removes the degeneracy while still maintaining an acceptable goodness-of-fit, as shown in *Figures 91* and *92*. However, unlike at Tomakstum Island and Adeane Point, the results of Fits #3 and #4 do *not* justify the exclusion of waves propagating towards the sill, since the amplitudes of

the up-inlet waves are comparable to those of the down-inlet waves. The results of the uni-directional fits at Protection Point and Lull Bay are given under columns #2, #5 and #6, but are not considered to be useful. The residual sums of squares in *Table 7* show that the fits are worse for the uni-directional fits than for the bi-directional fits. *Figure 93* is an example of an unacceptable fit arising from the exclusion of up-inlet waves at Protection Point.

These results indicate a *second source of internal tide seaward of Protection Point.* Indeed, when the longitudinal depth profile of the inlet is studied, a secondary sill can be seen. Its slightly gentler bottom slope can be compensated by its stronger barotropic velocities in terms of its internal tide generating potential.

3.12 Comparison of Fluxes with Stacey's Model

Stacey (1984, 1985) developed a simple linear model of internal tide generation by the sill of an inlet to estimate the energy flux in each mode. The model was proposed by Stigebrandt (1976, 1980) with a linear density profile, but Stacey modified it for the case of arbitrary stratification. The sill is modeled by a vertical wall, and the bottom is assumed to be flat on either side of it, although not necessarily at the same depth on both sides. The velocity field in the vicinity of the sill is expressed as a sum of normal modes, and the crux of the model is to make the horizontal velocity at the sill vanish below sill depth, and equal to a constant barotropic value above sill depth. He obtained the formula

$$\varepsilon_n = \frac{\bar{\rho}_0 W c_n U_{bt}^2 Z_n^2(-d)}{2\int_0^H Z_n'^2\, dz} \tag{3.55}$$

where ε_n is the energy flux away from the sill in the n^{th} mode,

d is the depth of the sill crest,

U_{bt} is the barotropic tidal velocity amplitude over the sill,

and H is the depth of water next to the sill.

The calculation of the normal modes Z_n is done for the deep water on the side of the sill towards which the energy flux is required. A similar model was applied by Buckley (1980) to Alberni Inlet.

Applying Stacey's formula to the normal modes at Lull Bay (*Figure 80*) for the M_2 constituent, the following flux estimates were obtained for the first three internal modes: 1.89, 1.48, and $0.02\,MW$. The data from Lull Bay were used because that station is the closest to the sill. These values are therefore estimates of the down-inlet flux from the sill.

The flux estimates from this simple model are very sensitive to the shapes of the modes, because they are proportional to the square of the value of the w-eigenfunction at sill depth. However, the mode fitting procedure is also very sensitive to the modal shapes, so it seems that any technique for estimating energy fluxes will be sensitive to the modal shapes. The only way to escape the decomposition of the internal tidal flux into normal modes is by direct calculation of the total flux from velocity and density data. An expression for the local energy flux can be extracted from the 3-D energy conservation equation. Unfortunately, this direct flux calculation was not possible with the cyclesonde data because of the problem of the missing upper $20\,m$.

The above values for the down-inlet fluxes associated with the first three internal modes obtained from Stacey's model can be compared with the values 0.35 and $0.12\,MW$ for the second and third modes at Lull Bay obtained from the modal fitting. The up-inlet fluxes obtained at Tomakstum Island for the first three internal modes were 0.66, 0.49 and $0.26\,MW$. It seems reasonable to assume that the sill will radiate similar amounts of energy in each direction in each mode. With this assumption, the modal fitting indicates that the sill radiates about $1.4\,MW$ in each direction in the first three internal modes at M_2 frequency. Only about $0.2\,MW$ makes it around the bend to Adeane Point. This result at the sill compares to $3.4\,MW$ in each direction from Stacey's model. As mentioned in Section 1.3, Stacey plotted his estimates of the total flux being radiated away from the sill at M_2 frequency against time from November 1976 to May 1978. The fluxes from the first 10 modes were summed, as well as the contributions from up- and down-inlet propagating waves. He found that it agreed very well with estimates of the power withdrawn from the barotropic tide between Protection Point and Tomakstum Island based on the difference in the phase of the surface elevation oscillation at those two stations. This estimate was also

plotted against time for the same period. The two curves followed the same seasonal cycle, with a maximum around July. The values from July to September were 7–9 MW. Because the two curves agreed so well, he concluded that most of the power being withdrawn from the M_2 barotropic tide at the sill was being fed into a progressive internal tide, and that the other processes occurring at the sill, such as hydraulic jumps, turbulence and high frequency internal wave generation, were relatively unenergetic.

If this were the case, however, and the results of this thesis referring to the reflection coefficient at bends are correct, then one would expect that half of the energy lost from the barotropic tide (i.e. the half that propagates up-inlet) would be dissipated in the sinuous section of the inlet, and the other half would be dissipated in the straight section or propagate out to sea. This is not consistent with the results of Freeland and Farmer (1980), who found that much more energy went into the mean circulation (i.e. much more mixing of the water column occurred) in the straight section containing the sill than in the sinuous section. One alternative possibility is that Stacey's model does not contain enough dynamics of internal tide generation mechanisms, and that his predicted amplitudes are too high. If about 40% ($= 2.8\,MW \div 7\,MW$) of the power being withdrawn from the barotropic tide was being fed into a progressive internal tide, then only $1.4\,MW$ would have to be dissipated via the internal tide in the sinuous section, $1.4\,MW$ via the internal tide down-inlet of the sill, and $4.2\,MW$ directly at the sill. These values would then be in better agreement with Freeland and Farmer. Another possibility is that most of the power lost from the barotropic tide initially goes into the internal tide, but about 60% of it is rapidly dissipated through turbulence within a couple of kilometers of the sill.

3.13 Conclusion

With the exclusion of mode 1 from the fitting procedure on the grounds that this mode has a negligible manifestation in currents and density oscillations below $20\,m$, it was found that *the up-inlet energy flux at both stations landward of the sill was much larger than the down-inlet flux.* When down-inlet waves were excluded from the fit, and mode 1 retained, it was still possible to obtain a good fit to the data, and the phase differences between the

stations for the various modes were in agreement with the phase speeds of those modes. This is consistent with the very low reflection coefficient (< 1%) at the bend predicted in Chapter 2. The reduced amplitude of the internal tide up-inlet of the bend (i.e. at Adeane Point) must therefore be attributed to dissipation, perhaps through turbulence in the presence of the large horizontal velocity shears near the inside corner of the bend predicted by Chapter 2, and to scattering of the energy by the very irregular features in the vicinity of the bend. Subsequent bends will reduce the amplitude still further, until a negligible energy flux reaches the head.

It was found that the up-inlet flux at the two stations seaward of the sill was the same order of magnitude as the down-inlet flux, suggesting the existence of a subsidiary sill seaward of these stations. This sill can be seen on longitudinal depth profiles of the inlet. Its slightly gentler bottom slope can be compensated by stronger barotropic velocities in terms of its internal tide generating potential. There could be some reflection of the up-inlet waves at Lull Bay by the main sill, and the resulting down-inlet waves would interfere (either constructively or destructively) with the down-inlet waves generated by that sill.

The results of the fitting indicate that only 30–50% of the power being removed from the barotropic tide (7–9 *MW* in 1977) is being fed into the internal tide in the summer, so that the remaining energy must be dissipated directly at the main sill. This conclusion is at variance with the results of Stacey (1980), whose model shows that most of the power is being fed into the internal tide. However, an interpretation that is consistent with both results is that most of the power lost from the barotropic tide initially goes into the internal tide, but 50–70% of it is rapidly dissipated through turbulence within a couple of kilometers of the sill.

4. Low Frequency Currents in Knight Inlet

4.1 Power Spectra of Currents

Figures 94–97 show the power spectra of longitudinal currents at the four stations in July 1983. The spectra for September 1983 are similar and are therefore not included. The 1981 time-series were considered to be too short for use in this chapter.

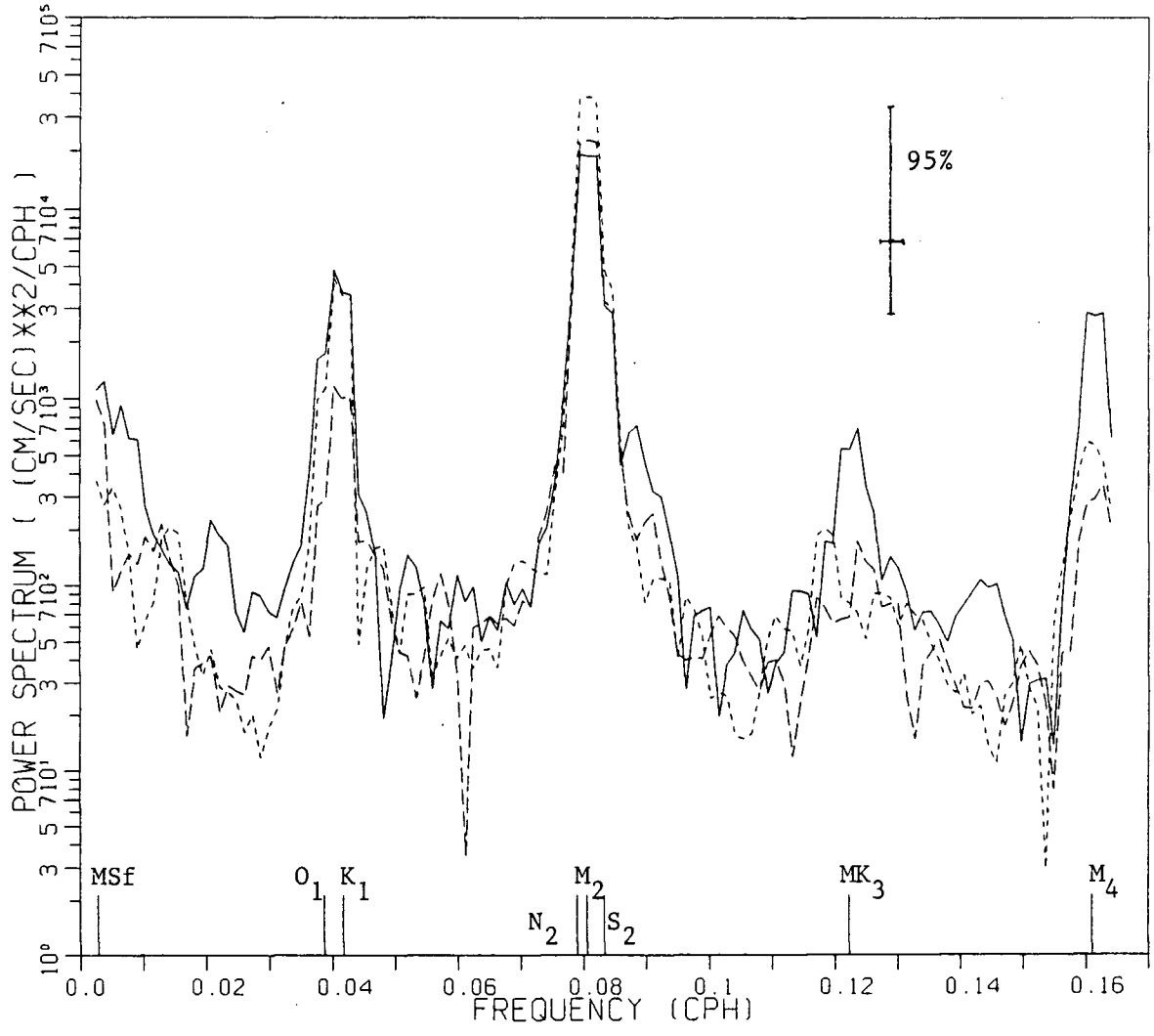

Figure 94 Power spectra of longitudinal velocity at Protection Point.
Solid line = 20 *m*, long dashed line = 80 *m*, short dashed line = 155 *m*.

The energy density is plotted on a log scale because the M_2 peak is an order of magnitude higher than any other peak. The use of a log scale means that the plot is *not* energy preserving (i.e. the area under the curve between two frequencies does not represent the

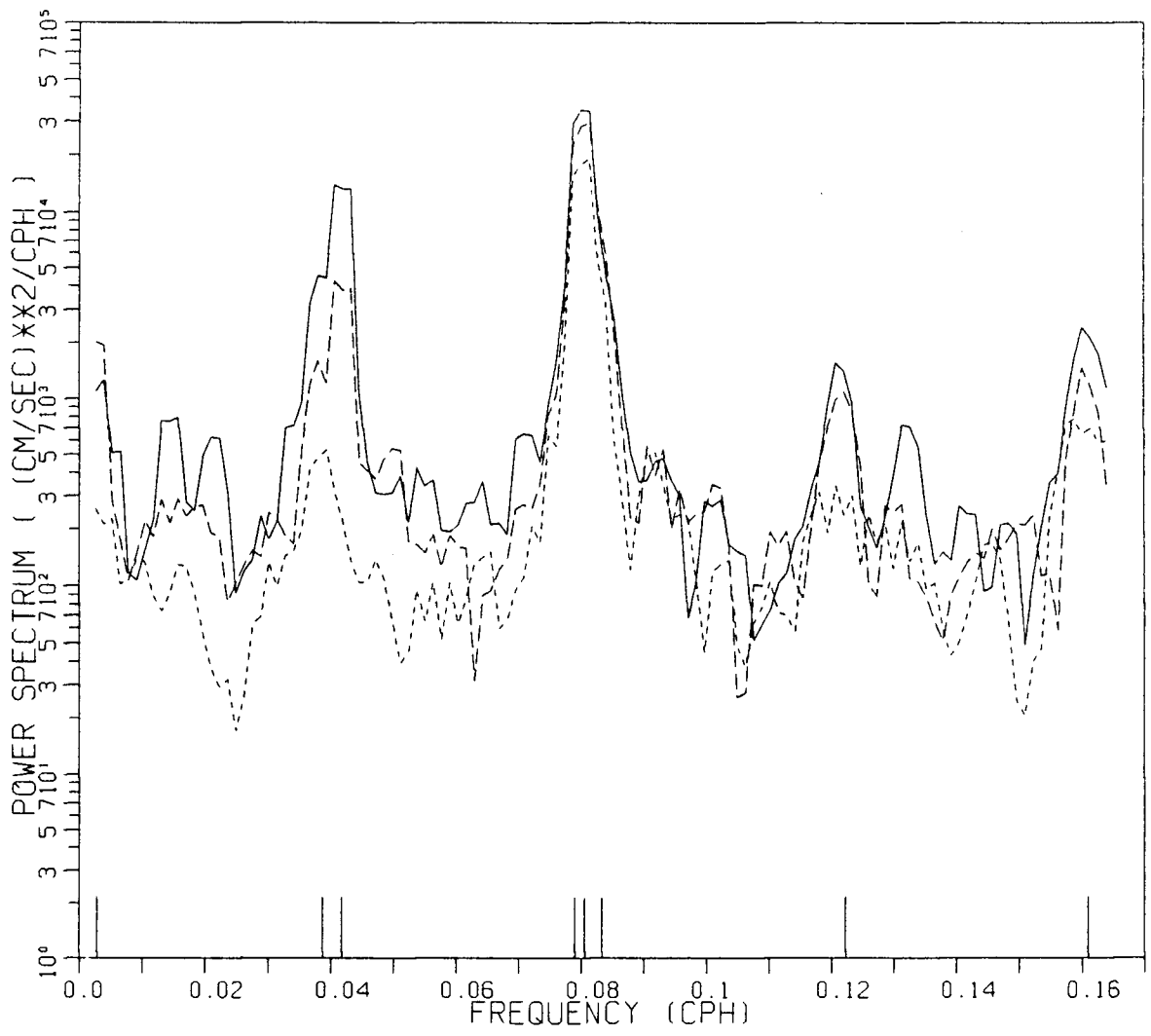

Figure 95 Power spectra of longitudinal velocity at Lull Bay.
Solid line = 25 m, long dashed line = 65 m, short dashed line = 125 m.

energy in that band). The mean and trend of the signals were removed before the Fourier transform was calculated. The Nyquist frequency is $\frac{1}{2\Delta t} = 0.166\,cph$, where Δt is the sampling interval ($3\,hrs$). This frequency is just greater than the frequency of the M_4 constituent. The frequency resolution is $\frac{1}{T} \approx 1.3 \times 10^{-3}\,cph$, where T is the record length ($\approx 750\,hrs$, depending on the record). The power spectra were smoothed with a 3-point moving average, so that the values plotted are actually the mean energy in three consecutive energy bands. The power spectra were calculated at three depths — the shallowest standard depth (solid line), the deepest standard depth (short dashed line), and a middle depth (long dashed line). The frequencies of the constituents used in the harmonic analysis

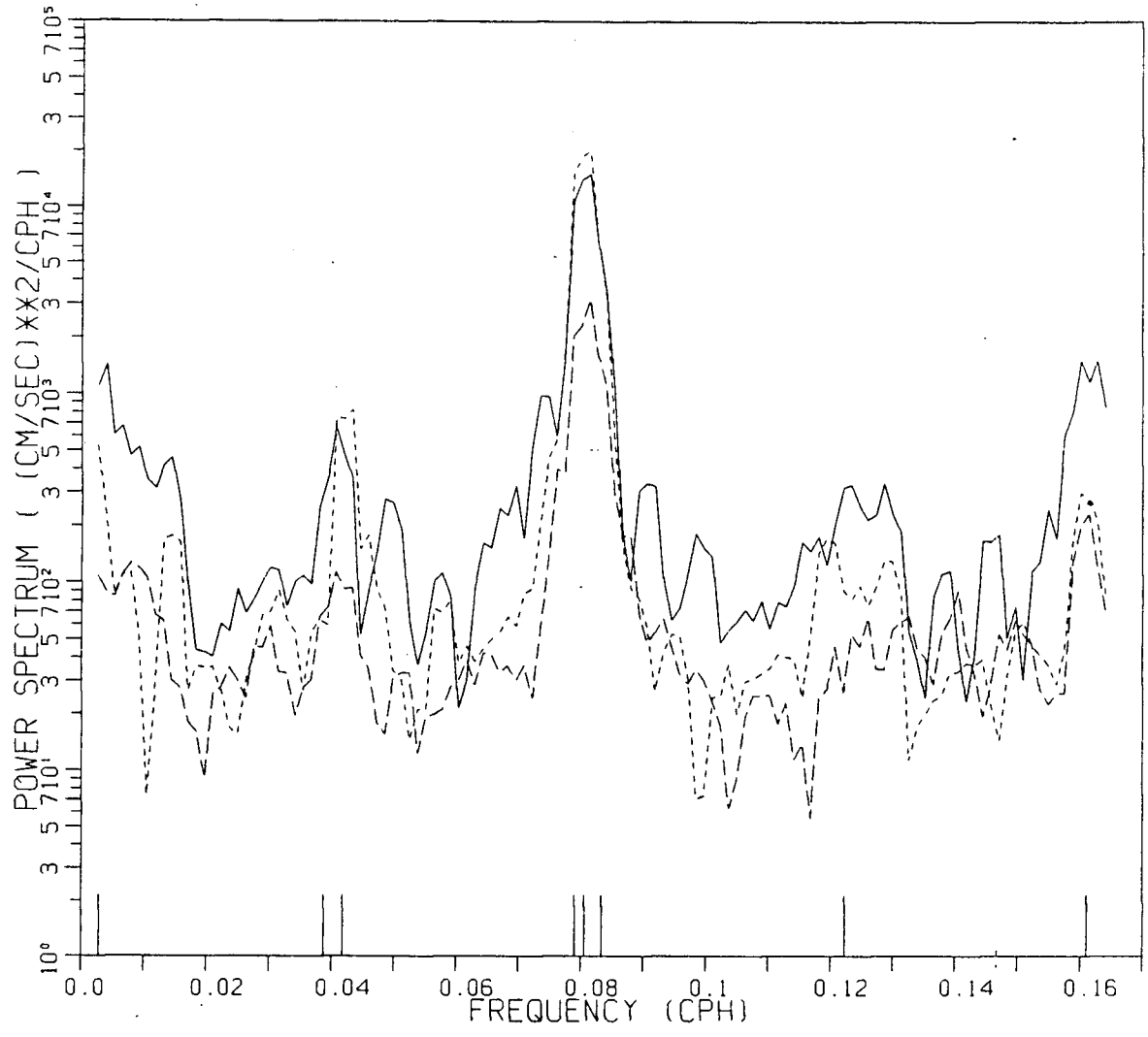

Figure 96 Power spectra of longitudinal velocity at Tomakstum Island. Solid line = 20 m, long dashed line = 80 m, short dashed line = 170 m.

are plotted as ticks on the frequency axis.

The dominant feature in each plot is the peak at semi-diurnal frequency, with lesser peaks at diurnal frequency, quarter-diurnal frequency (M_4), and at low frequency (less than 0.01 cph). There is also a significant peak at MK_3 frequency in most plots. The power spectra at low frequencies show peaks at different frequencies at the various stations. In an attempt to identify a peak associated with the passage of weather systems and corresponding wind shifts, which is generally taken to be at a period of 3–5 days, the mean power spectrum at the shallowest depth of all eight records from 1983 was calculated. This

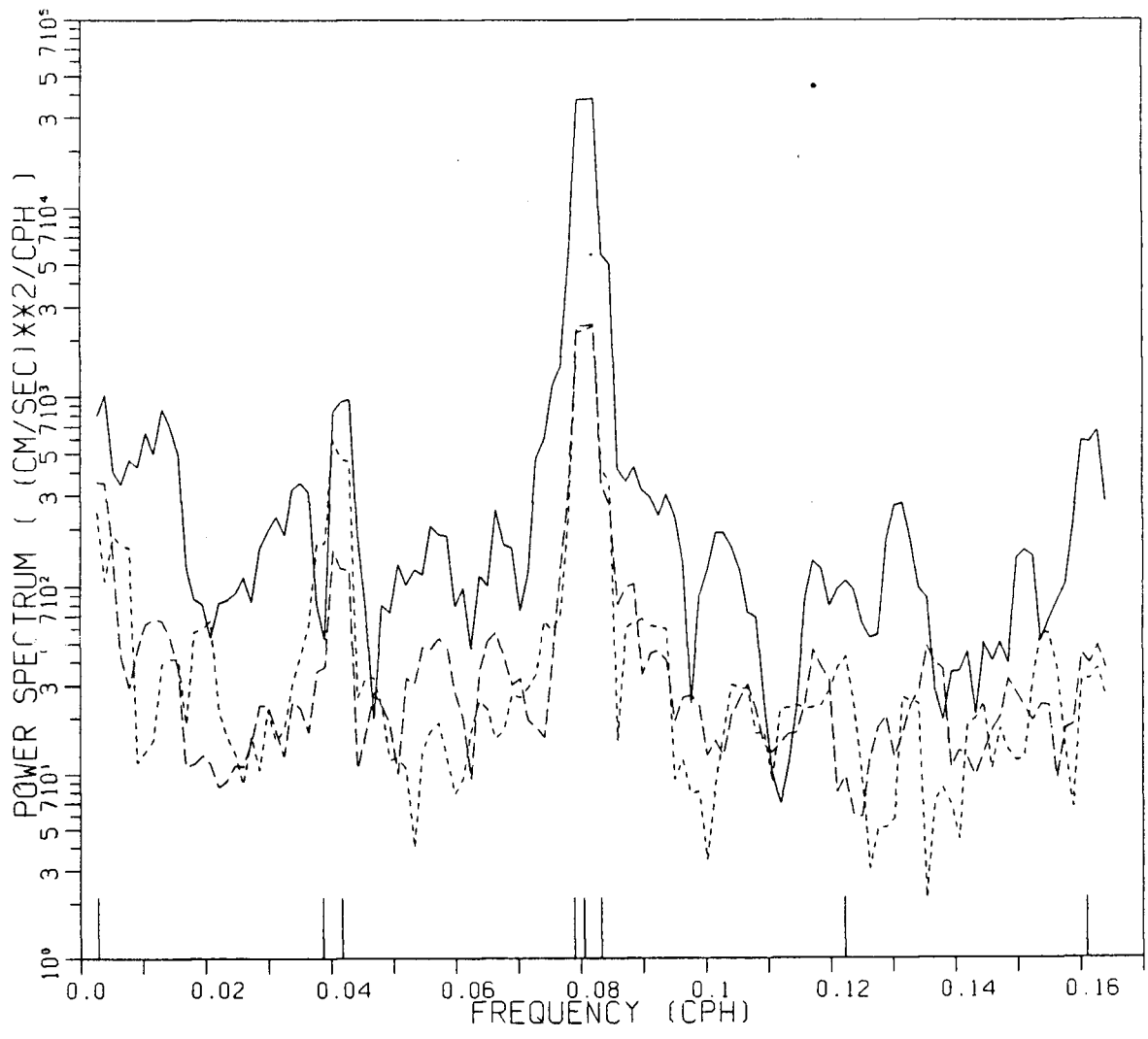

Figure 97 Power spectra of longitudinal velocity at Adeane Point.
Solid line = 20 *m*, long dashed line = 80 *m*, short dashed line = 170 *m*.

spectrum is shown in *Figure 98*. The shallowest depth was chosen because it is the one most likely to show currents associated with wind stress. A broad peak at a frequency of 0.011 *cph*, corresponding to a period of 3.8 days, can indeed be observed, although its significance is questionable.

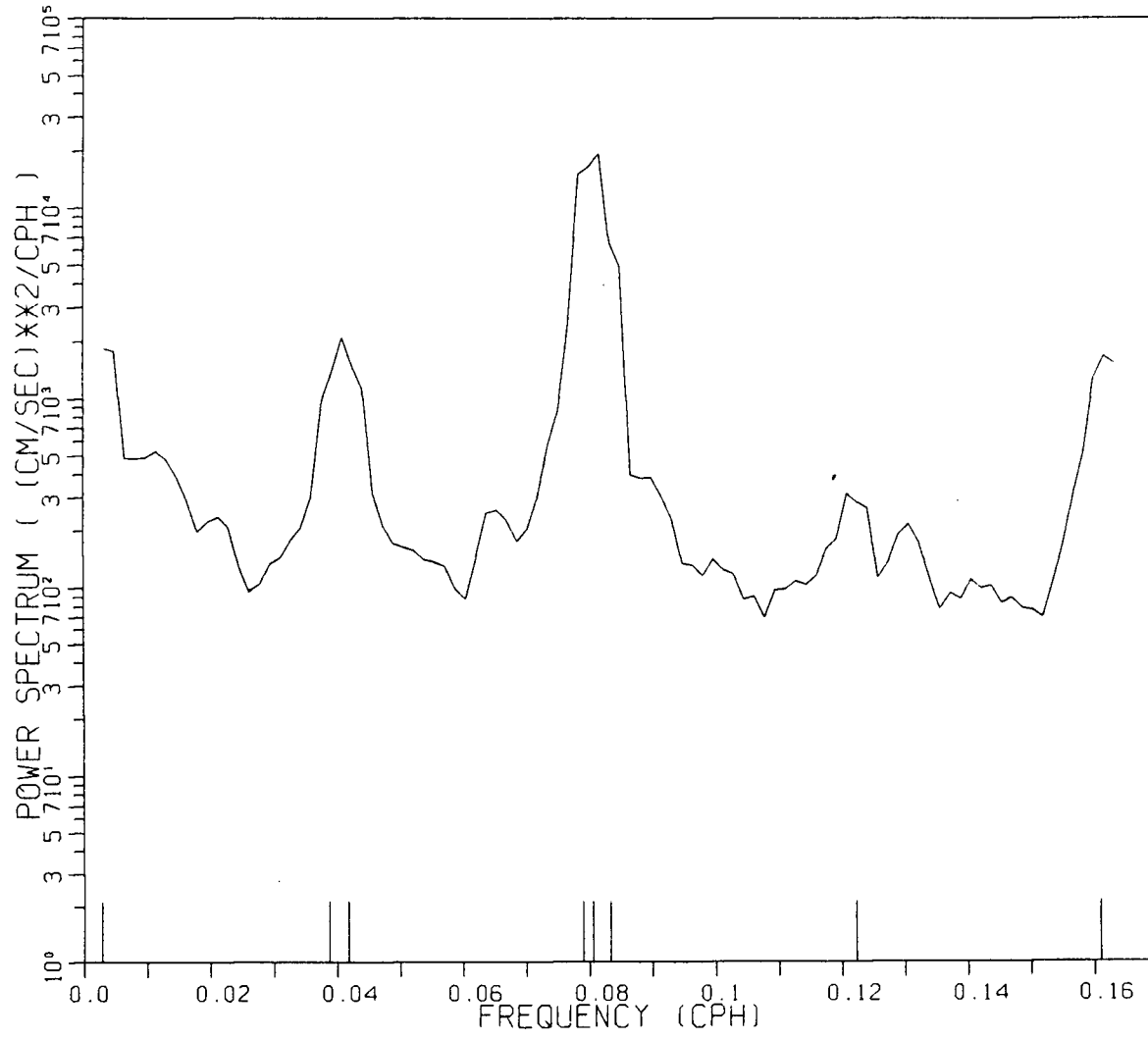

Figure 98 Power spectrum of velocity at shallowest depth averaged over all stations.

4.2 Time Series of Longitudinal Velocities with the Tide Removed

In order to extract the low-frequency signal from the longitudinal velocity records, the tidal component was reconstructed using the amplitudes and phases from the harmonic analysis and subtracted from the original signal. The seven constituents at and above diurnal frequency were used to recontruct the tidal signal. As a check on the process a harmonic analysis was done on the residual. In all cases it was found that there was indeed a negligible component ($< 1\,cm/s$) at the frequencies that had been removed. When the power spectra of these residuals were calculated, it was found that the tidal peaks had been removed and in some cases they appeared as troughs in the power spectra. However,

the energy at frequencies between the tidal frequencies was unaffected. This energy was also evident in the residual time series, where there was a considerable amount of high-frequency (periods less than 1 day) noise. It was therefore necessary to smooth the residual with a $24\,hr$ (8-point) moving average. The resultant low-pass filtered signals are shown in *Figures 99–106.* The power spectra of these filtered signals were found to be identical to the power spectra of the original signals at low frequency.

The fortnightly oscillation of the MSf tide is plainly evident in the filtered signals, especially in September. This oscillation seems to have the same phase at all stations, with maximum near surface up-inlet flows being attained on or near Julian days 208, 223, 252 and 268. A sudden inflow occurs near the surface at Protection Point around day 253. The filtered signals are very similar at Tom-N and Tom-S in September, indicating that there is little cross-channel variability there.

4.3 The MSf Tide

The complex amplitudes of the MSf constituent from a harmonic analysis of the longitudinal velocity are shown in *Figures 107–110.* The same results can be obtained by doing a harmonic analysis of the low-pass filtered signals shown in *Figures 99–106.* The loci all show the same general features, with the shallowest depth usually located in the first quadrant of the complex plane. The loci at Tomakstum Island and Adeane Point are particularly repeatable, with a doubling back of the loci at 110–140 m at Tomakstum Island, and a spiral shape at Adeane Point. The irregularity of the low-pass filtered signals makes the validity of using harmonic analysis for the MSf constituent questionable. However, the repeatability of the loci implies that the results are meaningful and worthy of future interpretation.

Freeland and Farmer (1980) used Fourier analysis to determine the amplitude of the MSf velocities at Montagu Point (near Protection Point). They found similar results to those presented in *Figure 107,* with amplitudes of $4.8\,cm/s$ at $15\,m$, $1.1\,cm/s$ at $100\,m$ and $3.1\,cm/s$ at $165\,m$. These values compare to amplitudes ranging from 0 to $5\,cm/s$

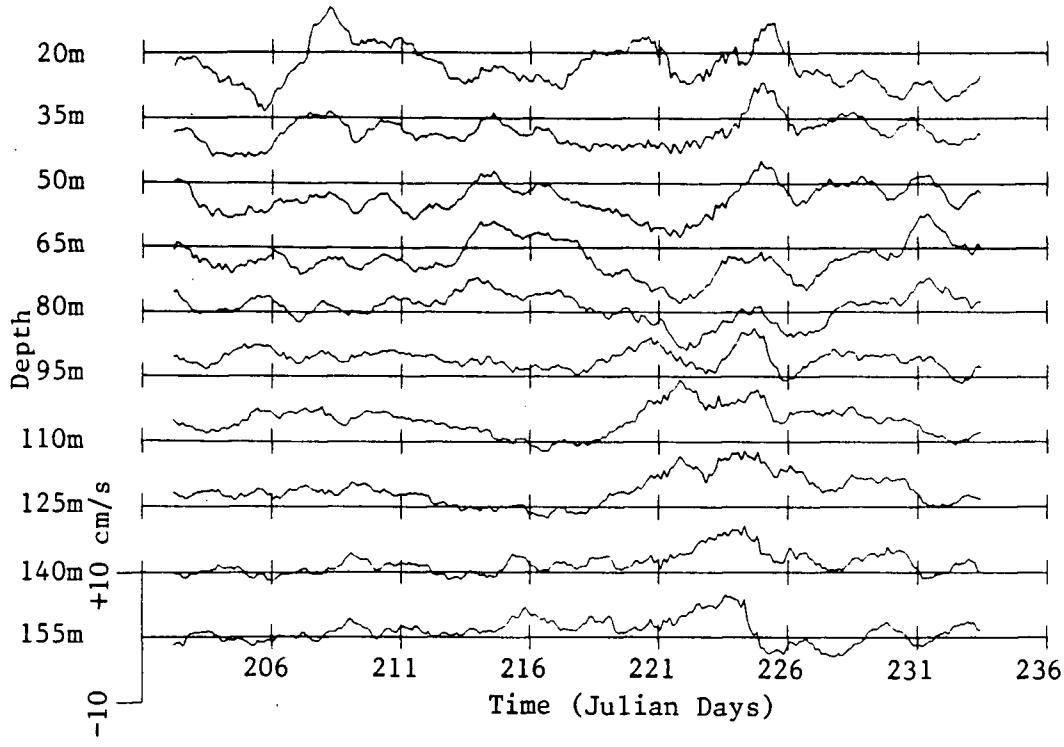

Figure 99 Low-pass filtered longitudinal velocity at Protection Point in July 1983. Positive is up-inlet.

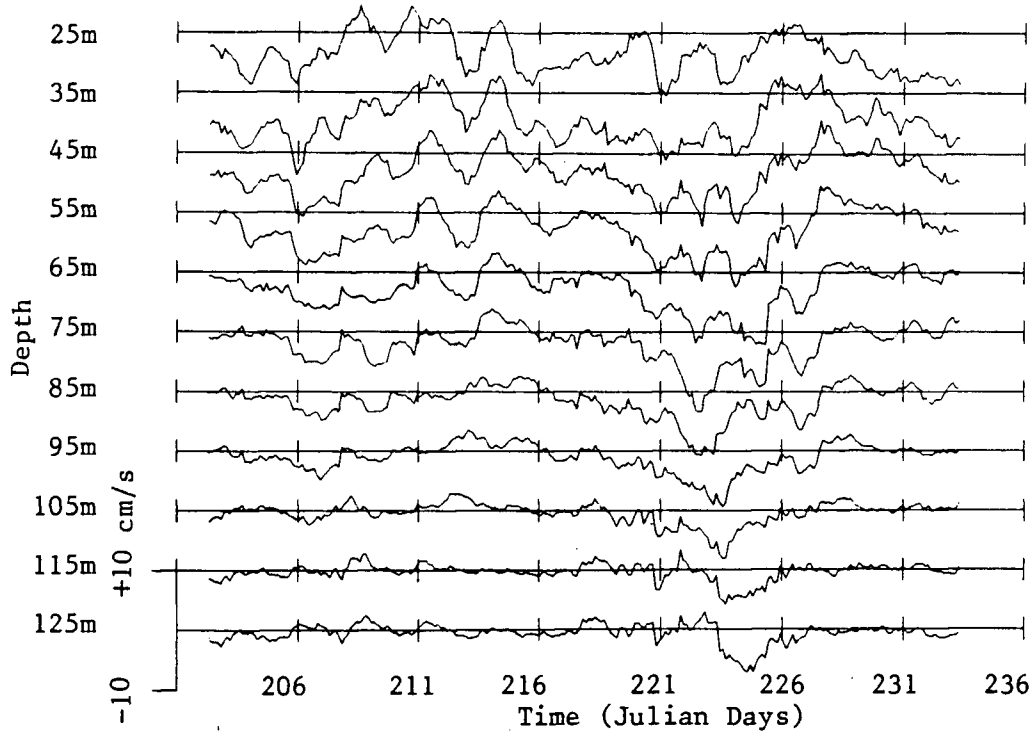

Figure 100 Low-pass filtered longitudinal velocity at Lull Bay in July 1983.

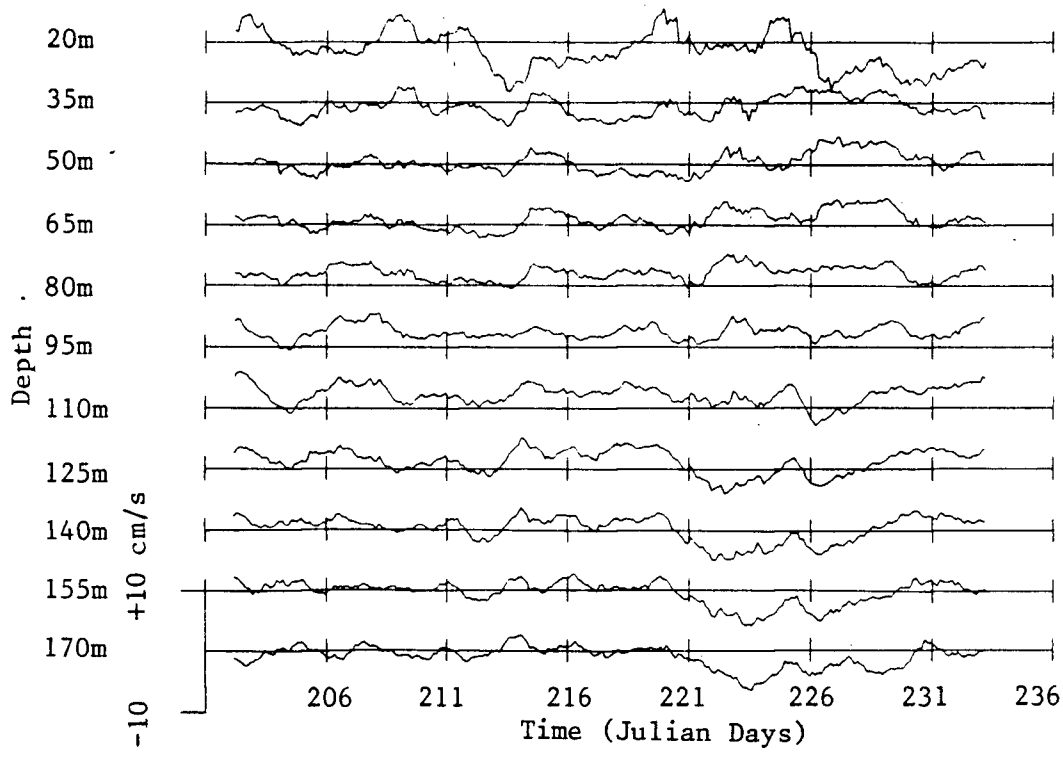

Figure 101 Low-pass filtered longitudinal velocity at Tomakstum Island in July 1983. Positive is up-inlet.

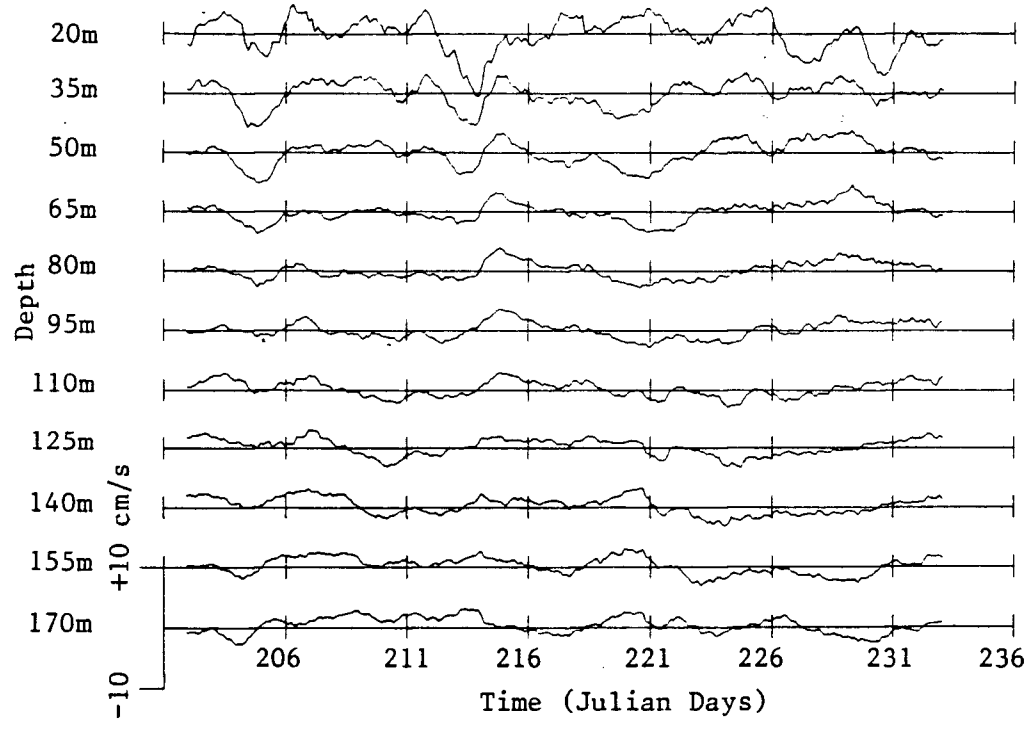

Figure 102 Low-pass filtered longitudinal velocity at Adeane Point in July 1983.

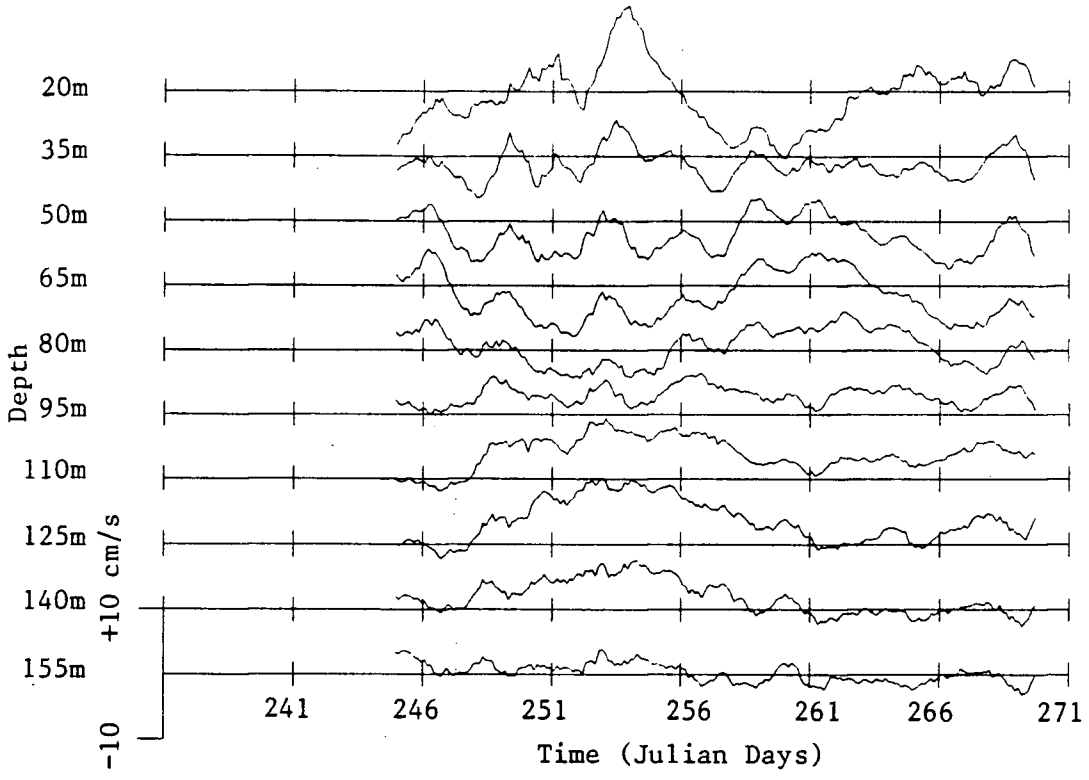

Figure 103 Low-pass filtered longitudinal velocity at Protection Point in September 1983. Positive is up-inlet.

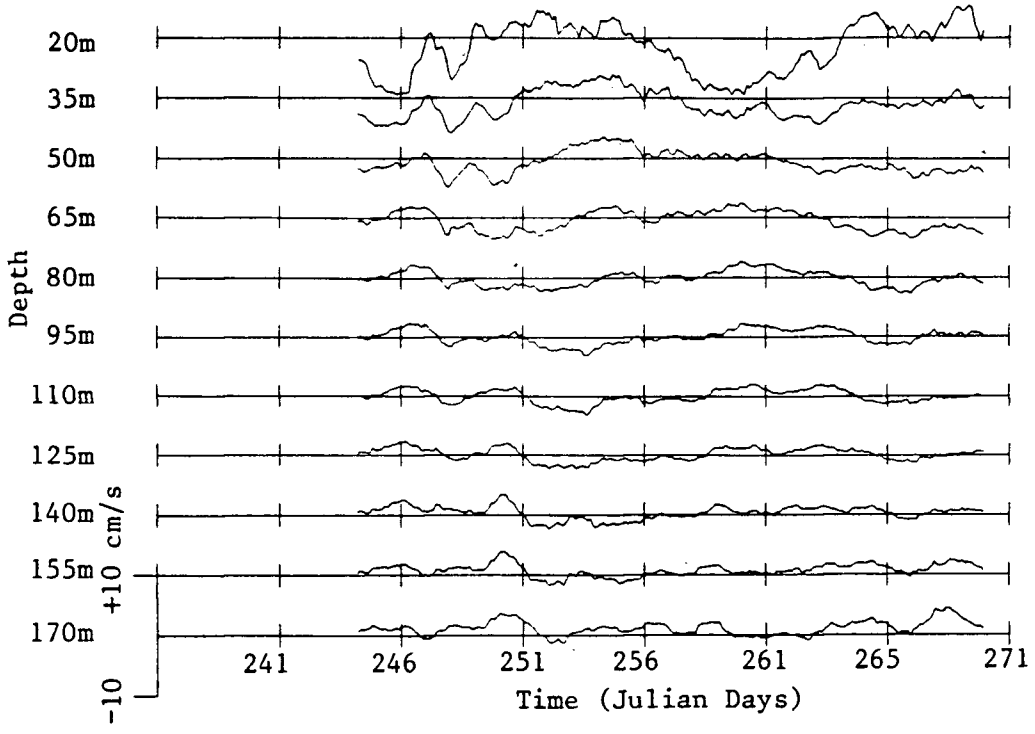

Figure 104 Low-pass filtered longitudinal velocity at Adeane Point in September 1983.

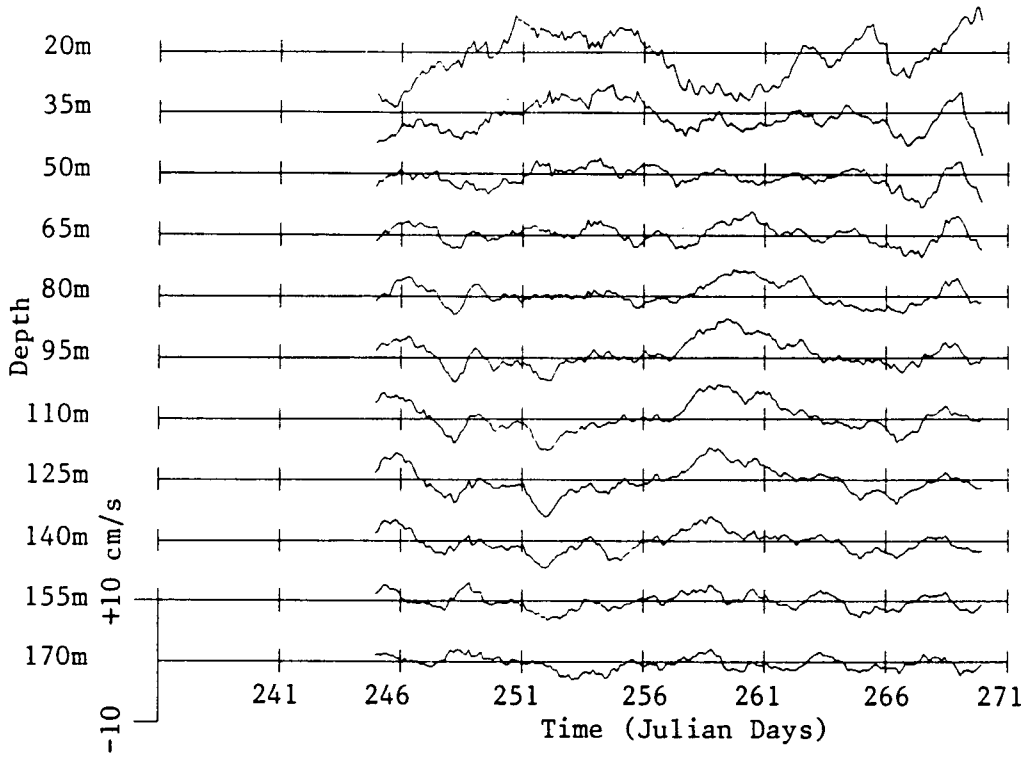

Figure 105 Low-pass filtered longitudinal velocity at Tom-N in September 1983. Positive is up-inlet.

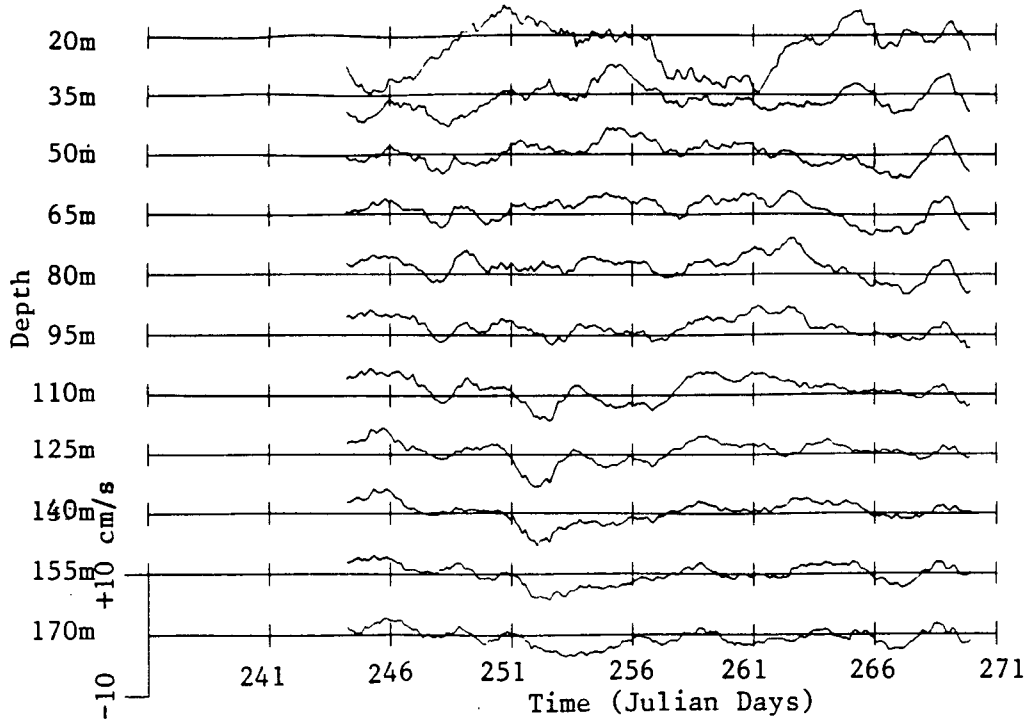

Figure 106 Low-pass filtered longitudinal velocity at Tom-S in September 1983.

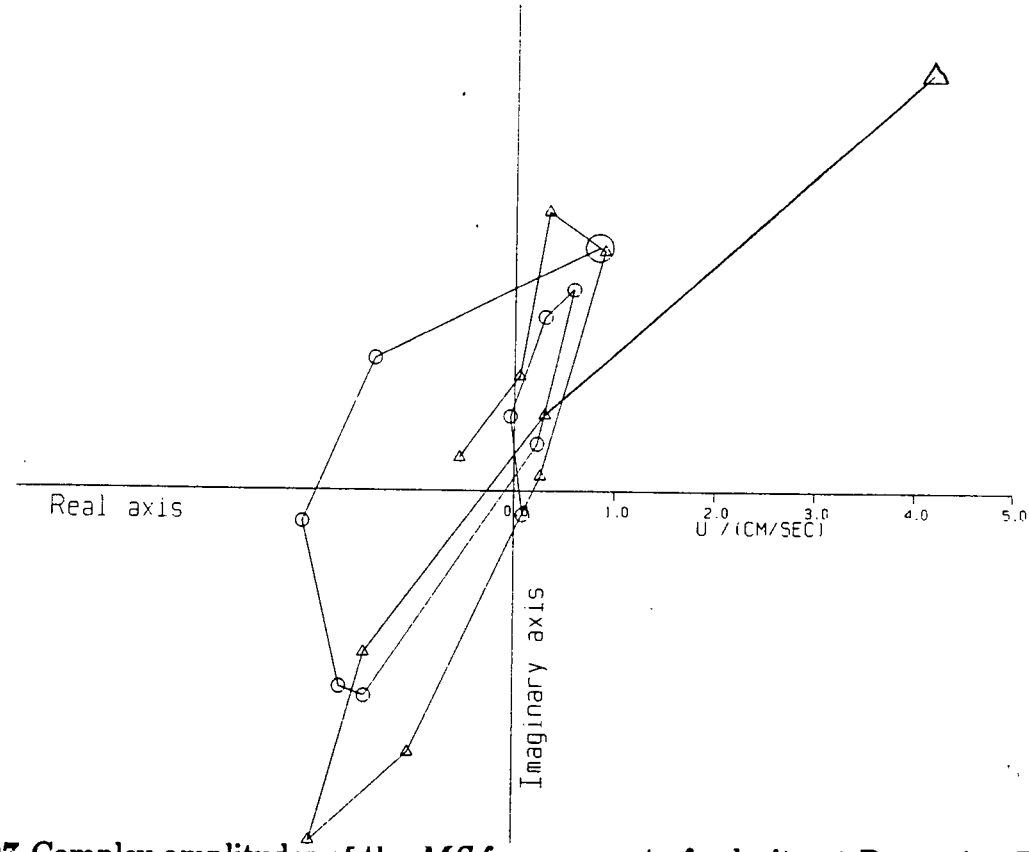

Figure 107 Complex amplitudes of the MSf component of velocity at Protection Point.
o July 1983, △ September 1983.
The shallowest standard depth is marked by a larger symbol.

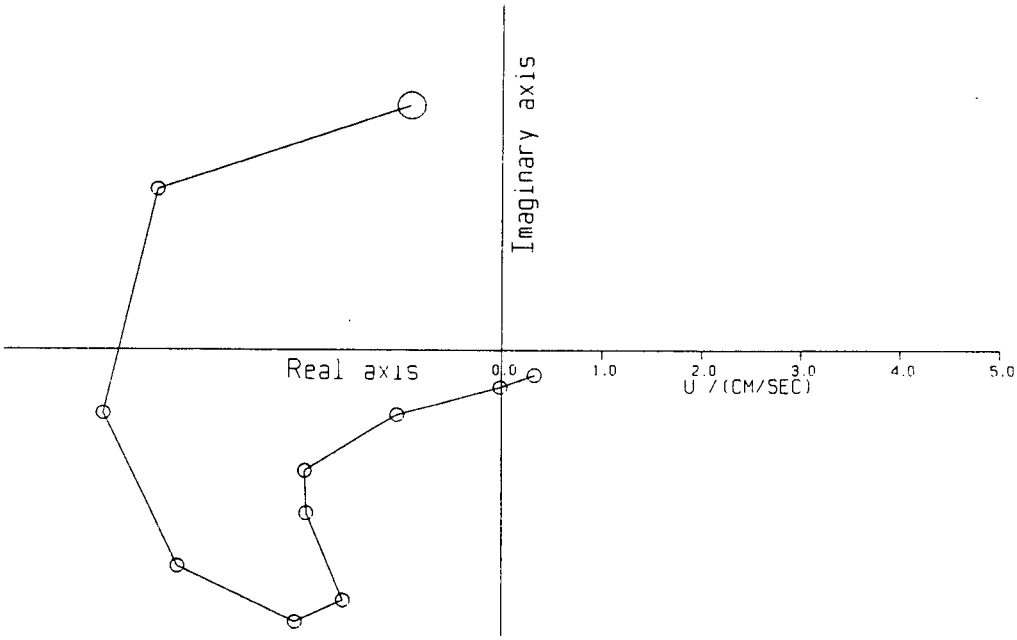

Figure 108 Complex amplitudes of the MSf component of velocity at Lull Bay.
o July 1983.

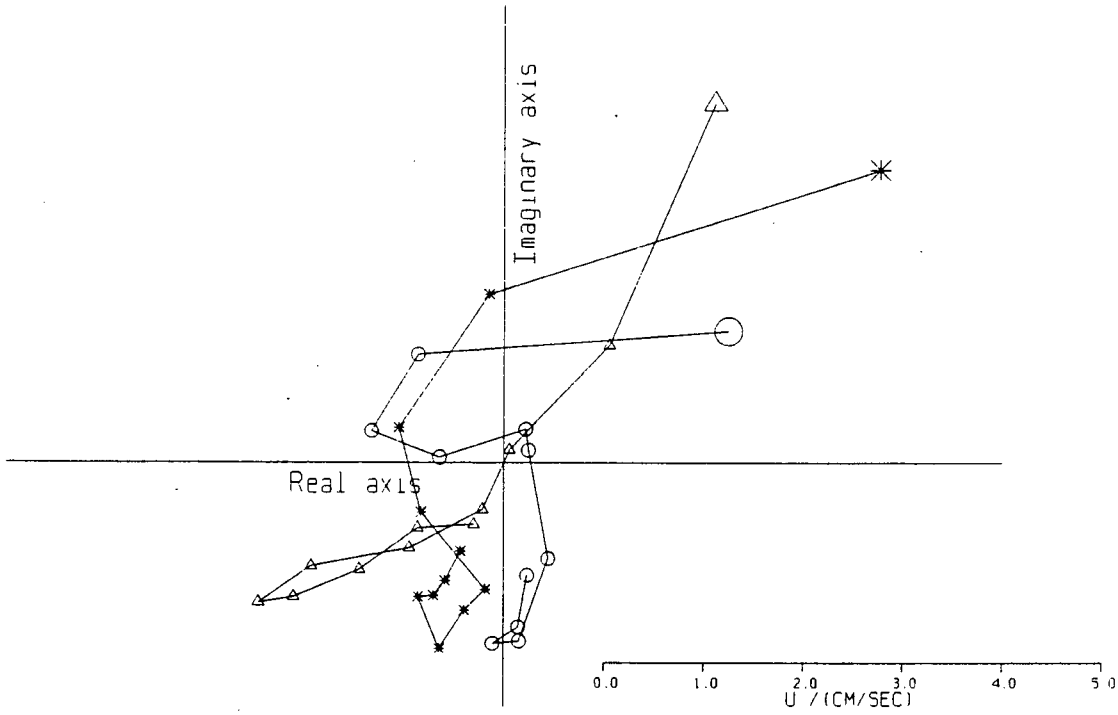

Figure 109 Complex amplitudes of the MSf component of velocity at Tomakstum Island. ∘ July 1983, △ Tom-S September 1983, ∗ Tom-N September 1983.

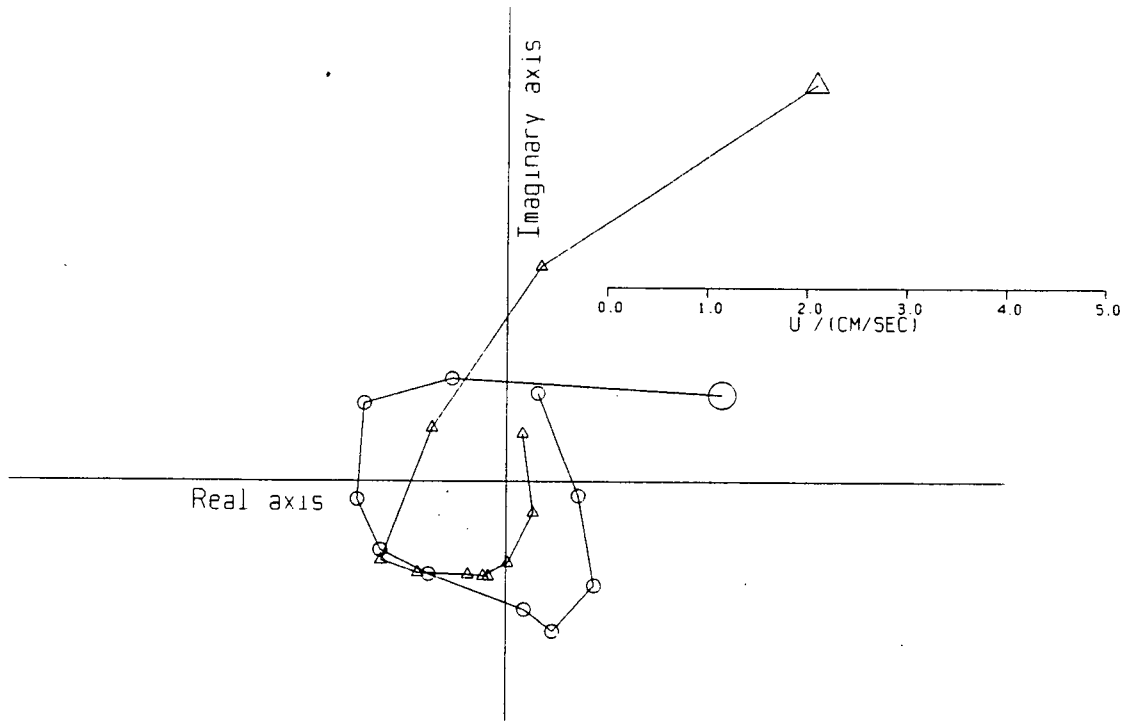

Figure 110 Complex amplitudes of the MSf component of velocity at Adeane Point. ∘ July 1983, △ September 1983.

in *Figure 107.* The surface elevation data were also analysed for the MSf constituent. Values ranging from 6 cm to 21 cm were found from the eight cyclesonde records from 1983. Freeland and Farmer obtained a value of 4.1 cm using tide gauge data. If the entire surface of the inlet is moving up and down with period 14.7 days, then a barotropic current of 0.02–0.06 cm/s (from the cyclesondes) or 0.01 cm/s (from Freeland and Farmers' tide gauge) could be expected at Protection Point. Clearly the currents observed are much larger than the calculated barotropic current.

Freeland and Farmer argue that the large baroclinic MSf frequency currents are due to variations in the strength of the estuarine circulation. If more energy is available for mixing at spring rather than neap tides, then the circulation would be modulated at MSf frequency.

4.4 Residual Velocity Profiles

Having observed so much variability in the non-tidal longitudinal velocities, the definition and relevance of the "mean circulation" become questionable. It is certainly not a steady circulation. However, in an attempt to calculate mean velocity profiles, the eight cyclesonde records from 1983 were averaged over two MSf cycles (= 29.5 days). In July the first 29.5 days of data were used, but in September, where the records are only about 26 days long, a small amount of aliasing must be accepted. The results are shown in *Figures 111–114.*

The profiles are quite repeatable from month to month, especially at Protection Point and Tomakstum Island. At Protection Point the profile has the classical structure of outflow at the surface and inflow at depth, with a zero crossing at 75 m (much deeper than the pycnocline)! This behaviour is also true at Adeane Point, with a zero crossing at 100 m. However at Tomakstum Island the profile takes on a 3-layered structure, with outflow at the surface and at depth, and inflow at intermediate depths. The zero crossings are at about 50 m and 150 m. Curiously, the profile at Lull Bay shows outflow at all depths. This result is not consistent with the idea of lateral homogeneity, since mass must be conserved.

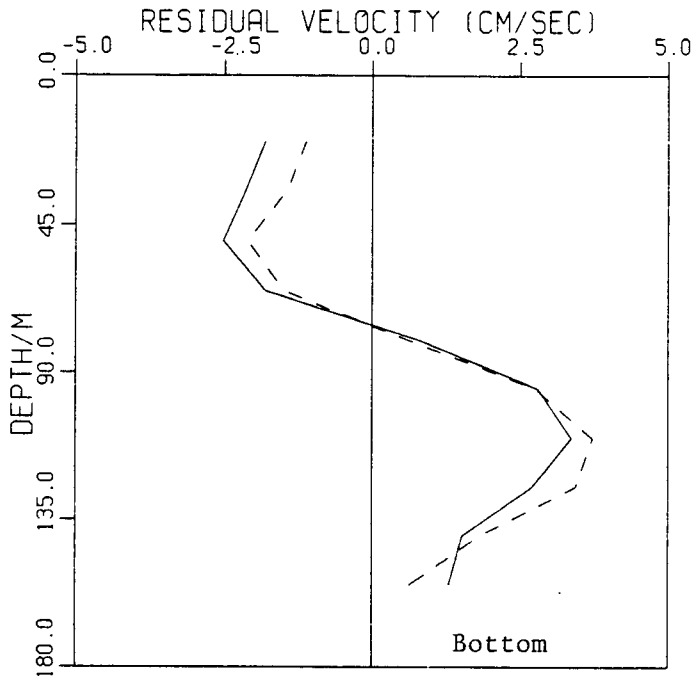

Figure 111 Residual longitudinal velocity profiles at Protection Point. Solid line = July 1983, dashed line = September 1983. Positive is up-inlet.

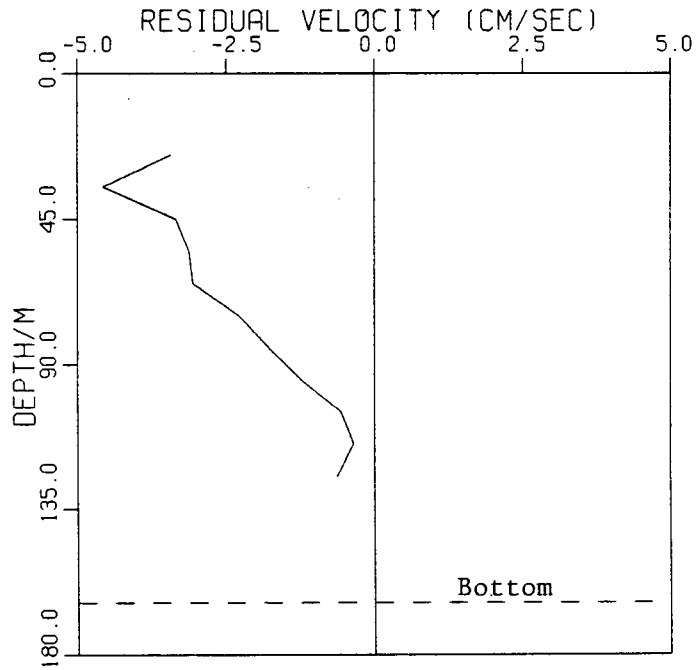

Figure 112 Residual longitudinal velocity profile at Lull Bay. July 1983

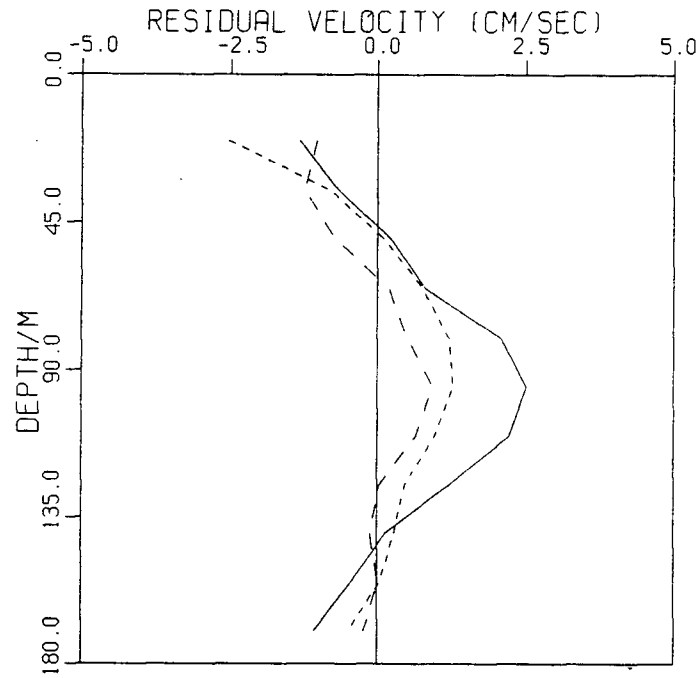

Figure 113 Residual longitudinal velocity profiles at Tomakstum Island. Solid line = July 1983, long dashed line = Tom-S September 1983, short dashed line = Tom-N September 1983. Positive is up-inlet.

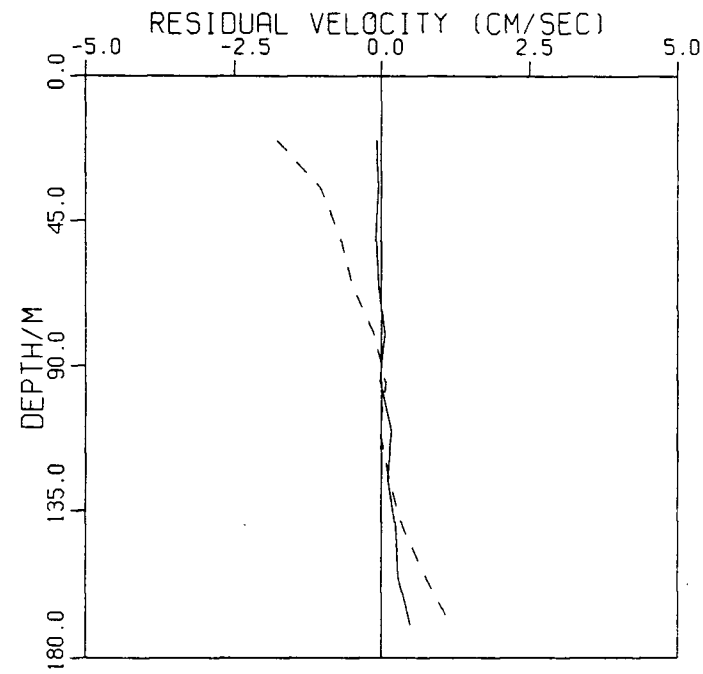

Figure 114 Residual longitudinal velocity profiles at Adeane Point. Solid line = July 1983, dashed line = September 1983

A possible explanation is that tidal flows over the sill produce eddies in the vicinity of Lull Bay. These non-linear features may have non-zero means, causing lateral inhomogeneity in the mean velocity field.

4.5 Summary

In this Chapter some interesting data relating to the low frequency component of the longitudinal velocity signal, which could be of use in further studies, are presented. Firstly the velocity power spectra are calculated at the various stations. In addition to validating the choice of constituents used in the harmonic analysis, they show a broad peak at a period of 3.8 days at the shallowest depth when averaged over all stations. This peak is probably associated with wind driven currents. Secondly the low-pass filtered velocity time series are presented, with the fortnightly oscillation of the MSf tide in evidence. There is scope for future work in analysing the convergences and divergences at various depths, and in interpreting sudden inflows and outflows. Finally, both the complex amplitudes of the MSf constituent and the residual velocity profiles (averaged over two MSf cycles) show repeatable features from month to month, indicating that they are worthy of further investigation. The latter are particularly repeatable, and could be of use in validating general circulation models.

Appendix A: Simple Models of The Stratification

A.1 Model 1 — Two Layers of Constant N^2

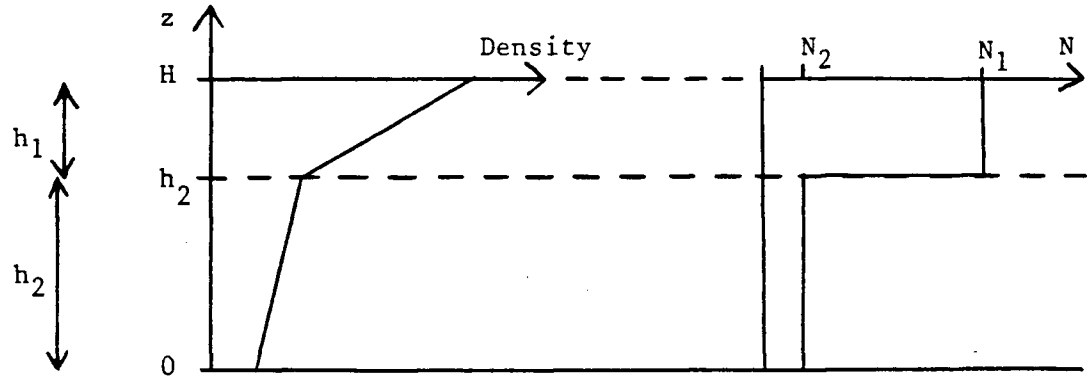

Figure 115 Density and N structure used in Model 1. $H = h_1 + h_2$.

In this model N^2 is taken to be constant in both layers, so that the density profile is piecewise linear and continuous. *Figure 115* shows the density and N structure. Assuming that $\omega^2 \ll N^2$ and making the rigid lid approximation, the eigenvalue problem 3.3–3.5 becomes

$$\frac{d^2Z}{dz^2} + \frac{N^2}{c^2}Z = 0, \tag{A.1}$$

with $Z = 0$ at $z = O$ and H. The solution is

$$Z_1 = \sin\frac{N_2 h_2}{c}\ \sin\frac{N_1(H-z)}{c}, \tag{A.2}$$

$$Z_2 = \sin\frac{N_1 h_1}{c}\ \sin\frac{N_2 z}{c}, \tag{A.3}$$

with the following dispersion relation:

$$N_2 \sin\frac{N_1 h_1}{c}\cos\frac{N_2 h_2}{c} + N_1 \sin\frac{N_2 h_2}{c}\cos\frac{N_1 h_1}{c} = 0. \tag{A.4}$$

Suppose that

$$\varepsilon \equiv \frac{N_2}{N_1} \ll 1, \tag{A.5}$$

i.e. that the density stratification in the upper layer is much stronger than in the lower layer. Note, however, that $N_2 h_2$ is not necessarily smaller than $N_1 h_1$. Expanding all

variables as an asymptotic expansion in powers of ε,

$$c \equiv c^0 + \varepsilon c^1 + \varepsilon^2 c^2 + \ldots \tag{A.6}$$

$$Z_1 \equiv Z_1^0 + \varepsilon Z_1^1 + \varepsilon^2 Z_1^2 + \ldots \tag{A.7}$$

$$Z_2 \equiv Z_2^0 + \varepsilon Z_2^1 + \varepsilon^2 Z_2^2 + \ldots. \tag{A.8}$$

The dispersion relation becomes

$$\varepsilon \sin\frac{N_1 h_1}{c} \cos\frac{N_2 h_2}{c} + \sin\frac{N_2 h_2}{c} \cos\frac{N_1 h_1}{c} = 0. \tag{A.9}$$

Now, $\sin\frac{N_1 h_1}{c} \cos\frac{N_2 h_2}{c}$ is bounded, so to $O(1)$,

$$\sin\frac{N_2 h_2}{c^0} \cos\frac{N_1 h_1}{c^0} = 0, \tag{A.10}$$

which has solutions

$$c^0 = \frac{N_2 h_2}{\beta\pi}, \qquad \beta = 1,2,3\ldots \qquad (\text{"}\beta\text{-modes"}),$$

or

$$c^0 = \frac{N_1 h_1}{(\alpha+\frac{1}{2})\pi}, \qquad \alpha = 0,1,2\ldots \qquad (\text{"}\alpha\text{-modes"}).$$

The β-modes are due to the lower layer stratification, since to $O(1)$ their phase speed depends only on $N_2 h_2$. The α-modes are due to the upper layer stratification, since their phase speed depends only on $N_1 h_1$. These α- and β-modes comprise the infinite set of eigenfunctions to the problem, with the n^{th} mode corresponding to the n^{th} largest phase speed in the union of the sets

$$\left\{\frac{N_2 h_2}{\beta\pi};\ \beta = 1,2,3\ldots\right\} \bigcup \left\{\frac{N_1 h_1}{(\alpha+\frac{1}{2})\pi};\ \alpha = 0,1,2\ldots\right\}.$$

So either the $\beta = 1$ mode (if $\frac{N_2 h_2}{N_1 h_1} > 2$) or the $\alpha = 0$ mode (if $\frac{N_2 h_2}{N_1 h_1} < 2$) could be the first mode, depending on which has the higher phase speed. The order in which these phase speeds arrange themselves into descending order is completely determined by the ratio $\frac{N_2 h_2}{N_1 h_1}$.

A.1.1 "α-Modes" or "Upper Layer Modes"

The first two terms in the asymptotic expansion of c are

$$c^0 = \frac{N_1 h_1}{(\alpha + \frac{1}{2})\pi}, \qquad \alpha = 0, 1, 2 \ldots \tag{A.11}$$

$$c^1 = -\frac{{c^0}^2}{N_1 h_1} \cot\left(\frac{N_2 h_2}{N_1 h_1}(\alpha + \tfrac{1}{2})\pi\right), \tag{A.12}$$

$$c^2 = \ldots$$

and the $O(1)$ term of the eigenfunction is

$$Z_1^0 = \sin\left(\frac{N_2 h_2}{N_1 h_1}(\alpha + \tfrac{1}{2})\pi\right) \sin\left(\frac{H - z}{h_1}(\alpha + \tfrac{1}{2})\pi\right), \tag{A.13}$$

$$Z_2^0 = (-1)^\alpha \sin\left(\frac{N_2 z}{N_1 h_1}(\alpha + \tfrac{1}{2})\pi\right). \tag{A.14}$$

Figure 116 illustrates the structure of these eigenfunctions for various values of $\frac{N_2 h_2}{N_1 h_1}$.

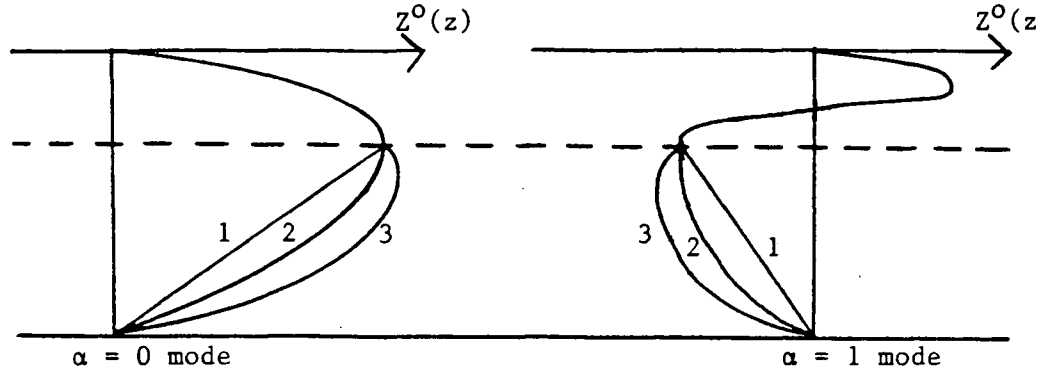

Figure 116 $O(1)$ eigenfunctions for α-modes.
Case 1: $\frac{N_2 h_2}{N_1 h_1}(\alpha + \frac{1}{2}) < \frac{1}{2}$, case 2: $\frac{N_2 h_2}{N_1 h_1}(\alpha + \frac{1}{2}) = \frac{1}{2}$, case 3: $\frac{N_2 h_2}{N_1 h_1}(\alpha + \frac{1}{2}) > \frac{1}{2}$.

The asymptotic expansion will not converge if the argument of *cot* in equation A12 is close to $i\pi$; $i = 1, 2, 3 \ldots$, since then $c^1 \to \infty$; i.e. it will not converge if

$$\frac{N_2 h_2}{i\pi} = \frac{N_1 h_1}{(\alpha + \frac{1}{2})\pi} \text{ for } i = 1, 2, 3 \ldots . \tag{A.15}$$

This is true precisely when the phase speed of an α-mode is close to the phase speed of an β-mode. Then the ranking of the phase speeds is ambiguous, because it is not clear which mode has the higher phase speed.

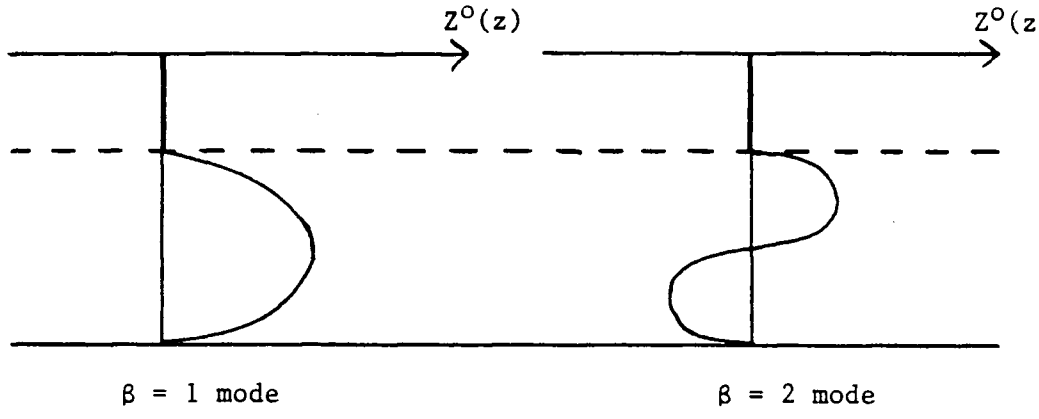

Figure 117 $O(1)$ eigenfunctions for β-modes.

The vertical gradient of Z^0 does not match across the interface to $O(1)$; the matching becomes however better and better as higher order terms of the asymptotic expansion are incorporated. There are $\alpha+1$ extrema in the upper layer in an α-mode, with the remaining $(n-\alpha-1)$ of the n^{th} mode situated in the lower layer. The n^{th} mode can be any one of the first n α-modes, or any of the first n β-modes. For example, the 3^{rd} mode could be the $\alpha=0$, $\alpha=1$, $\alpha=2$, $\beta=1$, $\beta=2$ or $\beta=3$ mode, depending on the value of $\frac{N_2h_2}{N_1h_1}$. This parameter controls which mode is the n^{th} mode, and hence also how many extrema are required in the lower layer to bring the total number up to n.

A.1.2 "β-Modes" or "Lower Layer Modes"

The first two terms in the asymptotic expansion of c are

$$c^0 = \frac{N_2h_2}{\beta\pi}, \qquad \beta = 1,2,3\ldots \tag{A.16}$$

$$c^1 = \frac{c^{0^2}}{N_2h_2}\tan\left(\frac{N_1h_1}{N_2h_2}\beta\pi\right), \tag{A.17}$$

$$c^2 = \ldots$$

and the $O(1)$ term of the eigenfunction is

$$Z_1^0 = 0, \tag{A.18}$$

$$Z_2^0 = \sin\left(\frac{N_1h_1}{N_2h_2}\beta\pi\right)\ \sin\left(\frac{\beta\pi z}{h_2}\right). \tag{A.19}$$

Figure 117 shows these eigenfunctions.

The asymptotic expansion will not converge if the argument of *tan* in equation A17 is close to $(j+\frac{1}{2})\pi$; $j = 0, 1, 2\ldots$, since then $c^1 \to \infty$; i.e. it will not converge if

$$\frac{N_2 h_2}{\beta\pi} = \frac{N_1 h_1}{(j+\frac{1}{2})\pi} \text{ for } j = 0, 1, 2\ldots . \tag{A.20}$$

Again this is true precisely when the phase speed of an α-mode is close to the phase speed of a β-mode.

There are β extrema in the lower layer in an β-mode, with the remaining $(n-\beta)$ of the n^{th} mode situated in the upper layer. To find the position of the remaining extrema it is necessary to go to $O(\varepsilon)$ in Z_1, since the positions of the upper layer extrema are ambiguous to $O(1)$. After some algebra, one obtains

$$Z_1^1 = (-1)^{\beta+1} \frac{c^1 N_2 h_2}{c^0} \sin\left(\frac{N_1(H-z)\beta\pi}{N_2 h_2}\right), \tag{A.21}$$

$$Z_2^1 = -\frac{c^1 N_2 z}{c^{0^2}} \cos\left(\frac{z\beta\pi}{h_2}\right) \sin\left(\frac{N_1 h_1 \beta\pi}{N_2 h_2}\right). \tag{A.22}$$

Hence the extrema in the upper layer occur at

$$\frac{N_1(H-z)\beta}{N_2 h_2} = \frac{1}{2}, \frac{3}{2}, \frac{5}{2}, \cdots . \tag{A.23}$$

A.1.3 Summary

β-modes are due to the lower layer stratification, since their $O(1)$ phase speed $c^0 = \frac{N_2 h_2}{\beta\pi}$ only depends on $N_2 h_2$. α-modes are associated with the upper layer stratification, since their $O(1)$ phase speed $c^0 = \frac{N_1 h_1}{(\alpha+\frac{1}{2})\pi}$ only depends on $N_1 h_1$. The n^{th} mode can be either an α-mode or a β-mode, since its phase speed is the n^{th} element of the ranked series of the two sets of phase speeds.

β-modes have β zero crossings in their u-eigenfunctions in the lower layer at the following fixed positions:

$$\frac{\beta z}{h_2} = \frac{1}{2}, \frac{3}{2}, \frac{5}{2}, \cdots, \frac{2\beta-1}{2}. \tag{A.24}$$

The remaining $(n-\beta)$ zero crossings occur in the upper layer at

$$\frac{N_1(H-z)\beta}{N_2 h_2} = \frac{1}{2}, \frac{3}{2}, \frac{5}{2}, \cdots, \frac{2(n-\beta)-1}{2}. \tag{A.25}$$

α-modes have $(\alpha+1)$ zero crossings in their u-eigenfunctions in the upper layer at the following fixed positions:

$$\frac{(H-z)}{h_1}(2\alpha+1) = 1,3,5,\ldots,(2\alpha+1). \tag{A.26}$$

The remaining $(n-\alpha-1)$ zero crossings occur in the lower layer at

$$\frac{N_2 z}{N_1 h_1}(2\alpha+1) = 1,3,5,\ldots,(2(n-\alpha-1)-1). \tag{A.27}$$

The order of ranking of the two sets of phase speeds depends solely on the ratio $\frac{N_1 h_1}{N_2 h_2}$.

A.2 Model 2 — Well mixed surface layer overlying a deep layer of constant N^2

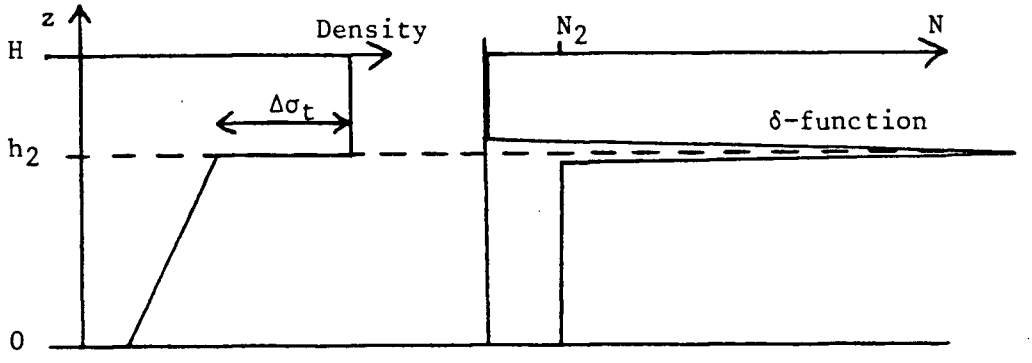

Figure 118 Density and N structure used in Model 2. $H = h_1 + h_2$.

This profile was used by Baines (1982) in an analysis of internal tide generation by the continental slope, and by Stacey (1985) in his study of the internal tide in Knight Inlet. See *Figure 118* for the density and N strucure. Assuming that $\omega^2 \ll N^2$ and making the rigid lid approximation, as in Model 1, one obtains the solution

$$Z_1 = \left(\frac{H-z}{h_1}\right) \sin\frac{N_2 h_2}{c}, \tag{A.28}$$

$$Z_2 = \sin\frac{N_2 z}{c}, \tag{A.29}$$

with the following dispersion relation:

$$(c^2 - g'h_1)\tan\frac{N_2 h_2}{c} + N_2 h_1 c = 0. \tag{A.30}$$

where $g' \equiv \frac{g\Delta\rho_0}{\bar{\rho}_0}$. This is the same dispersion relation as obtained by Stacey (1985, equation 13). Again, suppose that

$$\varepsilon \equiv N_2\sqrt{\frac{h_1}{g'}} \ll 1. \qquad (A.31)$$

By analogy with the ε defined in equation A5 for Model 1, this ε can be thought of as the ratio of the lower layer N-value to the mean upper layer N-value $\sqrt{\frac{g\Delta\rho_0}{\bar{\rho}_0 h_1}}$ if the δ-function in N^2 at the interface were smeared out over the upper layer. Expanding all variables as an asymptotic expansion in powers of ε, as given by equations A6–A8, the dispersion relation becomes

$$(c^2 - g'h_1)\tan\frac{N_2h_2}{c} \quad + \quad \varepsilon c\sqrt{g'h_1} \quad = \quad 0. \qquad (A.32)$$

It is not necessary to replace the N_2 by ε when it occurs with an h_2, because N_2h_2 is not a small quantity. To $O(1)$ this is

$$(c^{0^2} - g'h_1)\,\tan\frac{N_2h_2}{c^0} \quad = \quad 0, \qquad (A.33)$$

which has solutions

$$c^0 = \sqrt{g'h_1} \qquad \text{(the "surface mode")},$$

or

$$c^0 = \frac{N_2h_2}{\beta\pi}, \qquad \beta = 1,2,3\ldots \qquad (\text{"}\beta\text{-modes"}).$$

The surface mode is associated with the density jump at the interface, and has an $O(1)$ phase speed of $\sqrt{g'h_1}$ as expected. The β-modes are associated with the lower layer stratification as in Model 1. The collapse of the infinite series of α-modes associated with the surface layer in Model 1 to a single surface mode in this model is analogous to the way in which an infinite series of modes in a continuously stratified model collapses to a single internal mode in a model with two layers of constant density.

A.2.1 The Surface Mode

The first two terms in the asymptotic expansion of c are

$$c^0 = \sqrt{g'h_1}, \tag{A.34}$$

$$c^1 = -\frac{c^0}{2}\cot\frac{N_2h_2}{c^0} \tag{A.35}$$

$$c^2 = \ldots$$

and the $O(1)$ term of the eigenfunction is

$$Z_1^0 = \left(\frac{H-z}{h_1}\right)\sin\frac{N_2h_2}{c^0}, \tag{A.36}$$

$$Z_2^0 = \sin\frac{N_2z}{c^0}. \tag{A.37}$$

This eigenfunction is illustrated in *Figure 119* for various values of $\frac{N_2h_2}{c^0}$.

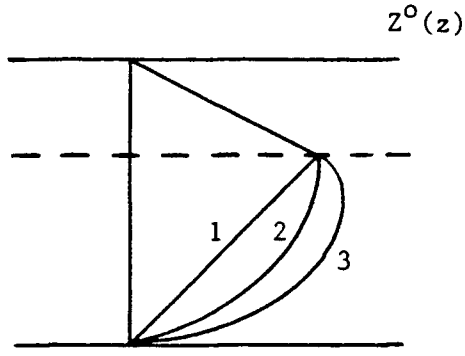

Figure 119 $O(1)$ eigenfunctions for the surface mode.
Case 1: $\frac{N_2h_2}{c^0} < \frac{\pi}{2}$, case 2: $\frac{N_2h_2}{c^0} = \frac{\pi}{2}$, case 3: $\frac{N_2h_2}{c^0} > \frac{\pi}{2}$.

A.2.2 "β-modes" or "Lower Layer Modes"

The first two terms in the asymptotic expansion of c are

$$c^0 = \frac{N_2h_2}{\beta\pi}, \tag{A.38}$$

$$c^1 = \frac{c^{0^2}\sqrt{g'h_1}}{\beta\pi\left(c^{0^2} - g'h_1\right)} \tag{A.39}$$

$$c^2 = \ldots$$

and the $O(1)$ term of the eigenfunction is

$$Z_1^0 = 0, \tag{A.40}$$

$$Z_2^0 = \sin \frac{z\beta\pi}{h_2}. \tag{A.41}$$

See *Figure 117.*

A.2.3 Summary

The surface mode is associated with the density jump at the interface, and to $O(1)$ has a phase speed of $\sqrt{g'h_1}$. The β-modes are associated with the lower layer stratification, and to $O(1)$ have phase speeds of $\frac{N_2h_2}{\beta\pi}$. As before, the n^{th} mode could either be one of the β-modes or the surface mode; it will be the n^{th} largest element of the set

$$\left\{\sqrt{g'h_1}, \quad \frac{N_2h_2}{\beta\pi};\ \beta = 1, 2, 3\ldots\right\}.$$

However, in the summer the first mode is most likely to be the surface mode.

The zero crossings in the u-eigenfunction will be at

$$z = \begin{cases} h_2, & \text{if } \frac{N_2h_2}{\sqrt{g'h_1}} < \frac{\pi}{2}; \\ \frac{\pi\sqrt{g'h_1}}{2N_2}, & \text{if } \frac{N_2h_2}{\sqrt{g'h_1}} \geq \frac{\pi}{2} \end{cases}$$

for the surface mode, and at

$$\frac{\beta z}{h_2} = \frac{1}{2}, \frac{3}{2}, \frac{5}{2}, \cdots, \frac{2\beta - 1}{2} \tag{A.42}$$

for the β-modes. There will be an additional zero crossing at the interface $z = h_2$ for β-modes when $n > \beta$ (e.g. the $\beta = 2$ mode acting as mode 3). This additional zero crossing comes from the $O(\varepsilon)$ expansion of Z_1.

Bibliography

BAINES, P.G. (1982) On internal tide generation models. *Deep Sea Research*, **29(3A)**, 307–338.

BLACKFORD, B.L. (1978) On the generation of internal waves by tidal flow over a sill – a possible nonlinear mechanism. *J. Mar. Res.*, **36(3)**, 529–549.

———(1984) Effect of a Tidal Stream on Internal Wave Observations and Predictions. *Atmosphere-Ocean*, **22(2)**, 125–143.

BROWN, P.J. (1973) Kelvin wave reflection in a semi-infinite canal. *J. Mar. Res.*, **31**, 1–10.

BUCHWALD, V.T. (1968) The diffraction of Kelvin waves at a corner. *J. Fluid Mech.*, **31**, 193–205.

———(1971) The diffraction of tides by a narrow channel. *J. Fluid Mech.*, **46**, 501–511.

BUCKLEY, J.R. (1980) A linear model of internal tides in sill fjords. In: *Fjord Oceanography*. H.J. Freeland, D.M. Farmer, and C.D. Levings, eds., Plenum Press, New York, 165–171.

FARMER, D.M. and FREELAND, H.J. (1983) The physical oceanography of fjords. *Progress Oceanog.*, **12**, 147–220.

FARMER, D.M. and SMITH, J.D. (1978) Nonlinear internal waves in a fjord. In: *Hydrodynamics of Estuaries and Fjords*, J.NIHOUL,ed., Elsevier Oceanography Series, No. 23, 465–494.

———(1980a) Tidal interaction of stratified flow with a sill in Knight Inlet. *Deep Sea Research*, **27A**, 239–254.

———(1980b) Generation of lee waves over the sill in Knight Inlet. In: *Fjord Oceanography*. H.J. Freeland, D.M. Farmer, and C.D. Levings, eds., Plenum Press, New York, 259–270.

FOREMAN, M.G.G. (1977) Manual for Tidal Heights Analysis and Prediction. *Pacific Mar. Sci. Report* 77–10, Institute of Ocean Sciences, Patricia Bay, B.C., 101pp.

———(1979) Tidal Analysis Based on High and Low Water Observations. *Pacific Mar. Sci. Report* 79–15, Institute of Ocean Sciences, Patricia Bay, B.C., 39pp.

FREELAND, H.J. (1984) The Partition of Internal Tidal Motions in Knight Inlet, B.C. *Atmosphere-Ocean*, **22(2)**, 144–150.

FREELAND, H.J. and FARMER, D.M. (1980) Circulation and Energetics of a Deep, Strongly Stratified Inlet. *Can. J. Fish. and Aquatic Sci.*, **37(9)**, 1398–1410.

FREELAND, H.J., FARMER, D.M. and LEVINGS, C.D. (1980) *Fjord Oceanography*, Plenum Press, New York, 715pp.

GILL, A.E. (1982) *Atmosphere-Ocean Dynamics*. Academic Press, New York, 662pp.

HALPERN, D. (1971a) Observations of short-period internal waves in Massachusetts Bay. *J. Mar. Res.*, **29**, 116–132.

———(1971b) Semi-diurnal internal tides in Massachusetts Bay. *J. Geophys. Res*, **76(27)**, 6573–6584.

HECHT, E. and ZAJAC, A. (1974) *Optics*. Addison-Wesley Publishing Co., Don Mills, Ontario, 565pp.

HENDERSHOTT, M.C. and SPERANZA, A. (1971) Co-oscillating tides in long narrow bays; the Taylor problem revisited. *Deep Sea Research*, **18**, 959–980.

JAMART, B.M. and WINTER, D.F. (1980) Finite element computation of the barotropic tides in Knight Inlet, B.C. In: *Fjord Oceanography*. H.J. Freeland, D.M. Farmer, and C.D. Levings, eds., Plenum Press, New York, 283–290.

LEBLOND, P.H. and MYSAK, L.A. (1978) *Waves in the Ocean*. Elsevier Scientific Publishing Co., New York, 602pp.

LONG, R.R. (1975) Circulations and density distributions in a deep, strongly stratified, two-layer estuary. *J. Fluid Mech.*, **71**, 529–40.

MØRK, G. and GJEVIK, B. (1982) Numerical Simulations of Internal Wave Generation in Sill Fjords. In: *Coastal Oceanography*. H.G. Gade, A. Edwards and H. Svendsen, eds., Plenum Press, New York, 397–410.

PACKHAM, B.A. and WILLIAMS, W.E. (1968) Diffraction of Kelvin waves at a sharp bend. *J. Fluid Mech.*, **34**, 517–529.

PEARSON, C.E. and WINTER, D.F. (1975) Analysis of stratified inlet flow by the method of weighted residuals. Symposium on modeling of transport mechanisms in oceans and lakes, Canada center for Inland Waters, Burlington, Ontario, Oct.6–8.

PICKARD, G.L. (1956) Physical features of B.C. inlets. *Trans. Roy. Soc. Can.*, Series III, **50**, 47–58.

———(1961) Oceanographic features of inlets in the B.C. mainland coast. *J. Fish. Res. Bd. Canada*, **18(6)**, 907–999.

———(1975) Annual and longer term variations of deepwater properties of the coastal waters of southern B.C. *J. Fish. Res. Bd. Canada*, **32**, 1561–1587.

PICKARD, G.L. and RODGERS, K. (1959) Current measurements in Knight Inlet, B.C. *J. Fish. Res. Bd. Canada*, **16(5)**, 635–678.

PICKARD, G.L. and TRITES, R.W. (1957) Fresh water transport determination from the heat budget with applications to B.C. inlets. *J. Fish. Res. Bd. Canada*, **14(4)**, 605–616.

PNUELI, A. and PEKERIS, C.L. (1968) Free tidal oscillations in rotating flat basins of the form of rectangles and of sectors of circles. *Philos. Trans. Roy. Soc. London*, **A, 263**, 149–171.

STACEY, M.W. (1984) The Interaction of Tides with the Sill of a Tidally Energetic Inlet. *J. Phys. Oceanogr.*, **14(6)**, 1105–1117.

———(1985) Some aspects of the Internal Tide in Knight Inlet, B.C. (in press, *J. Phys. Oceanogr.*, 1985.

STIGEBRANDT, A. (1976) Vertical diffusion driven by internal waves in a sill fjord. *J. Phys. Oceanogr.*, **6**, 486–495.

———, A. (1980) Some aspects of tidal interaction with fjord constricions. *Est. Coast. Mar. Sci.*, **11**, 151–166.

TAYLOR, G.I. (1920) Tidal Oscillations in Gulfs and Rectangular Basins. *Proc. London Math. Soc.*, **20**, 148–181.

VAN LEER, J.C.; W. DÜING, R. ENRATH, E. KENNELLY and A. SPEIDEL. (1974) The Cyclesonde: An unattended vertical profiler for scalar and vector quantities in the upper ocean. *Deep Sea Research*, **21**, 385–400.